Modelling Shear-Induced Platelet Aggregation in General Flow

Thesis submitted to the College of Engineering and Informatics, National University of Ireland, Galway in fulfillment of the requirements for the degree of

Doctor of Philosophy

Month 2016

Rudolf de Almeida Prado Hellmuth, MSc, Eng

Supervisor: Nathan J. Quinlan and Mark S. Bruzzi

Dedicated to the love of my life, Ana Carolina.

Acknowledgements

This thesis is dedicated to my adorable wife Ana, who supported me with love during these long years of post-graduate studies. I am truly and forever grateful.

I would like to thank to my family, my parents Harald and Margarida, and my parents in law Léo and Lucia, who have been faithfully supportive to both me and Ana while we were living in Ireland.

I would like to express my sincere appreciation to Dr. Marina Kameneva for her guidance and encouragement, not only throughout the months she hosted me in her laboratory in Pittsburgh, but also for on distance by e-mail. I am grateful to Dr. William Wagner and John Murphy for facilitating my placement in Dr. Kameneva laboratory at the McGowan Institute for Regenerative Medicine. Special thanks to Salim Olia, Megan Jamiolkowski, and the other friends from Dr. Kameneva's laboratory.

I also want to thank my friends from Galway, who made my stay in Galway more enjoyable. Special thanks to Ewa and Michał Klusak, Izabela Liszka, Mihai Basa, Libor Lobovský, Rory Sweeney, and all my other fellow PhD students. A big thank you to my friends from NUIG fencing club, and the gang from the trad sessions in Garvey's Bar.

I appreciate the funding of the Higher Education Authority (HEA) of Ireland to the Biomedical Engineering and Regenerative Medicine (BMERM) program. Special thanks to Prof. Peter McHugh, who has worked hard to establish the BMERM program.

Rudolf de Almeida Prado Hellmuth

National University of Ireland, Galway

Month 2016

Abstract

Blood-contacting biomedical devices are ubiquitous in current medical practice. Blood is very sensitive to non-physiological conditions, and it can be harmed by the biomedical device in a number of different ways. A very common and frequently fatal consequence of blood damage is thrombosis, which occurs when platelets and fibrin aggregate. Thrombosis occurs after intricate processes involving proteins of the coagulation and immune systems, thrombogenic surfaces, platelets, lymphocytes, and blood flow. This thesis is concerned with mathematical modelling of one aspect of the thrombosis process, namely the aggregation of platelets in shear flow. Yet, most of those models represented the growth of thrombi on thrombogenic surfaces, ignoring the possibility of thrombi forming in the bulk of flowing blood.

A mathematical model for shear-induced platelet aggregation (SIPA) was derived using aggregation and breakup rate equations controlled by shear rate. In this model, activated platelets adhere due to mutual collision caused by the flow of blood. On the other hand, viscous forces of flowing blood can also break up platelet aggregates, which might limit the aggregate growth. The aggregation and breakup effects form a mass-conservative population balance equation (PBE), which transforms cluster mass distribution (CMD) of platelets in time. Model parameters were determined by fitting experimental results from the literature, whose dynamics is determined by a dimensionless number called aggregation-breakup ratio. The aggregation-breakup ratio number is unique for the steady-state CMD, and it depends on shear rate, the total concentra-

tion of activated platelets, and empirical parameters. When aggregation rate is stronger than breakup rate, the CMD becomes similar to a log-normal distribution, whose mean value is determined by the aggregation-breakup ratio. On the other hand, when the aggregation ratio is weaker than the breakup ratio, just a relatively low concentration of small aggregates are observed.

Next, this 0-D model is coupled with the transport equation, in order to solve the spatial distribution of platelets aggregates in 3-D. Computational fluid dynamics (CFD) was used to simulated SIPA and aggregate transport in representative cases of blood flow found in medical devices. The 3-D computational model was verified against the 0-D model using a Couette flow simulation. The model was validated by comparing it with an experiment of SIPA in capillary tubes found in the literature, and with a clinical test called light transmission platelet aggregometry, where SIPA occurs in a stirred test tube. Other simulations included a microchannel with a sudden expansion mimicking a stenosis used in an experiment found in the literature, a flow over a crevice case, and flow between two eccentric cylinders. The sudden expansion in the microchannel showed that SIPA is not strong downstream from stenosis if wall adhesion is not occurring as well. In both the flow over a crevice and flow between two eccentric cylinders, platelet aggregates grew in the recirculation zone separated from the main flow field, where platelets got trapped in. The spatial evolution of the CMD was also analysed by dimensionless numbers, such as aggregation Péclet number and cell Damköhler number. The simulations demonstrate that SIPA is directly related to advective transport close to solid walls, where shear rates are highest. In most cases, advection is about three orders of magnitude stronger than SIPA, which generates very low concentration gradients of platelet aggregates. Thus, spatially heterogeneous concentration fields of aggregates are only observed when secondary flow fields, such as recirculation zones are observed. However, platelet aggregates grow intermittently at very slow rates in recirculation zones, because of low shear rates available there.

Finally, an experiment to measure and quantify SIPA in Couette flow is reported in detail. Time-resolved observations of SIPA were observed in a rheoscope, where platelets experienced a peak of high shear rates followed by a period of low shear rate. Platelets were very sensitive to activation when in contact with a viscosity-thickening polymer added to plasma to increase shear stress. Major care to decrease the content of fat in blood plasma had to be taken, because the viscosity-thickening polymer was found to precipitate fat particles which would aggregate with platelets. The CMD was successfully measured by image processing technique, and other measurement uncertainties were assessed and controlled.

The PBE model was able to replicate SIPA experiments, both in Couette flow and in general 3-D flow, where the CMD state could be observed evolving on time. Shear-induced platelet aggregation is a slow process compared to transport of platelets and aggregates, because the volume fraction of platelets in blood is too low for high platelet-platelet collision rates. Significant localized platelet aggregation is only observed for platelets trapped in recirculation zones, whose boundary with the primary flow stream presents high shear rates.

Contents

List of Figures

List of Tables

Nomenclature

Acronyms

AP Activated platelets.

CFD Computational fluid dynamics.

CFL Courant-Friedrichs-Lewy (condition).

CLT Central limit theorem.

CMD Cluster mass distribution.

EDM Enhanced diffusivity model.

LTPA Light transmission platelet aggregometry.

MHV Mechanical heart valve.

ODE Ordinary differential equation.

PBE Population balance equation.

PBS Phosphate buffered saline.

PDE Partial differential equation.

PMF Probability mass function.

PPD Platelet population distribution.

PPP Platelet-poor plasma.

PRP Platelet-rich plasma.

PVP Polyvinylpyrrolidone.

ADP Adenosine diphosphate.

RBC Red blood cell.

RMS Root mean square.

RP Resting platelets.

SIPA Shear-induced platelet aggregation.

VAD Ventricular assist device.

vWF von Willebrand factor.

WBC White blood cell.

Greek Symbols

$\dot{\gamma}$ Shear rate, s^{-1}.

ϵ Rate of energy dissipation, W.

Φ Volume concentration (or fraction), dimensionless.

ϕ Aggregate void fraction, %.

η Aggregation efficiency, %.

μ Dynamic viscosity, Pa s.

μ_0 Asymptotic viscosity at low shear rates, Pa s.

μ_∞ Asymptotic viscosity at high shear rates, Pa s.

μ_eff Effective viscosity of non-Newtoninan fluid, Pa s.

ν Kinematic viscosity, $m^2\,s^{-1}$.

ρ Density, $kg\,m^{-3}$.

$\boldsymbol{\sigma}$ Cauchy stress tensor, Pa.

$\boldsymbol{\tau}$ Shear stress tensor, Pa.

θ Polar coordinate, rad.

$\boldsymbol{\Psi}$ Drift diffusion potential, $m\,s^{-1}$.

Roman Symbols

a Linear paramenter of the break-up kernel, arbitrary dimensions.

a' Regularized linear paramenter of the break-up kernel, s^{-1}.

A_i Aggregation rate of cluster i, count $m^{-3}\,s^{-1}$.

A Area, m^2.

b, c Exponent parameters of the break-up kernel, dimensionless.

B_i Breakup rate of cluster i, count $m^{-3}\,s^{-1}$.

Co Courant number (CFL condition), dimensionless.

$\tilde{C}_i$ Relative concentration of aggregation cluster i in the PPD.

C_i Concentration of aggregation cluster i in the CMD, count m^{-3}.

C_p Absolute concentration of activated platelets, count m^{-3}.

Da Damköhler number, dimensionless.

D Brownian diffusivity, $\mathrm{m}^2\,\mathrm{s}^{-1}$.

D_E Euclidian dimension.

D_e Enhanced diffusivity, $\mathrm{m}^2\,\mathrm{s}^{-1}$.

D_F Fractal dimension.

$\boldsymbol{E}$ Strain rate tensor, s^{-1}.

f Collision rate, s^{-1}.

g Fragment mass distribution, dimensionless.

G Absolute shear rate, s^{-1}.

G^* Characteristic shear rate of the break-up kernel, s^{-1}.

Ht Haematocrit, %.

I_0 Zero angle light intensity.

k_B Boltzmann constant, $\mathrm{J\,K}^{-1}$.

k_b Pandya and Spielman breakup kernel, $\mathrm{m}^3\,\mathrm{s}^{-1}$ count^{-1}.

k_c Smoluchowski collision kernel, count^{-1} $\mathrm{m}^3\,\mathrm{s}^{-1}$.

k_d Diffusion collision kernel, $\mathrm{m}^3\,\mathrm{s}^{-1}$ count^{-1}.

k_s Shear collision kernel,count^{-1} $\mathrm{m}^3\,\mathrm{s}^{-1}$.

K_d Dissociation constant, arbitrary dimensions.

K_{ab} Aggregation-breakup ratio, dimensionless.

$\boldsymbol{L}$ Velocity gradient tensor, s^{-1}.

M_j Distribution moment of order j, count m^{-3}.

$\hat{\boldsymbol{n}}$ Normal unitary vector, dimensionless.

PA Fraction of aggregated platelets, %.

$PA_{\max}$ Steady-state fraction of aggregated platelets, %.

Pe Péclet number for cluster colision, dimensionless.

P Probability mass function (PMF).

Q Flow rate, $\mathrm{m}^3\,\mathrm{s}^{-1}$.

Re Reynolds number, dimensionless.

r Radial coordinate, m.

R_i Radius of gyration of aggregation cluster i, m.

R_p Mean radius of a platelet, m.

$\langle R \rangle_{\mathrm{RMS}}$ RMS radius of gyration, m.

R Radius of an object, m.

t Time, s.

t_a Characteristic aggregation time, s.

t_b Characteristic breakup time, s.

t_d Characteristic time of collisions by diffusion, s.

t_s Characteristic time of collisions by shear, s.

T Absolute temperature, K.

$\boldsymbol{v}$ Velocity, m s.

V Volume, m^3.

V_i Volume occupied by platelets in aggregate cluster i, m^3.

$\tilde{V}_i$ Apparent volume of aggregation cluster i.

$\langle w \rangle$ Mean number of platelets per cluster.

w_i Number of platelets in aggregation cluster i.

$\boldsymbol{W}$ Rigid-body rotation tensor, s^{-1}.

Operators

$\bar{x}$, $\langle x \rangle$ Average of quantity x.

$\boldsymbol{j}_x$ Flux of a quantity x, quantity x $\mathrm{m\,s}^{-1}$.

σ_x Standard deviation of quanitity x.

$\hat{x}$ Scaled quantity x, dimensionless.

[x] Concentration of a quantity x, m^{-3}.

Chapter 1

Introduction

This thesis covers mathematical models for thrombosis, and it focuses more specifically on thrombosis initiated in the bulk of blood flow, rather than on a thrombotic surface. Thrombi, which are normally found on the surface of damaged vessels or foreign materials, produce thrombogenic agonists, which activate platelets passing by in the bulk of the blood flow. Activated platelets aggregate upon collision caused by flowing streams, a phenomenon known as shear-induced platelet aggregation (SIPA). In this thesis, a mathematical model for the formation and evolution of platelet aggregate clusters is presented. This model is coupled with computational fluid dynamics (CFD) to predict SIPA in blood-contacting medical devices.

The mitigation of blood damage is a point of high concern in the design of blood-contacting biomedical devices. Blood damage includes haemolysis (either the partial rupture or complete destruction of erythrocytes), platelet and lymphocyte activation, alteration of the coagulation cascade, reduced functionality of lymphocytes, and destruction of von Willebrand factor (vWf) [7, 68, 88, 178]. The most common outcome of blood damage is thrombosis, which is the aggregation of platelets and coagulation of fibrin that can obstruct blood vessels. Biomedical devices normally initiate thrombosis either because of the chemistry of the exposed surface or by altering the characteristics

of blood flow. In either case, it initiates thrombus formation by activating platelets, which simultaneously enables them to aggregate and triggers the coagulation cascades. More commonly, aggregates form on the surface of the foreign material, but they can also form in the bulk of the blood. The latter case, which is the topic of this thesis, has not been studied as extensively as the former. Platelet aggregation far from a surface is modelled for simulation of SIPA in biomedical devices and diseased vessels. The ultimate goal of developing mathematical models for thrombosis is to give more reliable tools for engineers to improve blood compatibility of biomedical devices.

1.1 Blood Compatibility with Biomedical Devices

The theoretical definition of biocompatibility has evolved during the past decades. It used to be classically defined by Williams [230] as "the ability of a material to perform with an appropriate host response in a specific application". This definition was intended to address long-term implantable devices, whose materials should become inert at the specific place of implantation. However, complete inertness in any physiological situation has not been achieved by any artificial material, and newly developed biomedical devices demand materials which react with the host body, such as drug-eluting stents and tissue engineering scaffolds. Hence, the definition of biocompatibility has become more complex and diverse, with different definitions holding for different biomaterial applications. More recently, Williams [231] has devised a new definition for implantable devices: "The biocompatibility of a long term implantable medical device refers to the ability of the device to perform its intended function, with the desired degree of incorporation in the host, without eliciting any undesirable local or systemic effects in that host".

More specifically for blood-contacting devices, biocompatibility relates not solely to the blood and vessel damage caused by the material, but also to the physiologi-

cal reactions caused by the device's hydrodynamics. Notwithstanding the fact that no material has been found to be totally inert, many cardiovascular devices function with acceptable risks of complication [178]. Even when the risk of thrombotic complication appears to be low (varying between 2% and 10% depending on the device [88]), it may have fatal outcomes and the cost associated with the follow-up intervention is not negligible. The mandatory life-long anticoagulant drug therapy, which induces vulnerability to haemorrhage and is not a viable therapy for some patients, does not eliminate this risk. Thrombotic complications with cardiovascular devices occur despite the use of antiplatelet and anticoagulant therapies, reinforcing the inherent thrombogenicity of the materials [88, 177]. The thrombogenicity of the materials is strongly regulated by blood flow dynamics, which in many cases can be engineered in order to minimise thrombogenesis potential. However, the design of blood-contacting devices has improved in the last decades mostly by comparing outcomes of devices with their physical features. Much better optimisation strategies could be addressed if quantitative mathematical models of thrombosis were available [13, 12].

Blood coagulation is the physiological response to a traumatic event, such as injury at the vessel wall, exposure to a foreign material or diseases [88]. They trigger complex series of events that leads to the formation of fibrin, the fibrous protein that interconnects and stabilises platelet aggregates, forming a clot [52, p. 982]. Blood may also coagulate as a result of an inflammatory response to a foreign surface [164], because the immune and the coagulation systems are able to communicate in order to provide ample protection against invaders [147]. Figure 1.1 depicts the ways whereby these systems communicate to form a thrombus over a blood-contacting implant. Blood flow dynamics near the implant is a very important factor of blood compatibility, because it has the potential of activating platelets [38, 194] as well as of washing proteins away [7, 142]. Understanding blood coagulation is, thus, not only essential in the development of non-thombogenic prosthetics, but also in the treatment of bleeding

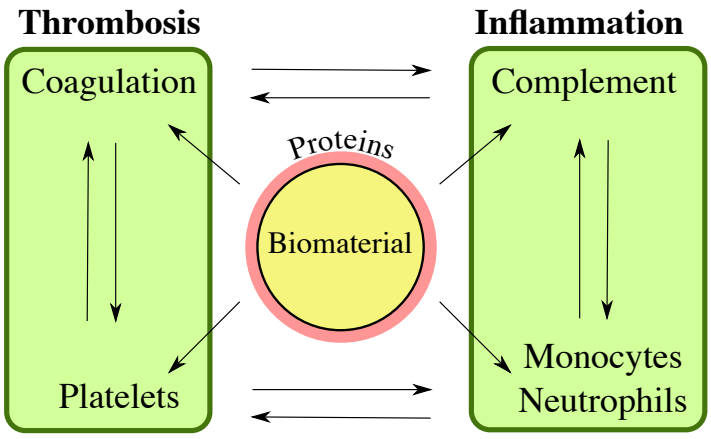

Fig. 1.1: Overview of blood–material interactions showing the components relevant to thrombosis. Arrows indicate activation of components associated with the thrombosis (left-hand side) and inflammation (right-hand side). The foreign biomaterial is firstly detected by a layer of adsorbing plasma proteins. They initiate a series of interconnected reactions leading to both inflammation and thrombosis [88].

disorders.

1.2 Blood-Contacting Biomedical Devices

Yearly, many implantable blood contacting devices have provided life-saving solutions to patients with severe cardiovascular diseases (see Table 1.1). However, common problems of haemolysis and thromboembolism remain an impediment to these devices, dictating the need to drastically reduce their complication rates.

More than 5.3 million patients suffered from heart failure in 2000 and this number is expected to grow by 50% over the next 15 years [32]. A significant proportion of those patients will not be immediate recipients of heart transplants, because of lack of donors. Therefore, they become candidates for receiving ventricular assist devices (VAD) to help to maintain safe levels of cardiac output and blood pressure. The REMATCH study [209] indicated that left ventricular assist devices (LVAD) are superior to drug therapy (48% decrease in mortality), paving the way for their use as long-term heart

Table 1.1: Worldwide usage estimation of common blood-contacting medical devices in 2007 [176].

Device	Blood-contacting material	Number per year
Catheters	Silicone, polyurethane, PVC, PTFE	200,000,000
Guidewires	Stainless steel, nitinol	Millions
Pacemaker	Silicone, polyurethane, platinum	300,000
Vascular graft	Dacron, PTFE	200,000
Heart valve	Pyrolytic carbon, dacron, fixed natural tissue	200,000
Stents	Stainless steel, styrene-isobutylene polymer	4,000,000
Extracorporeal oxygenation	Silicone rubber	20,000
Artificial kidney	Polyacrylonitrile, polysulfone, cellulose	1,200,000
Left ventricular assist device (LVAD)	Polyurethane	1000
Glucose or lactate sensors (experimental devices)	Hydrogels	No data

Fig. 1.2: Prosthetic heart valves. From left to right: ball in cage, tilting-disc, and bileaflet. Image reproduced from Zilla *et al.* [244].

replacement therapy for patients not eligible for heart transplants. However, VAD patients still suffer from unacceptable survival rates (only a 30% 2 year survival), and high complication rates of thromboembolism (3–35%) and strokes (16%).

Another common cardiovascular implantable device is the mechanical heart valve (MHV). Over 140,000 MHVs are implanted worldwide each year, with more than 45,000 implantations in the US alone [173]. Heart valves open and close over 40 million times per year [178, p. 2]. Disease and mechanical fatigue can deteriorate their function, making surgical repair necessary. There are many types of prosthetic heart valves (PHV) and they are fabricated from biomaterials like metals, elastomers, polymers, pyrolytic carbon (PyC), and chemically treated animal or human conjunctive tissues. Figure 1.2 shows some models of PHV that were designed over its history of more than 50 years. Generally, cardiac function is restored to near normal conditions almost as soon as the valve is implanted.

The successful development of PyC biomaterial during the late 1960s has drastically improved the biocompatibility of MHVs. Pyrolytic carbon (PyC) is the current state of the art in mechanical heart valve material technology. It provides outstanding blood compatibility and structural properties needed for long-term use. Therefore,

95% of the mechanical heart valves implanted worldwide have at least one structural component coated by this material. Pyrolytic carbon is fabricated by the pyrolysis, or thermal decomposition, of hydrocarbons in the absence of oxygen. It is believed that PyC's blood compatibility comes from its chemical inertness and its ability to quickly adsorb blood proteins without triggering denaturing reactions. Blood proteins on PyC do not suffer sensitive conformational changes, which passivates the surface. Prior to PyC, only surfaces coated with graphite, benzylalkonium chloride and heparin would resist thrombus formation when exposed to blood for long periods [178, p. 171]. Despite the advantages of PyC, its blood compatibility is not perfect and chronic anti-coagulant therapies is still needed for patients with this mechanical heart valves [178, p. 178-180].

The formation of thrombo-emboli in blood-contacting devices is influenced by regional flow phenomena. Traditionally, flow-induced blood trauma was almost exclusively studied in respect to haemolysis. However, recently it was shown that platelet activation and thrombogenesis is the most sensitive aspect of this blood trauma [183]. Erythrocytes are much more resistant to mechanical stresses than platelets, because erythrocytes are very elastic. Haemolysis and haemostasis are both aggravated for high exposure times. At exposure times of the order of minutes, haemolysis may occur at shear levels one order of magnitude larger ($\gtrsim 50\,\mathrm{Pa}$) than those required to activate platelets ($\gtrsim 5\,\mathrm{Pa}$) [7, 68, 126]. At shear stress levels lower than those that cause haemolysis, multimers of vWF undergo conformational change and attach to foreign surfaces and platelets, causing platelet aggregation followed by activation. Recent studies contrasting haemolysis by leakage flow with platelet activation in MHV demonstrated that while haemolysis barely increased [137], platelet activation increased between three- to eight-fold [34].

The non-physiological flow patterns generated in the devices are considered as one of the major culprits in enhancing the haemostatic response by chronically activat-

ing platelets. Yet, in the lack of appropriate methodology, it is necessary to rely on free assumptions based on previous experiences to optimise the device thrombogenic performance during the research and development (R&D) of medical devices. This means that they are likely to follow designs that have been proven to perform better in long-term clinical trials and animal experiments, rather than try new ideas based on scientific data. Hence, the development of reliable mathematical models is imperative for the future development of blood-contacting cardiovascular devices.

1.3 The Goals of Mathematical Modelling

The early stages of scientific investigation involve identification and classification of every element of the system in study. As the system's taxonomy becomes clearer, knowledge progresses by investigating the interactions between each individual element to fulfil the system's function as a whole. Lastly, the system dynamics are examined in order to quantitatively predict the influence of each interaction to the outcomes. Although these stages may interweave throughout scientific exploration, the research methodology applied for investigating each of them differ. The early stage is achieved primarily by observation, the second by qualitative experimentation, and the last by quantitative mensuration and mathematical modelling. While all those stages were extensively explored in many scientific fields, such as physics, chemistry, and biology research, to this day, is rarely done at the quantitative stage, due to the complexity and diversity of biological systems. Physicists praise the power of mathematical modelling for systems analysis, while biologists are still sceptical of what they term a "reductionist approach" [35, 149]. Nevertheless, this scepticism is decreasing as the knowledge advances and biologists begin to explore systems dynamics, the last stage of scientific progress [98, 13].

Mathematical modelling of natural phenomena enables one to better understand

natural processes, and in many cases enables one to reproduce and alter these processes in one's favour. Mathematical modelling provides a means of supporting experimental data and hence, forms a clearer picture of complex systems. The complexity of haemostasis is such that it is impossible to break down its dynamics without modelling. In fact, theoretical models have already helped to predict some kinetic stages of the blood coagulation cascades, before they were proved experimentally [12].

Even though mathematical modelling of blood damage is still primitive, a few complex mathematical models have been used to improve the performance of ventricular assistant devices (VADs) in terms of haemolysis [39, 68, 233] and thrombogenesis [32]. Of the two most studied modes of blood damage by medical devices, haemolysis and thrombogenesis, the latter is less understood, due to its complexity [68]. Realistic models of thrombosis would have the potential to predict regions susceptible to thrombus formation, as well as to track the extent of thrombosis once it is initiated. Engineers could apply mathematical models of haemodynamically induced thrombosis as tools for designing vascular implants such as stents, grafts and artificial valves, and procedures such as aneurysm coiling and vascular grafting. The success or failure of such procedures depends strongly on how the devices affect the coagulation mechanism. However, there is currently no standard, robust and reliable model available. Future design of cardiovascular devices may benefit tremendously from such models.

Other important advantages of mathematical modelling are the lower cost and execution time. Laboratories often require a large infrastructure of equipment and technicians to provide support to experiments. Therefore, the investment must be paid off by production of data in large scale, which requires queueing of the planned experiments. As expected, many times experiments either fail or produce unanticipated outcomes, thus demanding new rounds of expensive experiments. Mathematical modelling is a valuable tool in this kind of research, because it provides a rapid and inexpensive way to simulate experiments. By previously analysing possible outcomes, it would be pos-

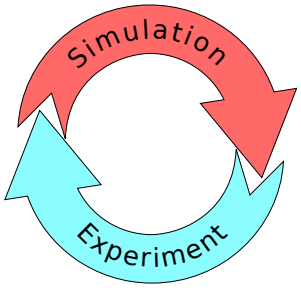

Fig. 1.3: Laboratory-modelling synergy.

sible to design more reasonable and focused experiments. Once more quantitatively reasonable experiments are performed, it is simpler to update and improve mathematical models, which creates a process of positive auto-improvement (depicted in Fig. 1.3). Mathematical models in essence can be as simple as an arithmetic equation, but in many cases they must be very sophisticated and abstract to properly and accurately represent real phenomena. In cases which require the observation of many degrees of freedom, direct solution of the models is impracticable and computer algorithms have to be implemented. The role of mathematical and computer modelling gradually becomes more and more important in the selection of the most effective experimental approaches, and blood coagulation is not an exception in this sense.

In recent decades, an explosion of mathematical modelling and computer simulation research in all areas of biochemistry and biology, including coagulation, has been observed. Ataullakhanov and Panteleev [12] state that there are two reasons for the rise in popularity of theoretical methods. First, efficient theoretical analysis is possible only when a sufficient amount of empirical information is collected. These authors mentioned the recent discovery of unknown components of the blood coagulation cascade in the early 1990s. Second, the complexity of biochemical systems makes analysis of mathematical models extremely complicated without computer simulation. Thus, the recent development of microcomputers was another stimulus for the use of mathematical modelling.

1.4 Objectives

The present work addresses the modelling of blood thrombosis caused by biomedical devices. Thrombosis is caused by a multitude of interacting mechanisms involving flow, foreign surface, and biochemistry. This thesis focuses on SIPA, a mechanism of thrombosis that has been less studied in the literature. Platelet aggregate growth and breakup is modelled as a population balance equation (PBE) of platelets, which alters the distribution of platelets in aggregate clusters of multiple sizes depending on flow shear rate. The PBE is correlated with experimental data of SIPA, and its dynamics is studied in terms of dimensionless quantities. Next, this model is coupled with CFD in order to simulate SIPA in complex blood flow situations. Finally, a protocol for experimentally measuring SIPA in real time is discussed.

1.5 Structure of this Thesis

In Chapter 2, the biological aspects of thrombosis are reviewed. They include the role of platelets, the serine protease coagulation system, and the immune system. Interactions between these aspects of coagulation and thrombosis are also discussed.

Chapter 3 consists of a review on the mathematical modelling of the physics and chemistry involved in thrombosis. Blood rheology takes a very important part in the transport of platelets, leukocytes, and chemical substances in blood flow. Red blood cells (RBCs) normally flow more concentrated at the centre of blood vessels, which causes a near wall excess of platelets and leukocytes. Moreover, the shearing of RBCs induces an augmented diffusion effect, which is strongest near the wall. The modelling of the reaction rates of the coagulation system is presented, along with a review of results in the literature that have been useful to understand the dynamics of positive and negative feedback loops in those enzymatic cascades. Chemical kinetics is also useful for modelling platelet activation and protein adsorption onto surfaces. A

historical review on the evolution of mathematical models of thrombosis is also present in Chapter 3. Earlier models encompassed fewer than ten rate equations, but more recent models encompass hundreds of rate equations and spatial transport of a number of species.

Chapters 4 and 5 treat platelet aggregation kinetics in flowing fluid. In Chapter 4, SIPA is analysed in time only, and the spatial distribution of aggregates and shear rate is considered uniform. A mass-conservative PBE is formulated, where aggregation rates of a cluster mass distribution (CMD) of platelets are computed by the Smoluchowski coagulation equation [222], and breakup rates by the empirical model devised by Pandya and Spielman [168, 169]. Several physical mechanisms that cause platelet collision are discussed, because collision rate controls aggregation rate. The aggregation-breakup PBE is correlated with experimental data from the literature, and its dynamics is analysed in terms of scaled quantities and dimensionless numbers. In Chapter 5 the SIPA model developed in Chapter 4 is extended to general flow. Simulations of computational fluid dynamics (CFD) of physiologically relevant cases are performed, and the PBE is solved both in space and time for an spatially inhomogeneous CMD. The solver consists of a series of transport equations for each bin of the CMD, where the PBE is treated as source terms controlled by shear rate.

Finally, Chapter 6 communicates an experimental test for measuring SIPA in real time. The experiments were conducted with fresh human platelet rich plasma (PRP) in a parallel-disk rheoscope, where shear rate is uniform and controlled by the rotational speed. The methodology of this experimental protocol is extensively discussed, including sample preparation, uncertainty analysis, aggregate classification, and aggregate measurement. A large number of video frames were recorded and processed by image analysis. Platelet aggregates were classified in bins forming a CMD. Peaks of high shear stresses broke large aggregates up, whereas low shear was essential for the growth of aggregates.

Chapter 2

Literature Review on Thrombosis and Haemostasis

Haemostasis is a complex process involving the kinetics of multiple proteins and cells, whose function is to stop bleeding and support the healing of severed vessels [52, 117]. Thrombosis is a dysfunction of the haemostasis process, whereby a clot is formed inside a blood vessel, obstructing the flow of blood through the circulatory system [12, 72, 190]. The aetiology of thrombosis depends on many factors, because haemostasis is complex, with many biochemical and biophysical triggers as well as many interacting loops of positive and negative feedback. The cells and proteins involved in haemostasis interact in various ways, which can change depending on the physiological state. Some effects are local, whereas others are systemic. This makes it somewhat unrealistic to separate the mechanisms leading to haemostasis in different conceptual boxes, for there are no independent systems whose stimulation would not be sensed by the others. Notwithstanding this fact, this chapter will be split into sections that may give a false impression of isolation of these mechanisms. This is done just for instructive purposes for more clarity.

The chapter begins with a short historical perspective on the pathophysiological

definition of thrombosis and haemostasis. Then, the roles of blood platelets, coagulation system, and the immune system for thrombosis and haemostasis are reviewed. Platelets are small blood cells that scan vessel surfaces for injuries, once they are chemically or mechanically stimulated by injury signals, they become activated. Activated platelets form a platelet plug in bleeding sites, what is known as primary haemostasis. Platelets have to aggregate to each other in order to produce primary haemostasis, but big aggregates can be harmful if they flow inside the circulatory system as an embolus. Either activated platelets or any other surface foreign to the circulatory system can trigger the coagulation system. The coagulation system is an enzymatic cascade that leads to the polymerisation of fibrin fibres. Fibrin fibres make platelet aggregates stronger and prevent further bleeding, therefore it is known as secondary haemostasis. The immune system physiologically interacts with platelets and coagulation by amplifying or even starting the haemostasis process. Any dysfunction in one of more of these three systems may lead to thrombosis. The literature review presented in this chapter is indispensable for understanding the next chapter (Chapter 3), where a literature review of the existing mathematical models describing the dynamics of haemostasis is presented.

2.1 Virchow's Triad

The first description of blood thrombi in the Western World dates from the 16th century, but the first theories of the aetiology of thrombosis arose only in the early 19^{th} century. At this time, the most accepted theory was authored by the famous French pathologist Jean Cruveilhier. He advocated that thrombogenesis was caused by venous inflammation (phlebitis). By the middle of the same century, in 1856, the German physician Rudolf Virchow was incensed by the idea that there was no scientific evidence for Cruveilhier's theory. He conducted a series of autopsies and meticulous

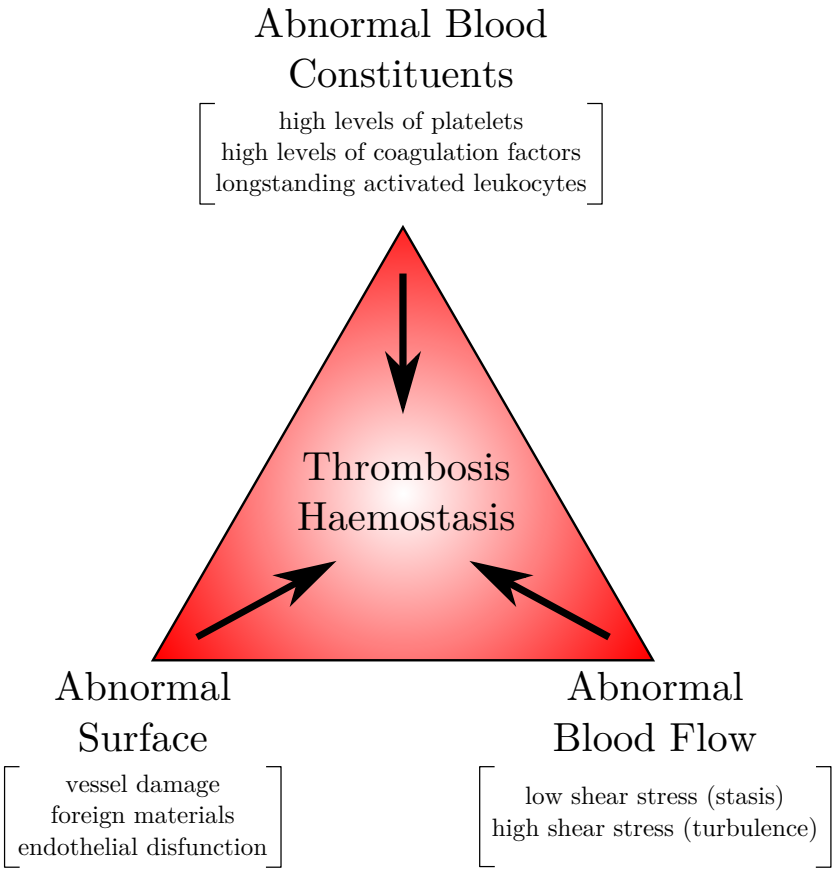

Fig. 2.1: Virchow's Triad.

experiments on dogs, where his results clearly refuted Cruveilhier's claims. Virchow laid out the mechanism of *embolisation* and pulmonary *thrombosis*, terms that were coined by him [219]. Nowadays, Virchow's Triad, illustrated in Fig. 2.1, is a model present in physiology textbooks. Although honoured in the Triad's name, Virchow himself was not the author. It dates from the mid-20$^{\text{th}}$ century [18].

Typically, a thrombus forms on a surface lacking a healthy endothelial covering, but it can also be initiated by abnormal levels of fluid shear stress, proteins and platelets in blood [72, 91, 133]. This includes local flow conditions, availability of membrane binding sites for catalysis, and concentrations of the biochemical factors involved in clot formation. The haemostatic system remains in an idle state, under sub-threshold

stimuli, which is primed to respond explosively once the threshold is crossed. During haemostasis, the system responds in a manner that eventually returns it to its idle state, while at the same time redressing the initial stimulus [52].

Haemostasis and *thrombosis* are related aspects of the Virchow's Triad, but whilst the former protects from bleeding after trauma, the latter is a disease mechanism. Haemostasis can either mean the stagnation of blood in any vessel or anatomical area or the arrest of bleeding from a damaged blood vessel. The opposite of haemostasis is *haemorrhage* [52, 117]. A damaged vessel can stop the bleeding of trivial injuries, whereas more serious haemorrhages require more substantial interventions. A *blood clot* consists of a fibrin matrix bound to platelet aggregates, erythrocytes, and leukocytes, within which plasma is entrapped. The fibrin fibres typically form less than 1% of the volume of the entire structure. There are three kinds of clots mentioned in the literature depending on the component proportions: *fibrin-rich clots*, *plasma clots* and *whole blood clots* [8].

2.2 Platelet Function

Platelets (or thrombocytes) are anuclear, small, discoid cell fragments, derived from megakaryocytes, and 3–4 µm in diameter (approximately 6 μm^3 in volume) [171]. When vascular harm occurs, platelets stick to exposed collagen and other subendothelial glycoproteins (*platelet adhesion*) to start the formation of a mechanical blockage. While this loose plug of platelets is being assembled, the endothelium of damaged blood vessels releases biochemical signals provoking vasoconstriction, which temporarily decrease blood flow and pressure within the vessel. Platelet plug and vasoconstriction simultaneously afford *primary haemostasis* to the wound. Clots form upon the stabilization of the platelet plug by a mesh of *fibrin* fibres, which grant *secondary haemostasis* to wounds [52, p. 982].

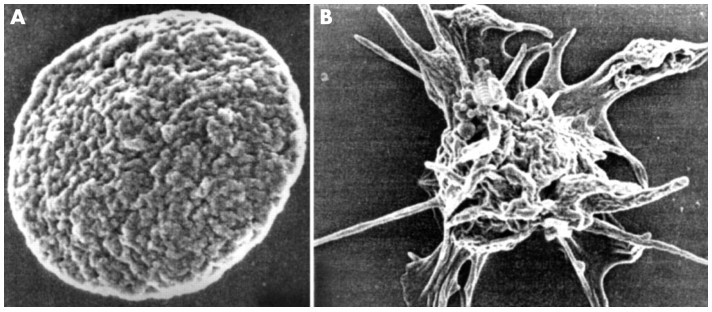

Fig. 2.2: Scanning electron micrographs showing morphological differences between (**A**) resting platelets and (**B**) activated platelets. Image reproduced from White [228].

When adhered, the resting discoid platelets undergo a series of chemical and morphological changes, and as a result, they become activated. Activated platelets release several biochemical signals which reinforce local vasoconstriction, activate more platelets, and stimulate the coagulation as well as the immune system. Activation can be started by either biochemical agonists or prolonged exposure to super-critical shear stresses [38, 161].

In flowing blood, red cells predominate in the centre of the blood vessel lumen, whereas platelets predominate along the margin of the vessel walls, where they are well positioned to monitor the integrity of the endothelium [3, 57, 243].

2.2.1 Platelet Activation

Platelet activation is the process by which the resting discoid platelet undergoes a series of chemical and morphological changes. As a result, the organelles get centralised, granules release their contents, glycoproteins on the platelet membrane change in conformation, and long pseudopods are extended. The pseudopods make activated platelets become a sticky, spiny, sphere. The morphological differences between resting platelets (RP) and activated platelets (AP) are displayed in Fig. 2.2.

Activation by Soluble Agonists

Platelet activation is stimulated or depressed by the detection of specific biochemical species (listed in Table 2.1) by receptors on the platelet membrane. The dynamics of the biochemistry of some of the most important factors controlling aggregation of a thrombus is illustrated in Fig. 2.3. Thrombin (IIa) is the most potent platelet activator, producing an effect at concentrations lower than those required for activation of the coagulation cascade [197]. Normally, endothelial cells inhibit platelet activation by producing nitric oxide (NO), endothelial-ADPase, prostacyclin (PGI2). Nitric oxide is a powerful vasodilator and inhibitor of platelet activation; endothelial-ADPase clears away the platelet activator adenosine diphosphate (ADP); and PGI2 function as an inhibitor of platelet activation as well as a vasodilator. When endothelium harm is detected by neighbouring endothelial cells, they stop secreting these substances. Besides endothelial-ADPase, there are other enzymes in plasma which break down ADP to AMP (adenosine monophosphate), which is a strong inhibitor of platelet activation. Therefore, sub-threshold release of ADP may inhibit activation as ADP decays [36].

Platelet activation results in at least five physiologic responses [88]:

1. Biologically active compounds stored in intracellular granules are secreted. The granules include ADP, serotonin, platelet-activating factor (PAF), vWF, coagulation factor XIII, and thromboxane A2 (TXA2), which, in turn, activate additional platelets.

2. P-selectin, a cell-surface glycoprotein is expressed. It plays an important role in mediating adhesion to neutrophils, monocytes and a set of lymphocytes.

3. The platelet eicosanoid pathway is initiated. The eicosanoid molecules function like local hormones controlling many systems, mainly inflammation and immunity.

Table 2.1: Activation and inhibition factors of platelets [88].

Effect	Stimulus
Activation	IIa, TXA2[a], PGH2, PGG2, vasopressin, PAF[b], 5−OH tryptamine (serotonin), epinephrine, ADP[c], ATP[d], PGE2, C1q, non-pysiological shear stresses.
Inhibition	AMP[e], NO[f], PGI2[g] , PGE1, PGD2.

Pertinent names: [a]thromboxane A2, [b]platelet activating factor, [c]adenosine diphosphate, [d]adenosine triphosphate, [e]adenosine monophosphate, [f]nitric oxide, and [g]prostacyclin.

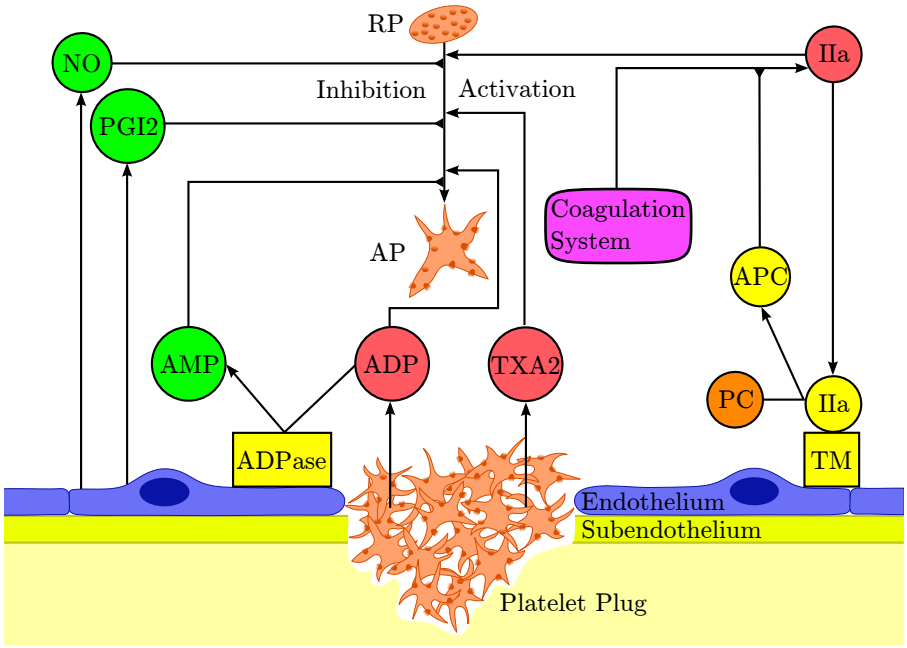

Fig. 2.3: Schematic diagram of primary haemostasis. In the centre, there is a platelet plug occluding a vascular injury, which is flanked by an intact endothelium. Resting platelets (RP) are activated by substances released by activated platelets (AP), such as ADP and TXA2. Thrombin (IIa), the key enzyme in the coagulation system, stimulate platelet activation as well. The coagulation system is inhibited by APC, which is activated by the interaction of TM on the surface of endothelial cells. Intact endothelium synthesises substances which inhibit the activation of platelets, such as NO, PGI2 and AMP.

Table 2.2: Estimation of typical ranges of wall shear rates and wall shear stresses [133].

Blood vessel	$\dot{\gamma}_w$ (s^{-1})	τ_w (Pa)
Large arteries	300–800	1.05–2.80
Arterioles	500–1,600	1.75–5.60
Veins	20–200	0.07–0.70
Stenotic vessel	800–10,000	2.80–35.0

Assuming viscosity $\mu = 3.5\,\mathrm{mPa\,s}$.

4. Rearrangement of the platelet membrane promotes the association of tenase and prothrombinase to its phospholipids.

5. Formation of platelet microparticles (PMP), which are anionic phospholipid particles rich in coagulation factor Va and platelet factor 3. These vesicular particles can adhere to fibrinogen, fibrin and platelets, and they serve as dock sites for protein complexes of the coagulation system.

Activation by High Shear Stress

The physiologically normal levels of shear stress can be estimated by considering the blood vessels as perfect tubes of radius R and laminar blood flow rate Q. In developed flow, the highest shear stress is found at the wall. Wall shear rate is given by

$$\dot{\gamma}_w = \dot{\gamma}(R) = \frac{dv(R)}{dr} = \frac{4Q}{\pi R^3} \ , \tag{2.1}$$

and the wall shear stress by

$$\tau_w = \mu\,\dot{\gamma}_w \ , \tag{2.2}$$

where μ is the dynamic viscosity for Newtonian fluids. Estimated values of $\dot{\gamma}_w$ and τ_w for different vessels are available in Table 2.2.

Brown [38] studied the effect of shear stress in platelet rich plasma (PRP) in a rotational viscometer. Prolonged (5 min) shear stress grades of $\tau \approx 5\,\mathrm{Pa}$ induced the

liberation of small amounts of ATP, ADP and serotonin, which eventually activated platelets. Levels of $\tau \approx 10\,\text{Pa}$ were able to cause some damage to platelets, whereas levels over $\tau \approx 25\,\text{Pa}$ resulted in cell fragmentation. Physiological shear stresses are lower than the levels which cause platelet activation (see Table 2.2). However, it might be unhealthly high in stenotic vessels.

Platelet activation under high shear stresses is mediated by the binding of von Willebrand factor (vWF) to platelet receptors GPIb/IX and GPIIb/IIa [156, 48, 155]. Molecules of vWF form long chains called multimers[1], which remain coiled, when flowing in blood plasma under physiological shear stresses. These multimers unfold at super-physiological shear stresses, exposing many binding sites to platelet receptors GPIb/IX and GPIIb/IIa [53, 188, 198, 227, 208]. Before activating platelets, vWF multimers promote platelet aggregation along their chains (see Section 2.2.2). Therefore, longer vWF multimers are more efficient in promoting platelet stimulus than shorter multimers. Both platelet aggregation and activation are 5–15 times more efficient when promoted by long vWF multimers, rather than normal vWF multimers [156]. Unusually, long vWF multimers are released locally from stimulated or disrupted endothelial cells, but shorter multimers are released from activated platelets [155]. The activation of platelets under high shear conditions seem to be partially reversible, if the high shear levels last for short amounts of time [161, 227]. This dependence of time for vWF-mediated platelet activation seems to be related to the process whereby Ca^{2+} concentration increases inside activating platelets. Whereas in agonist stimulated platelets (e.g. ADP or IIa) the majority of Ca^{2+} increase is the result of release from intracellular Ca^{2+} stores, platelets aggregated to vWF endure an influx of Ca^{2+} from extracellular plasma [48]. This fact seems to explain why brief vWF-mediated platelet aggregation does not cause sustained platelet activation [161, 227]. Nevertheless, elevated shear stresses also make platelets more susceptible to activation by

[1]In contrast to polymers, which are held by covalent bonds, multimers refer to macromolecules formed by non-covalent bonding of proteins or nucleic acids [52].

soluble agonists, because the agonist concentration threshold is lowered when platelets are adhered to vWF [227].

Shear-induced platelet aggregation to vWF is inhibited by plasmin (PN) [133] and ADAMTS13 (A Disintegrin And Metalloproteinase with a Thrombospondin type 1 motif, member 13) [188, 227, 198], because these enzymes cause proteolysis of uncoiled vWF. At physiological shear stresses, the sites where PN and ADAMTS13 break vWF molecules are protected, but they get exposed once the multimer unfolds. The vWF multimers are progessively cleaved into shorter pieces the longer these sites are exposed to PN and ADAMTS13. Endothelial cells help to control the concentration of long vWF multimers at unharmed vessels. At shear stress levels higher than 1.5 Pa, endothelial cells release tissue plasminogen activator (tPA), whereas they continue to normally release plasminogen activator inhibitor type 1 (PAI-1) [133]. Therefore, there is a physiological response to prevent thrombosis at high shear stresses, whereas allowing haemostasis in harmed vessels under high flow shear rates.

Platelets activated by shear stress promote further activation of other platelets by releasing their granules in the surrounding region. Schulz-Heik *et al.* [190] did an experiment measuring the concentration of activated platelets relative to the absolute concentration of platelets being sheared in a rheometer. The relative activation concentration was compared to suspensions containing only activated platelets, which was produced by a mechanical process named sonication. Platelet activation rate was higher in batches of higher platelet concentration, although the shear stress was the same. Figure 2.4 displays the results of an experiment which evidences the biochemical amplification of shear-induced activation. At lower concentration of platelets, fewer platelets were activated by the shear stress insult. Therefore, the concentration of agonists released from the granules of these shear-stressed activated platelets was insufficient to reach the threshold to activate other platelets. Nevertheless, these results do not represent physiological activation rates for a couple of reasons. First, the

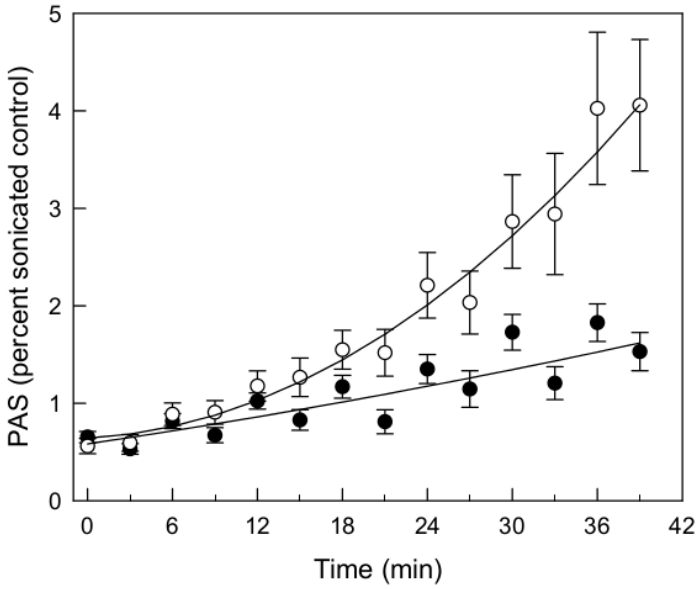

Fig. 2.4: The effect of platelet count on shear-induced activation. Gel-filtered platelets were subjected to an intermittent shear stress of $\tau = 0.9\,\mathrm{Pa}$ in a capillary loop (being under shear for approximately 25% of the experimental time course). Platelet activation state (PAS) of 20 000 µL and 200 000 µL are indicated by black and white circles, respectively. Image reproduced from Schulz-Heik *et al.* [190].

shear stress of $\tau = 0.9\,\mathrm{Pa}$ is physiological, the activation time is long ($t_{act} \approx 1$ min), and activation platelet activation state is very low ($PAS \approx 5\%$). Second, gel filtration potentially have the most sensitive platelets, that eventually become activated. However, the experiment succeeds in demonstrating that the granule content is helping to activate sheared platelets.

2.2.2 Platelet Adhesion

Platelet adhesion is the attachment of platelets to surfaces, and *platelet aggregation* is the attachment of platelets to other platelets. Both platelet adhesion and aggregation occur when glycoprotein (GP) receptors on the platelet membrane grasp their respective protein ligands either attached to a surface or to GP receptors on the membrane of other platelets. Adhesion and aggregation can occur on resting platelets

Table 2.3: Platelet adhesion receptors [88].

Receptor	Ligand
GPIa/IIa or VLA-2	Collagen
GPIb/IX or GPIb	vWF, thrombin (IIa)
GPIc/IIa or VLA-5	Fibronectin (FN)
GPIc'/IIa or VLA-6	Laminin
GPIIb/IIIa	Collagen, fibrinogen (I), FN, vitronectin, vWF
GPIV or GPIIIb	Collagen, thrombospondin
GPVI	Collagen
Vitronectin receptor	Vitronectin, thrombospondin

GP: glycoprotein; VLA: very late antigen.

(RPs) that rub on surfaces containing ligands, but activated platelets (APs) are much more susceptible to adhesion and aggregation because they have more membrane receptors than RPs. Exposure of platelet adhesive GPs to their ligands stimulate platelet activation (see Section 2.2.1) [88]. A list of platelet adhesive receptors and their ligands is available in Table 2.3.

Figure 2.5 illustrates the formation of a platelet plug (primary haemostasis) on a site of injury. First, RPs adhere to FN and collagen, either coated or not with von Willebrand factor (vWF). Initial adhesion is much stronger on collagen coated with vWF, than on collagen alone. Once the GPVI transmembrane receptor encounters collagen, it initiates intracellular signalling leading to platelet activation. Activated platelets are able to aggregate to each other via fibrinogen (factor I) cross-linking. Platelet aggregation increases the height of the platelet plug, or thrombus, and creates a microenvironment protecting activated proteins of the coagulation system from being convected downstream. Other adhesive proteins listed on Table 2.3, but not illustrated in Fig. 2.5, include laminin on exposed basal lamina (as FN), and thrombospondin and vitronectin on various surfaces, because they are adhesive molecules released by activated platelets [117].

The affinity of fibrinogen to GPIIb/IIIa is high at low shear rates, but this effect

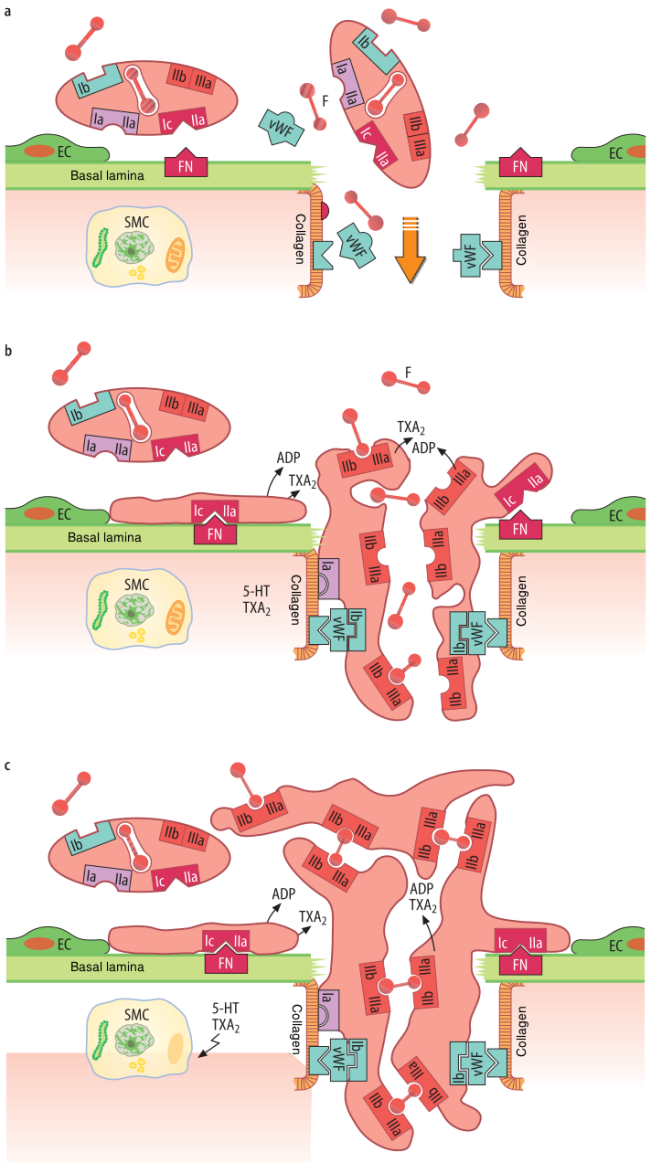

Fig. 2.5: Platelet adhesion in a vascular injury. (**a**) RPs flow from the blood stream to the injury, which contains FN and collagen. The integrins GPIc/IIa and GPIa/IIa bind to FN and collagen, respectively. Molecules of vWF improve the adhesion between collagen and glycoprotein complex GPIb/IX/V. (**b**) Platelets bound to FN and collagen become activated, and, thus, undergo shape change. Both APs and damaged endothelial cells release ADP and TXA2, which activate RPs in the proximity. The integrin GPIIb/IIIa which binds to fibrinogen (F) emerges onto the cellular membrane of APs. Thereby, neighbouring APs form stable aggregates interconnected with F. Additional F is secreted by APs. (**c**) The vascular defect is closed by the platelet aggregate (plug). TXA2 and serotonin (5-HT) released from activated platelets diffuse into the media, where they cause contraction of smooth muscle (SMC), which contributes to haemostasis. Image reproduced from Junqueira and Carneiro [117].

ceases over $\tau = 1.2\,\text{Pa}$ ($\dot{\gamma} = 1000\,\text{s}^{-1}$, for viscosity of platelet-rich plasma $\mu = 1.2$ mPa.s) [107]. However, the binding capacity of GPIIb/IIIa to vWF is still good at high shear rates, when vWF multimers uncoil exposing many binding sites for effective aggregation [208]. After GPIb/IX transiently binds with vWF, GPIIb/IIIa receptor is activated in order to more firmly bind with vWF [90]. Yet, GPIb/IX-vWF binding does not cause platelet activation [193]. For vWF to cause effective aggregation of non-activated platelets, it is necessary that both GPIIb/IIIa and GPIb/IX are active [107, 89]. In other words, the transient binding of GPIb/IX to vWF slows down the platelet speed, so that GPIIb/IIIa can grab vWF more firmly, which leads to platelet activation, which allows platelets to permanently aggregate to each other with fibrinogen molecules. Hence, fibrinogen is the main protein cross-linking platelet aggregates at low shear rates, and vWF is the main protein cross-linking platelets at high shear rates [133].

Amongst the different adhesion molecules, GPIb/IX/V and GPIIb/IIIa have the highest densities on platelets, whose membranes present approximately 25,000 and 40–80,000 receptors per platelet, respectively. The adhesive power of GPIIb/IIIa is much bigger in APs than in RPs. In RPs, GPIIb/IIIa stays in an inactive form, with low-affinity binding site for fibrinogen. Upon platelet activation, a conformational change of GPIIb/IIIa exposes molecular sites of high affinity for soluble fibrinogen. Furthermore, another portion of 40–80,000 GPIIb/IIIa, formerly stored in granules, are transferred to the membrane, which elevates the number of active GPIIb/IIIa to 80–160,000 [88]. Hence, whereas GPIb/IX/V initiates reversible platelet recruitment, particularly at elevated shear rates, GPIIb/IIIa stabilises forming aggregates, where the soluble platelet activation agonists are present (i.e. ADP, TXA2 and IIa).

Recruitment Mechanism of vWF

Platelets and endothelial cells constantly release soluble long multimers of vWF into the plasma [155]. Shear stress is an essential factor for platelet adhesion to collagen-bound vWF, since it inflicts the required conformational change for vWF to bind to GPIb/IX/V [88]. At a critical shear, vWF multimers undergo a reversible conformal transition from a compact globule shape to an uncoiled thread shape [188], see Fig. 2.6. The critical shear rate of $\dot{\gamma}_{crit} \approx 5 \cdot 10^3$ s^{-1} was obtained by Schneider *et al.* [188], which is equivalent to a critical shear stress $\tau_{crit} \approx 5$ Pa, since the testing medium was water. However, di Stasio and de Cristofaro [53] and Singh *et al.* [198] measured a $\tau_{crit} \approx 3$ Pa, and Shankaran *et al.* [193] measured a minimum shear stress associated with vWF-platelet activation of $\tau_{crit} \approx 8$. Shankaran *et al.* [193] demonstrated that it is shear stress, rather than shear rate, that controls vWF unfolding; regardless of collision rate between platelets and vWF multimers. In contrast to experiments with PRP, experiments with whole blood have shown a higher vWF-aggregation threshold of $\dot{\gamma}_{crit} \approx 10^4$ s^{-1} [217, 180]. It seems that the collision of tethering platelets with RBC might help to break the soft bonds between GPIb/IX and vWF. In the unfolded state, the multimer exposes many more adhesion sites than in the collapsed state [188, 208]. Furthermore, the unfolded thread has a length ranging 15–100 µm, which has the ability to capture many more platelets than a folded globule of 2 µm, see Fig. 2.7. The unfolded vWF can self-aggregate, forming web networks which are particularly efficient in the trapping process of flowing platelets [53, 182, 193]. Platelet activation caused by the adhesion to vWF is partially reversible, because it occurs via a different intracellular process than the one causing platelet activation by soluble agonists [48] (see discussion in Section 2.2.1).

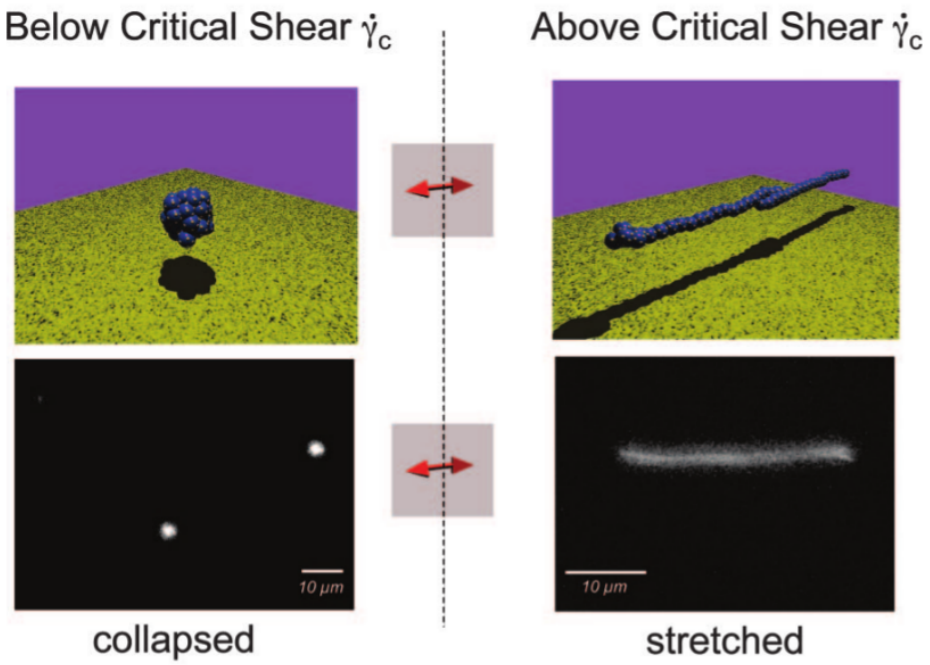

Fig. 2.6: Dynamic conformational change of vWF under shear. Cartoon (Upper) and selected fluorescence (Lower) images of a video sequence of vWF below and above the critical shear rate $\dot{\gamma}_{crit} \approx 5 \cdot 10^3$ s^{-1}. Above $\dot{\gamma}_{crit}$ the multimer becomes elongated. Image reproduced from Schneider *et al.* (2007) [188].

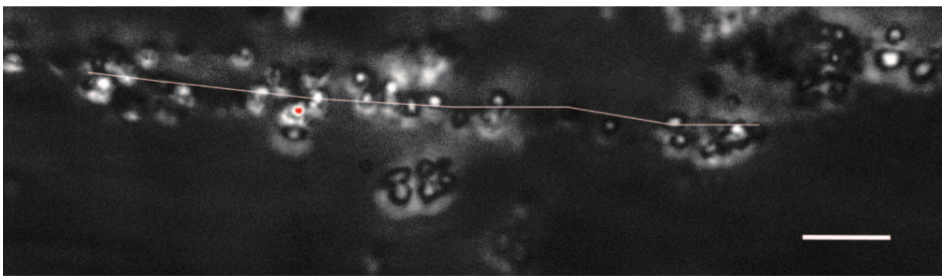

Fig. 2.7: Blood platelet-vWF aggregation under high shear flow ($\dot{\gamma} \approx 4 \cdot 10^3$ s^{-1}). Blood platelets ($\sim 1\,\mu$m) are immobilised on the free end of a vWF fibre only when $\dot{\gamma} \gtrsim 3.5 \cdot 10^3$ s^{-1}. The white line indicates the underlying vWF and is given as a guide for the eye. Scale bar: 10 µm. Image reproduced from Schneider *et al.* (2007) [188].

2.2.3 Shear-Induced Platelet Aggregation

Platelet aggregation is the attachment of platelets to other platelets. Platelet aggregation is governed by the kinetics of aggregation and clustering of colloid[2] particles. When two colloid particles collide, there is a chance that they will clump together to form a larger particle. As for platelet adhesion, platelet aggregation occurs when activated platelets are bridged by proteins, namely fibrinogen at low shear rate ($\dot{\gamma} \lesssim 1000\,\mathrm{s}^{-1}$) and vWF at high shear rate ($\dot{\gamma} \gtrsim 3000\,\mathrm{s}^{-1}$) (Table 2.3) [107, 138, 156, 236, 242]; it does not occur in the absence of those molecules. Aggregation occurs when free membrane receptors of a platelet grasp the bridging proteins already attached to the membrane receptors of another platelet. These assemblages occur when platelets collide. Collision mechanisms for suspended platelets include diffusion, velocity gradients (or shear rate, $\dot{\gamma} = \frac{\partial v_1}{\partial x_2}$), and sedimentation. Between those collision mechanisms the one normally causing the highest aggregation rates is shear-induced platelet aggregation (SIPA), which occurs in flowing blood. Diffusion- and sedimentation-induced platelet aggregation are more significant in stored blood samples, but the time-scale is of the order of days. On the other hand, SIPA time-scale depends on blood shear rate, which can be very high in non-physiological flows. The most common blood test used to assess platelet function in medical laboratories is called light transmission platelet aggregometry (LTPA). In this test, high shear rates induce platelet aggregation at the time-scale of a couple of minutes [36].

Although LTPA is the standard blood test for assessing platelet function in medical laboratories, its shear rate field is not uniform. The only situation where all platelets in the experiment endure the same history of shear rate is the Couette flow, because shear rate is uniform throughout the whole system. Therefore, Couette flow has been seen as the ideal flow condition in which to study SIPA [38, 42, 90, 102, 107, 156, 193,

[2]In chemistry, colloids are microscopically dispersed insoluble particles suspended throughout another substance. Unlike a solution, whose solute and solvent constitute only one phase, a colloid has a dispersed phase (the suspended particles) and a continuous phase (the medium of suspension).

190, 236, 242]. Couette flow field is preferred in scientific experiments, whose results are supposed to be numerically more accurate. In clinical tests, absolute numbers are not as important as relative numbers which can show time-scales and relative state differences. A less common experimental setup for SIPA is laminar flow in a tube, or Poiseuille flow [24, 27, 25, 26]. Although this experimental setup has the advantage of mimicking SIPA in the circulatory system, it requires very long narrow tubes, where the flow rate varies along the tube radius. All these three experimental setups are discussed in more detail below.

Light Transmission Platelet Aggregometry

In the 1960s, Born [36] developed LTPA, which is a method for studying the response of platelets to chemical agonists by recording changes in light transmission of a stirred platelet suspension as platelet aggregates are forming. In LTPA, platelet-rich plasma (PRP) is stirred in a glass cuvette with activation agonists, and this cuvette sits between a light source and a detector (see Fig 2.8). The detected light intensity depends on the light transmittance of the PRP sample, which is related to platelet aggregation. Disaggregated platelets are more evenly spread out throughout the sample, thus they scatter more light than the less disperse aggregates. The light transmittance of the PRP sample rises as platelets aggregate, up to a point where it becomes equivalent to the light transmittance of platelet poor plasma (PPP). The aggregation levels indicated by the LTPA are relative values, where the values of fully disaggregated and fully aggregated platelets are calibrated with samples of PRP and PPP from the same donor, respectively.

Once platelets are mixed with proper levels of activation agonists, they change shape and release more activation agonists inside the cuvette. Both these effects can be detected by the LTPA (see Fig. 2.9). The shape change slightly decreases the light transmittance. The release of internal activation agonists is seen as a second rise of

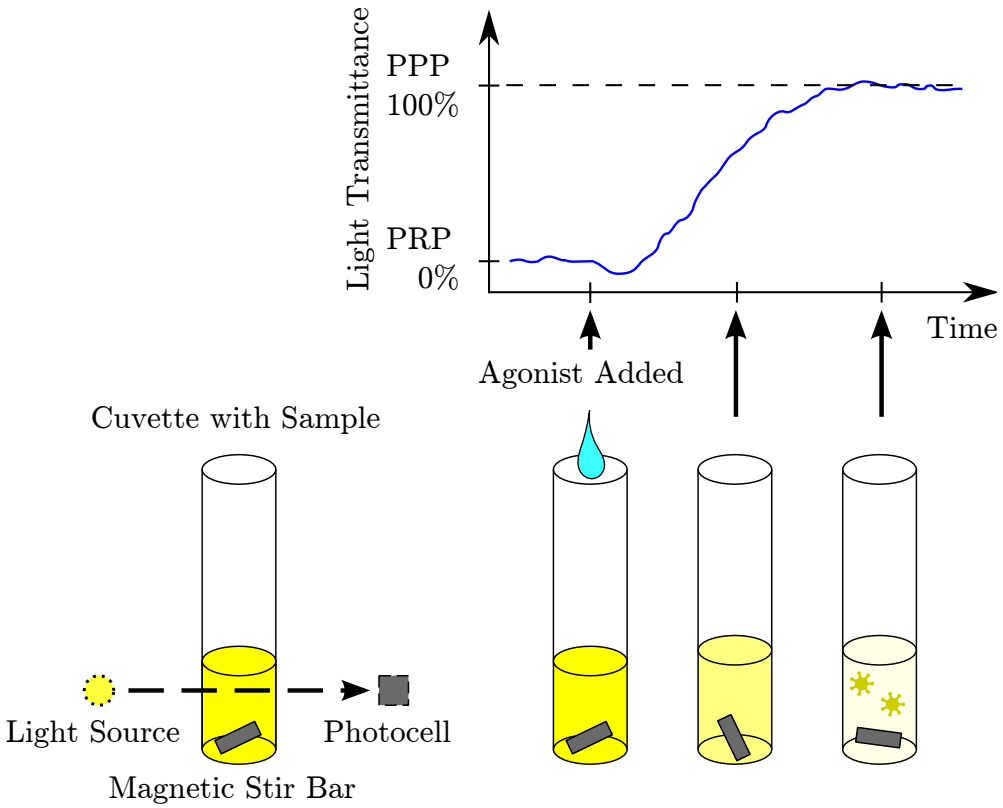

Fig. 2.8: Schematic diagram of Born LTPA. The relative light transmittance is used as a measurement of aggregation ratio. Once the activation agonist is added, the light transmittance decreases slightly due to platelet shape change. Then it increases with aggregation. The maximum aggregation level is compared to the light transmittance of PPP.

light transmittance, when the initial agonist level is not high enough to sustain full activation of the sample.

This platelet aggregometer had an immense impact on the study of platelet reactions, and it rapidly came into routine and widespread use [133]. Born and Cross [36] found that more aggregation occurred at higher than at lower stirring rates. Stirring rate not only enhances activation by agonists, but can also cause activation directly. The findings obtained with the LTPA have favoured the prevalent concept that fibrinogen is the essential adhesive protein mediating platelet-to-platelet contact. The

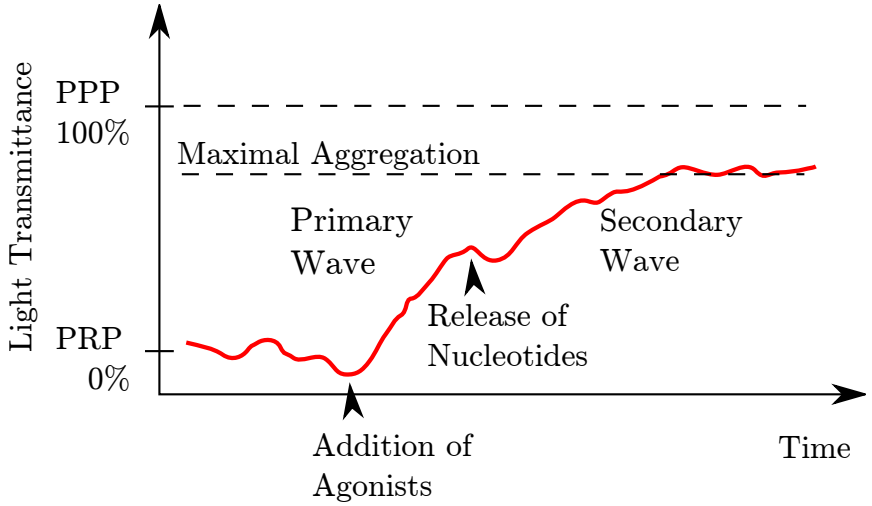

Fig. 2.9: Schematic diagram of LTPA curve at lower agonist concentration than in Fig. 2.8. A primary wave caused by the addition of external agonists is followed by a secondary wave caused by the release of agonists from activated platelets.

efficiency of SIPA is highly decreased either when fibrinogen is in very low or very high concentration. In low fibrinogen concentrations, there are no sufficient fibrinogen molecules connected to glycoproteins IIb/IIIa (GPIIb/IIIa) in order to make strong bonds between platelets. In high fibrinogen concentrations, the GPIIb/IIIa of both platelets become saturated with fibrinogen. Thus, there are insufficient free GPIIb/IIIa on one platelet for linking to the fibrinogen molecules bound to the GPIIb/IIIa on the other platelet [160, 150].

There are several drawbacks of LTPA. For instance, shear rate varies throughout the platelet suspension in a complex and uncharacterised way. In contrast to Couette flow, the stirred container mixes platelets with distinct histories of mechanical stress. Another drawback is that of LTPA assesses of platelet aggregation only on a relative scale. The relative values of light transmittance lack any information about the distribution of platelets between aggregate sizes [37]. Light transmittance similar to the PPP value is not the same as having all platelets in the PRP activated and aggregated [163]. On the other hand, Couette flow systems also have many drawbacks for mea-

surement of SIPA, due to its lower practicality and lower reproducibility. Therefore, LTPA is the standard test in medical laboratories, and Couette flow is mostly used in scientific investigations. Light transmission platelet aggregometry is a very simple test, which is mostly automatic, and it returns clear information on the sensitivity of platelets to activation agonists.

SIPA in the Couette Flow

Normally, SIPA is experimentally observed in cone and plate [38, 90, 102, 103, 104, 107, 156, 242] or concentric cylinder rheometer [42, 236], because shear rate is uniform in Couette flow. This means that all platelets in the suspension experience the same history of shear stress cycles, independently of their positions in space. Normally, platelet aggregates are sampled after an exposure time, and quickly fixated prior to particle counting. The particle counting measures either just the concentration of free platelets [38, 156, 236, 242] or the concentration of many sizes of aggregates [102, 103, 104]. More rarely, the aggregate distribution is indirectly measured by light scatter technique [42, 107].

SIPA in the Poiseuille Flow

Shear-induced platelet aggregation is expected to occur in the circulation, since it is clearly observed in LTPA and in rheometers. However, it is difficult to determine about the origin of a platelet embolus clogging a patient's artery, whether it was formed by aggregating platelets in the bulk of the flow, or it was formed at a thrombotic surface and got detached from it. The simplest flow condition that mimics blood flow in the circulatory system is Poiseuille flow, which is the flow with a parabolic velocity profile that occurs in developed laminar flow inside tubes. Bell *et al.* [24, 27] ran activated platelets in PRP through tubes of 100 µm in diameter, and visualised the aggregation rates in real time by image processing. The image technique had a limitation in the flow

rate, because sharp photographs require a minimum exposure time of the objects on scene. Another problem involved the mixing of ADP (the activation agonist) and PRP, which occurred by diffusion. Therefore, Bell *et al.* [25, 26] overcame these limitations by changing the measuring system and changing the mixing system. In their new setup, the aggregated PRP was collected into a tube containing glutaraldehyde in order to fixate the aggregates, as illustrated in Fig 2.10. The new system had a rapid mixing chamber with a stir bar similar to LTPA. Platelet rich plasma and ADP were independently infused into the mixing chamber by independent tubes, and the residence time inside the chamber was in no case longer than 4 s. The size distribution of the fixated platelet aggregates was measured with a Coulter counter [106].

Background particles present in plasma (like fat particles) had to be subtracted from the measured particle-size distribution, which yielded the expected log-normal distribution of free platelet volumes [171]. Volume concentration (or fraction) Φ_i of aggregated particles measured by the Coulter counter can be associated with number concentration C_i by the relation

$$\Phi_i := \frac{V_i}{V} = V_i\, C_i = w_i\, V_p\, C_i \ , \tag{2.3}$$

where V_i is the volume occupied by clusters made of w_i platelets, V is the volume of control, and V_p is the volume of a single platelet. The response of the setting to particle size was calibrated with microspheres, with a particle volumetric uncertainty of 8%. The authors assured no aggregate breakup by the fixation and storage procedure, by comparing fresh samples from fixated stored samples.

The mean transit times of the activated platelet suspension through the flow tube was calculated as

$$\bar{t} := \frac{L}{\bar{v}} \ , \tag{2.4}$$

where L is the tube length and $\bar{v}$ is the mean velocity. Since it is Poiseuille flow, the

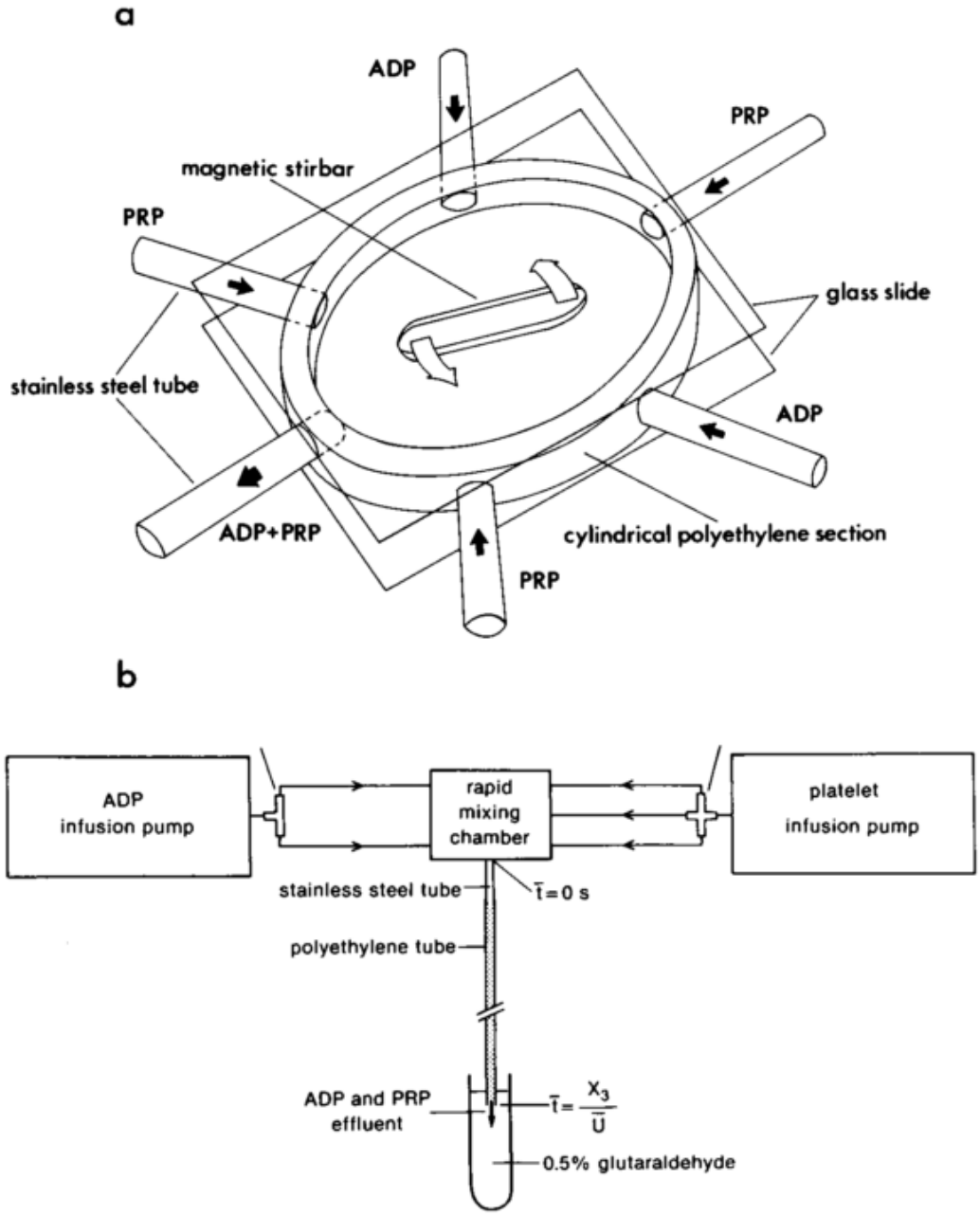

Fig. 2.10: The flow system used by Bell *et al.* [25, 26] to measure SIPA in Poiseuille Flow. PRP and ADP were simultaneously infused into a common mixing chamber (a) by independent syringe pumps (b). After rapid mixing, the activated platelet suspension flowed through polyethylene tubes, and the effluent was collected into tubes with glutaraldehyde. Reproduced from Bell *et al.* [25].

velocity profile along the tube is parabolic, i.e.

$$v(r) = v_{max}\left(1 - \frac{r^2}{R^2}\right) \ , \tag{2.5}$$

where v_{max} is maximum velocity, r is the radial coordinate centred at the tube's axis, and R is the tube's radius. The maximum velocity v_{max} is related to the flow rate Q given by the infusion pumps from the relation

$$Q = \int_0^{2\pi}\int_0^R v(r)\, r\, dr\, d\theta \quad \Rightarrow \quad Q = \frac{\pi\, R^2}{2} v_{max} \ . \tag{2.6}$$

Since the flow rate is defined by the relation of the mean velocity and the cross-sectional area ($A = \pi\, R^2$),

$$Q := \bar{v}\, A = \pi\, R^2\, \bar{v} \quad \Rightarrow \quad \bar{v} = \frac{v_{max}}{2} = \frac{Q}{\pi\, R^2} \ . \tag{2.7}$$

The shear rate field along the radial direction is defined in absolute terms for simplicity,

$$\dot{\gamma} = \left|\frac{dv}{dr}\right| = \frac{4\,\bar{v}\, r}{R^2} \ . \tag{2.8}$$

Thus, the mean shear rate endured by the collected sample is the mean flow of shear rate,

$$\bar{\dot{\gamma}} := \frac{1}{Q}\int_0^{2\pi}\int_0^R \dot{\gamma}(r)\, v(r)\, r\, dr\, d\theta = \frac{32}{15}\frac{\bar{v}}{R} = \frac{32}{15\pi}\frac{Q}{R^3} \ . \tag{2.9}$$

Finally, the Reynolds number for flow inside tubes is

$$Re = \frac{2R\,\bar{v}}{\nu} \ , \tag{2.10}$$

where $\nu = 1.25 \cdot 10^{-6}\,\mathrm{m^2\,s^{-1}}$ is the kinematic viscosity of PRP.

Two tube radii were used throughout the experiments, 595 and 380 µm, with the respective flow rates preset to 13–104 and 54–81 $\mu\mathrm{L\,s^{-1}}$. Tube length varied up to 15 m in order to achieve the desired transit time (Eq. 2.4). These long capillary tubes were vertically coiled with a radius that made the rotation forces negligible. The derived parameters of the experiments are listed in Table 2.4. Reynolds numbers are one order of magnitude lower than the minimum value for turbulent transition.

Table 2.4: Parameters of the experiments of Bell *et al.* [25, 26].

R (µm)	Q (µL s^{-1})*	$\bar{v}$ (mm s^{-1})	$\bar{t}$ (s)†	$\bar{\dot{\gamma}}$ (s^{-1})	Re
595	13–104	12–94	0–1,300	42–340	11–89
380	54–81	120–180	0–130	670–1000	73–110

* µL s^{-1} = 10^{-9} m^3 s^{-1}.

† Equation 2.4, $L < 15.25$ m.

Aggregation rate was modelled with the two-body collision theory (Eq. 3.78), although this aggregation model accounts only the aggregation of free platelets and neglects aggregate breakups. Nevertheless, the authors recognised that breakup was occurring, due to the evolution of the CMD's shape at $\bar{t} > 43$ s. They reported few large aggregates being present before this transit time, but they could not increase in concentration before medium-sized aggregates had been formed in significant concentrations. The authors assumed that large aggregates should not have insignificant growth rate, unless they were being broken up, because this would create higher concentrations of medium-sized aggregates [25].

2.2.4 Reversible Aggregation at High Shear Stresses

Temporary platelet aggregation without signs of activation have been observed at low shear rate sites downstream from high shear rate sites. Figure 2.11 shows this phenomenon occurring both *in vitro* and *in vivo* in experiments carried out by Nesbitt *et al.* [161]. *In vivo*, they induced a stenosis on injured sites of mice arterioles by crushing them with a blunted needle (Fig. 2.11.a). *In vitro*, they recreated a blood vessel narrowing in a microchannel (Fig. 2.11.c). In both cases, a platelet aggregate developed downstream from the narrowing site, and its size was directly related to the shear rate. In the mice arterioles, the aggregate size grew as the narrowing got tighter (stenosis increased). In the fixed-wall microchannel, the aggregate size grew as the flow rate increased. The aggregate size could be dynamically controlled by flow rate,

to whom the peak shear rate is directly related. The aggregate size decreased, as the flow rate was reduced in time, indicating that the aggregate was reversible. Besides, no aggregation was seen further downstream from the expansion site, indicating that this effect was spatially restricted.

Stenosis in the absence of vessel injury did not result in platelet aggregation in the crushed arteriole, indicating that the endothelium was impeding aggregation there. However, in both of the cases mentioned above, the pattern of high followed by low shear is essential for thrombus formation. This fact was corroborated by Westein *et al.* [227], who also showed that this aggregation is mediated by vWF. Neither Nesbitt *et al.* [161] nor Westein *et al.* [227] could initiate platelet aggregation under conditions of elevated shear in the absence of a downstream shear drop. Zhang *et al.* [242] recreated this same shear pattern, a peak of high shear stress followed by low shear stress, in uniform shear (i.e. Couette flow) in a cone and plate rheometer. These authors obtained higher vWF-mediated platelet aggregation using this pattern, than with simple constant high shear stress.

In another experiment, Nesbitt *et al.* [161] noticed an inverse correlation between downstream shear rate and adhesion lifetimes. At shear rate $\dot{\gamma} \approx 800\,\mathrm{s}^{-1}$, aggregation turned highly unstable, breaking up in less than 2 s. Platelet aggregation seemed to be sensitive to shear rate drop (or negative gradient of shear rate, $\frac{\partial \dot{\gamma}}{\partial x_i} < 0$). The higher was the shear rate drop on the flow direction, the larger was the aggregate.

Nesbitt *et al.* [161] showed that initial platelets recruited at the peak shear zone required the binding function of GPIb/IX/V to vWF. Inhibition of GPIb/IX/V precluded any aggregation. On the other hand, blocking GPIIb/IIIa function had no inhibitory effect on initial platelet recruitment at the peak-shear zone, but it markedly reduced platelet aggregation in the downstream zone. Still, the linking of platelets by GPIIb/IIIa and fibrin was essential to stabilise the thrombus, because this type of bond lasts much longer than GPIb/IX/V-vWF bonds. Thus, two requirements would

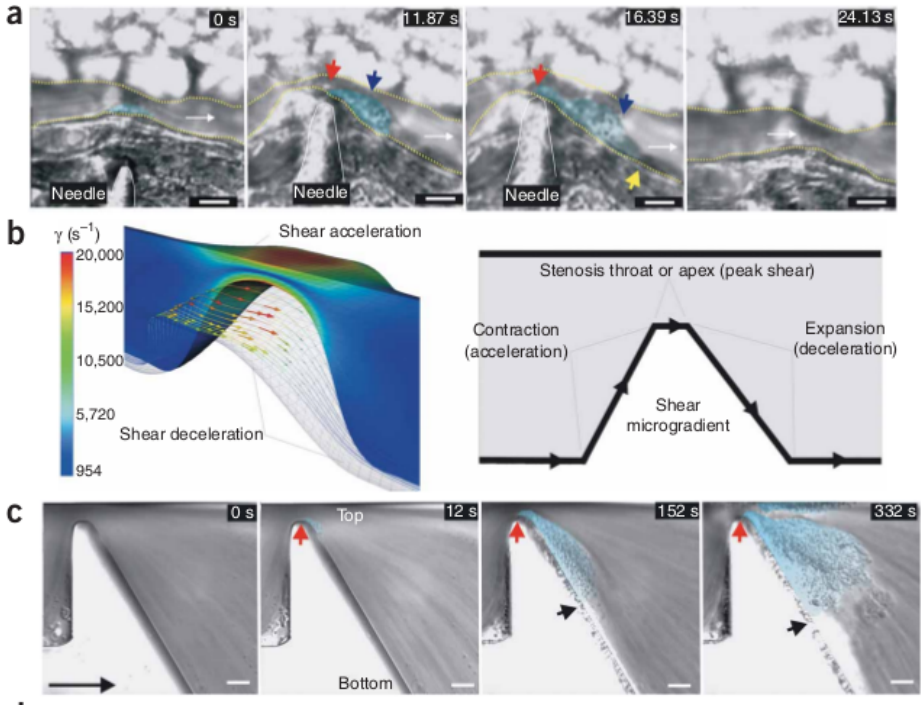

Fig. 2.11: Temporary aggregation downstream of obstructions. (**a**) Frame sequences demonstrating the effect of a stenosis at a mouse arteriole crushed by a needle. Small platelet aggregates are present at $t = 0\,\mathrm{s}$ (cyan shading). After stenosis (11.87 s), a marked increase in platelet aggregation was observed (blue arrow), which specifically developed downstream from the site of vascular injury (red arrow). Aggregate growth ceased at the downstream stenosis margin (yellow arrow; 16.39 s) where the vessel returned to its native geometry. Subsequent removal of the microneedle led to the rapid embolisation of the platelet aggregate (24.13 s). (**b**) CFD simulation of blood flow dynamics after localised vessel wall compression (left) and schema illustrating the three principal components defining a shear microgradient or stenosis (right). The contraction demarcates the region of shear growth. The throat or apex demarcates the stenotic region at which peak shear is experienced. The expansion demarcates the region of shear drop. (**c**) Image sequence of blood perfusion through a microchannel comprising a side-wall geometry designed to induce a sharp phase of accelerating shear from $1800\,\mathrm{s}^{-1}$ coupled to an immediate shear drop approaching $200\,\mathrm{s}^{-1}$. Red arrow indicates the point of initial aggregation (t = 12 s) and black arrow indicates the limit of thrombus growth in the expansion zone. Scale bars: 10 µm. Image reproduced from Nesbitt *et al.* [161].

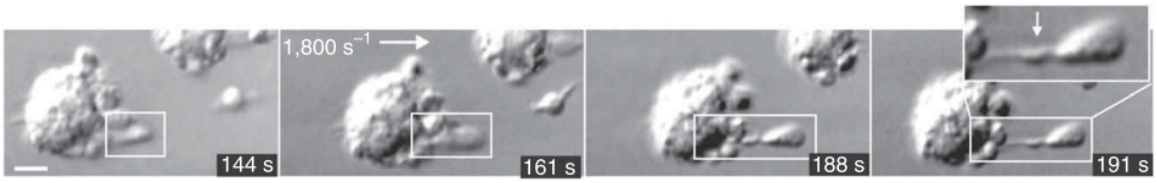

Fig. 2.12: Differential interference contrast (DIC) imaging showing platelet tether restructuring at the downstream face of a thrombus, once it separated from the thrombus at bulk shear rate of $1800\,\mathrm{s}^{-1}$. The white box highlights the progression of a discoid platelet tether: initial platelet interaction results in the formation of a short tether (144 s) that rapidly thickens (161–188 s) to produce a bulbous membrane structure proximal to the discoid body (white arrow; 191 s). Scale bar: 2 µm. Image reproduced from Nesbitt *et al.* [161].

have to be fulfilled for stabilising the thrombus. First, platelets would have to attach to vWF at sites of high shear stress, where they formed aggregate tethers. Second, these tethering platelets would have to move to a zone of sufficiently low shear stress, where GPIIb/IIIa-fibrin bonds could be formed. This corroborated previous experiments demonstrating the same effects in microchannels [135].

Once this happens, the platelet tethers produce a bulbous membrane structure proximal to the discoid body, as shown in Fig. 2.12. This tether restructuring was Ca^{2+} dependent, and only occurred at $\dot{\gamma} < 300\,\mathrm{s}^{-1}$. Restructured platelets have the power to pull themselves upstream, shortening their tethers and increasing thrombus density. This requires an influx of Ca^{2+} into those platelets, but does not activate them. Activation was detected only in the compact core of the thrombus, and late after thrombus formation. This demonstrates that the adhesive stimulus is much weaker than the agonist stimulus for platelet activation.

Embolization occurred more frequently as shear rate in the deceleration zone increased. Although non-stabilised aggregates would disperse, stabilised aggregates of non-activated platelets did not, even past 10 min of experiment time. Yet, they remained reversible and rapidly disaggregated after termination of flow. These emboli of non-activated platelets could be a problem, because they would possibly have suf-

ficient tensile strength to transiently occlude small blood vessels. On the other hand, emboli formed by activated platelets would be more hazardous, because they would be irreversible. Activation depended on soluble agonists, which have no effect on the aggregation dynamics induced by stenosis. Nesbitt *et al.* demonstrated that by blocking the activation effects of ADP, TXA2, and thrombin.

There is a disagreement between the platelet tethering models of Nesbitt *et al.* [161] and Schneider *et al.* [188]. On one hand, Nesbitt *et al.* described platelets tethering by their membranes. Platelets would bounce on a vWF-coated surface, where a membrane region would stick, and the rest of the platelet would be dragged downstream. The membrane portion ligating the platelet body and the stuck part would have a stretched thin cylindrical shape. On the other hand, Schneider *et al.* describe long filaments of vWF multimer, to which round platelets adhere. In fact, Schneider *et al.* properly visualised those long filaments. However, the microscopic technique used by Nesbitt *et al.* did not have enough resolution for that. Thus, it appeared that vWF multimer would stick to a surface, and would uncoil there if the shear stress is sufficiently high. Threads of vWF multimer would oscillate in this flow, catching platelets moving by that region, as illustrated in Fig. 2.13. Oscillating threads can extend much longer in space for capturing platelets than a fixed wall. Platelets would have a greater chance of keeping themselves on the thread, if they could either stick to other platelets or hold to more binding sites on the vWF fibre. Therefore, platelet cylindrical-shaped membrane parts could be forming along a vWF multimer, as the platelet body is being dragged downstream. In this manner, the number of GPIb/IX/V integrins connected to the vWF multimer would be increasing along with the cylindrical membrane part. The platelet grip on the vWF multimer would increase with more bonding sites, which would help to explain the platelet restructuring observed by Nesbitt *et al.* in Fig. 2.12.

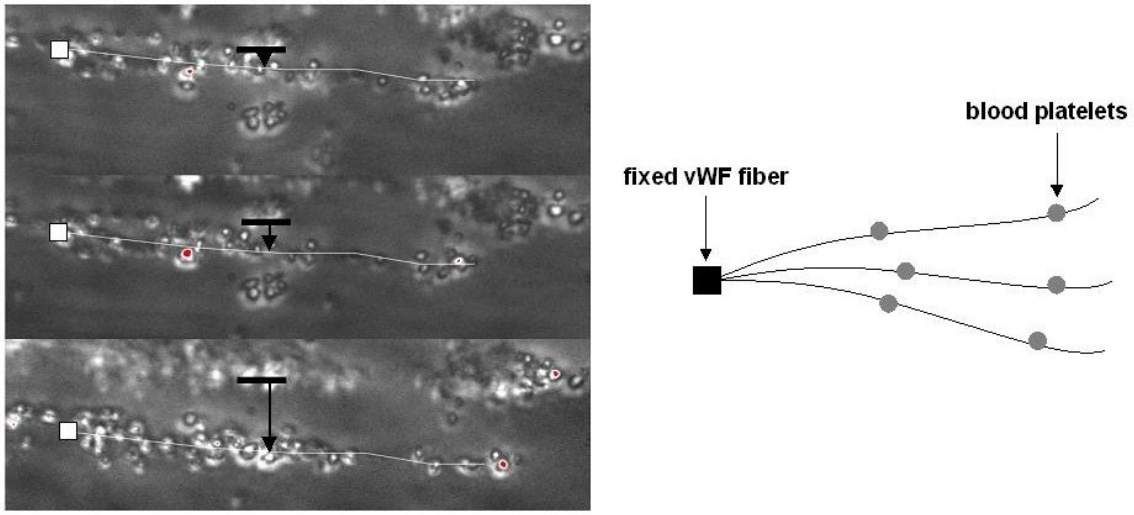

Fig. 2.13: Sequence of platelets attached on an oscillating vWF fibre under high shear flow. The square marks the point where one end of the vWF string is attached to the surface of a microfluidic channel, and the arrow indicates the position of the platelet aggregate chain. The other end is free. Blood platelets are able to bind to the flapping vWF chain. Time intervals: 1 s; scale bar: 10 µm. Image reproduced from Schneider *et al.* [188].

2.3 The Coagulation System

Blood clots are formed not only by platelets, but also by a mesh of fibrin polymer, which results from a series of biochemical reactions of the blood coagulation system. Some biochemical factors involved in the coagulation system also promote platelet adhesion and aggregation in the damaged regions. Haemostasis requires the balance of *procoagulation* (the process of clot formation), *anticoagulation* (the process for preventing clot formation) and *fibrinolysis* (the process for clot dissolution). One process does not end before another begins, they often coexist in a dynamic process of signal amplification and modulation [52, p. 982].

2.3.1 Procoagulation

The procoagulation process is typically initiated by the damage of endothelial cells, but other situations can promote the procoagulation process in the absence of any vessel injury. Endothelial cells in healthy individuals serve to protect against the spontaneous accumulation of platelets and fibrin on the vessel wall. When endothelial injury occurs, the endothelial cells stop secreting coagulation and aggregation inhibitors which initiate the maintenance of haemostasis after injury. In addition to vascular injury, other conditions can excite procoagulation. In prolonged (chronic) inflammation, endothelial cells, monocytes and neutrophils express procoagulant factors. In the presence of a foreign surface, proteins from the complement immune system can act as mediators for procoagulant proteins [88].

In the classical blood coagulation model, the coagulation process can be initiated from two distinct reaction cascades: the *intrinsic* and the *extrinsic* pathways, which converge into a common pathway. These two pathway names allude to the fact that the intrinsic pathway leads to thrombin formation, using only protein factors present in plasma, whereas the extrinsic pathway requires the presence of tissue factor (TF),

which occurs only under the endothelium. However, it is becoming clear that the division in two branches is somewhat artificial, since there is a substantial degree of interaction between both pathways. Nevertheless, their names remain due to their historical acceptance [52, p. 982].

Both the intrinsic and extrinsic processes lead to the activation of an enzyme of the common pathway known as factor X. Activated factor X (Xa) is responsible for the activation of prothrombin (or factor II, see Table 2.5), whose transformation results in thrombin (IIa), which is a key enzyme for fibrin (Ia) activation, as well as for the activation of many other coagulation and anticoagulation factors. The central proteins involved in the coagulation system are listed in Table 2.5 and a scheme of the overall coagulation mechanism is illustrated in Fig. 2.14. Structural anomalies, primarily mutations in critical regions of any of these molecules, may lead to clotting diseases.

The Extrinsic Pathway

TF, or III, is a membrane receptor present on the cell membrane of the subendothelial tissue, such as stromal fibroblasts and leukocytes. Following damage to the blood vessel, VII leaves the circulatory system and binds with TF. In the presence of Ca^{2+}, it forms the complex VII-Ca^{2+}-TF. Factor VII is activated by trace amounts of IIa, IXa, Xa, XIa, XII and already activated TF-VIIa. Trace concentrations of VIIa normally circulate in blood, and are believed to directly form the VIIa-TF (Ca^{2+} omitted), thus initiating the extrinsic pathway [88]. VIIa has a long half-life and the small amount normally present in blood has no adverse effects, since VIIa is not catalytically active outside the VIIa-TF complex [52, p. 984]. VIIa-TF can make a specific cut in X, changing it to Xa. Both a complex VIIa-TF bound to a cell membrane and a molecule of X are illustrated in Fig. 2.15. As well as X, VIIa-TF can also activate IX [88].

Table 2.5: The major participants of the blood pro-coagulation processes.

Abbrev.	Name	Location
I[a]	Fibrinogen	Dissolved or bound to AP membrane
Ia[b]	Fibrin	Dissolved or polymerised in the clot
II	Prothrombin	Dissolved in plasma
IIa	Thrombin	Dissolved in plasma
III/TF	Tissue factor	Membrane of subendothelial cells[c]
IV/Ca^{2+}	Calcium ions	Dissolved in plasma
V	Proaccelerin	Dissolved or bound to AP membrane
VI	Term not in active use[d]	—
VII	Proconvertin	Dissolved in plasma
VIII	Antihemophilic factor	Bound to vWF dissolved in plasma
IX	Christmas factor	Dissolved in plasma
X	Stuart factor	Dissolved in plasma
XI	Thromboplastin antecedent	Bound to HMWK
XII	Hageman factor	Dissolved or on anionic surfaces
XIII	Proglutamidase	Dissolved and in platelet granules
IXa-VIIIa	Tenase	On AP membrane phospholipids
Xa-Va	Prothrombinase	On AP membrane phospholipids
TF-VIIa	Extrinsic tenase	Membrane of subendothelial cells[c]
PK	Prekallikrein	Bound to HMWK
K	Kallikrein	Bound to HMWK
HMWK	High-molecular-weight kininogen	Dissolved or on anionic surface

[a] Coagulation factors are referred to by the Roman number designating that factor. For instance, X refers to Factor X.

[b] The activated form for a factor has an "a" following its abbreviation. Only factors possessing special names for their activated form are listed here.

[c] Endothelial cells, monocytes and neutrophils express TF under chronic inflammation.

[d] First used by Owren to describe what is now recognised as FVa, but which was initially referred to as accelerin [76].

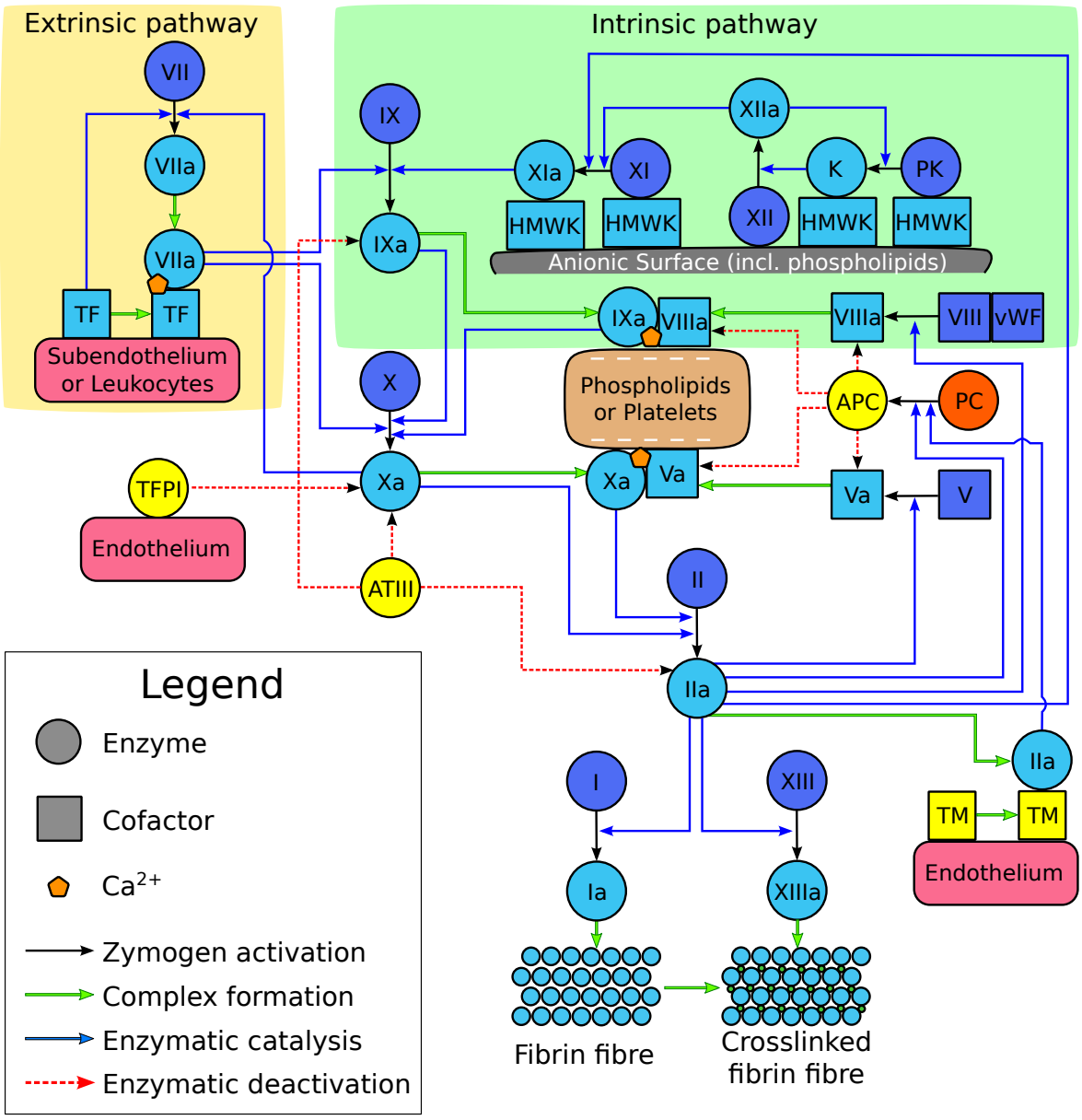

Fig. 2.14: Scheme of the coagulation system. Procoagulation (blue) and anticoagulation factors (yellow) are represented in the coagulation system.

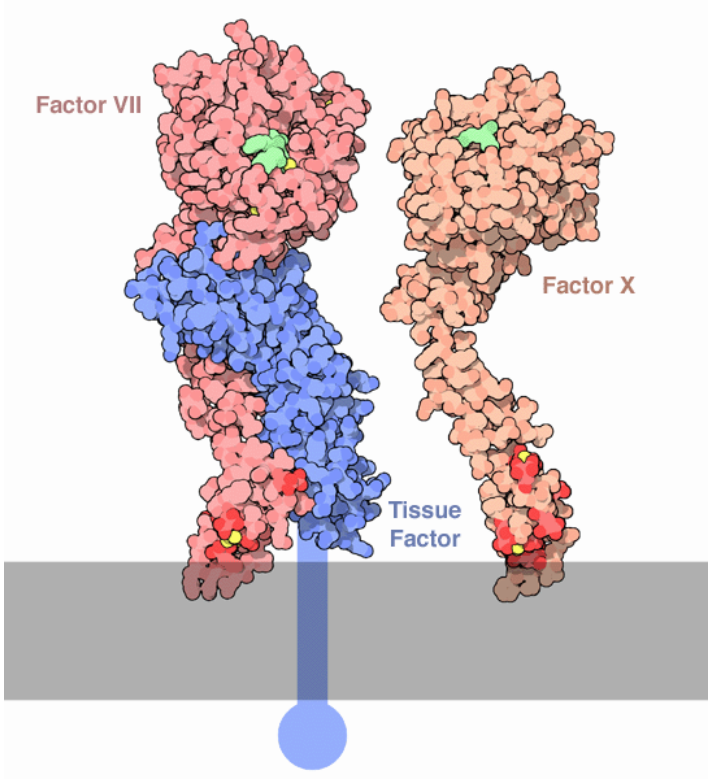

Fig. 2.15: Coupling site of factor X at VIIa-TF complex. Image reproduced from Goodsell *et al.* [87].

The Intrinsic Pathway

Blood spontaneously clots when exposed to an anionic surface. Anionic surfaces are found on the inside part of the cellular membrane of endothelial cells and platelets. The inside part of endothelial cells becomes exposed, when the endothelial cells are lysed (harmed). In the case of platelets, their phospholipid membranes are flipped inside out once they become activated. Historically, this effect originated the name of the pathway, because spontaneous coagulation was observed in clean glass testing tubes, drawing the idea that all the components of this clotting process were contained in the blood. Now, it is known that this process is initiated on anionic points of the glass surface [52, p. 984].

Factor XII binds directly to anionic surfaces and undergoes a conformational change, which increases its catalytic activity about 10^4- to 10^5-fold. Prekallikrein (PK) and XI circulates in blood flow as complexes with HMWK, see Fig. 2.14. PK-HMWK and XI-HMWK complexes bind to anionic sites by the HMWK parts. Prekallikrein is activated to kallikrein (K) by trace levels of XIIa, see Fig. 2.16. At the surface, K-HMWK is surrounded by a higher concentration of XII, also bound to the surface. K-HMWK cleaves specific sites of XII, activating it permanently. The XIIa activates more PK, which activates more XIIa in a cyclic autocatalytic chain reaction [91].

The membrane-bound XI-HMWK complex is activated by XIIa by proteolytic cleavage as well. The complex XIa-HMWK transforms IX into IXa, which can in turn activate X to Xa.

The importance of the intrinsic pathway to vascular injury remains speculative, as the occurrence of negatively charged surface under the endothelium is limited. Although anionic surfaces are present on APs, the extrinsic pathway impelled by TF has much more significance for achieving haemostasis. The lack of relevance of the intrinsic pathway for vascular healing is consistent with the fact that deficiencies of HMWK, PK and XII have not been associated with abnormal bleeding. Notwithstanding this fact,

Table 2.6: Activated factors with their activating and inactivating enzymes.

Factor	Activators	Inactivators
Ia	IIa	PL[d]
IIa	Xa-Va	ATIII[b]
Va	IIa	APC[b]
VIIa	IIa, TF, Xa[a]	
VIIIa	IIa	APC[b]
IXa	TF-VIIa[b] , FXIa-HMWK	ATIII[b]
Xa	TF-VIIa, VIIa, IXa-VIIIa	ATIII[b] , TFPI[b]
XIa	FXIIa, IIa[c]	
XIIa	K-HMWK	
XIIIa	IIa	
K	FXIIa	

*References to standard relations found in biochemistry textbooks (like [52, p. 984]) are omitted.
Other references: [a][196], [b] [7], [c] [197], [d]Sec. 2.3.3.

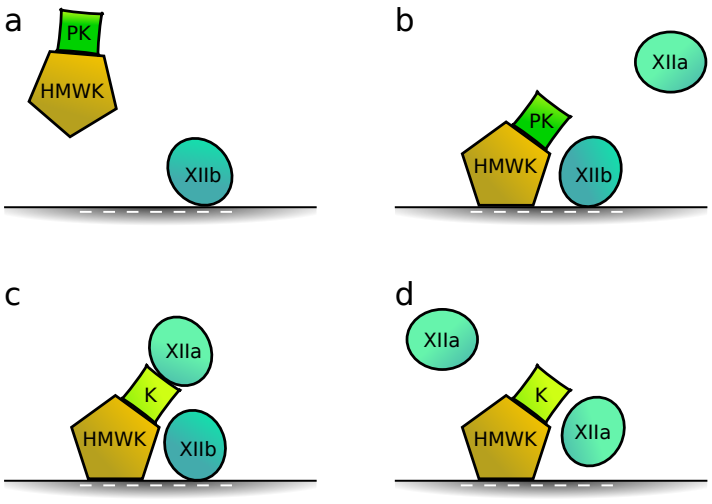

Fig. 2.16: Cyclic autocatalytic activation of PK-HMWK and XII. (a) PK-HMWK approach a anionic surface where XII is bound. (b–c) On the surface, HMWK holds PK in position for activation by XIIa free in the bulk. (d) K now activates XII, either which approaches the surface or which is bound there.

the intrinsic pathway tenase (IXa-VIII) has been shown to significantly contribute to IIa generation. It appears that in this case, the extrinsic tenase VIIa-TF is responsible for the onset of coagulation, whereas the intrinsic tenase IXa-VIII is a major player in the propagation phase [88].

The Common Pathway

The result of either extrinsic or intrinsic pathway is Xa. It can then form an enzyme complex with V (Xa-V, referred to as prothrombinase), which catalyses thrombin (IIa) from prothrombin (II), by the proteolytic cleavage reaction. Thrombin has a very short half-life time (1–2 min). Besides being the central protease in the coagulation cascade, it also plays a role in inflammation, cellular proliferation and activation of angiogenesis [197]. The primary role of IIa in the coagulation cascade is the conversion of fibrinogen (I) to fibrin (Ia). It cleaves four highly negative charged parts from fibrinogen, which prevent it from aggregating into a network, thus forming a clot. Thrombin has the additional role of catalysing the activation of V, VII, VIII, XI and XIII (see Table 2.6 and Fig. 2.14). The coagulation cascade is maintained in a prothrombotic state by the continued activation of VIII and IX to form the tenase (VIIIa-IXa) complex, until it is down-regulated by the anticoagulant pathways. Furthermore, IIa plays a function in the anticoagulation process, by activating protein C (PC) and in the inhibition of fibrinolysis, via the activation of thrombin-activable fibrinolysis inhibitor (TAFI).

The trick of the cascading process in coagulation is that a few molecules of TF and VII can activate many copies of X, which in turn can activate even more II, which finally activates lots and lots of fibrin (in a fibrin burst). The same amplification effect is present in the three steps of cascade of the intrinsic pathway ($\mathrm{K{-}HMWK} \rightleftharpoons \mathrm{XIIa} \longrightarrow \mathrm{XIa{-}HMWK} \longrightarrow \mathrm{IXa} \longrightarrow \mathrm{Xa}$).

Finally, the function of XIII in the coagulation process is to actively catalyse cross-links between fibrin monomers in the soft clot, to form a hard clot (see Fig.

2.14). Factor XIII exists both in plasma and inside platelet granules, which are released released upon platelet activation in the proximity of a clot [52, p. 988].

2.3.2 Anticoagulation

The anticoagulation process begins in parallel with the procoagulation process, as soon as it is kinetically possible. It prevents excessive clot formation, since procoagulation is a positive-feedback process. A positive-feedback process can run out of control without a suppression mechanism. In this case, without the anticoagulation process, all circulating blood in the body would clot [51, p. 563].

The endothelial cells of intact vessels prevent blood clotting with a heparan sulfate (HS) proteoglycan and thrombomodulin (TM) (see Table 2.7); and platelet aggregation primarily with NO, ADPase and PGI2 (see Fig. 2.3 and Table 2.1). Thrombin binds to TM on endothelial cells and this complex (IIa-TM) activates PC. Activated PC (APC) inactivates Va and VIIIa. Protein S (PS) is a necessary cofactor for APC. More than half of PS in plasma is bound to the complement system protein C4b and not functionally active [88].

The action of the TF is impeded by tissue factor pathway inhibitor (TFPI), which is released almost immediately after initiation of coagulation. The molecule of TFPI has two inhibitory sites, one for Xa and one for VIIa-TF. Simultaneous linkage forming a Xa-TFPI-(VIIa-TF) complex is required for inhibition. Leukocyte elastase cleaves TFPI, which impairs the inhibitory ability and restores Xa and VIIa-TF catalytic activities [88].

Factor Xa is inactivated by protein Z-dependent protease inhibitor (ZPI), a serine protease inhibitor (serpin). The affinity of ZPI for Xa is increased 1000-fold by the presence of protein Z (PZ), while it does not require PZ for degradation of XIa. Defects in protein Z lead to increased factor Xa activity and a propensity for thrombosis. Furthermore, factors Xa, IIa, IXa, XIa and XIIa are inactivated by ATIII, by forming

Table 2.7: The major participants of the blood anti-coagulation processes.

Abbrev.	Name	Location
ATIII	Antithrombin III	
PC	Protein C	
APC	Activated PC	
PS	Protein S	Dissolved, free or bound to C4b
A2M	α_2-macroglobulin	Dissolved in plasma
ZPI	Z-dependent protease inhibitor	
PZ	Protein Z	
A1PI	α_1-protease inhibitor	
HCII	Heparin cofactor II	
TFPI	Tissue factor pathway inhibitor[a]	Endothelium, plasma, platelets, monocytes
TM	Thrombomodulin	Endothelial cell membrane
HS	heparan sulfate	On endothelial cell proteoglycans

[a] Formerly known as lipoprotein-associated coagulation factor (LAC1).

a complex with the enzymes, in which their active site is blocked. Inhibition rates rise significantly in the presence of polysaccharide heparin or HS [88].

The enzyme Va is degraded by APC, one of the principal physiological inhibitors of coagulation. In the presence of thrombomodulin, IIa acts to decrease clotting by activating PC. Therefore, the concentration and action of PC are important determinants in the negative feedback loop through which IIa limits its own activation.

2.3.3 Fibrinolysis

Eventually, as the damaged vessel repairs itself, the fibrinolysis process induces the clot retraction and dissolution by the enzyme plasmin (PN), as illustrated in Fig. 2.17 and summarised in Table 2.8. Plasmin breaks and inactivates fibrin molecules (I) which constitute the fibrin fibres. Plasmin appears in the blood plasma upon the activation of plasminogen (PLG) by tissue plasminogen activator (tPA) and urokinase (uPA) [41, 43]. Plasminogen circulates in blood plasma, after being produced in the liver. Plasminogen has a great affinity with fibrin, even though it cannot cleave fibrin in its inactivated

form. Because of that, many PLG molecules are incorporated into the the fibrin fibres when the clot is formed. The clot fibrin mesh is broken down once the entrapped PLG is activated. This occurs several days after the clot had formed, because tPA and uPA are slowly released into to the blood by the damaged endothelium. Both tPA and uPA are inhibited by plasminogen activator inhibitor-1 and plasminogen activator inhibitor-2 (PAI-1 and PAI-2). While tPA is a weak activator of PLG in the absence of fibrin, its catalytic efficiency for PLG activation is enhanced by at least two orders of magnitude in the presence of fibrin. The affinity between tPA and PLG is low in the absence of fibrin, but increases significantly in its presence. This elevated activation rate of (tPA) on fibrin is attenuated by thrombin-activatable fibrinolysis inhibitor (TAFI), which modifies fibrin to make it more resistant to the tPA-mediated PLG. Once a threshold level of tPA and uPA is reached, the PN production increases significantly, because PN has the ability cleave pieces of tPA and uPA, converting single chain tPA and uPA (sc-tPA and sc-uPA) into double chain forms (dc-tPA and dc-uPA), which are much more efficient activators of PN. This positive feedback is very important to overcome the inhibition process, and, thus, it fires the dissolution of the clot. Finally, the excess of PN is inactivated by α_2-antiplasmin (A2AP) and α_2-macroglobulin (A2M). Plasmin bound to fibrin is protected from A2AP, but TAFI decreases this protection by deleting the binding sites of PN on fibrin. Once fibrin is dissolved, double chain forms of tPA and uPA (dc-tPA and dc-uPA) are then rapidly inhibited because they are not any more bound to fibrin or to cell surface receptors [41].

Under certain conditions, enzymes of the intrinsic pathway of the coagulation cascade have been shown to activate PLG directly. These include kallikrein, factor XIa and factor XIIa, but these enzymes normally account for no more than 15% of total PN activation [41].

Table 2.8: Major participants of the fibrinolysis processes [41].

Abbrev.	Name	Location
PNG	Plasminogen	Plasma and bound to I
PN	Plasmin	Inside clots
tPA	Tissue plasminogen activator	In plasma after injury
uPA	Urokinase	In plasma after injury
PAI-1	Plasminogen activator inhibitor-1	Dissolved in plasma
PAI-2	Plasminogen activator inhibitor-2	Dissolved in plasma
A2AP	α_2-antiplasmin	Dissolved in plasma
A2M	α_2-macroglobulin	Dissolved in plasma
TAFI	Thrombin-activatable fibrinolysis inhibitor	Plasma and bound to I

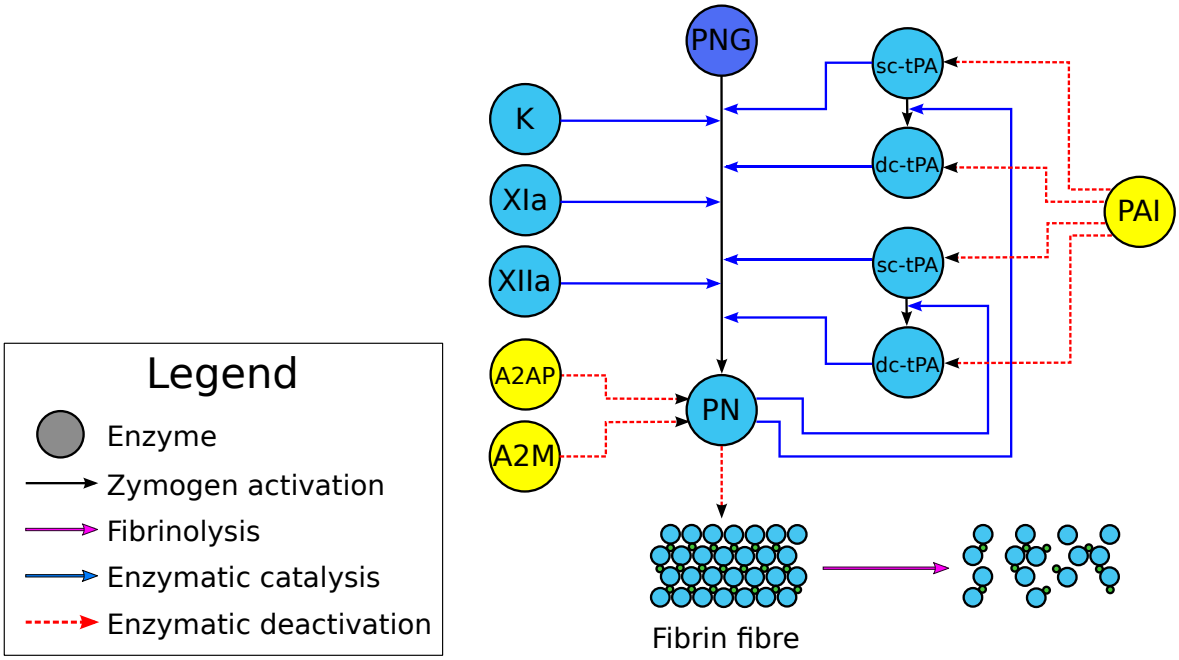

Fig. 2.17: Scheme of the fibrinolysis process. Blue enzymes promote fibrinolysis and yellow inhibit fibrinolysis.

2.4 Association with the Immune System

As Virchow's triad implies, thrombosis may occur without any vascular damage, which relates to the contact of blood with connective tissue. The formation of fibrin on an implanted biomaterial would first suggest that the coagulation system was activated through the intrinsic pathway by surface-mediated activation of XII and PK-HMWK. However, *in vitro* studies have shown that the amounts of generated IIa and IIa-ATIII did not correlate with the levels of adsorbed XIIa and K-HMWK on biomaterials incubated with plasma alone [29]. This result indicated that the adhered proteins of the intrinsic pathway play are not the sole activators of the coagulation cascade. Moreover, normal levels of IIa generation in a patient with severe XII deficiency during cardiopulmonary bypass were observed [178]. This proves the limited potential of the intrinsic pathway alone to produce thrombi. The mystery of thrombosis occurring with a patient with intrinsic deficiency seems to be clarified by the fact that TF expression has been observed on monocytes in the presence of biomaterials. This is strong evidence for inflammation being one of the causes of thrombosis. Nonetheless, the time scales associated with leukocyte TF expression and protein reactions are clearly dissimilar. Contact phase activation of proteins occurs in a few seconds or minutes, whereas the synthesis of TF in monocytes of a normal patient requires at least 60 min [88].

2.4.1 Leukocytes

Leukocytes, or white blood cells (WBCs), are the cells of the immune system. They include neutrophils, monocytes, lymphocytes, basophils and eosinophils (or white blood cells, WBCs). Neutrophils and monocytes are found in the blood in higher quantity than the other WBC types; they are the major players in the inflammatory response with respect to cardiovascular devices. Other WBC types do not normally remain inside the blood stream, they are more comonly found either in the lymphatic system

or they are spread in the connective tissue. Neutrophils and monocytes possess receptors for many pro-inflammatory mediators, which can be produced by other activated leukocytes in- or outside the blood stream, by activated platelets or by the complement system. Other activating stimuli include bacteria and their products, such as endotoxins, and cell adhesion. Endotoxins are large molecules found in the outer membrane of bacteria.

Leukocyte activation results in a number of physiological responses. Changes in expression of membrane receptors occur, such as synthesis of TF. Inflammatory mediators are released from granules. They have various properties comprising chemoattractants for leukocytes, promoters of adherence to endothelial cells, and further activation of platelets and leukocytes. Furthermore, activation may result in a burst of oxidants, such as O_2^- and H_2O_2, which damage tissues, neutralise anticoagulants and activate platelets.

Activated neutrophils and monocytes also have an increased adhesive capacity on endothelium and other surfaces. Adhesion to the endothelium is an important means by which these cells participate in the inflammatory response. Leukocyte contact adhesion involves a three-step mechanism. First, endothelial cells activated by inflammatory signals (such as histamine and thrombin) move a series membrane receptor called P-selectin to their surfaces. Leukocytes have ligands that bind to P-selectin, causing the initial rolling of these leukocytes on the endothelium. As well as activated endothelial cells, activated platelets also present P-selectins on their membranes, which cause initial aggregation of platelets and WBCs [187]. Second, the rolling enables leukocytes to slow their movement and sample the local environment, by means of which they may become activated due to local stimulation. Third, the receptor CD11/CD18 mediates firm adhesion of activated neutrophiles and monocytes. A functional change and increase in the number of receptor CD11b results in increased binding affinity of certain ligands, such as factor I (fibrinogen) and factor X [11]. The increased concentration of factors

I and X enhances the reaction rate of the coagulation cascades around the leukocytes. Moreover, fibrinogen is a key factor in strong platelet adhesion, making leukocyte-platelet bindings very likely to occur.

Contact with cardiovascular devices *in vivo* activates both neutrophils and monocytes, with clear increased adhesion and the release of inflammatory mediators. Normally, those leukocytes remove solid foreign particles that they encounter by engulfing them, in a process known as phagocytosis. Since objects larger than a leukocyte cannot be engulfed, adherent neutrophils and monocytes undergo a frustrated phagocytosis. whereby they release their array of potent oxygen metabolites and proteolytic enzymes. Nevertheless, material characteristics and proteins at the interface modulate the level of activation of these cells. Activated leukocytes may adhere in the endothelium downstream of the biomaterial site.

The mechanisms of leukocyte adhesion on biomaterials are not completely clear, but it appears to be mediated in part by the complement product iC3b. Inhibition of complement activation *in vitro* has shown significant reduction of leukocyte adhesion. Monocyte TF expression is only partially dependent on the complement system, but appears to be dependent on the presence of AP as well [88].

2.4.2 The Complement System

Once blood plasma proteins adhere to a biomaterial surface, they trigger a complex series of events that may lead to thrombogenesis [152]. These proteins include not only members of the coagulation system, but also members of the complement system. The complement system is a critical element of the innate immune response, where one of its principal functions is to serve as a primitive self-/non-self discriminatory defence system. This is accomplished by coating non-specific foreign elements, marking them, and recruiting phagocytic cells to attempt to destroy these intruders. The complement system may contribute to thrombogenesis by activating platelets, leukocytes, and some

Table 2.9: Complement activities against infections

Activity	Complement protein
Identification opsonization of pathogens	C3, C4
Recruitment activation of inflammatory cells	C3a, C5a
Lysis of pathogens cytotoxicity	C5b-9
Clearing immune complexity and appoptotic cells	C1q, C3b, C4b
Augment cellular immune response to T and B cells	C3, C3a, C4, C5a

coagulation factors.

The complement system is composed of more than 30 distinct plasma and membrane bound proteins. The activities of some of these proteins for protecting the body against intruders are summarised in Table 2.9 [159]. The activation of the complement system is very similar to the activation of the coagulation system; both are cascades of serine proteases activated by distinct pathways. The complement cascades can be activated via two distinct, but interacting, pathways: the classical and the alternative pathways, which lead to a common terminal pathway [164], see Fig. 2.18. The classical pathway typically requires antigen-antibody complexes for activation (specific immune response), whereas the alternative pathway can be activated by C3 hydrolysis or antigens, without the presence of antibodies (non-specific immune response). Therefore, the presence of biomaterials is believed to activate the complement system via the alternative pathway. However, the type of activation is not unique. Some activating materials generate high levels of both C3b and C5b-9, whereas others will generate high C3b levels but little C5b-9.

The Classical Pathway

The classical pathway proteins are C1, C1-Inh[3], C2, C4, and C4b. The proteolytic cascade is initiated by the binding of antigen-antibody complexes with the C1 complex.

[3]The suffix "Inh" denotes the protein *inhibitor*.

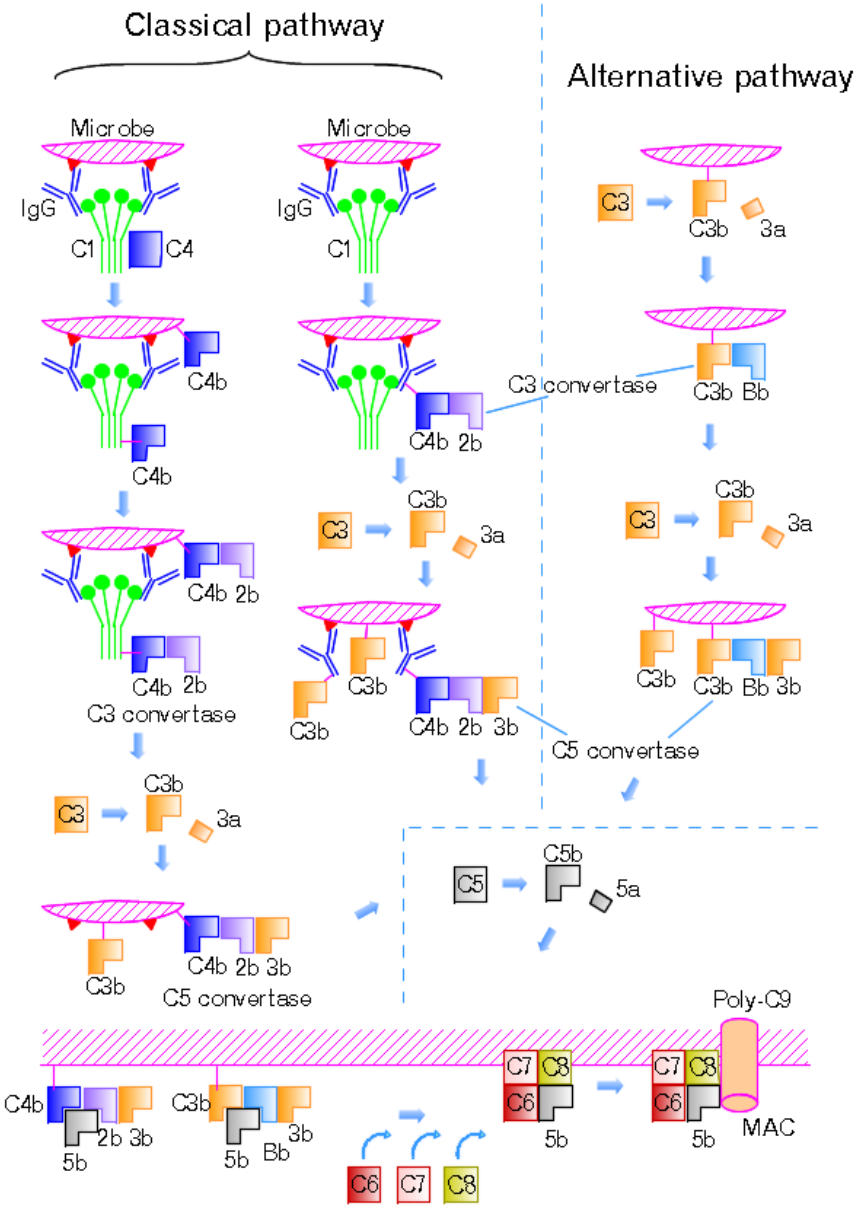

Fig. 2.18: Pathways of complement activation.

Once connected to an antigen-antibody complex, C1 is able to cleave the C4 protein in two pieces, C4a and C4b. Protein C4b binds to surfaces containing either amino or hydroxyl moieties, but it does not bind efficiently to membrane surfaces, and it is rapidly inactivated by the loss of its binding site. The complement protein C2 binds to C4b, where it is cleaved by C1. The break of C2 releases C2a and creates the classical C3 convertase: C4bC2b. The classical C3 convertase can cleave C3 into C3a and C3b, which by the combination with C4bC2b and C3b forms the C5 convertase: C4bC2bC3b.

The Alternative Pathway

The alternative pathway does not require an antibody, for any foreign surface can trigger its activation. Complement activation via this pathway occurs spontaneously at a low rate. C3 can bind and cleave factor B into Ba and Bb, as well as cleave another C3 into C3a and C3b. On the surface, the alternative C3 convertase, C3bBb, is formed. When attached to a surface, C3bBb power is amplified. The alternative C5 convertase is formed by a clustering of C3b, denoted C3bBbC3b.

The Terminal Pathway

The convertase C5 can cleave C5 into C5a and C5b, which is the first product of the terminal complex pathway. Protein C6 has a high affinity for C5b, creating the complex C5bC6. This complex then binds with C7, C8 and up to 12 molecules of C9, which form the terminal complement complex: C5b-9. If C5b-9 is attached to a cellular membrane, it is called membrane attack complex (MAC), or mC5b-9. This complex inserts itself in the membrane resulting in cell lysis. Homologous membrane proteins prevent lysis of autologous cells, which restrict C5b-9 to properly assemble onto their membranes.

Table 2.10: Interactions between the complement and the coagulation systems [88]

Protein	Type of interaction
Thrombin (IIa)	Proteolysis of C3, C5, C6 and factor B
Factor XIIa	Proteolysis of C1r, C1s and C3
Kallikrein (K)	Proteolysis of C1, C5 and factor B
Antithrombin (AT)	Protect RBC from lysis by mC5b-9
Bb	Proteolysis of II
C3bBb	Proteolysis of II
C1 inhibitor	Inactivates XIIa and kallikrein
SP	Stabilises plasminogen activator inhibitor 1
C4b-binding protein	Binds to the vitamin K-dependent SP

Complement Regulation

The classical pathway is regulated by C1-Inh, and C4b-binding protein (C4b-bp) inhibiting C4b bound to a surface. Complement factor I inactivates C4b and C3b, therefore it is also known as C3b/C4b inactivator. The degradation power of complement factor I for C4b is increased when it is bound with the cofactor C4b-bp. Factor H is another cofactor of complement factor I, but for the degradation of C3b. The activity of C3 and C5 convertases is regulated by three membrane proteins. On RBC membrane, the activity of C3 convertase is destabilised by the decay-accelerating factor (DAF). On WBC and platelets, the membrane cofactor protein (MCP) favours the dissociation of factor B and promotes the association of C3b with complement factor I. On RBC and WBC, the complement receptor type 1 (CR1) acts like factor H by aiding complement factor I in the degradation of C3b.

Association of Complement and Coagulation Systems

The complement factor C1q is an agonist for platelet activation. Additionally, the complement and coagulation systems interact and modulate each other, as outlined in Table 2.10.

The activation of leukocytes by complement proteins plays an indirect role in thrombogenesis [152]. Leukocytes have a number of receptors for complement proteins, including C1q, C3a, C3b, C4b, iC3b[4] and C5a. On one hand, C3b, C4b and iC3b bind to foreign particles and immune complexes in order to alter the surface so that it becomes more readily and efficiently engulfed by phagocytes. This process is known as *opsonization*. On the other hand, factors C3a, C4a and C5a are soluble leukocyte activators. Activated leukocytes have increased stickiness and release proinflammatory agonists which are able to activate platelets [88]. Moreover, these activated leukocytes begin to express new membrane receptors such as tissue factor (TF), known for triggering the extrinsic coagulation cascade.

The total distinction between the immune and coagulation system may be an impediment in the understanding of coagulation mediated by a biomaterial. The interrelation between these systems may be closer than expected. While the immune system induces coagulation by complement and neutrophil activation, blood coagulation helps to prevent bacteria for entering the body in the case of an injury. Beyond that, a recent study by Loof *et al.* demonstrated that mice with factor XIII deficiency were more susceptible to *Streptococcus pyogenes* infection than normal mice [147]. The induction of coagulation by inoculated bacteria leads to immobilization and killing of the bacteria inside the clot. This evidence supports the concept that coagulation can be seen as part of the innate immune system. The authors stressed the similarities between the complement and coagulation cascades, both of which involve serine proteases. They also did an evolutionary comparison of these proteases with the immune system of *Drosophila* and horseshoe crabs (*Limulus polyphemus*). In the first case, *Drosophila* has a serine protease that can be triggered by either development signals or by the immune system. In the second case, the immune system of *Limulus polyphemus* depends primarily on the clotting protease, which traps the invaders before phagocytosis. The

[4]The "i" prefix denotes the *inhibited* protein.

structural similarity of the coagulation and immune processes, as well as the synergy they share in protecting the circulatory system, suggest that these two systems are in fact a single inseparable system. This idea is supported by physiological comparison with other species, where aspects normally associated with one system execute the function normally associated with the other system.

2.4.3 Complement Activation and Biomaterials

Complement activation is known to occur during cardiopulmonary bypass and haemodialysis grafts, with catheters and prosthetic vascular grafts. The consequences of complement activation include leukopenia (reduction of WBCs in blood), WBC activation, hypotension, pulmonary injury, and thrombosis.

One of the most investigated materials from the perspective of the complement system is the cuprophrane membrane used extensively for heamodialysis. Craddock *et al.* [49] showed that some of the symptoms present in heamodialysis patients could be reproduced in animals when they were infused with autologous plasma that had been incubated in vitro with Cuprophran. This effect did not happen when the plasma was treated to inhibit complement activation. Later in 1984, Chenoweth [45] identified C3a and C5a in plasma of patients during dialysis therapy. A typical patient response is shown in Fig. 2.19, where C3a and C5a concentrations rise during the first 15 min, during the period where WBCs become hyperadherent and are trapped in the lungs, resulting in peripheral loss of these cells (neutropenia). The foreign surface activates the alternative pathway, and WBCs become activated by C3a and C5a. In time, C3a and C5a are regulated, decreasing towards baseline concentrations, but WBCs remain primed in a more activated state. This mechanism relating the complement activation by the biomaterial with neutropenia was confirmed by the infusion of purified C5a in sheep [110]. The inflammatory and immune responses were identical to those of sheep subjected to haemodialysis.

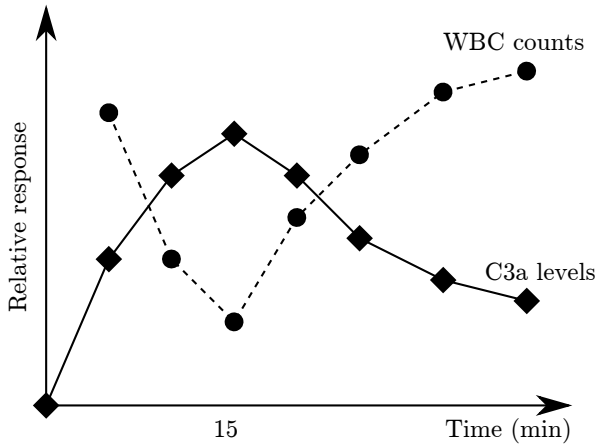

Fig. 2.19: Typical response pattern of the complement system to dialysis. Image reproduced from Chenoweth [45].

Although the alternative pathway is the most prominent complement activator pathway of biomaterials, activation can occur through the classical pathway as well. Adsorbed immunoglobulin G and M (IgG and IgM) have been shown to initiate the classical complement pathway on the surface of a type of silicone [213]. The relative importance of the different activation pathways is observed in patients with C4 deficiency (who lack the classical pathway) undergoing haemodialysis. In this case, complement activation is much delayed, but eventually it reaches the same amplitude as normal patients, because the small amounts of C3b produced by the classical pathway bind to the the material, generating an amplification loop through the alternative pathway.

Cardiopulmonary bypass circuits induce exactly the same immunological response as observed in haemodialysis. The group symptoms in this case are known as "postperfusion" or "postpump" syndrome. The importance of inhibiting complement activation during cardiopulmonary procedures was clearly demonstrated. Fitch *et al* [62] used C5 antibodies to inhibit C5a and MAC generation. This lowered WBC activation, blood loss, myocardial injury and cognitive deficits. An other study demonstrated that a cardiopulmonary bypass circuit coated with heparin produced lower inflammatory indices and improved clinical outcomes [212]. This experiment has shown that the modifica-

tion of the material's surface can dramatically limit complement activation. Heparin competes with C3b for the surface area, thus limiting C3b deposition on surface nucleophiles. The diminished capacity of binding C3b results in lower levels of C3 and C5 convertase.

Besides heparin, other molecules that also get adsorbsed on biomaterials have given positive results against complement activation [164, 165]. The method most widely tested is the PEGylation (polyethylene glycol coating). PEGylation increases the hydrophilicity of the biomaterial surface and prevents direct adsorption of proteins. Other encapsulation methods use various kinds of alginate or polysulphone coatings. A method directed more to the inhibition of the complement system is to coat the surface with factor H. Factor H is immobilised to the surface by either a cross-linking agent, like end-group activated Pluronic; or a specific peptide, antibody, or antibody fragment. Immobilised factor H reduces the amount C3b and iC3b fragments deposited on the biomaterial surface after incubation with either serum, plasma, or whole blood [10].

Some activating materials generate high levels of both C3b and C5b-9, whereas others generate high C3b but little C5b-9. However, even low amounts of C5b-9 are able to activate leukocytes [122]. The safe levels of complement activation, either in short or long term, are still not known [152].

2.5 Concluding Remarks

The physiology of haemostasis and thrombosis was reviewed in this chapter. It is initiated by any of the disfunctions embodied in Virchow's triad: abnormal blood composition, abnormal flow, or abnormal surface. These disfunctions trigger physiological signals to platelets, coagulation proteins, and the immune system, which lead to a series of physiological relations that culminate in a blood clot. The haemostasis processes are

essential for stopping bleeding, but they are potentially dangerous when a thrombus is formed inside the circulatory system impeding blood flow. Platelets participate on haemostasis, once they detect specific proteins either diluted or adsorbed on thrombogenic surfaces. Then, platelets become activated and aggregate. Activated platelets release biochemical factors that cause activation of other platelets, the immune system, and the coagulation system. Likewise, the immune and coagulation systems can also become activated by unphysiological substances and surfaces, and end up activating platelets. One interesting aspect of platelet aggregation and activation, that was thoroughly reviewed in this chapter, was the relation with shear stress. The aggregation efficiency of platelets depend on fluid shear stress. Platelet aggregates are cross-linked with fibrinogen at low shear stresses, but they are cross-linked with von Willebrand factor at high shear stresses. The latter protein form long coiled multimer chains that unfold at high shear stresses, binding platelets with high efficiency. The transformation rates of the mechanisms of haemostasis presented in this chapter will be discussed in the next chapter (Chapter 3), where mathematical models of thrombosis are presented.

Chapter 3

Literature Review on Mathematical Models for Haemostasis

In this chapter, the literature on the physico-chemical dynamics of thrombosis is reviewed. The non-linear rheology of blood plays an important role in thrombosis. The flow of red blood cells (RBCs) is inhomogeneous inside vessels, and it strongly influences the spatial distribution and transport of platelets and coagulation factors. The chemical kinetics of the coagulation cascades is reviewed in terms of individual reaction rates, reaction chains with positive and negative feedback loops, and correlation with empirical data. Lastly, a brief review of a few recent models, which include various aspects involved in thrombosis, are presented. These multi-physics models are very promising in the study of thrombosis, because they venture to predict the spatio-temporal formation of thrombi, coupling transport and reaction models for proteins and platelets.

3.1 Haemorheology

Haemorheology is the science of deformation and flow of blood and its formed elements, including micro- and macroscopic properties both *in vitro* and *in vivo* [73, p. 63]. Therefore, the understanding of the coupling between the blood composition and its physical properties is essential for developing suitable constitutive models to describe blood flow behaviour. Whole blood is a concentrated suspension of cells and proteins whose non-Newtonian behaviour is largely due to the presence of RBCs. Haematocrit is the volume concentration of RBCs, which ranges from 40 to 45% in normal conditions. Other blood cells occupy a minimum volume concentration, as can be seen in Table 3.1. The non-linear rheology of blood is due to three aspects: (1) RBCs aggregate and form three-dimensional branched networks at low shear rates, (2) deformability of RBCs, and (3) their tendency to align with the flow field at high shear rates [47, 71, 243]. After serious blood loss, dehydration, long exposure to low-oxygen atmosphere, or disease, the haematocrit level can vary. The mechanical properties of blood are strongly dependent on the haematocrit level.

The RBC is a highly flexible biconcave disc with a diameter of 7–8 µm (see Fig. 3.1c), when suspended unstressed in plasma, or other isotonic fluid. The biconcave disc has a greatly increased surface area to volume ratio compared to spheres, facilitating gas transfer. It makes it possible for RBCs to greatly deform with insignificant strain, when compared to spherical cells [70, p. 120]. Deformability is important for RBCs to squeeze through small capillaries, as well as to stretch along the flow at high shear rates (see Fig. 3.1c). The tendency of stretching parallel to the shear contributes to lower the local effective viscosity, and improves flow-derived lift from the vessel wall [79]. The properties of an individual RBC change as it ages and the normal life-span of a RBC in human blood is 100–120 days. At low shear rates, RBCs have a tendency to aggregate. If blood is smeared onto a microscope slide, RBCs can be seen to attach themselves side-by-side to form branched stacks called rouleaux (see Fig. 3.1a). Rouleaux can develop

Table 3.1: Quantity, shape, size and concentration of cellular components in normal human blood [73, adapted from p. 66].

Cell	Concentration (m^{-3})	Resting Shape and Dimensions (µm)	Volume Concentration (%)
Erythrocytes (RBCs)	$(4-6)\cdot 10^6$	Biconcave Disc $(1-3)\times(7-8)$	45
Leukocytes (WBCs)			1
Total	$(4-11)\cdot 10^3$		
Granulocytes			
Neutrophils	$(1.5-7.5)\cdot 10^3$	Roughly Spherical $7-22$	
Eosinophils	$(0-4)\cdot 10^2$		
Basophils	$(0-2)\cdot 10^2$		
Lymphocytes	$(1.0-4.5)\cdot 10^3$		
Monocytes	$(0-8)\cdot 10^2$		
Thrombocytes (Platelets)	$(250-500)\cdot 10^3$	Discoid 0.6×1.6	

in vivo, as well as *in vitro*, at low shear rates ($\dot{\gamma} \lesssim 50\,s^{-1}$, for healthy individuals) [73, p. 81]. The rouleaux 3-D structure increases the macroscopic viscosity of blood at low shear rates. The process of rouleaux formation depends on the presence of certain large asymmetric macromolecules in the external environment, particularly fibrinogen and globulins. As a result, the mechanical properties of blood have a larger variance from donor to donor at low shear rates because the concentration of those macromolecules and the haematocrit can vary, especially in diseased individuals.

3.1.1 Haemostasis in Flowing Blood

Blood is a complex fluid composed of water, proteins and cells. It is the main transport medium for nutrients, gasses, biochemical signal molecules, and immunological cells within the body. Haemostasis exists to close damaged blood vessels, in order to stop blood of leaking out of the body, and to prevent malignant germs to invade the body. As discussed previously, flow is an important aspect in haemostasis because it

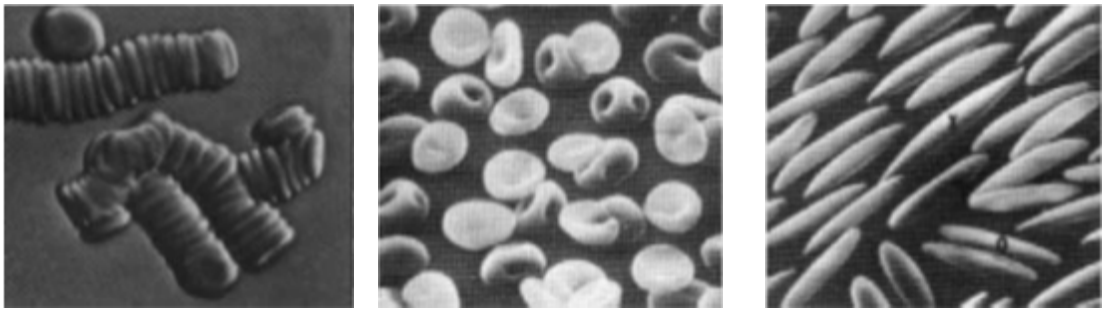

(a) RBC rouleaux at 0.1 Pa. (b) RBCs at 10 Pa. (c) RBCs at 300 Pa.

Fig. 3.1: View of erythrocytes from normal human blood. RBCs in (b) and (c) were fixed with glutaraldehyde while sheared in a viscometer. Images reproduced from Galdi *et al.* [73, p. 73].

transports platelets and coagulation proteins to the site of damage. Abnormal flow is one of the aspects of Virchow's Triad which can trigger haemostasis (see Fig. 2.1). It has been demonstrated that both blood rheology and dynamics have a major impact in the development and stabilization of thrombi [17]. Both too low and too high shear stresses are sensed by platelets and endothelial cells, triggering physiological cascades which lead to haemostasis. Special rheological characteristics of blood have to be considered, when haemostasis is modelled to simulate the thrombogenesis in flowing blood. The tumbling and rolling of RBCs create a number of rheological characteristics which are absent in blood plasma alone. Both viscosity and molecular transport are increased in whole blood, due to the presence of RBCs. Finally, the transport of molecules and cells is an important aspect of thrombus formation. A thrombus is a porous medium where transport is minimised compared with the free flowing region outside the thrombus. The decreased transport power inside the thrombus is important to control the development of the thrombus. Thus, slow reactions are allowed to happen in the core of the thrombus, while fast reactions are more concentrated at the boundary of the thrombus and blood flows freely.

3.1.2 The Transport Equation

The transport equation is a partial differential equation (PDE) which computes the transport of any physical quantity in a continuum medium. The general transport equation was first derived by Smoluchowski (1916a) [221] by coupling equations of elastic forces between particles, diffusion, and source points in the control volume. Thus, the transport equation for a particle concentration $C = C(\mathbf{x}, t)$ is

$$\underbrace{\frac{\partial C}{\partial t}}_{\substack{\text{spatial} \\ \text{change rate}}} = \underbrace{\boldsymbol{\nabla} \cdot (\boldsymbol{D} \boldsymbol{\nabla} C)}_{\text{diffusion}} - \underbrace{\boldsymbol{\nabla} \cdot (\boldsymbol{v} C)}_{\text{advection}} + \underbrace{S_C}_{\text{source term}} . \tag{3.1}$$

In Eq. 3.1, the term $\boldsymbol{D}$ is the diffusivity tensor for the scalar C, $\boldsymbol{v}$ the medium's velocity vector, and S_C is the source term representing the rate of production or consumption of C in the control volume. In an isotropic medium, the diffusivity tensor becomes $\boldsymbol{D} = D\boldsymbol{I}$, the diffusion term can be simplified as $\boldsymbol{\nabla} \cdot (D\boldsymbol{I}\boldsymbol{\nabla} C) = D\nabla^2 C$, where $\boldsymbol{\nabla}^2(\cdot) := \boldsymbol{\nabla} \cdot \boldsymbol{\nabla}(\cdot)$ is the Laplacian operator. The source (or sink) term S_C combines all other effects that create or destroy C. Some examples of common source mechanisms are: chemical reactions, body field forces, or modelled physical assumptions that represent empirical losses or gains of C at specific conditions. The transport equation is applicable for the transport of any intensive physical quantity, such as density (ρ), temperature (T), specific internal energy (u), and specific momentum ($\mathbf{v}$).

Continuity Equation

The continuity equation is obtained by taking $C = \rho$ and $D = 0$, where no mass can be either created or destroyed (i.e. $S_\rho = 0$). Hence, the continuity equation is

$$\frac{\partial \rho}{\partial t} = -\boldsymbol{\nabla} \cdot (\boldsymbol{v}\rho) . \tag{3.2}$$

For incompressible media, the isochoric constraints $\frac{d\rho}{dt} = 0$ and $\nabla \cdot \rho = 0$ are imposed to Eq. 3.2 (i.e. the density following the path of a fluid element is constant). Thus,

the continuity equation for incompressible fluids is

$$\boldsymbol{\nabla} \cdot \boldsymbol{v} = 0 \ . \tag{3.3}$$

Momentum Equation

Another noteworthy transport equation is the transport of linear momentum in an incompressible fluid, also known as the Navier-Stokes equation for incompressible fluids. By taking $C = \boldsymbol{v}$, $D = \nu$ and $\mathbf{S_v} = (\mathbf{f} - \boldsymbol{\nabla}\mathbf{p})$, where ν is the kinematic viscosity, $\boldsymbol{f}$ field forces such as gravity, and p is the pressure field, Eq. 3.1 becomes

$$\frac{\partial \boldsymbol{v}}{\partial t} = \nu \nabla^2 \boldsymbol{v} - \boldsymbol{\nabla} \cdot (\boldsymbol{v} \otimes \boldsymbol{v}) + \boldsymbol{f} - \boldsymbol{\nabla} p \ . \tag{3.4}$$

The viscous term can also be represented by the shear stress tensor

$$\boldsymbol{\tau} = 2\mu \boldsymbol{E} \ , \tag{3.5}$$

where

$$\boldsymbol{E} := \frac{1}{2} \left(\boldsymbol{\nabla} \boldsymbol{v} + \boldsymbol{\nabla} \boldsymbol{v}^T \right) = \frac{1}{2} \left(\frac{\partial \boldsymbol{v}}{\partial \boldsymbol{x}} + \frac{\partial \boldsymbol{v}}{\partial \boldsymbol{x}}^T \right) \tag{3.6}$$

is the strain-rate tensor, and μ is the dynamic viscosity determined from a constitutive equation. The advective term is typically written as $\boldsymbol{\nabla} \cdot (\boldsymbol{v} \otimes \boldsymbol{v}) = (\boldsymbol{v} \cdot \nabla)\boldsymbol{v}$. Therefore, Eq. 3.4 can also be written as

$$\frac{\partial \boldsymbol{v}}{\partial t} = \nabla \cdot \boldsymbol{\tau} - (\boldsymbol{v} \cdot \nabla)\boldsymbol{v} + \boldsymbol{f} - \boldsymbol{\nabla} p \ . \tag{3.7}$$

Using the stress tensor definition for incompressible fluids,

$$\boldsymbol{\sigma} = \boldsymbol{\tau} - p\boldsymbol{I} \ , \tag{3.8}$$

where $\boldsymbol{I}$ is the identity tensor, Eq. 3.7 becomes

$$\frac{\partial \boldsymbol{v}}{\partial t} = \nabla \cdot \boldsymbol{\sigma} - (\boldsymbol{v} \cdot \nabla)\boldsymbol{v} + \boldsymbol{f} \ . \tag{3.9}$$

3.1.3 Blood Viscosity

The viscosity of whole blood generally decreases with increasing shear rate. This shear-thinning non-Newtonian characteristic is seen in Fig. 3.2. When the shear rate is about $\dot{\gamma} = 100$–$200\ \mathrm{s}^{-1}$, which is a typical level for many blood vessels *in vivo*, the non-Newtonian behaviour becomes insignificant, and the apparent viscosity[1] approaches an asymptotic value, which is in the range of $\mu = (3\text{–}4) \cdot 10^{-3}\,\mathrm{Pa\,s}$. The reasons for this shear-thinning property are the disaggregation of the rouleaux, radial migration of RBCs away from the walls, and the individual orientation RBCs along the flow direction. However, with reduction of the shear rate, the apparent viscosity increases slowly, until at a shear rate $\dot{\gamma} < 1\ \mathrm{s}^{-1}$ it rises extremely steeply.

Below a haematocrit of about 12%, suspensions of RBCs in plasma are found to be Newtonian at all shear rates (see Fig. 3.3). Nevertheless, the RBC suspensions still have higher viscosity than plasma, which is normally $\mu = (1.2 \pm 0.1) \cdot 10^{-3}\ \mathrm{Pa\,s}$ at body temperature $\mathrm{T} = 37\,^{\circ}\mathrm{C}$ (see Fig. 3.4) [73, p. 95]. When the haematocrit is further raised, not only the viscosity of the suspension increases, but non-Newtonian behavior is observed, detectable first at very low shear rate [70, p. 82].

Temperature is an important aspect to be considered when measuring rheologic properties of blood. As for most liquids, viscosity increases as temperature decreases, so too does plasma viscosity. At room temperature ($T = 20$–$25^{o}\mathrm{C}$), blood plasma is more viscous, $\mu(20^{o}\mathrm{C}) = (1.7 \pm 0.1) \cdot 10^{-3}\ \mathrm{Pa\,s}$, than at physiological temperature, $\mu(T = 37^{o}\mathrm{C}) = (1.2 \pm 0.1) \cdot 10^{-3}\ \mathrm{Pa\,s}$. The difference in plasma viscosity affects the apparent viscosity of whole blood. Figure 3.5 shows the temperature dependence of blood viscosity.

The shear-thinning effect in blood occurs at about 92% due to the aggregate

[1] *apparent viscosity* is the viscosity that is measured. In complex fluids, the actual viscosity can vary inside the sample due to heterogeneous distribution of components. In the case of suspensions like blood, normally the actual viscosity close to the wall is much lower than the actual viscosity further from the wall [70, p. 92].

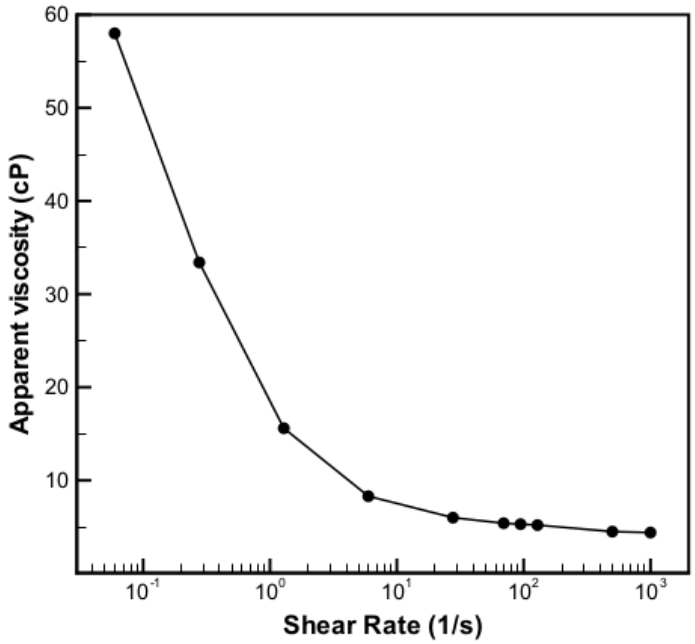

Fig. 3.2: Apparent viscosity as a function of the shear rate for whole blood obtained from a 25 year old female donor with haematocrit $Ht = 40\%$, T = 23 °C. Images reproduced from Galdi *et al.* [73, p. 85].

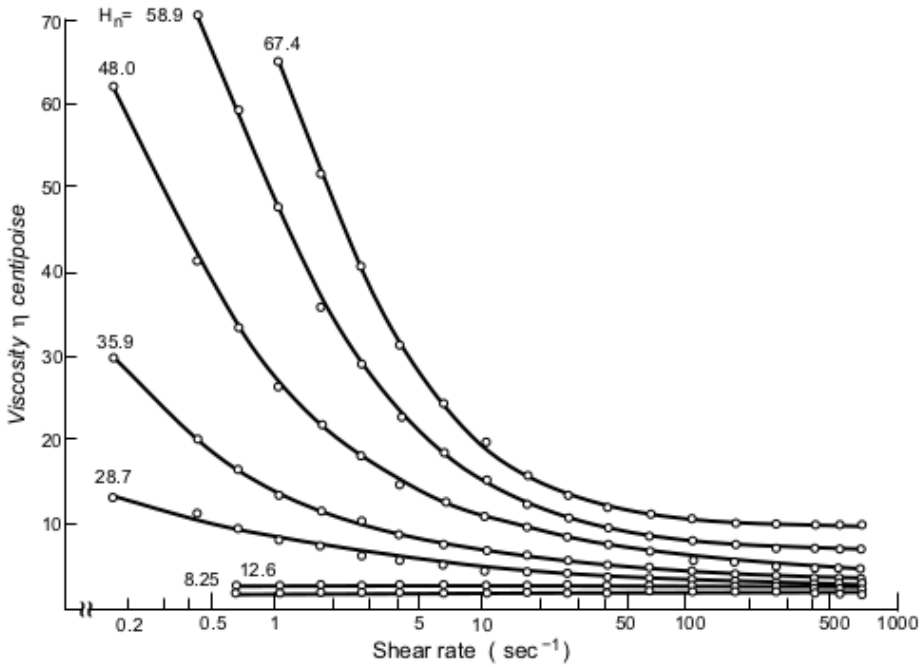

Fig. 3.3: Apparent viscosity as a function of the shear rate for various volume concentration of RBCs defined through Hn ($Hn = 0.96Htc$). RBCs were suspended in ACD-plasma (acid-citrate-dextrose anticoagulant) at $T = 25\,°\text{C}$. Image reproduced from Galdi *et al.* [73, p. 94].

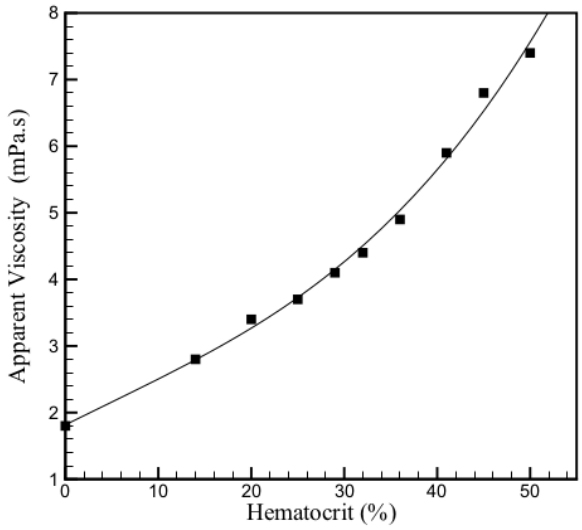

Fig. 3.4: Apparent viscosity as a function of haematocrit for human blood diluted with autologous plasma at 21 °C and $\dot{\gamma} = 128\ \mathrm{s}^{-1}$. Image reproduced from Galdi *et al.* [73, p. 93].

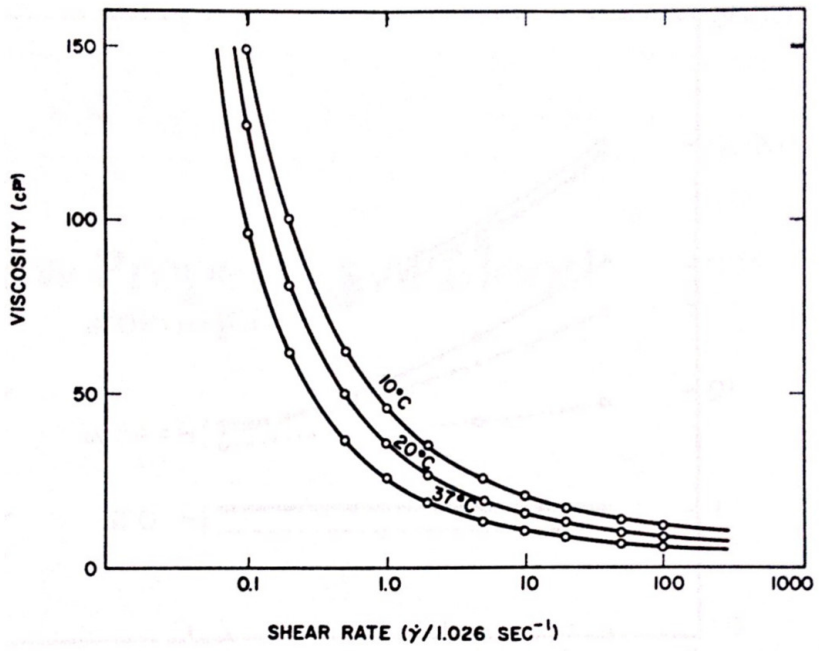

Fig. 3.5: Apparent blood viscosity as a function of shear rate for distinct temperatures. Image reproduced from Fung [70].

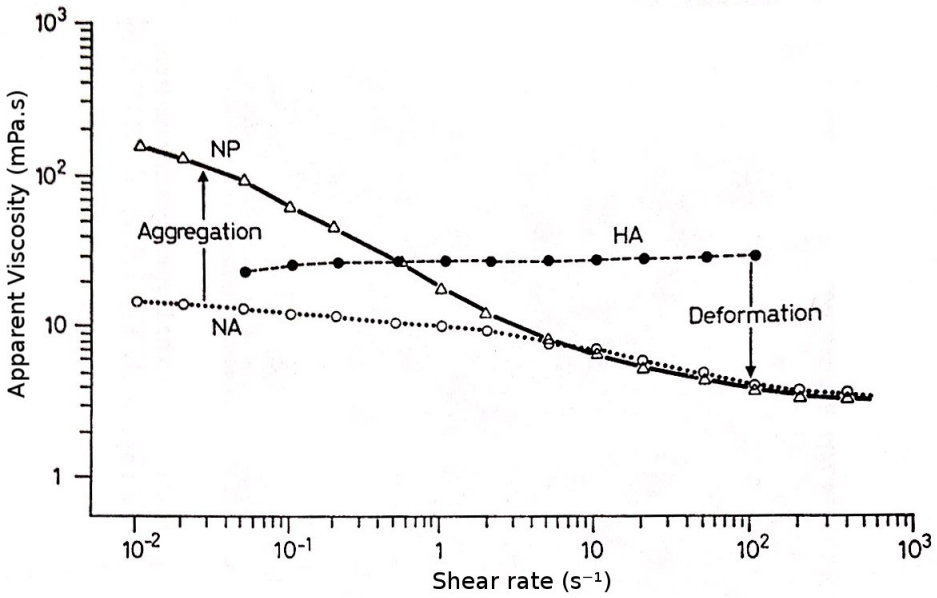

Fig. 3.6: Logatithmic relation between apparent viscosity and shear rate in three types of RBC suspension, each containing 45% of haematocrit. (NP) normal RBC in plasma, (NA) normal RBC in 11% albumim, and (HA) hardened RBC in plasma. Both the plasma and albumin solution had $\mu = 1.2$ mPa s [46, 70, 73].

formation at low shear rates and at about 8% due to the alignment of stretched RBCs along streamlines at high shear rates. It is possible to see in Fig. 3.2 that most of the viscosity thinning occurs over the range of 0.01 to 6 s^{-1} due to RBC aggregation [73, p. 88]. Figure 3.6 comparatively displays the apparent viscosity of three distinct RBC suspensions: normal blood, RBCs in albumin solution lacking fibrinogen and globulins, and hardened RBCs in normal plasma. In albumin solutions, RBCs could not aggregate, therefore the apparent viscosity was much lower at $\dot{\gamma} < 6\,s^{-1}$. On the other hand, the hardened RBCs were not stretched, therefore the apparent viscosity remained approximately constant because RBCs could neither aggregate or align along the streamlines [47]. The deformability of RBCs is not only important to decrease overall blood viscosity, but it is extremely important for erythrocyte passage through minute blood vessels [79].

Haemorheology experiments at low shear rates are exceedingly difficult to perform.

As a result, there remains a controversy over the behaviour of blood at the limit of shear rate tending to zero. Even at very low shear stresses, blood hardly becomes a gel-like solid, since even when RBCs are tightly aggregated, blood plasma is still able to flow around the packed RBCs. Nonetheless, the shear-thinning nature of normal blood is expected to play a minor role in the majority of the arterial circulation, where shear rate fluctuates a lot throughout streamlines. Thus, the Newtonian fluid model can be applied to non-steady cases where healthy blood flows at high shear rates. Newtonian fluids satisfy the linear relation

$$\tau = \mu\dot{\gamma} \tag{3.10}$$

between shear stress τ and shear rate $\dot{\gamma}$, where μ is the constant dynamic viscosity. Equation 3.10 is one-dimensional because viscometers generally operate in 1-D flow conditions, where shear-rate is homogeneous. For general flow conditions, where shear rate is a tensor with three spatial coordinates, the viscosity obtained from a 1-D viscometer can still be used if the general shear rate

$$G := \sqrt{2\,\boldsymbol{E} : \boldsymbol{E}} = \sqrt{2\,tr\boldsymbol{E}^2} \tag{3.11}$$

is applied in place of the 1-D shear rate $\dot{\gamma}$ (i.e. $\dot{\gamma} \equiv G$). Equation 3.11 is derived from the second invariant of the shear-rate tensor (Eq. 3.6) [215].

Normally, the constitutive models used for the shear-thinning characteristic of blood are of the so-called *generalised Newtonian fluids*. The generalised Newtonian constitutive models satisfy the non-linear behaviour

$$\tau := \mu_{eff}(\dot{\gamma})\,\dot{\gamma}\ , \tag{3.12}$$

where the effective viscosity μ_{eff} depends on the local shear rate (Eq. 3.11). Some generalised Newtonian fluids easily applied to blood flow modelling include the viscoplastic behaviour, but others do not. The most popular generalised Newtonian fluids, readily applied to blood flow modelling, are the Bingham, Ostwald-de Waele (power-law), Herschel-Bulkley, Casson and Luo-Kuang models [214].

When blood yield stress is not considered, the viscosity would tend towards a finite value μ_0 as shear is decreased. Similarly, because blood is a shear-thinning fluid, an asymptotic viscosity μ_∞ is found as shear is increased. Although in practice those values are defined as

$$\mu_0 := \lim_{\dot{\gamma}\to 0} \mu(\dot{\gamma}) \quad \text{and} \quad \mu_\infty := \lim_{\dot{\gamma}\to \infty} \mu(\dot{\gamma}) \tag{3.13}$$

for the range limits of the rheological characterization, in theory Eq. 3.13 is not actually valid for neither $\dot{\gamma} = 0$ or $\dot{\gamma} = \infty$. At low shear, viscosity of whole blood is difficult to measure, and at high shear rates $\dot{\gamma} > 10^4$–10^5 s^{-1} the RBCs are lysed [73, p. 85]. Nonetheless, the constants μ_0 and μ_∞ are easy to determine as part of a non-linear regression of consecutive models of blood viscosity. In the Newtonian model (Eq. 3.10), the dynamic viscosity considered is equivalent to the asymptotic viscosity, $\mu \equiv \mu_\infty$.

A very common viscosity model used for shear-thinning fluids like blood is the power-law fluid model, or the Ostwald-de Waele model. In this case, the effective viscosity is defined as

$$\mu_{eff} := K\,\dot{\gamma}^{(n-1)} \ , \tag{3.14}$$

where n and K are termed the power-law index and consistency constant, respectively. The power-law index is $n < 1$ to reflect the shear thinning properties of blood. The power-law fluid model has the limitation of rising very steeply as shear rate approaches zero. Therefore, it can only be applied to a bounded shear rate range.

Other common constitutive models for blood viscosity have a finite value for both μ_0 and μ_∞. They are normally written in a non-dimensional bounded form as

$$\frac{\mu_{eff} - \mu_\infty}{\mu_0 - \mu_\infty} := f(\dot{\gamma}) \ , \tag{3.15}$$

where $f(\dot{\gamma})$ is any mathematical function which can fit the experimental data. Examples of bounded generalised Newtonian models are listed in Table 3.2. The material constants listed in Table 3.2 were obtained by non-linear regression of data points of

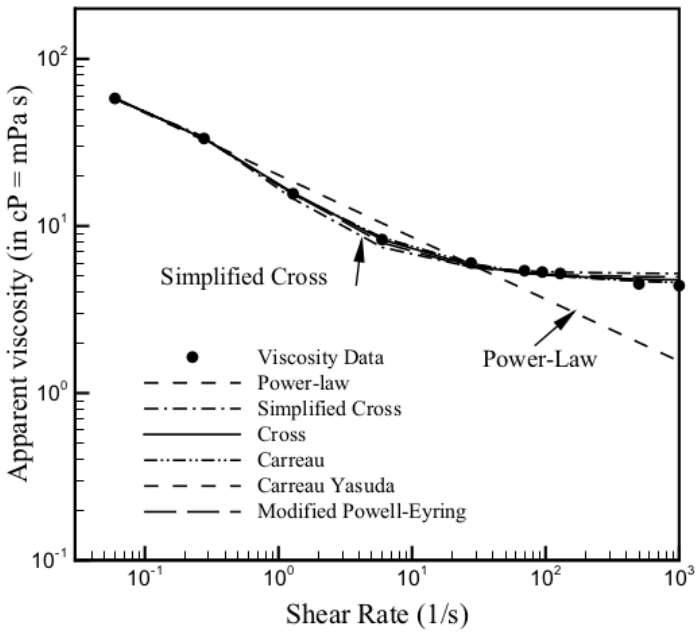

Fig. 3.7: Apparent blood viscosity as a function of shear rate (same data points as in Fig. 3.2). Also shown are curves for six generalised Newtonian constitutive models fit to this same data set. The definitions of viscosity functions and associated material constants are given in Tab 3.2. Image reproduced from Galdi *et al.* [73, p. 92].

Fig. 3.2. The fitted curves are shown in Fig. 3.7. All models except Ostwald-de Waele (power-law) and Powell-Eyring had excellent fits, with $R^2 > 0.998$.

Although, as previously mentioned, the existence of a yield stress in blood is controversial, many viscoplastic constitutive models have been used to simulate RBC aggregation. Yield stress models are useful in the low shear rate region, where viscosity appears to grow unbounded as the shear rate approaches zero. Notwithstanding this fact, when experiments are run at smaller values of shear rate, the viscosity plateaus to a finite value, because plasma still flows and some rouleaux rearrange themselves into 3-D structures. Hence, as any other constitutive parameter, the apparent yield stress is a mathematical curve-fitting constant used to fit an equation, which describes the flow curve of a material over a limited range of shear rates [21]. Analogously to the generalised shear rate derived in Eq. 3.11, the second invariant of the shear stress

Table 3.2: Representative generalised Newtonian models for blood viscosity with corresponding material constants. Constants were obtained using a non-linear regression analysis of experimental data shown in Fig. 3.2. Data adapted from Galdi *et al.* [73, p. 91].

Constitutive Model	Equation	Material constants
Ostwald-de Waele	$\mu_{eff} := K\,\dot{\gamma}^{(n-1)}$	$K = 20.2\,\mathrm{mPa\,s}$ $n = 0.628$
Powell-Eyring	$\frac{\mu_{eff}-\mu_\infty}{\mu_0-\mu_\infty} := \sinh^{-1}(\lambda\dot{\gamma})$	$\mu_0 = 60.2\,\mathrm{mPa\,s}$ $\mu_\infty = 4.9\,\mathrm{mPa\,s}$ $\lambda = 1206.5\,\mathrm{s}$
Modified Powell-Eyring	$\frac{\mu_{eff}-\mu_\infty}{\mu_0-\mu_\infty} := \frac{\ln(1+\lambda\,\dot{\gamma})}{(\lambda\,\dot{\gamma})^m}$	$\mu_0 = 57.46\,\mathrm{mPa\,s}$ $\mu_\infty = 4.93\,\mathrm{mPa\,s}$ $\lambda = 5.97\,\mathrm{s}$ $m = 1.16$
Cross Model	$\frac{\mu_{eff}-\mu_\infty}{\mu_0-\mu_\infty} := \frac{1}{1+(\lambda\,\dot{\gamma})^m}$	$\mu_0 = 87.5\,\mathrm{mPa\,s}$ $\mu_\infty = 4.70\,\mathrm{mPa\,s}$ $\lambda = 8.00\,\mathrm{s}$ $m = 0.801$
Simplified Cross	$\frac{\mu_{eff}-\mu_\infty}{\mu_0-\mu_\infty} := \frac{1}{1+\lambda\,\dot{\gamma}}$	$\mu_0 = 70.0\,\mathrm{mPa\,s}$ $\mu_\infty = 5.18\,\mathrm{mPa\,s}$ $\lambda = 4.84\,\mathrm{s}$
Carreau	$\frac{\mu_{eff}-\mu_\infty}{\mu_0-\mu_\infty} := \frac{1}{[1+(\lambda\,\dot{\gamma})^2]^{(1-n)/2}}$	$\mu_0 = 63.9\,\mathrm{mPa\,s}$ $\mu_\infty = 4.45\,\mathrm{mPa\,s}$ $\lambda = 10.3\,\mathrm{s}$ $n = 0.350$
Carreau-Yasuda	$\frac{\mu_{eff}-\mu_\infty}{\mu_0-\mu_\infty} := \frac{1}{[1+(\lambda\,\dot{\gamma})^a]^{(1-n)/a}}$	$\mu_0 = 65.7\,\mathrm{mPa\,s}$ $\mu_\infty = 4.47\,\mathrm{mPa\,s}$ $\lambda = 10.4\,\mathrm{s}$ $n = 0.34$ $a = 1.76$

tensor $\boldsymbol{\tau}$ can also be used as an 1-D measurement of stress,

$$\tau := \sqrt{\frac{1}{2}\,\boldsymbol{\tau} : \boldsymbol{\tau}} = \sqrt{\frac{1}{2}\,tr\boldsymbol{\tau}^2}\ . \tag{3.16}$$

A relatively simple and finite physically relevant yield criterion is to define a yield stress constant τ_0, below which the fluid does not flow (i.e., $\dot{\gamma}(\tau < \tau_0) = 0$).

A list of viscoplastic models is given in Table 3.3. The models in Table 3.3 and some of the generalised models previously listed in Table 3.2 are compared in Fig. 3.8 by fitting them with experimental data. The best agreement is achieved for the Luo-Kuang and generalised Herschel models. Models such as Ostwald-de Waele (powe-law) and Hereschel-Bulkley are not able to predict viscosity at high shear rates, whereas they fit perfectly for middle values of shear rates. Surprisingly enough, the Casson model, which is a very popular model for blood viscosity, does not fit the experimental data well, except for constant values (overestimated) at high shear rates.

Thixotropy is an important aspect normally ignored in the constitutive models of blood viscosity. The viscosity data points in both Figs. 3.2 and 3.6 represent the *equilibrium viscosity* after the viscometer was run at a fixed shear rate for either a few seconds at high shear rate or a few minutes at low shear rates. Those values of apparent viscosity are not reached if fluid shear rate changes fast in a Lagrangian point of view. Blood apparent viscosity is transient where the flow field is not developed. Hence, it is important to consider under what circumstances shear thinning will play a role, because it is much less significant in physiological conditions. The half-time of the formation of RBC aggregates in blood ranges from 3–5 s for normal blood, and 0.5–1.5 s for pathological blood samples [184, 185]. On the other hand, the half-life for both rouleau breakup and RBC flow alignment is only about 1–2 s [74]. The characteristic time of this transient phase is potentially sensitive to shear rate $\dot{\gamma}$, and the time derivative of shear rate $\frac{d\dot{\gamma}}{dt}$, because RBC aggregation and rouleaux breakup have different rates. Since it takes a few seconds for the 3-D structures of RBC aggregates (rouleau) to form or breakup, then, for normal blood, viscosity will only significantly

Table 3.3: Viscoplastic constitutive models.

Constitutive Model	Shear Stress	Effective Viscosity
Bingham	$\tau = \tau_0 + k\,\dot{\gamma}$	$\mu_{eff} = \frac{\tau_0}{\dot{\gamma}} + k$
Casson	$\sqrt{\tau} = \sqrt{\tau_0} + \sqrt{k\,\dot{\gamma}}$	$\mu_{eff} = \left(\sqrt{\frac{\tau_0}{\dot{\gamma}}} + \sqrt{k}\right)^2$
Generalised Casson	$\tau^{1/n} = \tau_0^{1/n} + (k\,\dot{\gamma})^{1/n}$	$\mu_{eff} = \left[\left(\frac{\tau_0}{\dot{\gamma}}\right)^{1/n} + k^{1/n}\right]^n$
Herschel-Bulkley	$\tau = \tau_0 + k\,\dot{\gamma}^n$	$\mu_{eff} = \frac{\tau_0}{\dot{\gamma}} + k\,\dot{\gamma}^{n-1}$
Generalised Herschel	$\tau = \tau_0 + k\,\dot{\gamma}^n + \mu_\infty\dot{\gamma}$	$\mu_{eff} = \frac{\tau_0}{\dot{\gamma}} + k\,\dot{\gamma}^{n-1} + \mu_\infty$
Luo-Kuang	$\tau = \tau_0 + k\,\sqrt{\dot{\gamma}} + \mu_\infty\dot{\gamma}$	$\mu_{eff} = \frac{\tau_0}{\dot{\gamma}} + \frac{k}{\sqrt{\dot{\gamma}}} + \mu_\infty$
Szulman	$\tau^{1/n} = \tau_0^{1/n} + (k\,\dot{\gamma})^{1/m}$	$\mu_{eff} = \left[\left(\frac{\tau_0}{\dot{\gamma}}\right)^{1/n} + k^{1/m}\dot{\gamma}^{(1/m-1/n)}\right]^n$

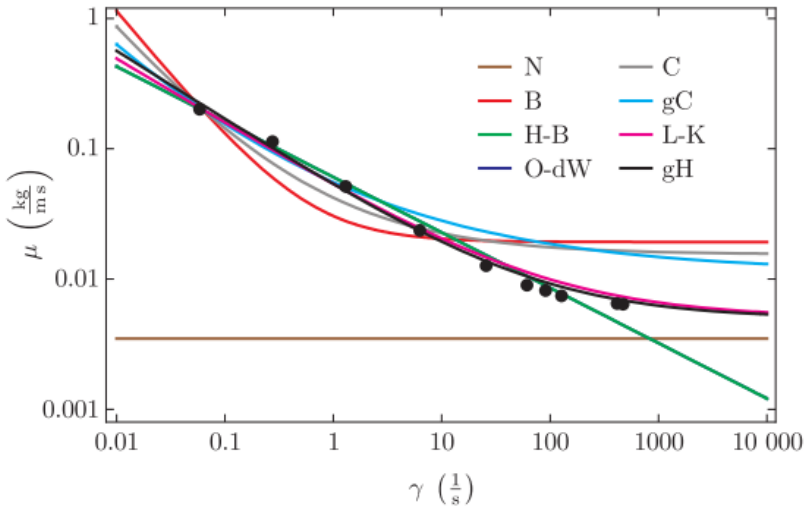

Fig. 3.8: Apparent blood viscosity as a function of shear rate. Fitted models: (N) Newtonian model, (B) Bingham, (H-B) Herschel-Bulkley, (O-dW) Ostwald-de Waele, (C) Casson, (gC) generalised Casson, (L-K) Luo Kuang, (gH) generalised Herschel. Image reproduced from Tesch (2012) [214].

rise in developed flow of low shear rates. This situation may occur in segments of stable recirculation regime, or at regions of nearly stagnant flow ($\dot{\gamma} < 1\,\mathrm{s}^{-1}$). Hence, strongly shear-thinning constitutive models should only be used in cases where blood becomes nearly stagnant for more than a few seconds. Otherwise, it is more appropriate to employ either the constant viscosity model or a weaker shear-thinning model, where only the RBC alignment to flow is considered. The shear-thinning characteristic of blood is also apparent in the developed flow profile recorded in a long tube. In this situation, the flow profile is not parabolic (Poiseuille flow), rather it becomes blunted in the centre. The flow in the centre region may be called a *partial plug flow*. The flexibility of the RBCs helps to diminish the viscosity of packed suspensions, so this partial plug flow is relatively smaller for RBCs than for hardened discs [79].

The rouleau structures can store elastic energy. Therefore, blood is viscoelastic at shear rates $\dot{\gamma} < 6\ \mathrm{s}^{-1}$ when rouleaux are present [186]. Rouleau structures can be stretched up to three-fold before rupturing under increasing shear rate. Under increasing shear, contact between some cells is eventually lost and the resulting segments then recoil. If the shear rate is decreased prior to reaching the rupture level, recoil of the whole structure is observed. The viscoelastic properties of blood are measured by generating oscillatory (or pulsatile) flows and step transient flows. Viscoelastic properties are often presented in terms of a complex viscosity, split into real and imaginary parts,

$$\mu = \mu' + i\,\mu'' \ . \tag{3.17}$$

The material constants μ' and μ'' are referred to as the viscosity and elasticity, respectively, and $i = \sqrt{-1}$ is the imaginary unit. Perfect viscous fluids have $\mu'' = 0$. The apparent viscosity changes depending on the shearing frequency f, (Fig. 3.9), because of the ability to store elastic energy. It can be seen that μ'' is relatively constant in the range associated with a normal human pulse (0.5 to 20 Hz). In Fig. 3.10, the steady flow viscosity is compared to the components of the complex viscosity, where $\dot{\gamma} = f\,\gamma$, and γ is the shear strain. Both components of the complex viscosity are

relatively constant ($\mu' = 11.5\,\mu\text{Pa}\,\text{s}$ and $\mu' = 3.9\,\mu\text{Pa}\,\text{s}$) for shear rates $\dot{\gamma} < 1.5\,\text{s}^{-1}$. Viscoelasticity becomes non-linear for $\dot{\gamma} > 1.5\,\text{s}^{-1}$, where the elastic component μ'' rapidly drops as shear rate is increased, and the viscous component μ' margins with the steady flow viscosity μ_s. This sharp decrease is attributed to the breakdown of the blood microstructure, formed by RBC aggregates.

Since viscoelasticity is observed only at low shear states, it would be a significant factor only at situations where the viscous thinning effect are also present (e.g. stable recirculation or stagnation zones), because there RBCs had enough time to form stable rouleaux structures. Viscoelasticity can be significant for pathological blood whose potential to aggregate is greatly strengthened. In these cases, blood viscoelasticity may be significant in extensive regions of circulation and could be an important factor in arterial flow for patients with these conditions. A significant challenge in developing non-linear viscoelastic constitutive models for blood, is selecting the simplest model that captures the frequency and shear rate dependence found in physiologically relevant flows. Whereas the linear material constants at $\dot{\gamma} < 1.5\,\text{s}^{-1}$ are indicative of aspects of the microstructure, non-linear viscoelastic models are required if the finite viscoelastic behaviour of blood at $\dot{\gamma} > 1.5\,\text{s}^{-1}$ is to be modelled. In order to capture this non-linearity, the extended Maxwell model and Oldroyd-B type models, which are thermodynamically consistent, have been proposed [9].

The rheology of blood is complex. It manifests non-linear viscoelasticity at low shear stresses due to aggregation of RBCs. As shear rises and aggregates break up, blood loses its elasticity and viscosity decreases. A variety of circulatory-related diseases are associated with pathological changes in the mechanical properties of blood such as blood and plasma hyperviscosity, diminished RBC deformability, and increased RBC aggregation. Myocardial infarction, sickle cell anaemia, and hypoxic pulmonary vasoconstriction are a few examples of diseases which can be diagnosed by changes in haemorheology [73, p. 108]. Many constitutive models have been proposed to repre-

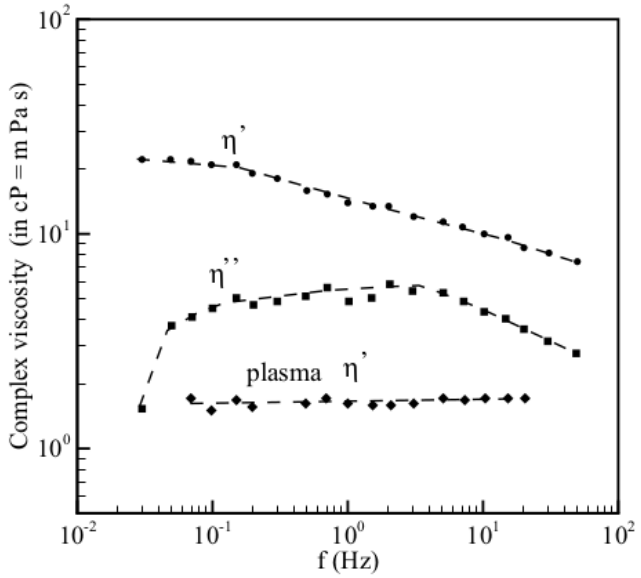

Fig. 3.9: Dependence of the viscous μ' and elastic μ'' components of the complex viscosity on the frequency of oscillation compared with the viscous component of complex viscosity for plasma. Image reproduced from Galdi *et al.* [73, p. 104].

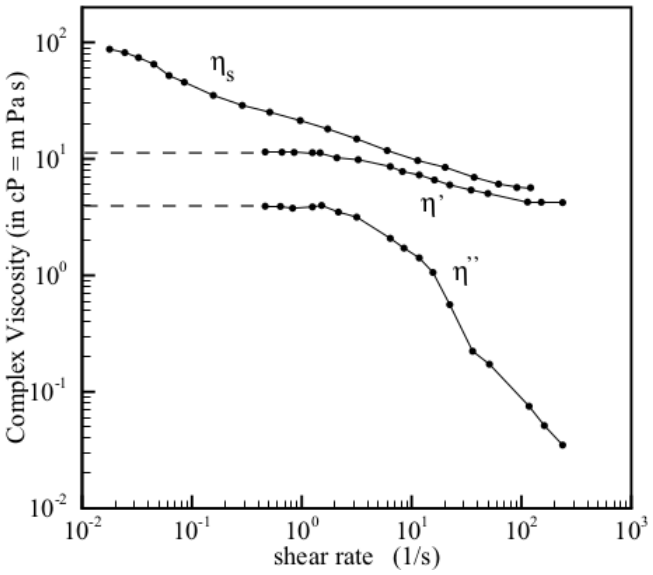

Fig. 3.10: Dependence of the steady flow viscosity μ_s on shear rate and the dependence of the viscous μ' and elastic μ'' components of the complex viscosity on the RMS value of wall shear rate (capillary rheometer). Human blood from healthy donors for $Ht = 43\%$ and $T = 22\,^{\circ}\mathrm{C}$. Oscillatory data measured at a frequency of 2 Hz. Image reproduced from Galdi *et al.* [73, p. 105].

sent the rheological response of blood. As shown in Figs. 3.7 and 3.8, most non-linear models are able to represent well the shear-thinning characteristics of blood, regardless whether they have or not a yield-stress value. The attribute that seems to make a constitutive equation to fit better the experimental points is the number of constitutive parameters it has. Therefore, the choice of the constitutive equation depends more on the balance of its mathematical simplicity regarding to the complexity of the flow field. Normally in arterial flows, the mean shear rate is high and the flow is not developed. Therefore, the RBCs cannot align or aggregate, thus viscosity is nearly Newtonian ($\mu_{eff} \rightarrow \mu_{\infty}$). On the other hand, in slow venous flows, at stable points of recirculation, and at small vessels, more complex characteristics of haemorheology (such as shear-thinning, viscoelasticity and thixotropy) can become important.

3.1.4 Spatial Distribution of RBCs in the Blood Vessels

Normally, the distribution of RBCs across the radius of blood vessels is far from uniform due to geometric, gravitational and fluid dynamic effects. This inhomogeneity can lead to some important physiological phenomena and unusual features such as the RBC packing, plasma skimming and the Fåhraeus-Lindqvist effect. Avoiding inhomogeneities in spatial distribution of RBC in rheometers is one of the biggest challenges in obtaining accurate measurements of the mechanical properties of blood.

Sedimentation is more significant in stored blood than in flowing blood because moving RBCs promote mixing of proteins and cells. With RBC and plasma density of $\rho_{RBC} = 1093$ kg/m^3 and $\rho_f = 1027$ kg/m^3 [235], respectively, the resulting sedimentation rate for individual RBCs is of the order of a few mm/h. However, in stored blood, with a haematocrit of the order of 40%, sedimentation is augmented by RBC aggregation.

The RBC concentration near the wall is always lower than that of the centre of the vessel. This effect is called the *excluded volume effect* or the *Vand effect*, and it

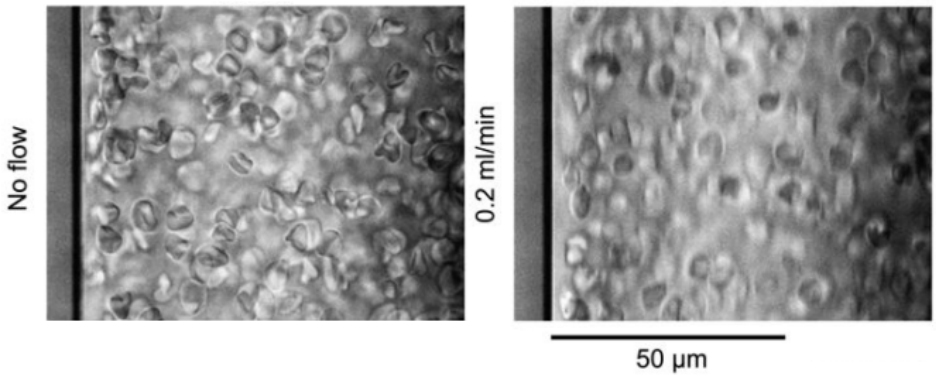

Fig. 3.11: RBC suspension in a 100 µm wide rectangular straight channel. Blood flowing at 0.2 mL min^{-1} from top to bottom has $Re \approx 20$, and has the RBC-free layer of (5.5 ± 1.0) µm. Image reproduced from Marhefka *et al.* (2009) [151].

arises because the centre of the RCBs must stay at least a RBC radial length away from the vessel wall. The lower concentration of RBCs causes a lower viscosity near the wall. The Vand effect becomes more prominent when rouleaux are present, because the centre of the rouleaux must stay nearly half of its length away from the vessel wall [73, p. 76]. Whereas the Vand effect is a geometrical factor, the RBC exclusion near the wall is further enhanced when blood is flowing (see Fig. 3.11). This effect is named *Segré–Silberberg* effect, and it arises because RBCs near the wall experience flow-derived lift due to the radial gradient of velocity [191, 192]. Rigid neutrally buoyant spherical particles slowly migrate away from the wall, until they reach an equilibrium position experimentally shown to be 60% of the tube radius. This equilibrium radial position was found to be independent of particle radius, fluid density and fluid viscosity. However, fresh RBCs are able to shift radially considerably more than hardened cells, because of RBC deformability and aggregability.

An interesting result of both the Vand and the Segré–Silberberg effects is the *plasma skimming effect*, where blood flowing from a larger vessel into smaller lateral vessels is drawn preferentially from the region of lower haematocrit. Thus, the haematocrit in lateral vessels is usually lower than in the parent vessel. Plasma skimming is

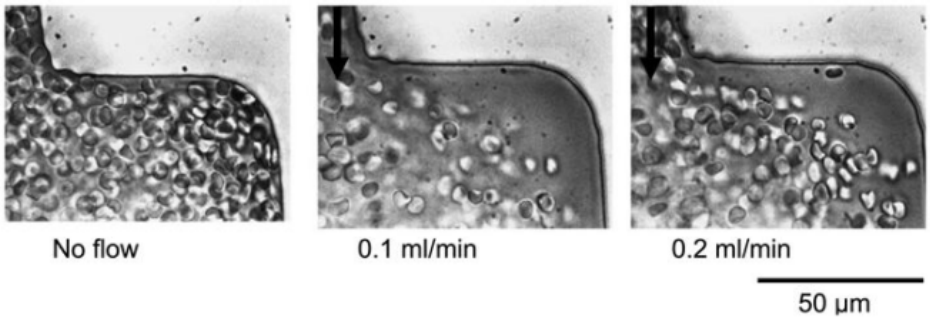

Fig. 3.12: Blood flowing from a 50 to 200 µm expansion exhibits RBC-depleted pockets. Flow direction is from top to bottom. Image reproduced from Marhefka *et al.* (2009) [151].

strong at the corners of sudden expansions of vessel diameter where strong separation of RBCs is observed (see Fig. 3.12) [121, 120]. This effect is important in terms of engineering medical devices where tube connectors and blood reservoirs are present. It can also occur in acutely narrowed stenosed arteries, where it is believed to promote thrombosis.

The haematocrit gets naturally diminished, when the vessel diameter decreases below 0.3 mm. This is known as the *Fåhræus effect* [82]. It is attributed to the pronounced axial migration of RBCs in smaller vessels [66, 67]. As the RBCs migrate toward the centre of the capillary tube, their average velocity becomes higher than the plasma average velocity, because plasma becomes more concentrated near the wall (as depicted in Fig. 3.13). Consequently, the concentration of RBCs inside the capillary tube decreases in order to maintain the same mass flux (of RBCs plus plasma) entering and leaving the tube. That is,

$$j_{RBC}^{in} = j_{RBC}^{out} \quad \Leftrightarrow \quad Ht^{in}\, v_{RBC}^{in} = Ht^{out}\, v_{RBC}^{out}\ , \tag{3.18}$$

where j_{RBC} is the flux of RBCs, Ht is the haematocrit, and v_{RBC} is the RBC average velocity. Since $v_{RBC}^{out} > v_{RBC}^{in}$, because RBCs concentrate at the centre of the tube at the exit, then $Ht^{out} < Ht^{in}$. This is a separate effect from any change in the tube haematocrit due to entrance effects, such as the plasma skimming effect.

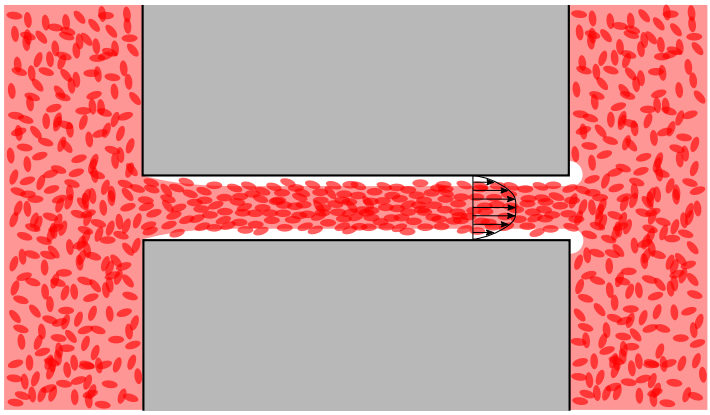

Fig. 3.13: In capillary tubes, the erythrocytes are more concentrated towards the centre of the vessel, leaving a significant RBC-free layer near the vessel walls. The Fåhræus effect occurs because the average RBC velocity is higher than the average plasma velocity.

The decrease in haematocrit inside capillary tubes results in a decrease of apparent viscosity, known as the *Fåhræus-Lindqvist effect* [82]. Fåhræus and Lindqvist measured the relationship between flow rate and pressure drop in long viscometer tubes whose diameter ranged from 0.04–0.5 mm [67]. In that experiment, the effect of the RBC microstructure would be negligible because the average shear rates were large. For tubes of diameters less than 0.3 mm, the relative viscosity appeared to strongly decrease with decreasing diameter. In this case, the RBCs cannot be considered homogeneously distributed in the cross-section. Instead, a significant RBC-free layer is formed near the wall. The Fåhræus-Lindqvist effect is very important to maintain lower viscosity in the arterioles and capillaries, where the circulatory pressure drop is highest.

Mathematical Models to Compute RBC Distribution

There are two methods used to numerically simulate the transport of cells in blood: *discrete models* and *fluid-continuum models* [105, 157].

Discrete models explicitly represent the microstructure of the blood. They either compute the dynamics of all individual cells or the dynamics of representative particles

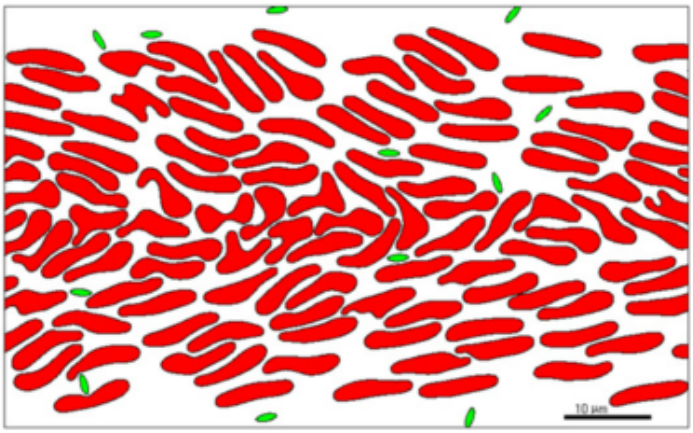

Fig. 3.14: Lattice-Boltzmann simulation of 2-D whole blood (haematocrit $Ht = 0.4$) flow in a microvessel. After 600 ms of flow, RBCs concentrate in the centre of the vessel, and platelets become distributed preferentially near the wall. Image reproduced from Skorczewski *et al.* (2013) [199].

on a mesocopic scale. Therefore, cells are either treated as deformable capsules or node particles, depending on the scale of the domain with respect to the size of the cells [64, 199, 237]. The lattice-Boltzmann method has become a popular method to represent the microstructure of blood. An example of a 2-D lattice-Boltzmann simulation of deformable RBCs and rigid platelets is shown in Fig. 3.14. In this approach, it is possible to simulate blood flow of deformable cells in capillaries and arterioles in which tractions are imposed on the cells by both the surrounding fluid and collisions and adhesions between other cells. This is a promising approach to predict rheological phenomena that are difficult to be observed experimentally. Notwithstanding this fact, these models, applied on the micro-scale, tend to be computationally intensive and hence are prohibitively expensive in large flow domains.

Fluid-continuum models assume that cells are sufficiently smaller than the spatial discretization used to numerically integrate the flow field. Fluid-continuum methods overcome the limitation of high computational cost associated with discrete models but still provide useful information [116, 115, 105]. Instead of computing separate

events, such as individual cell collisions, fluid-continuum methods compute the average "deterministic" spatio-temporal behaviour of blood [157]. Haemorheology is replicated by considering blood as two or more fluids (or components) that are mixed. The treatment of the cellular phase as a continuum was demonstrated to be valid for WBCs and platelets, even though they are considerably more diluted than RBCs [105]. The momentum equation can be processed by considering either the average properties of whole blood [64, 142, 196, 203, 204] or the properties of each component fraction [116, 115, 154, 234, 235]. The former approach is the most traditional, but the latter (applying the continuum mixture theory) has been recently used to homogenize the flow of plasma and haematocrit in order to simulate features such as the spatial distribution of RBCs.

In the case of a two-fluid system containing RBCs and plasma, the mixture theory separates the mass conservation equation (Eq. 3.2) as two mixing phases,

$$\frac{\partial \rho_f}{\partial t} + \nabla \cdot (\rho_f \boldsymbol{v}_f) = 0 \tag{3.19}$$

and

$$\frac{\partial \rho_{RBC}}{\partial t} + \nabla \cdot (\rho_{RBC} \boldsymbol{v}_{RBC}) = 0 \ , \tag{3.20}$$

where the subscript f refers to the fluid (plasma). The densities of the two components are coupled by the haematocrit Ht (volume fraction of RBCs). Therefore,

$$\rho_f = (1 - Ht)\, \rho_{f0} \tag{3.21}$$

and

$$\rho_f = Ht\, \rho_{RBC0} \ , \tag{3.22}$$

where ρ_{f0} and ρ_{RBC0} are the pure densities of plasma and RBC, respectively. The balance of the linear momentum (Eq. 3.9) can be written as

$$\rho_f \frac{\partial \boldsymbol{v}_f}{\partial t} = \nabla \cdot \boldsymbol{\sigma}_f - \rho_f (\boldsymbol{v}_f \cdot \nabla) \boldsymbol{v}_f + \rho_f \boldsymbol{b}_f + \boldsymbol{f} \tag{3.23}$$

and

$$\rho_{RBC}\frac{\partial \boldsymbol{v}_{RBC}}{\partial t} = \nabla \cdot \boldsymbol{\sigma}_{RBC} - \rho_f(\boldsymbol{v}_{RBC} \cdot \nabla)\boldsymbol{v}_{RBC} + \rho_f \boldsymbol{b}_{RBC} - \boldsymbol{f} \ , \tag{3.24}$$

where $\boldsymbol{\sigma}_f$ and $\boldsymbol{\sigma}_{RBC}$ are the Cauchy stress tensors for plasma and RBCs, respectively, $\boldsymbol{b}_f$ and $\boldsymbol{b}_{RBC}$ stand for body forces, and $\boldsymbol{f}$ refers to interaction forces. The interaction forces exchange of momentum between the components of the mixture. The total mixture stress tensor is idealised as

$$\boldsymbol{\sigma} = (1 - Ht)\,\boldsymbol{\sigma}_f + Ht\,\boldsymbol{\sigma}_{RBC} \ . \tag{3.25}$$

Equation 3.25 is valid in a limited range of *Ht*. At a certain *Ht*, called the maximum packing fraction, the RBCs are in such a close proximity to each other that unless they are crushed or deformed, *Ht* can no longer change. Therefore, in the numerical solution, the haematocrit has to be bounded at $0 \leq Ht < Ht_{max}$. To close these equations, constitutive relations are needed for the individual stress tensors and for the interaction force.

Wu *et al.* (2015) [235] assumed the plasma and the RBC phases to behave as a Newtonian fluid and a viscoelastic shear-thinning fluid, respectively. Hence,

$$\boldsymbol{\sigma}_f = [-p(1 - Ht) + \lambda_f\, tr\boldsymbol{E}_f]\boldsymbol{I} + 2\mu_f(1 - Ht)\boldsymbol{E}_f \ , \tag{3.26}$$

where p is the pressure of the mixture, and λ_f and μ_f are the bulk and shear viscosity constants of plasma; and

$$\boldsymbol{\sigma}_{RBC} = [-p\,Ht + \beta_{20}(Ht + Ht^2)\, tr\boldsymbol{E}_{RBC}]\boldsymbol{I} + \mu_{RBC}Ht\,\boldsymbol{E}_f \ , \tag{3.27}$$

where β_{20} is a constant, and λ_{RBC} and μ_{RBC} are the bulk and shear viscosity constants of the RBC phase. The shear viscosity constitutive equation used by Wu *et al.* was taken from Yeleswarapu *et al.* (1998) [238],

$$\mu_{RBC}(Ht, G_{RBC}) = \frac{1}{Ht}\left[\mu_\infty(Ht) + (\mu_0(Ht) - \mu_\infty(Ht))\,\frac{1 + ln\,(1 + k(Ht)\,G_{RBC})}{1 + k(Ht)\,G_{RBC}}\right] \ , \tag{3.28}$$

where G_{RBC} is the generalised shear rate (Eq. 3.11) for the RBC phase, and $\mu_0(Ht)$, $\mu_\infty(Ht)$ and $k(Ht)$ are a polynomial function which depends on the haematocrit Ht. These functions are fitted from experimental data. Finally, both the Stokes drag force and the Saffman's shear-lift force were considered in the term of the interaction forces between mixture phases,

$$\boldsymbol{f} = \left(\frac{9\mu_f}{8R_{RBC}^2} f(Ht) + \frac{3(6.46)\sqrt{\rho_f \mu_f}}{4\pi\, a} Ht \frac{\boldsymbol{E}_f}{\sqrt{G_f}} \right) (\boldsymbol{v}_{RBC} - \boldsymbol{v}_f) \,, \tag{3.29}$$

where R_{RBC} is the RBC mean radius, and $f(Ht) = exp(2.68Ht) + Ht^{0.43}$ is the drag model.

Wu *et al.* validated the mixture continuum model by comparing CFD simulations of the model with experiments conducted in microchannels and microtubes [235]. An example of those validations tests is seen in Fig. 3.15. There, a homogeneous 45% haematocrit suspension containing fluorescently labelled platelet-sized beads enters a microchannel comprised of a number of crevices of various shapes and sizes. Both in the experiment and simulation, it is possible to see the separation of RBCs from the plasma phase, which gets stronger once the RBC-free layer is formed. The Fåhræus effect is clearly visible in the simulation, because haematocrit is decreased along the microchannel length, as the RBC-free layer is formed. The RBC phase borders as well as the zones of recirculation of the simulation have great agreement with the experiment. The platelet-sized beads are better observed inside the crevices for two reasons. First, the flow velocity is slower inside the crevices, which is more appropriate for the camera to capture the minimal fluorescent light emitted by the beads. Second, the majority of the platelet-sized beads are displaced by the RBCs concentrated in the centre of the channel. Therefore, most of the beads are found in the RBC-free layer, which in the separation regions forms the lines highlighted in Fig. 3.15. Occasionally a portion of RBCs and fluorescent particles deviate from the main stream and migrate into the depths of the crevices, and become trapped. The highly bright regions correspond to

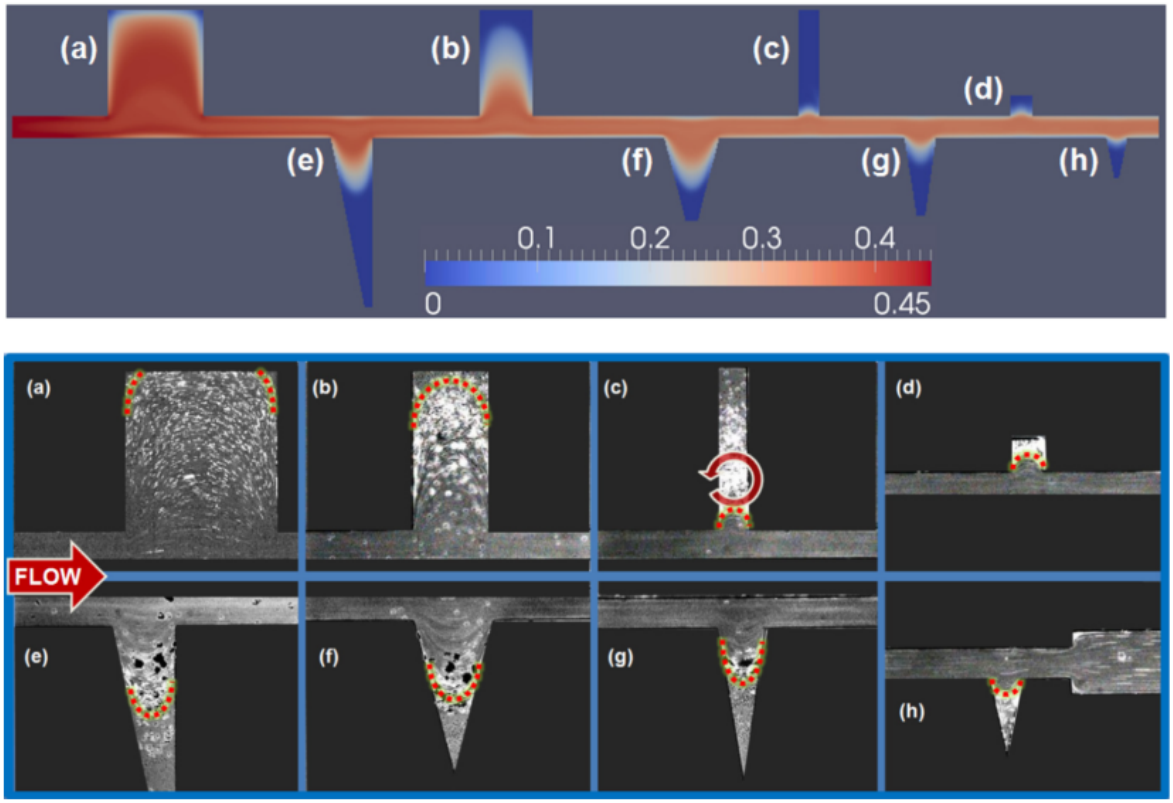

Fig. 3.15: Volume fraction of the RBCs obtained from simulation (top) compared with experimental observations of RBC ghosts seeded with 3 µm fluorescent particles (bottom). Both simulation and experiment correspond to inlet haematocrit of 40%. The scale bar represents haematocrit. The highly bright regions correspond to concentrated accumulation of fluorescent particles. Image reproduced from Wu *et al.* (2015) [235].

concentrated accumulation of fluorescent particles.

3.1.5 Platelet and WBC margination

Haemorheology is considered to be important for blood damaging phenomena, such as thrombosis and atherogenesis. The thrombus initiation and growth on the walls of vessels or medical devices is strongly influenced by the number density of platelets near the walls. The radial distribution of flowing RBCs strongly influences the distribution of platelets due to particle collision [5]. Erythrocytes concentrated at

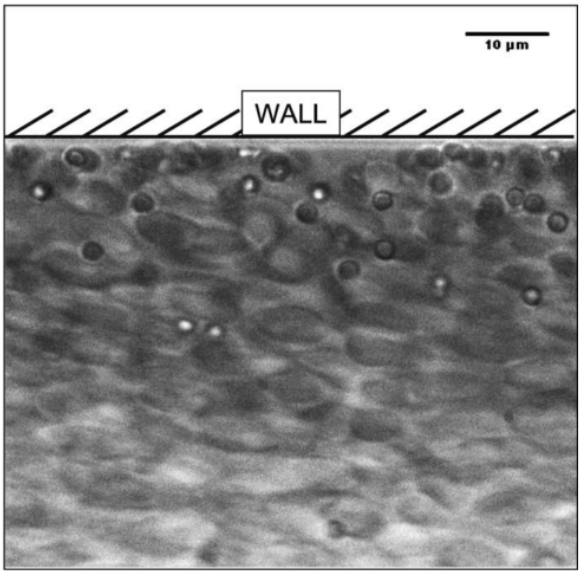

Fig. 3.16: Bright field image showing near-wall excess of platelet-sized beads, and red blood cell deformation. Image reproduced from Zhao *et al.* (2007) [243].

the centre of the vessel exclude the platelets from the core, either through collision or volume displacement. Platelets end up being more concentrated in the RBC-free layer where the collision with RBCs push them further against the vessel walls, as shown in Fig. 3.16. This phenomenon lets a higher concentration of platelets to screen for sites of injuries on the vessel walls. Consequently, thrombi are more likely to form in areas of flow separation such as seen in Fig. 3.12. This occurs not only because of flow stasis and prolonged deposition to the artificial surface, but also because of decreased viscosity in the region of RBC separation [113, 121, 120]. Identifying the regions of RBC separation is thus a major concern in the medical device industry, because thrombus formation either *in vivo* or in blood wetted medical devices may cause serious health problems or device malfunction.

Near-wall excess of fluorescent labelled platelets was first visualised *in vivo* by Tangelder *et al.* (1982) [211]. The radial distribution of platelets and platelet-sized latex beads flowing in ghost RBC suspensions was measured by Aarts *et al.* (1988)

[57] and Eckstein *et al.* (1988), respectively. Ghost RBCs provide an excellent physical model for RBC rheology, with the advantage of being much more transparent than normal RBCs because they lack haemoglobin [77]. Experimental results showed that the near-wall concentration of platelet-sized particles can be more than three times the concentration in the central region of the flow, as shown in Fig. 3.17. The near-wall excess is associated with a shear stress that is sufficiently high to deform the RBCs in the near-wall region [57]. Platelet margination is dependent on haematocrit because different haematocrit levels cause different radial concentration distribution of RBCs. The magnitude of near-wall excess is more sensitive to wall shear rate in narrower channels than in broader channels ($> 100\,\mu m$). The platelet concentration, however, did not change the relative distribution of platelets, as demonstrated in Fig. 3.18, because the radial concentration distribution changes monotonically as a function to the average concentration. In the absence of RBCs, either active or fixed platelets are distributed according to the Segré–Silberberg effect, as shown in Fig. 3.19.

In later studies, Eckstein *et al.* (1989) [56] observed that the concentration profile has a peak that is slightly off the wall ($\sim$ 3–6 µm). In order to investigate which model of near-wall excess of particles is correct, Zhao *et al.* (1989) [243] measured the concentration profile of platelet-sized beads flowing with RBC suspension in a microchannel. Zhao *et al.* applied an image processing method to automatically detect the radial position of the microparticles in various video frames. Next, the average concentration profile was obtained after placing the positions of all particles into bins. When the binning had a lower spatial resolution, the profile agreed with Aart's model. Yet, when the binning had a higher spatial resolution, the profile agreed with Eckstein's model, as illustrated in Fig. 3.20. The fine partitioning (of $1\,\mu m$ bin length) revealed a small depletion in the layer nearest the wall (within approximately $1\,\mu m$) which demonstrated a unimodal distribution with a peak approximately $2\,\mu m$ from the wall. The main disadvantage of using a higher resolution is the higher measurement noise,

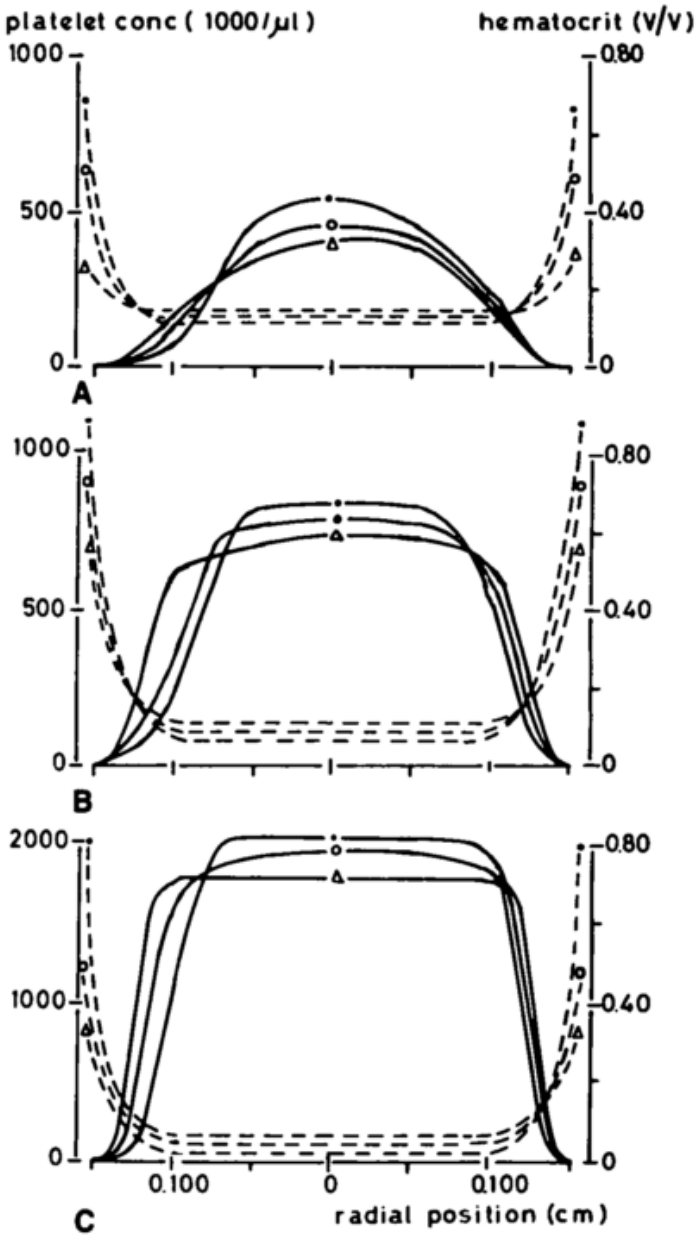

Fig. 3.17: Radial concentration distribution of platelets (--) and ghost RBCs (—) at haematocrits of 20% (A), 20% (B), and 60% (C). Wall shear rates of $240\,\mathrm{s}^{-1}$ ($\triangle$), $760\,\mathrm{s}^{-1}$ ($\circ$) and $1200\,\mathrm{s}^{-1}$ ($\bullet$). Erythrocytes concentrate in the centre and platelets near the wall. Image reproduced from Aarts *et al.* (1988) [3].

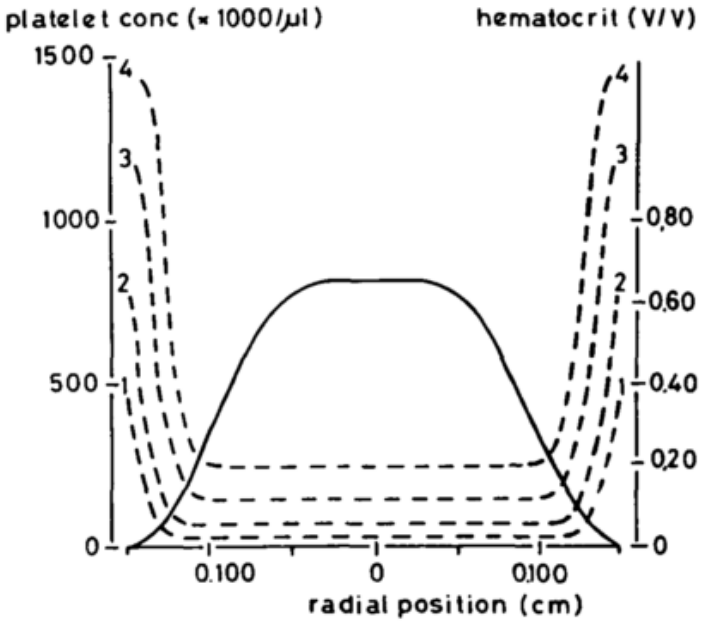

Fig. 3.18: Radial concentration distribution of platelets (--) and ghost RBCs (—) at haematocrits of 40% and wall shear rate of $1260\,\mathrm{s}^{-1}$. Platelet concentrations of $50\,000\,\mu\mathrm{L}^{-1}$ (1), $120\,000\,\mu\mathrm{L}^{-1}$ (2), $250\,000\,\mu\mathrm{L}^{-1}$ (3), and $500\,000\,\mu\mathrm{L}^{-1}$ (4). Image reproduced from Aarts *et al.* (1988) [3].

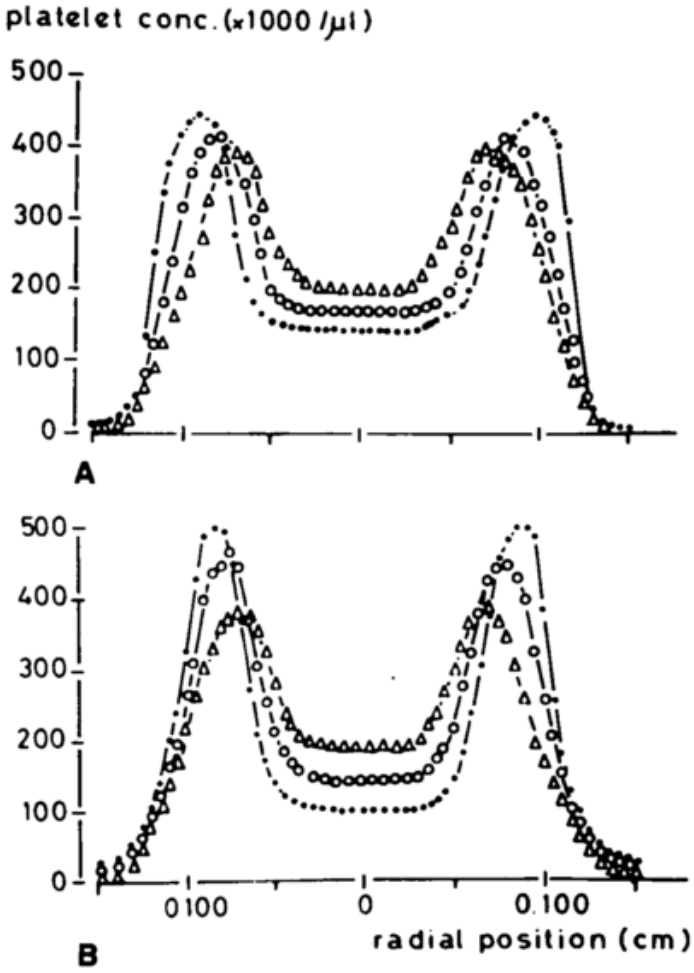

Fig. 3.19: Radial concentration distribution of flowing fresh (A) and fixed (B) platelets in the absence of RBCs. Wall shear rates of $240\,\mathrm{s}^{-1}$ ($\triangle$), $760\,\mathrm{s}^{-1}$ ($\circ$) and $1200\,\mathrm{s}^{-1}$ ($\bullet$). Measurements were made in steps of $50\,\mu\mathrm{m}$. Image reproduced from Aarts *et al.* (1988) [3].

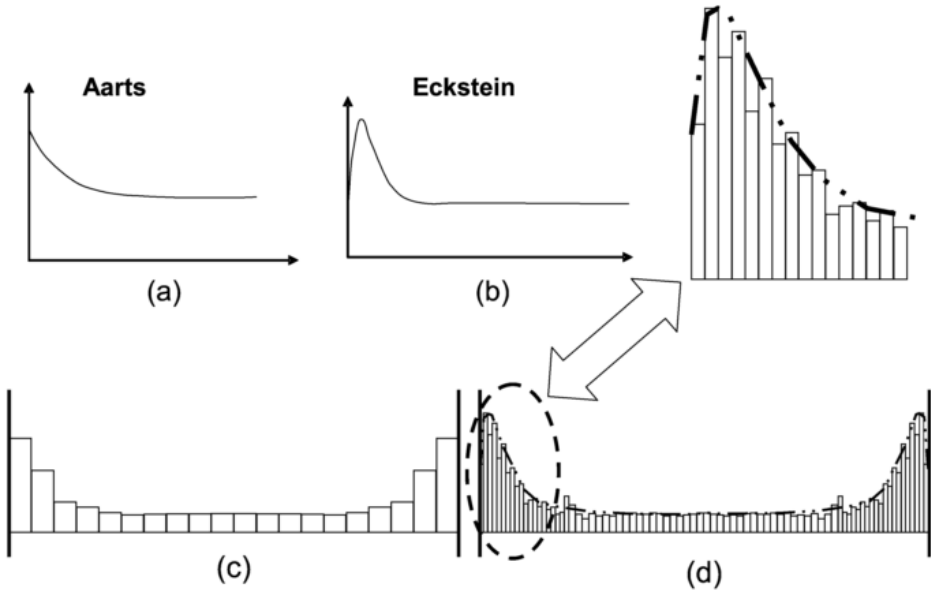

Fig. 3.20: Concentration profile of platelet-sized beads in microchannel. (a) Aart's model [3] and (b) Eckstein's model [56]. Both (a) and (b) are from curve fitting of the same data which was processed using (c) a coarse and (d) a fine sample binning, respectively. according to different binning grade. Image reproduced from Zhao *et al.* (2007) [243].

compared to lower binning resolution. Despite the resolution, the radial increase of particle concentration from the centreline towards the wall is always detected. Finally, the role of shear stress pointed out by Eckstein *et al.* (1988) [57] was corroborated by Zhao *et al.*, where the viscosity of the RBC suspension was altered with Dextran, but flow and shear rates remained unaltered. Higher viscosity resulted in higher platelet margination, although the haematocrit was the same. This demonstrated that the deformation of RBCs, which was increased by higher viscosity, is directly related to platelet margination.

Like platelets, leukocytes (WBCs) marginate to the RBC-free layer in small vessels, although, unlike platelets, WBCs are larger than RBCs (see Table 3.1) [85, 81, 99, 166]. This evidences the importance of both RBC deformability and aggregability in the radial distribution of RBCs, because both the Vand and the Segré–Silberberg effects

influence platelets and WBCs as much as RBCs. Goldsmith demonstrated that in capillary tubes (100–340 µm in diameter) an "inverse" Fåhræus effect occurs, since the mean velocity of blood is higher than the mean velocity of the marginating WBCs and platelets [85].

Mathematical Models to Compute WBC and Platelet Distributions

Eckstein and Belgacem (1991) [55] introduced a diffusion potential that resulted in a drift term in the transport equation (Eq. 3.1). They assumed that the perpendicular motion of platelets in flowing blood can be described by a drift function, with a shape that is determined from fully developed, steady-state concentration profile for platelets (either model seen in Fig. 3.20). They used the potential derived from the empirical steady-state developed profile in microchannel for any flow situation, because they could not find any direct way to mathematically derive the potential. Therefore, the potential was invariant over the length of the channel, regardless of its shape or geometrical changes. The deterministic portion describes those flow-associated events that act to redistribute the platelets to particular locations. Finally, the drift term is related to the rheological events that increase the effective diffusion of particles and molecules due to the motion of RBCs. This augmented diffusion effect is later discussed in Section 3.1.6. The augmented diffusion is used to describe rheological events that redistribute cells and solutes in the blood due to the motion of RBCs. Thus, it is highest near the wall. The drift diffusion potential $\Psi(\boldsymbol{r})$ is introduced as follows in the diffusion flux

$$\boldsymbol{j}_i = -\frac{\partial \Psi(\boldsymbol{r})}{\partial \hat{\boldsymbol{r}}}\, C - D\, \boldsymbol{\nabla} C \ , \tag{3.30}$$

where C is the concentration of platelets or WBCs, D is their Brownian diffusivity, and $\boldsymbol{r} = r\,\hat{\boldsymbol{r}}$ is the radial position perpendicular to the flow. Equation 3.30 is readily solved for the special case where both the velocity and concentration profiles are fully developed (hence, $\boldsymbol{j} = 0$), because then Eq. 3.30 becomes an ordinary differential

equation (ODE). The integration of this ODE yields the drift potential Ψ in

$$\ln(C)\,\hat{\boldsymbol{r}} = -(\Psi/D + k)\,\hat{\boldsymbol{r}}\ , \tag{3.31}$$

where k is a constant of integration, which is lost in the differentiation to Eq. 3.30. The drift term follows from the curve in Fig. 3.20 as

$$\Psi(\boldsymbol{x}) = -\frac{D}{C}\frac{\partial C}{\partial r}\ , \tag{3.32}$$

where $\frac{\partial C}{\partial \boldsymbol{r}}$ is the radial derivative of the curve in Fig. 3.20. Given an uniformly mixed blood in the inlet of a tube, the drift potential in the diffusion flux eventually leads to the empirical radial distribution of platelets and WBCs. However, the drift potential model requires *a priori* knowledge of the final profile and is valid only in tube flow [105].

Hund and Antaki (2009) [105] developed a new potential model that interacts with the concentration profile of RBCs. The RBC profile has to be prescribed either by experiments or by a multi-phase mixture simulation, as previously described in Sec. 3.1.4. Hund defines a general field potential $\Psi'(C, Ht)$ which incorporates the various factors that cause migration of platelets or WBCs, whose concentration is C. The diffusion flux with this field potential reads as

$$\boldsymbol{j} = -D\,\boldsymbol{\nabla}\Psi'(C, Ht)\ . \tag{3.33}$$

There are two physical conditions that Ψ' must obey. First, the flux must reduce to Brownian diffusion when the haematocrit is zero (i.e., $\lim_{Ht\to 0}\Psi' = C$). Second, all fluxes in the platelet equation must vanish in the absence of platelets (i.e., $\lim_{C\to 0}\Psi' = 0$). The most general form that satisfies these two constraints is the polynomial function

$$\Psi'(C, Ht) = \left(1 + \sum_{j=1}^{N}\psi_i Ht^i\right)\ C\ , \tag{3.34}$$

where ψ_i are empirical coefficients and N is the order of the polynomial function. Equation 3.34 implies an inverse relationship between the concentration C and the

haematocrit *Ht*. Therefore, a regional increase in RBC concentration causes a reduction (exclusion) of platelets or WBCs. It is assumed that the platelets and WBCs are too dilute to affect the concentration of RBCs.

Hund and Antaki were able to validate the field potential model for enhanced diffusivity. They demonstrated that this model outperformed previous models intended to predict the concentration profile of platelets and WBCs, which is greater near the wall. They obtained a good regression with an empirical platelet profile with $N = 1$ and $\psi_1 = 11.4$, for a blunt haematocrit profile. For the WBC concentration profile, the regression yielded a good fit with $N = 1$ and $\psi_1 = 1.0$. The authors stressed that ψ_i should, however, not be constant, but it should depend on shear rate, time and RBC aggregation. The augmented diffusion as a function of shear rate, which is observed in flowing blood, is discussed in Sec. 3.1.6. In contrast to Eckstein's model, which requires *a priori* knowledge of the platelet (or WBC) concentration profile, Hund's model is more applicable to more general flows, if the RBC profile is either measured or simulated. Bark and Ku (2013) [20] applied Hund's model for platelet margination to simulate thrombus formation over a collagen-coated stenosis.

3.1.6 Augmented Diffusion in Moving Blood

Red blood cells have been shown to have a shear-dependent, "diffusion-augmenting" effect on the transport of platelets, WBCs and solutes. The rotation and collision of particles cause the increase of the lateral transport of these substances. The augmented diffusion is generally several orders of magnitude (100–1000×) greater than Brownian motions, and it is highest at the wall [81, 224]. Goldsmith (1971) [78] tracked the motions of platelet-sized latex beads in low shear-rate blood flows. He computed the formula for augmented diffusion with measurements of the change of lateral position over a fixed time interval. Turitto *et al.* (1972) [218] measured the effective lateral diffusion coefficient for platelets in low shear-rate blood flow through a 200 µm tube.

In a review article, Goldsmith and Turitto stated that their measurements of the augmented diffusivity were in fair agreement [86]. Both authors were only able to measure platelet diffusivity in low shear-rate flows, because in higher shear rates non-uniform distributions of platelets occurred [218]. Platelet diffusivity in blood was shown to be a function of shear rate, haematocrit, and RBC size [1]. Values for platelet diffusivity at high wall shear rates have been deduced by applying transport theory models to measurements of platelet deposition on surfaces [2]. Shear augmented diffusion is also an important factor in the transport of oxygen [174] and other macromolecules [224], and in haemofiltration [245].

The flow-enhanced lateral motion of platelets is believed to occur because of two mechanisms [224], depicted in Fig 3.21. First, shear flow allows platelets to collide with other suspended cells. In shear flows, particles have different velocities than their neighbours moving in parallel streamlines. Because of these collisions, each platelet has random lateral movements that are described by random walk theory. As expected by the central limit theorem (CLT), the net outcome of a series of random small lateral displacements is the Gaussian distribution [55]. This idea has its roots in the microrheological studies of Mason *et al.* (1975) [119], particularly in their studies of dilute suspensions. They showed that no significant lateral motion resulted from the collision of a pair of rigid spheres in a low-Reynolds-number shear flow. However, lateral motion was readily detected when either the Reynolds number was increased or when flexible particles were used.

The second mechanism was proposed by Keller (1971) [123]. It focuses on the fluid around the suspended RBCs, which is stirred by their rotation, as illustrated in Fig. 3.21. This effect is analogous to the augmented diffusion observed in turbulent flows, where each particle and its nearby fluid would be likened to a turbulent eddy. This stirring motion mixes the adjacent material with that of nearby streamlines. The analogy is intuitively attractive for situations involving small molecules that are dis-

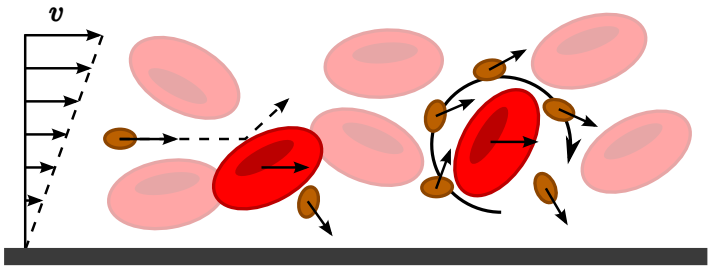

Fig. 3.21: The two mechanisms of the augmented diffusion observed in blood flow. Platelets bounce to RBCs due to the gradient of velocity (left highlighted RBC), and platelets are stirred due to the rotation of RBCs (right highlighted RBC).

solved in the suspending fluid, but it also extends to particles that are of roughly the same size as suspended stirring particles, such as platelets and WBCs. The outcome of stirring is characterised as an enhancement of the diffusive motion that would accompany a concentration gradient caused by external events [55]. According to this theory, the rotation of RBCs in the shearing field enhances the diffusion of platelets with increasing haematocrits and shear rate [123].

The increased near-wall excess of platelets and WBCs by itself, however, is not likely to be completely responsible for the enhanced platelet and WBC adherence onto vessel walls, since Brownian diffusion of cells is very low. Therefore, the augmented diffusivity is of utmost importance for platelets to adhere to injuries, and for WBCs to adhere to inflamed vessels and exit into infected tissues. Augmented diffusivity is responsible for increasing the outward movement of platelets and WBCs. Even though the RBC concentration near the wall of microvessels is lower, it is not absolutely zero [3]. The few erythrocytes (and rouleaux) in the RBC-free layer exhibit fully free rotational motion dependent on shear rate [83], which enhances platelet diffusion and which makes the near-wall excess of platelet and WBCs highly effective for the transport of these cells onto injured surfaces.

Mathematical Models for Enhanced Diffusion

The augmented diffusivity is normally added to the thermal diffusivity in order to yield the enhanced diffusivity

$$D_e = D + D_{EDM} \ , \tag{3.35}$$

where D_{EDM} is the enhanced diffusion model (EDM), and D is the Brownian (or thermal) diffusivity of molecules, platelets or WBCs.

Brownian diffusion is the average motion of the random movement of particles caused by the random collisions they suffer due to their thermal energy. The diffusivity constant of a particle of any size can be calculated by the Einstein-Smoluchowski relation. This theory was developed independently by those two authors in the early 20^{th} century, and unified Fick's Law with Brownian motion [59, 220]. The general diffusivity constant by the Einstein-Smoluchowski (also known as Stokes-Einstein) relation is

$$D = \frac{k_B\, T}{C_D} \ , \tag{3.36}$$

where $k_B = 1.38 \cdot 10^{-23}$ J/K is the Boltzmann constant, T the absolute temperature in kelvin, and C_D the frictional resistance of the randomly moving particles. The drag coefficient can be obtained by Stokes' Law for spherical bodies,

$$C_D = 6\pi\, \mu\, R \ , \tag{3.37}$$

where μ is the dynamic viscosity of the fluid, and R is the radius of the particle, which can be either a chemical molecule or a colloid particle such as a cell. Hence, by taking Eq. 3.37 in Eq. 3.36 the Brownian diffusivity is obtained,

$$D = \frac{k_B\, T}{6\pi\, \mu\, R} \ . \tag{3.38}$$

The Brownian diffusivity constant for platelets and WBCs is obtained by taking the mean radius of these cells in Eq. 3.38 at body temperature $T = 37\,^{\circ}\text{C} = 310\,\text{K}$ and

plasma viscosity $\mu = 1.2{\cdot}10^{-3}$Pa s (Sec. 3.1.3). Thus, the mean radius of $R_{plt} = 1.16\,\mu$m (Sec. 4.1.3) and $R_{WBC} = 3.5$–$11\,\mu$m (Table 3.1) would yield the diffusivity constant $D_{plt} = 1.6 \cdot 10^{-13}\,\mathrm{m^2\,s^{-1}}$ for platelets and $D_{WBC} = (1.7\text{–}5.4) \cdot 10^{-14}\,\mathrm{m^2\,s^{-1}}$ for WBCs, respectively[2].

A few EDMs have been proposed in the literature. As previously mentioned, Keller (1971) [123] proposed the first model based in the augmented diffusion caused by turbulent eddies. He applied the EDM of turbulent flows assuming that the eddies had the size of RBCs. Hence, Keller's EDM reads as

$$D_K = 0.18\, R_{RBC}^2\, \dot{\gamma}_{wall}\ , \tag{3.39}$$

where $R_{RBC} = 2.5$–$2.8\,\mu$m is the mean radius of an erythrocyte [105, 203], and $\dot{\gamma}_{wall}$ is the wall shear stress. Zydney and Colton (1988) [245] investigated the effects of various haematocrits in the augmented diffusion effect, and proposed the following EDM

$$D_{ZC} = 0.15\, R_{RBC}^2\, Ht\,(1 - Ht)^{0.8}\, \dot{\gamma}_{wall}\ . \tag{3.40}$$

Sorensen *et al.* (1999) [203, 204] introduced an EDM which is scaled by the Brownian diffusivity,

$$D_S = 1.05\, D\, \dot{\gamma}_{wall}\ . \tag{3.41}$$

Hund and Antaki (2009) [105] tested an anisotropic EDM

$$\boldsymbol{D}_{HA} = 0.01\, \dot{\gamma}_{wall} \begin{bmatrix} 1 & 0 & 0 \\ 0 & 1 & 0 \\ 0 & 0 & 1 \end{bmatrix} + 1.75\, \dot{\gamma}_{wall} \begin{bmatrix} 1 & 0 & 0 \\ 0 & 0 & 0 \\ 0 & 0 & 0 \end{bmatrix}\ , \tag{3.42}$$

where the first dimension is the radial direction $\hat{\boldsymbol{e}}_1 \equiv \hat{\boldsymbol{r}}$, which is perpendicular to the flow ($\boldsymbol{v} \cdot \hat{\boldsymbol{e}}_1 = 0$). These authors compared this model (Eq. 3.42) with the other EDMs (Eqs. 3.39, 3.40 and 3.41) with experimental data of platelet adhesion in a

[2] Authors [86, 105, 203, 216] normally use a diffusivity number with more significant digits, $D_{plt} = 1.58 \cdot 10^{-13}\, m^2/s$, but it is unreasonable to give such precision to a general group of samples.

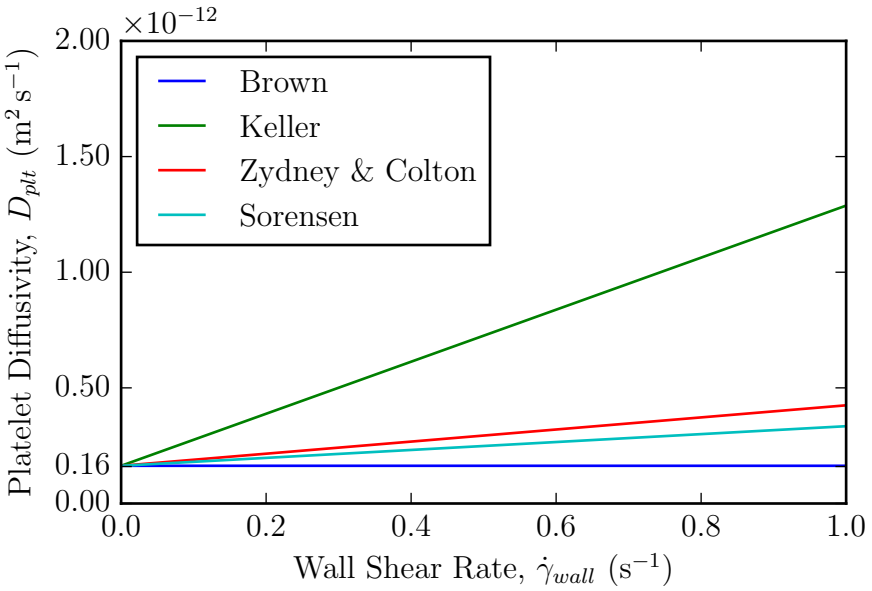

Fig. 3.22: Diffusivity in function of shear rate for different EDMs.

microchannel. All simulated EDMs achieved almost instantaneous arrival of platelets onto the wall, because they increased the diffusivity by three orders of magnitude. These results were consistent with their experimental data.

Tokarev *et al.* (2011) [216] derived an analytical formula for the convective flux of platelets towards a surface, enhanced by the collision with flowing RBCs and other platelets. Their model was not intended as an EDM, however this enhanced convection requires the flow of RBCs, similar to what was previously reported as augmented diffusivity. The EDM flux was estimated using the shear-induced collision rate of colloids by applying Eq. 4.36 to Eq. 4.35, as devised by Smoluchowski. Thus, Tokarev's convective flux is given by

$$j_p = \frac{1}{2}\frac{4}{3}\left[0.116\,(R_{RBC}+R_P)^3\,R_{RBC}\,[RBC] + 0.196\,(2\,R_P)^3\,R_p\,[P]\right]\,\dot{\gamma}\,[P]\;, \qquad (3.43)$$

where R_{RBC} and R_P, and $[RBC]$ and $[P]$ are the mean radii and concentrations of RBCs and platelets, respectively. The factor $\frac{1}{2}$ in Eq. 3.43 stands for the the fact that only half of the collisions will bring platelets towards the wall. The idea behind Eq.

3.43 can be extend to an EDM, because this is a convective flux. If the contribution of platelet-to-platelet collision is considered insignificant close to the contribution of RBC-to-platelet collision, diffusivity is considered proportional to R_{RBC}, and haematocrit $Ht = V_{RBC}\,[\mathrm{RBC}]$ is used instead of [RBC], Eq. 3.43 becomes

$$D_T = 0.116\,\frac{4}{3}\,(R_{RBC} + R_P)^3\,R_{RBC}^2\,\frac{Ht}{V_{RBC}}\,\dot{\gamma}\ , \tag{3.44}$$

where V_{RBC} is the volume of one erythrocyte. Interestingly, Eq. 3.44 is similar to both the EDMs of Keller, and Zydney and Colton (Eqs. 3.40 and 3.39, respectively), but the rate constant is obtained analytically.

It is important to stress that the drift potential models used to generate the near-wall excess of platelets and WBCs [55, 105] are also EDMs. They add an enhanced diffusion term to the diffusion flux of the transport equation. However, the potential models for diffusion proposed by Eckstein [55] and Hund and Antaki [105] do not reflect the linear relationship of diffusivity and shear rate at the vessel wall that were measured experimentally [78, 81, 123, 204, 218, 224, 245]. On the other hand, drift potential models succeed to create the near-wall excess, which cannot be achieved by EDMs alone because diffusion alone acts to smooth, and eventually eliminate concentration gradients. An accurate transport model for platelets and WBCs should incorporate both an EDM and a potential drift term for the near-wall excess of these cells. Hund and Antaki (2009) [105] proposed incorporating a recalibrated version of Zydney and Colton's EDM (Eq. 3.40), because it could include the spatial distribution of haematocrit. The EDM adapted from the work of Tokarev *et al.* (2011) [216] could possibly be an even better candidate, because it not only incorporates the haematocrit, but it is derived from the physical mechanism causing augmented diffusivity in whole blood.

3.2 Kinetics of Thrombosis and Haemostasis

Chemical reactions are transformations of species of molecules into other species. In chemical kinetics, this transformation is expressed by a mathematical equation, used to link the reaction rate to the concentration of each reactant.

Extensive research work has been published on the development of mathematical models for blood coagulation. A broad review on this field of development was produced by Ataullakhanov and Panteleev [12]. More recently, Moiseyev and Bar-Yoseph [157] have published a review on the application of coagulation models for the optimisation of vascular implant design.

3.2.1 General Rate Equation

Consider a chemical reaction of the form

$$\mathrm{aA} + \mathrm{bB} \longrightarrow \mathrm{pP} + \mathrm{qQ},$$

where a, b, p, and q are called *stoichiometric coefficients*. They express the smallest whole number of molecules of each species required for a complete transformation of reagents A and B to products P and Q. The *rate equation* of this reaction is formulated as:

$$r = -\frac{1}{a}\frac{d[A]}{dt} = -\frac{1}{b}\frac{d[B]}{dt} = \frac{1}{p}\frac{d[P]}{dt} = \frac{1}{q}\frac{d[Q]}{dt} \;=\; k[A]^{\alpha}[B]^{\beta}\,, \tag{3.45}$$

where the square brackets $[\cdot]$ denote concentration of each species, k is the rate constant, and α and β are powers to which the concentration terms are raised. If the reaction occurs in a single step (no intermediary steps), then the exponents coincide with the stoichiometric coefficients, i.e. $\alpha \equiv a$ and $\beta \equiv b$. However, this is often not true for complex (multistep) reactions, whose exponents are determined by the intermediary conversion rates. The *order of reaction* is the sum of these exponential indices, as shown in Table 3.4 [14, p. 818].

Table 3.4: Classification of direct rate equations.

Reaction Order	Reaction Equation	Dimension of k
0	$r = k$	$\mathrm{mol\,s^{-1}}$
1	$r = k[A]$	$\mathrm{s^{-1}}$
2	$r = k[A][B]$, or $r = k[A]^2$	$\mathrm{mol^{-1}\,s^{-1}}$
3	$r = k[A]^a[B]^b$, where $a + b = 3$	$\mathrm{mol^{-2}\,s^{-1}}$
...	...	...

3.2.2 Chemical Equilibrium

In many cases, chemical reactions are two-way reactions

$$\mathrm{aA + bB} \underset{-}{\overset{+}{\rightleftharpoons}} \mathrm{pP + qQ},$$

where there is a forward process on the left-hand side and a backward reaction on the right-hand side. Chemical equilibrium is the state in which reactants and products are present in concentrations which have no further tendency to change with time. Therefore, forward and backward reaction rates are zero,

$$r = k_+ [A]^a[B]^b = k_- [P]^p[Q]^q = 0 \ , \tag{3.46}$$

where k_+ and k_- are the forward and backward rate constants. The ratio of the rate constants is the equilibrium constant

$$K = \frac{k_+}{k_-} = \frac{[P]^p[Q]^q}{[A]^a[B]^b} \ , \tag{3.47}$$

which describes the thermodynamic equilibrium state of the system. Because K is a thermodynamic constant, it depends only on pressure and temperature, the total proportion of primary molecules present in the system does not change the equilibrium constant.

3.2.3 Dissociation constant

Commonly used in biochemistry, the dissociation constant K_d is the equilibrium constant for a chemical reaction of the kind

$$\mathrm{A_aB_b} \underset{-}{\overset{+}{\rightleftharpoons}} \mathrm{aA + bB},$$

and it is defined as

$$K_d = \frac{k_+}{k_-} = \frac{[A]^a[B]^b}{[A_aB_b]} \ . \tag{3.48}$$

The dissociation constant represents the disposition of a larger object to separate (dissociate) reversibly into smaller components [30, p.12]. For example, it can be applied to the case of a protein complex falling apart into its component molecules. The inverse of the dissociation constant is known as the association constant $K_a = K_d^{-1}$, but it is less often used.

The quantity of protein molecules A and B forming a protein complex AB is measured by the concentration of dissociated molecules A and B in the system. Thus, if the initial concentrations $[A]_0$ and $[B]_0$ of unbound molecules are known, then at any time the concentration of bound molecules [AB] can be tracked by measuring the concentration of free molecules $[A]$ or $[B]$, because of mass conservation equations

$$[A]_0 = [A] + [AB] \qquad \text{or} \qquad [B]_0 = [B] + [AB] \ . \tag{3.49}$$

The concentration of the complexes is obtained by combining Eq. 3.48 and Eq. 3.49,

$$[AB] = \frac{[A]_0[B]}{K_d + [B]} = \frac{[B]_0[A]}{K_d + [A]} \ . \tag{3.50}$$

Concentration of Proteins Bound to Cell Membrane Receptors

The equilibrium of proteins bound to cell membrane receptors can be measured in the same way as to proteins bound in a complex. However, instead of just one binding site, there are many binding sites per cell. Proteins that bind to cell receptors are called

ligands to those receptors. A simplified mechanism can be formulated if the binding affinity of all receptors can be considered independent of the number of ligands bound to them. Assuming that each of all n cell receptors are identical and they possess only one single binding site, the concentration of bound ligands $[A]_{bound}$ can be written as

$$[A]_{bound} = \frac{n[C]_0[A]}{K_d + [A]} \ , \tag{3.51}$$

where $[C]_0$ is the concentration of cells, and $[A]$ is the concentration of ligands dissolved in the medium [30, p.14]. In this case, $[A]_{bound} \neq [AC]$, as in Eq. 3.50, but $[A]_{bound}$ comprises all partially saturated forms of the cell, i.e.

$$[A]_{bound} = [AC] + 2[A_2C] + 3[A_3C] + ... + n[A_nC] \ , \tag{3.52}$$

where the saturation occurs stepwise

$$\begin{array}{lll}
[A] + [C] \rightleftharpoons [AC] & K_1' = \dfrac{[A][C]}{[AC]} & [AC] = \dfrac{[A][C]}{K_1'} \\
[A] + [AC] \rightleftharpoons [A_2C] & K_2' = \dfrac{[A][AC]}{[A_2C]} & [A_2C] = \dfrac{[A]^2[C]}{K_1'K_2'} \\
[A] + [A_2C] \rightleftharpoons [A_3C] & K_3' = \dfrac{[A][A_2C]}{[A_3C]} & [A_3C] = \dfrac{[A]^3[C]}{K_1'K_2'K_3'} \\
\vdots & \vdots & \vdots \\
[A] + [A_{n-1}C] \rightleftharpoons [A_nC] & K_n' = \dfrac{[A][A_{n-1}C]}{[A_nC]} & [A_nC] = \dfrac{[A]^n[C]}{K_1'K_2'K_3' \cdots K_n'}
\end{array} \ . \tag{3.53}$$

Even if the dissociation constants of all binding sites are identical, the dissociation constant of the cell as a whole increases as the binding sites are occupied by ligands. The macroscopic dissociation constant depends on the availability of binding sites in each binding step. The general relationship between both types of dissociation constants for n binding sites is

$$K_i' = K_d \frac{1}{n - i + 1} \tag{3.54}$$

For the derivation of the general binding equation, a saturation function

$$r := \frac{[A]_{bound}}{[C]_0} = \frac{[AC] + 2[A_2C] + 3[A_3C] + ... + n[A_nC]}{[C] + [AC] + [A_2C] + [A_3C] + ... + [A_nC]} = \frac{\sum_{i=1}^{n} \left(\frac{i[A]^i}{\prod_{j=1}^{i} K'_j} \right)}{1 + \sum_{i=1}^{n} \left(\frac{[A]^i}{\prod_{j=1}^{i} K'_j} \right)} \tag{3.55}$$

is defined as the quotient from the portion of bound agonists (Eq. 3.52) to the total concentration of cells $[C]_0$, and the definitions of the stepwise saturation in Eq. 3.53. By applying Eq. 3.54 in 3.55, the saturation function becomes

$$r = \frac{\sum_{i=1}^{n} i \left(\prod_{j=1}^{i} \frac{n-j+1}{j} \right) \left(\frac{[A]}{K_d} \right)^i}{1 + \sum_{i=1}^{n} \left(\prod_{j=1}^{i} \frac{n-j+1}{j} \right) \left(\frac{[A]}{K_d} \right)^i} = \frac{\sum_{i=1}^{n} i \binom{n}{i} \left(\frac{[A]}{K_d} \right)^i}{1 + \sum_{i=1}^{n} \binom{n}{i} \left(\frac{[A]}{K_d} \right)^i} , \tag{3.56}$$

where $\binom{n}{i} = \frac{n!}{(n-i)!i!}$ is the binomial coefficient. Equation 3.51 is proven by applying the binomial rule

$$r = \frac{n \left(\frac{[A]}{K_d} \right) \left(1 + \frac{[A]}{K_d} \right)^{n-1}}{\left(1 + \frac{[A]}{K_d} \right)^{n}} = \frac{n \left(\frac{[A]}{K_d} \right)}{\left(1 + \frac{[A]}{K_d} \right)} = \frac{n[L]}{K_d + [A]} . \tag{3.57}$$

The concentration of bound ligands to the cell (Eq. 3.51) is obtained from the definition made in Eq. 3.55 and the derivation attained in Eq. 3.57.

3.2.4 Enzyme Kinetics

Enzymes participate in many metabolic reactions as catalysts. The mechanism of enzyme catalysis is depicted in Fig. 3.23. Enzymes connect with specific species promoting a decrease of the activation energy, which speeds up the reaction rate. As soon as the reaction is processed, the enzyme releases the product without being consumed. Catalysis does not alter the position of equilibrium between substrates and products, but it can display saturation. For relatively low substrate concentrations, the reaction rate increases linearly with substrate concentration, because of a large number

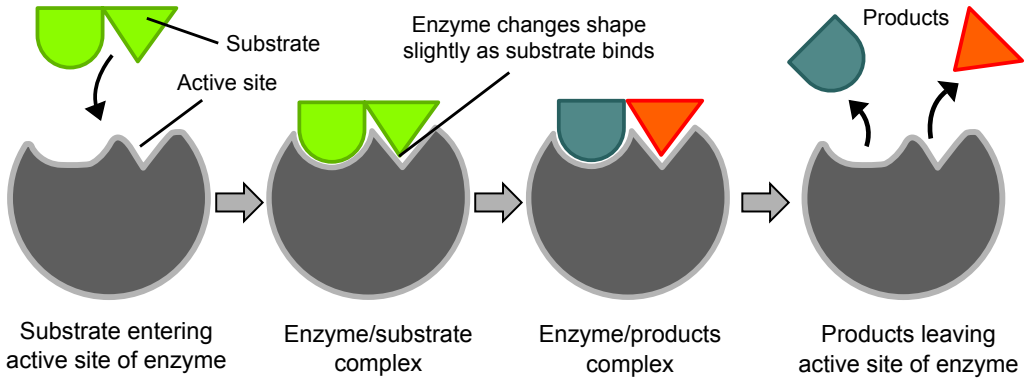

Fig. 3.23: Schematic diagram of enzyme catalysis of a substrate.

of free enzymes, and an increasing substrate concentration implies an increasing rate at which the enzyme and substrate molecules collide into one another. On the other hand, for relatively high substrate concentrations, the enzyme active sites become saturated and the reaction rate is determined by the intrinsic turnover rate of the enzyme [30, p.63].

The following chemical reaction illustrates the enzyme kinetics

$$\mathrm{E} + \mathrm{S} \underset{k_r}{\overset{k_f}{\rightleftharpoons}} \mathrm{ES} \xrightarrow{k_{\mathrm{cat}}} \mathrm{E} + \mathrm{P} \ ,$$

where E is the enzyme, S is the substrate, ES is the intermediate enzyme-substrate complex, and P is the product. The double arrows between S and ES represent the fact that enzyme-substrate binding is a reversible process. Therefore, k_f, k_r, and k_{cat} are the forward, the reverse, and the catalytic rate constants, respectively. The kinetics of this reaction is represented by the system of equations

$$\begin{cases} \frac{d[S]}{dt} &= -\ k_f[E][S] + k_r[ES] \\ \frac{d[E]}{dt} &= -\ k_f[E][S] + k_r[ES] + k_{\mathrm{cat}}[ES] \\ \frac{d[ES]}{dt} &= +\ k_f[E][S] - k_r[ES] - k_{\mathrm{cat}}[ES] \\ \frac{d[P]}{dt} &= + k_{\mathrm{cat}}[ES] \end{cases} , \tag{3.58}$$

whose typical evolution is shown in Fig. 3.24. By using the conservation law for the

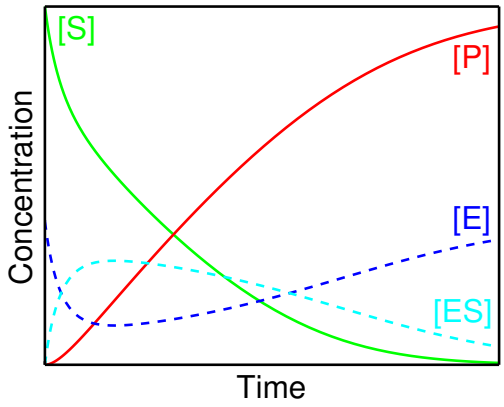

Fig. 3.24: Change in concentration over time of the reactants in a typical enzymatic reaction.

enzyme (Eq. 3.49), one can reduce one equation of the system of Eqs. 3.58. Therefore,

$$\frac{d[ES]}{dt} = k_f([E]_0 - [ES])[S] - (k_r + k_{\text{cat}})[ES] \tag{3.59}$$

and

$$\frac{d[S]}{dt} = -k_f([E]_0 - [ES])[S] - k_r[ES]. \tag{3.60}$$

Michaelis-Menten model

Equation system 3.58 can be simplified further by imposing an additional assumption. The most popular model for enzyme reaction rate is the Michaelis-Menten model. It assumes the enzyme-substrate complex reaction (Eq. 3.59) is in steady state during the whole process,

$$\frac{d[ES]}{dt} = 0 \Rightarrow [ES] = \frac{[E]_0[S]}{K_m + [S]}, \tag{3.61}$$

where

$$K_m = \frac{k_r + k_{\text{cat}}}{k_f} \tag{3.62}$$

is known as the Michaelis constant. Although Eq. 3.61 resembles Eq. 3.50, the Michaelis constant K_m is not a kind of dissociation constant K_d, because it also includes

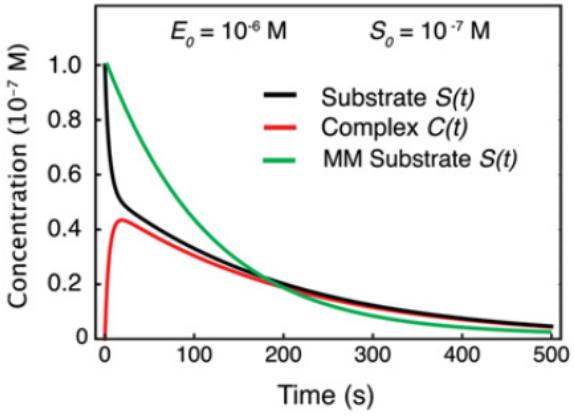

Fig. 3.25: Comparison of an enzymatic system which does not fulfil the requirements for the Michelis-Menten model (black and red lines representing Eqs. 3.59 and 3.60, respectively) with the Michelis-Menten model (green line representing Eq. 3.63, with $\frac{1}{S_0}|\frac{dS}{dt}|_{\max}\hat{t}_{ES} = 0.5$). Image reproduced from Chen *et al.* (2010) [44].

the catalytic reaction rate. The overall reaction rate of the Michaelis-Menten model derives from Eq. 3.61 in Eq. 3.58,

$$r = \frac{d[P]}{dt} = -\frac{d[S]}{dt} = k_{\text{cat}}[E]_0\frac{[S]}{K_m + [S]} = r_{\max}\frac{[S]}{K_m + [S]}. \tag{3.63}$$

The Michaelis constant K_m is equivalent to the substrate concentration which holds half the maximum rate in Eq. 3.63.

The Michaelis-Menten model is valid when either $S_0 \gg E_0$ or $k_r \gg k_{\text{cat}}$, but a more general condition is

$$\frac{1}{S_0}\left|\frac{dS}{dt}\right|_{\max}\hat{t}_{ES} \ll 1, \tag{3.64}$$

where $\hat{t}_{ES}$ is the characteristic time for Eq. 3.59 to reach steady state. This means that the relative change of the substrate must be small before Eq. 3.59 reaches steady state [44]. Figure 3.25 shows an example where this condition fails.

3.2.5 Dynamics of Enzymatic Cascades

After years of confusion, Macfarlane (1964) [148] established the enzymatic cascade model for coagulation of plasma proteins. Levine (1966) [143] was the first to come

up with a linear system of ordinary differential equations (ODEs) to represent the sequence of enzymes, as follows in Fig 3.26.

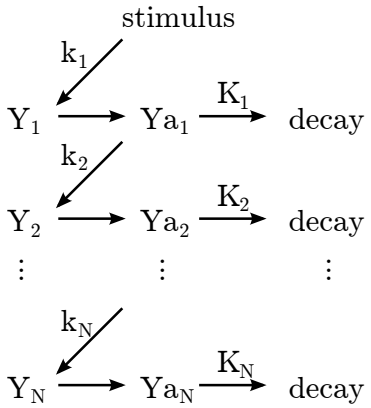

Fig. 3.26: Chemical representation of reactions in an enzymatic cascade.

Levine's ODE system consisted of a chain of second order activation reactions rates summed to first order deactivation (decay) reactions. The chain or reaction can be represented as a vector of reaction rates

$$\frac{d}{dt}[Ya_i] = k_i[Y_i][Ya_{(i-1)}] - K_i[Y_i] \ , \tag{3.65}$$

Y_i is the chemical component $i \in \{1, ..., N\} \subset \mathbb{N}$ and Ya_i is its respective activated form, k_i is the second order reaction constant for Y_i activation, and K_i is the first order reaction constant for Y_i decay. When the system is in steady state, the gain G of the enzymatic cascade is given by

$$G = \frac{[Ya_N]}{[Ya_1]} = \prod_{i=2}^{N} \frac{k_1[Y_i]_0}{K_i} \ , \tag{3.66}$$

where $[Y_i]_0$ is the initial concentration of component Y_i. Levine analysed the linear case of Eq. 3.65, assuming constant proenzyme, $[Y_i](t) = [Y_i]_0 = \text{constant}$. In 1969, Moro and Bharucha-Reid [158] derived the non-linear analytical solution of the same equation.

Later, as the experimental knowledge was growing, this model was expanded to incorporate other features of the coagulation cascades. First, Martorana and Moro

(1974) [153] included the negative feedback loops given by the activation of anticoagulation enzymes (Sec. 2.3.2). In negative feedbacks, products of the cascade inactivate enzymes required in earlier steps (see Fig. 3.27). Next, between 1989 and 1995, other groups included the positive feedback loops given by the activation of platelets, V, VII, VIII, XI, and PK (see Fig 2.14) [125, 124, 108, 19, 28]. In positive feedbacks, products of the cascade can activate enzymes required in earlier steps (see Fig. 3.27). Normally, the positive feedback loops have higher conversion rates than the initial pathway.

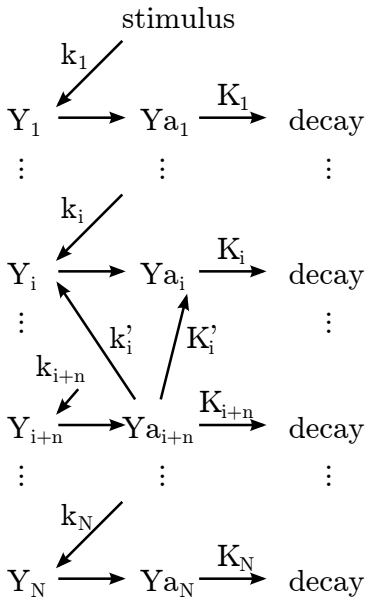

Fig. 3.27: Kinetics of enzymatic cascade with the activated enzyme Ya_{i+n} producing a positive (k_i') and a negative (K_i') feedback.

Khanin *et al.* (1991) [124] analysed the stimulus response of ODE systems with the topology of enzymatic cascades. They showed that enzymatic cascades with both positive and negative feedback loops can present an activation threshold. The threshold represents the hypersurface in the phase space where enzyme activation rates equals inhibition rates. They considered the dimensionless system, where concentration of factor Ya

$$[\mathrm{Ya}]^* = \frac{[\mathrm{Ya}]}{[\mathrm{Y}]_0} \tag{3.67}$$

is scaled by the initial concentration of its zymogen[3] $[Y]_0$. In this system, factor Xa activates thrombin (IIa), which initiates positive feedbacks due to the action of of Va and VIIIa, but also initiates negative feedbacks due to APC. Both $[IIa]^*$ and $[Xa]^*$ are constantly being inactivated by ATIII. In this non-linear dynamic system, thrombin concentration is attracted to a stationary point of low magnitude ($[IIa]^* \approx 0$) for any sub-threshold stimulation of Xa, but it will be attracted to a stationary point of high magnitude ($[IIa]^* \approx 1$) for any over-threshold stimulation of Xa (Fig. 3.28). Both the existence of a threshold and its level depends on the magnitude of the system's positive and negative rate constants, k_i and K_i, respectively. Changing these parameters may cause bifurcation of the equilibrium points. Later, this theoretical dynamics ruling the cascade threshold was confirmed experimentally by Jesty *et al.* (2005) [109]. The expression of thresholds is imperative to quantitatively analyse the pathogenic mechanisms of hypo- and hypercoagulation.

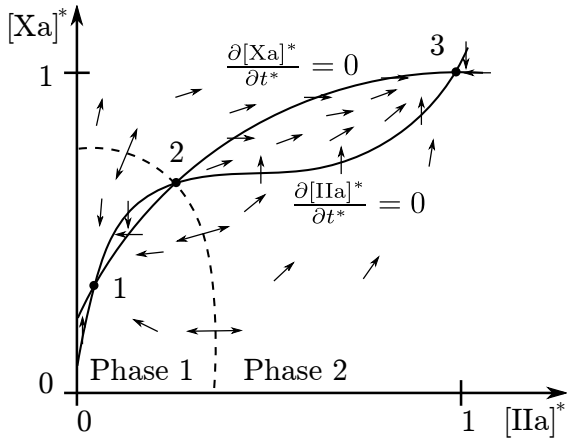

Fig. 3.28: Phase space of scaled factors IIa and Xa, as presented by the model of Khanin *et al.* (1991) [124]. Solid lines represent points where either $\frac{\partial [IIa]^*}{\partial t^*} = 0$ or $\frac{\partial [Xa]^*}{\partial t^*} = 0$, and the dashed line separates phases 1 and 2. Points 1 and 3 are limit points, and point 2 is a saddle point.

[3]A zymogen, also called a proenzyme, is an inactive precursor of an enzyme. A zymogen requires a biochemical change (such as a hydrolysis reaction revealing the active site, or changing the configuration to reveal the active site) for it to become an active enzyme.

3.2.6 Platelet Activation Rate

Activated platelets are required for the assembly of coagulation complexes, and they aggregate to form the initial plug in fresh bleeding sites. As indicated earlier (in Sec. 2.2.1), there is a distinction between resting platelets (RP) and activated platelets (AP). Resting platelets screen the vessel walls for injuries. Once they are stimulated over a certain threshold of biochemical or mechanical stimuli, RPs become activated. However, the modelling of platelet activation and function remains in an early stage of development [54]. As indicated earlier, there are several chemicals that act in a qualitatively similar fashion to activate RPs (Table 2.1). Therefore, current models are coarse descriptions which consider the platelet as either fully resting or fully activated. Activation occurs depending on the threshold concentration of platelet activation agonists. Typically, activation models lump together the concentration of several important species to signal platelet activation. Platelets can also be activated by unphysiological shear rates. Models for mechanical activation of platelets are in an even more primitive state [157, 194, 195].

Fogelson (1992) [63] introduced an activation model in which it was unnecessary to distinguish between all the activation factors. Platelet activation

$$\mathrm{RP} \longrightarrow \mathrm{AP},$$

was described by a first-order rate equation (Table 3.4)

$$\frac{d[AP]}{dt} = -\frac{d[RP]}{dt} = k_{pa}\,[RP]\ , \tag{3.68}$$

where $k_{pa} = k_{pa}([\cdot])$ is the activation rate, which depends on the present concentration $[\cdot]$ of an activation molecule [63]. Fogelson did not specify a functional form for k_{pa} in his model, but rather assumed a static distribution of initially activated platelets in his simulations.

Sorensen *et al.* (1999) [203] extended this idea by adding the capability for multiple platelet agonists, rather than a single, lumped one, as well as the possibility of

agonist inhibition via first-order reactions. Because very little quantitative information is known about the kinetics of platelet activation, Sorensen *et al.* assumed a simplistic linear equation with an activation threshold,

$$k_{pa} = \begin{cases} 0, & \Omega < 1.0 \\ \frac{\Omega}{t_{pa}}, & \Omega \geq 1.0 \end{cases} , \tag{3.69}$$

where

$$\Omega = \sum_{i=1}^{n_a} \omega_i \frac{[a_i]}{[a_i]_{crit}} \tag{3.70}$$

is the activation function, and t_{pa} is the characteristic time for platelet activation (assumed $t_{pa} = 1$). In Eq. 3.70, n_a is the number of agonists in the model, $[a_i]$ is the concentration of the i$^{\text{th}}$ agonist, $[a_i]_{crit}$ is the threshold concentration of that agonist for platelet activation, and ω_i is the weight of that agonist for the activation rate. Activation agonists have $\omega_i > 0$, whereas inhibition agonists have $\omega_i < 0$; strong agonists have greater $|\omega_i|$ than weak agonists. No activation takes place in Eq. 3.68 until the weighted sum of the normalised agonist concentrations (Eq. 3.70) is equal to at least one (i.e., $\Omega \geq 1.0$).

Non-physiologic (pathologic) flow patterns can also activate platelets (see Sec. 2.2.1). Sheriff *et al.* (2010) [194, 195] developed a mathematical model for platelet activation due to high shear stress patterns ($\tau > 4\,Pa$). They tested washed platelets (no plasma proteins) in a rheometer with different impulses of pathological and physiological shear stresses. For comparing the effect of different shear insults, the authors normalised the concentration of activated platelets with the total concentration of platelets. They called this normalisation as platelet activation state (PAS), which was defined as

$$PAS(t) := \frac{[AP]}{[AP] + [RP]} . \tag{3.71}$$

Platelets that underwent supra-physiological shear stresses became primed for subsequent activation at physiological shear. They activate at least 20-fold faster at sub-

sequent low shear stress than platelets which were not initially exposed to high shear stress. However, platelets that suffered only supra-physiological shear stresses were less activated than the ones that suffered high then low shear stress pattern [194]. Platelets exposed beyond a threshold of high-shear stress retain a memory for subsequent activation. Therefore, Sheriff *et al.* defined a model for shear stress platelet activation as

$$\begin{aligned} PAS(t) &= \int_{t_0}^{t} \frac{d}{dt}\left(c_1\,\tau^{c_2}\,t^{c_3}\right) dt + PAS(t_0) \\ &= \int_{t_0}^{t} \left(c_1\,c_3\,\tau^{c_2}\,t^{c_3-1} + c_1\,c_2\,\tau^{c_2-1}\,\frac{d\tau}{dt}\,t^{c_3} \right) dt + PAS(t_0)\ , \end{aligned} \tag{3.72}$$

where c_1, c_2 and c_3 are constants, and $PAS(t_0)$ is the memory of the stress insults that happened prior to t_0 (initial experiment time) [195]. All the shear insult that occurred prior to t_0 is measured as $PAS(t_0)$, but the shear history prior to t_0 is unknown.

A few criticisms of this model can be easily made. First, the data was obtained from washed platelets. Therefore, the samples lack von Willebrand factor (vWF), which would cause a much faster aggregation and activation of platelets at $\tau \gtrsim 5\,\mathrm{Pa}$ (with $\dot{\gamma} \gtrsim 5 \cdot 10^3\,\mathrm{s}^{-1}$ for uncoiling vWF in water, $\mu = 1\,\mathrm{mPa\,s}$) [188]. Furthermore, washed platelets lack inhibitor agonists for platelet activation, which would damp the PAS rate (see Table 2.1). Second, individual platelets release activation factors from their granules once activated by shear stimulus. This chemical positive feedback is completely ignored by Sheriff *et al.* [194, 195], but it could be the main cause of the time dependent activation. Last, Eq. 3.72 is a model where the activation rate is a relative quantity, independent of the current concentration of resting platelets $[RP]$, because of the definition of $PAS(t)$ in Eq. 3.71. Equation 3.71 implied that $[AP] + [RP] = [AP]_0 + [RP]_0 = const$, so that

$$\frac{d[AP]}{dt} = \frac{dPAS}{dt}([AP]_0 + [RP]_0)\ . \tag{3.73}$$

Therefore, if a first order kinetics (Eq. 3.68) is considered for the activation rate of this model, then the activation rate would be independent of the concentration of resting

platelets, because the rate parameter would be

$$k_{pa} = \frac{[AP]_0 + [RP]_0}{[RP]} \left(c_1\, c_3\, \tau^{c_2}\, t^{c_3 - 1} + c_1\, c_2\, \tau^{c_2 - 1}\, \frac{d\tau}{dt}\, t^{c_3} \right) \tag{3.74}$$

There is no evidence for the rate parameter to be inversely dependent of the current concentration of resting platelets $[RP]$, and the independence of Eq. 3.72 to $[RP]$ also implies a lack of theoretical upper limit for $PAS(t)$.

3.3 Coagulation Models with Empirical Parameters

Concurrently with the discovery of the theoretical aspects of enzymatic cascades (discussed in Sec. 3.2.5), some research groups were simulating the coagulation cascades with empirical values of concentration of plasma proteins and coefficients of reaction rates. Although in those simulations most of the values were empirically measured, some of them had to be indirectly estimated due to the lack of practical means of directly measuring those quantities. These numerical investigations theoretically confirmed some aspects of the coagulation cascades. Moreover, they achieved quantitative correlation with laboratory tests.

Earlier models using empirical parameters investigated theoretical aspects of the common pathway of the coagulation cascade. Those aspects were related to the mechanisms causing the burst of thrombin once a significantly high concentration of prothombinase complex (Xa-Va) was formed. Next, mathematical models of mechanisms of the extrinsic and intrinsic pathways emerged, in order to simulate the initiation of the coagulation cascade through tissue injury and artificial materials, respectively.

3.3.1 Early Models: Aspects of the Common Pathway

Nesheim *et al.*[4] (1984) [162] simulated the role of the formation of prothrombinase (Xa-Va) on negatively charged surfaces of activated platelets and an phospholipid

[4]group led by Dr. Kenneth Mann, Departament of Biochemistry, University of Vermont, USA.

vesicules in the procoagulation kinetics (see Fig. 2.14). Both Xa-Va and Xa act as enzymes to catalyze thrombin (II) into prothrombin (IIa), but the complex Xa-Va adsorbed on negatively charged phospholipids is able to convert IIa more than 3000-times faster than Xa diluted in plasma. Therefore, the activation of thrombin occurs as the sum of two Michaelis-Menten equations (Eq. 3.63)

$$\frac{d[IIa]}{dt} = \frac{k_{\text{cat}}[Xa]_0[II]}{K_m + [II]} + \frac{k'_{\text{cat}}[Xa\text{-}Va]_{ads,0}\,[II]_{ads}}{K'_m + [II]_{ads}}\,\delta\,[L]_0\ , \tag{3.75}$$

where δ is a constant of proportionality for the available phospholipid area, and

$$[L]_0 = [L] + n_{II}\,[II]_{ads} + n_{Xa\text{-}Va}\,[Xa\text{-}Va]_{ads}\ , \tag{3.76}$$

is the nominal concentration of activated platelets or phospholipid vesicules, with n_{II} and n_{Xa-Va} being stoichiometric constants. The adsorbed prothrombin (II) and Xa-Va are defined by Eq. 3.50, where both species have different dissociation constants. This kinetic model with 12 empirical parameters successfully predicted the initial rate of thrombin generation for various initial levels of Xa-Va, Xa, and phospholipid vesicle. This model is also able to explain the reason why excessively high availability of negatively charged vesicle surface can inhibit the reaction rate. As the phospholipid surface becomes more receptive to Xa-Va adsorption, this enzyme complex competes for surface area with II, as a consequence, the concentration of adsorbed II decreases.

With a system of 14 kinetic equations and 23 rate constants, Willems *et al.* (1991) [229] simulated the positive feedback loop of prothrombinase (Xa-Va), being inhibited by heparinised antithrombin III (ATIII) and activated protein C (APC). The model predicted a threshold value for factor Xa production. Under this threshold, variations of Xa concentration hardly affected thrombin (IIa) production. On the other hand, concentrations of Xa over the threshold resulted in explosive and complete activation of Xa-Va, which ended up firing IIa activation. This threshold value depended on different negative feedback reactions, e.g. inactivation of IIa and factor Xa by ATIII (+ heparin). It could be increased by two orders of magnitude by accelerated inactivation

of factor Xa and Xa-Va, but was hardly affected by a tenfold increase in the rate of IIa inactivation, or by increased production of APC. Nevertheless, the level of APC was able to slow down the input-response relation between factor Xa input and the extent of Xa-Va formation. The simulated results correlated well with experimental curves.

3.3.2 Vessel Wall Injury: Activation through the Extrinsic Pathway

In the work of Jones *et al.* (1994) [111], the group of Dr. Mann formulated a model initiated by tissue factor (TF) on the extrinsic pathway, and finishing at the activation of thrombin (IIa). The experimental data was specially obtained by the same group to foster the mathematical model with accurate rate constants and concentration of species [141]. This model consisted of 19 ODEs and 20 rate constants, but, in contrast to the work of Nesheim *et al.*, saturation of phospholipid membranes for assembly of prothrombinase was neglected because an excess of phospholipids was added to the experiments. The model provided a realistic account of the fates of each of the proteins in the coagulation cascade through a range of initial concentrations of VIIa-TF.

Hockin *et al.* (2002) [100] (from the group led by Dr. Mann) expanded the model of Jones *et al.* to include anticoagulation factors (coagulation inhibitors). The Hockin-Mann model consisted of 34 ODEs and species, 42 rate constants, and 10 non-zero initial concentration of species. It could simulate the initiation of the extrinsic cascade with tissue factor (TF) forming the extrinsic tenase (TF-VIIa), the propagation phase with the production of factor Xa and Xa-Va, and the termination phase with the activation of the anticoagulants AT-III and TFPI. The generation of thrombin (IIa) displayed a non-linear dependence upon TF, AT-III, and TFPI and the combination of these factors displayed kinetic thresholds for thrombin generation. At sub-threshold TF, IIa production was suppressed by the combination of TFPI and AT-III. However, the production rate of IIa is always quantitatively equivalent for TF concentrations

above the TF threshold. A comparison of this model with empirical laboratory data demonstrated that most experimentally observable parameters were captured, and the pathologies that resulted from enhanced or deficient IIa generation were accurately described.

More complex models of the coagulation cascades have evolved from the Hockin-Mann model. They included mode details of the coagulation cascades, as well as other aspects such as flow rate (dispersion) and fibrinolysis [94, 187]. These complex models were able to yield information on more complex aspects of coagulation. For instance, under flow conditions, the effects of convection usually mitigate the formation of fibrin fibres, because fibrin bundles are transported downstream before attaching to fibres, which are aligned with the flow. More recently, some groups are starting to investigate the linkages between different genotypes and phenotypes on the coagulation response, with systems of 100–1000 reactions, which is very challenging to validate [54].

Kuharsky and Fogelson (2001)[134] were the first to formulate a model of a set of rate equations (ODEs) of the coagulation system, including interactions with platelets and an injured surface. Transport of coagulation proteins and platelets to and from an injury was controlled largely by the convective mass transfer equation:

$$\frac{d[A]_{surf}}{dt} = k_A^{flow}([A]_{bulk} - [A]_{surf}) \ , \tag{3.77}$$

where $[A]_{bulk}$ and $[A]_{surf}$ are the concentrations of a species A in plasma and adsorbed to a surface, respectively; and k_A^{flow} is the mass transfer coefficient, which depends on the wall shear rate $\dot{\gamma}_w$ and the species diffusivity D_A. This model consisted of 59 ODEs of 9 original species, which could be in a number of states combining their activated and non-activated forms, in complex with other species, on or off the platelet membranes, or on or off the injured wall. The simulation exhibited threshold behaviour of thrombin production, and the relation of shear rate and near-wall platelet concentrations to the development of growing thrombi. Because in this model platelets compete with TF for covering the subendothelium, it was suggested that platelets rather than chemical

inhibitors, might play the dominant role in blocking the activity of the TF:VIIa enzyme complex. Therefore, once the TF:VIIa complex is covered, the intrinsic IXa-Xa tenase would continue factor Xa on platelets.

3.3.3 Reactivity of Biomaterials: Activation through the Intrinsic Pathway

The reactivity of a biomaterial depends primarily on the affinity of blood proteins to adsorb and transform on the biomaterial's surface. This is inherently done through the intrinsic pathway, because tissue factor will never turn up on artificial surfaces.

Gregory and Basmadjian (1994) [91] derived a model of intrinsic pathway activation on a foreign surface. They were the first to add convection terms to the ODE system of reaction rates. Their model was comprised of a set of 20 dominant reactions with 11 components, from the contact phase up to the common pathway of the blood coagulation cascade. System of ODEs was reduced to four coupled equations, while equilibrium of the other kinetic equations was simplified to a single polynomial equation. The analysis showed that the extrinsic pathway never has more than one stable steady state. The model included transport of coagulation factors onto the surface and its products away from it, which is regulated by convection. The analysis of the effects of convection and concentration of XII bound to the surface was the principal result of this work. Figure 3.29 shows the reactivity of a surface to the intrinsic coagulation pathway. The presence of regions where reactivity does not vary with adsorbed XII suggests that a less affine material surface would not improve blood compatibility. However, full conversion is attained only over a relatively narrow intermediate range of mass transfer and shear rates. Moreover, changes in flow regime would induce large changes in blood compatibility, according to this model. According to the results of this model, even a highly biocompatible biomaterial would be highly thrombogenic at medium to low transport regimes. This conclusion is consistent with current techno-

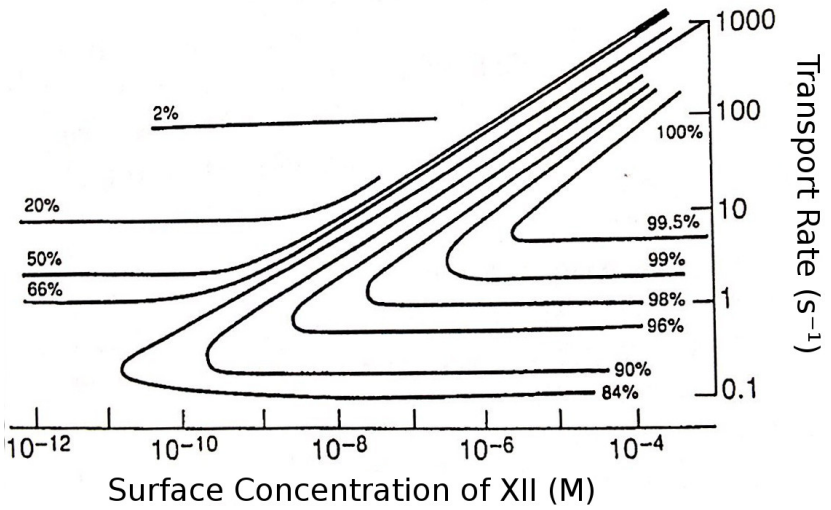

Fig. 3.29: Contour map of XI activation according to the surface model of Gregory and Basmadjian (1994) [91].

logical inability of producing a completely inert blood contacting material [23].

Zarnitsina *et al.*[5] (1996) modelled [240] and analysed [241] a mathematical model of the intrinsic pathway based on empirical data of the coagulation kinetics. The model was comprised of 23 kinetic equations describing the dynamics of activation of 19 different species, including the inhibitors activated protein C (APC) and antithrombin III (ATIII). They also considered the concentration of calcium ions as a regulator for the assembly of tenase and prothrombinase complexes. The diffusion of soluble species was considered in order to analyse the extent of fibrin formed in the direction perpendicular to the material surface. Similarly to the work of Gregory and Basmadjian (1994) [91], the model of Zarnitsina *et al.* showed a threshold dynamics of coagulation. The concentration of generated thrombin (IIa) remained minimal, when factor XIa activation was subthreshold. In contrast, overthreshold levels of XIa, the concentration of IIa explosively increased and then abruptly decreased. With respect to free calcium concentration, the system also behaved in a threshold manner, because it limited the formation of tenase and prothrombinase. The simulations were in good

[5]group leaded by Dr. Fazly Ataullkhanov, Russian Academy of Medical Sciences, Russia.

agreement with experimentally recorded kinetics of IIa activation at different concentrations of free calcium. Analysis of spatial dynamics of coagulation over the surface where XIa activation takes place showed that if activation exceeded the threshold level at a certain point, the concentration wave of IIa arises and propagates at a high speed from the activation zone. The characteristics of this wave depended primarily on the activity of the feedback loops. The positive feedback loops of the intrinsic pathway (autoactivation of factor X or activation of factor XI by IIa) had potential for unlimiting the propagation of the thrombin wave. On the other hand, the negative feedback loop, with increasing activity of activated protein C, caused oscillating regimes to the thrombin wave. A first strong thrombin wave was followed by several secondary waves, whose amplitudes increased as they approached the periphery of the clot, consolidating its surface layer. Later, Zarnitsina *et al.* (2001) [239] analysed the dynamics of this cyclic reaction-diffusion system causing that wave pattern of fibrin production at the clot periphery. They showed that this system was able to display different dynamic behaviours depending on a given set of parameters. With parameters obtained experimentally, the reaction-diffusion model behaved as described before. However, with other given parameters, the same model can produce a pulse which either stops running at a certain distance from the excitation point, or it reaches the boundaries as an autowave. Moreover, there is a parameter range where the pulse does not disappear after stopping and persists stationary.

Similar to Nesheim *et al.* (1984) [162], who demonstrated the kinetic relation of phospholipid vesicle surface are in the coagulation cascade, Guo *et al.* (2006) [93] showed the direct relation of biomaterial surface to blood clotting rate. Guo *et al.* produced a kinetic model of the intrinsic pathway, where the activation of factor XII was limited by surface area available for XII and kallikrein (K) deposition on the biomaterial. They correlated the mathematical model with experiments, showing the cascade could not be triggered by contaminating traces of XIIa, but rather only by the

autoactivation of XIIa on the surface, which is amplified by adsorbed K.

3.3.4 Spatially Inhomogeneous Models

Spatial heterogeneity is a complicating aspect of coagulation *in vivo*. While the concentration of many metabolic species is homogeneous in space and, therefore, they could be described by ordinary differential equations (ODEs), blood coagulation is initiated at specific sites, from where it propagates. Clotting is normally initiated on a surface, by either extrinsic or intrinsic pathways, before soluble activated factors are produced and transported to proximities. Besides producing fibrin, which forms a gel in proximity of the active surface, soluble thrombin is a strong platelet activator. Both platelets and coagulation proteins have to be convected to location of harm to which they attach, thus depleting their overall concentration in the bulk of blood. Blood flow controls platelet fluxes, delivery and removal of coagulation factors, adhesive bonding, and von Willebrand factor conformation. The transport of platelets and proteins in blood is strongly influenced by the motion of erythrocytes (RBCs). In certain conditions (such as in sharp expansions, bifurcations and small vessels) RBCs separate, forming RBC-free regions into which platelets and WBCs are pushed by packed RBCs. Furthermore, motion and rotation of RBCs perturb the plasma, which increases the observed diffusivity of species and cells in flowing blood (see Section 3.1.6). This augmented diffusivity perceived in blood is directly proportional to the shear rate. Shear rate is highest at the walls and edges of sharp expansion, where thrombi are normally found. Therefore, a correct representation of coagulation should use partial differential equations (PDEs) and their solution in a two- or three-dimensional region. Flow should, thus, be solved by the Navier-Stokes equation (Eq. 3.7), and spatial distribution of species, such as platelets and coagulation factors, should be solved by the transport equation (Eq. 3.1), whose source term consists of reaction rates. Haemorheological effects should be considered depending on the case. Such multi-physical spatio-temporal

models have emerged recently, in order to combine platelet function and coagulation kinetics into complete physics-based descriptions of thrombosis under flow.

At this stage, investigators are beginning to consider multi-physical spatio-temporal models to effectively capture the growth of clots. Two approaches have been used to tackle the multi-physics of thrombosis: top-down (continuous methods) and bottom-up (particle-based methods) [157]. Continuous methods are computationally cheaper compared to particle-based methods, because their results reflect the average flow and reactions of fields (examples in Fig. 3.30), whereas the results of particle-based methods would depend on the position of individual particles on space and time (examples in Fig. 3.31). Particle-based methods resolve the fate of each cell, including it's kinematics, activation level, it's interaction with chemicals, and it's potential to aggregate. A particle-based method applied to simulate a non-linear system can yield a vast variability of fates, depending on the initial conditions. Some of these fates could not possibly be predicted by a continuous method, which should resolve the average fate of the system as a whole, disregarding individual cells. Because top-down models are cheaper and more capable of replicating the average outcome of experiments, they are potentially more suitable as an engineering tool for assessing blood compatibility of medical devices. On the other hand, particle-based methods are potentially more suitable for testing different biophysical mechanisms of thrombosis in a theoretical perspective, because the state of the various cells can be controlled individually.

Sorensen *et al.* (1999) [203, 204] were the first to formulate a continuous model incorporating spatial effects to describe convection, diffusion and reaction effects of inhomogeneous distribution of species. In the first article, Sorensen (1999a) *et al.* [203] developed a 2-D finite volume (FV) model of platelet deposition and activation in flowing blood. The model comprised of a series of transport equations (Eq. 3.1) for resting (RP) and activated platelets (AP), activation agonists released by APs, prothrombin (II), thrombin (IIa), and antithrombin II (ATIII). The transport equation for platelets

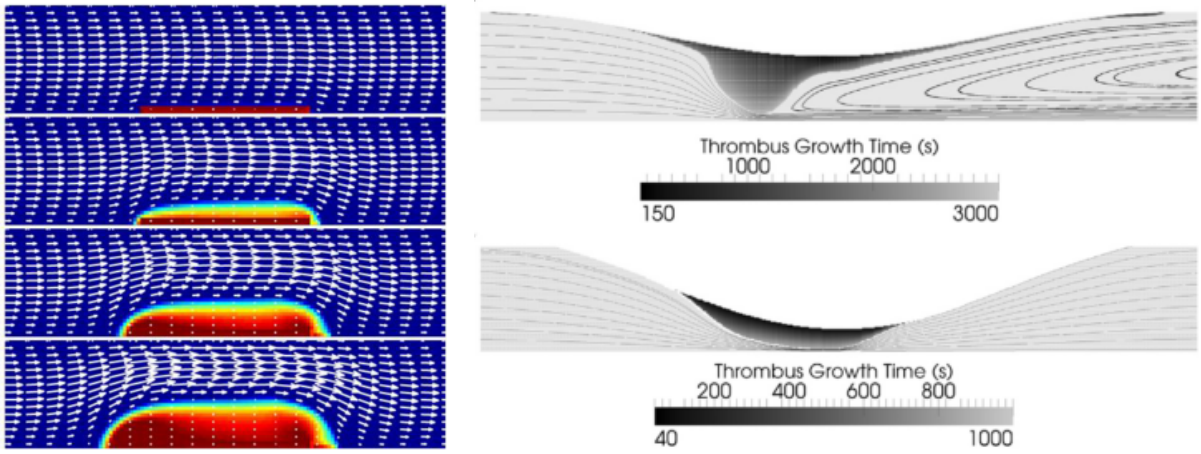

(a) Finite difference method (FDM) [142].

(b) Finite volume method (FVM) [20].

Fig. 3.30: Thrombosis simulated by different continuous methods.

simulated platelet-surface and platelet-platelet adhesion. Platelet activation rate was calculated by a weighted linear combination of agonist concentrations (Eqs. 3.69 and 3.70). The agonists of activation were: IIa, and a set of non-specified agonists either released or synthesised by APs. Thrombin activation was dependent of the anionic surface of the phospholipid membrane of APs, and thrombin inhibition was dependent of ATIII catalysed by heparin.

In the second article, Sorensen *et al.* (1999b) [204] fitted this model with experimental data, after estimating four non-measured parameters: shear-enhanced platelet diffusivity, and the rate constants for platelet-platelet aggregation and for attachment of both RP and AP to a surface wall. These parameters were estimated for platelet deposition onto a collagen substrate inside a simple rectangular microchannel. The samples consisted of whole blood, in both the presence and absence of thrombin. The fitted parameters were used to simulate similar test cases from the literature for parallel-plate Poiseuille flow over collagen at both higher and lower wall shear rates, and in the presence of various anticoagulants. The predicted values agreed well with the experimental results in the literature, where the anticoagulant was heparin. However, the

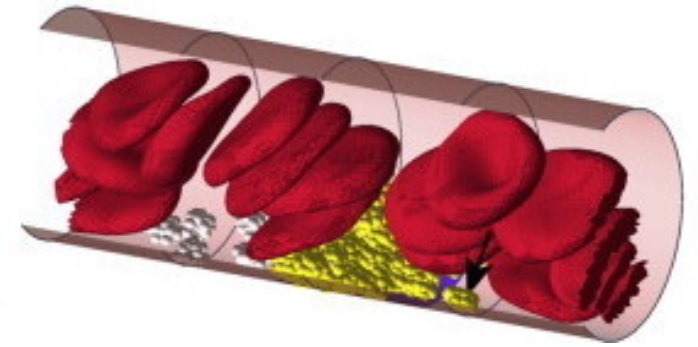

(a) Moving particle semi-implicit (MPS) method [118].

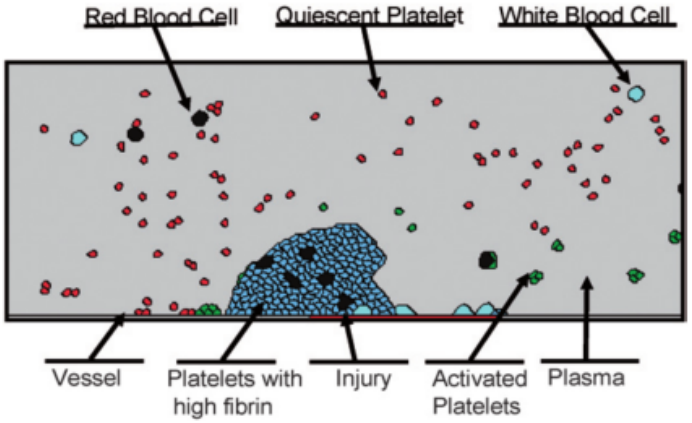

(b) Cellular Potts model (CPM) [237].

Fig. 3.31: Thrombosis simulated by different particle-based methods. Images reproduced from respective references.

model could not be validated for citrate.

Anand *et al.* (2003) [7] developed a complex PDE model coupling multiple interaction mechanisms controlling the formation and dissolution of clots. The model included mechanisms involving platelets, the coagulation system (with pro- and anti-coagulation species), fibrinolysis, flow, and the rheologies of blood and thrombus. The same shear-thinning viscoelastic model [9] was applied for the rheology of both blood and thrombus, however the thrombus viscosity was 16 times larger than the blood viscosity. The evolution of a 1-D PDE was solved in time for a set of boundary conditions using the Petrov–Galerkin method. Later, the same authors [8] updated the

model and applied it to simulate two clinically relevant hypercoagulable states, caused by deficiency of either antithrombin III or protein C. They validated the model by comparing it with published experimental data, using the assumption of steady state flow condition.

Shibeko *et al.* (2010) [196] incorporated both the reaction and convective transport of 28 coagulation species (including anticoagulation) with the finite difference method (FDM). They simulated the flow of platelet free plasma in a microchannel with a patch of collagen on one of its walls. The objective of the study was to analyse the effect of flow on the growth of a fibrin clot, from the time between TF exposure and the clot appearance. The simulations demonstrated that clotting is inhibited by flow, because it removes factor Xa from the site of vascular damage, which prevents the activation of VIIa, and, thus, the formation of the extrinsic tenase TF-VIIa. This inhibition was strongly non-linear, being milder within a certain range of flow rates, but being totally efficient in preventing fibrin coagulation at higher shear rates. The authors speculated that this switching off of the extrinsic pathway can serve to prevent uncontrolled spreading of procoagulation factors by flow throughout the vasculature. However, in whole blood, platelets adhere to collagen, which forms a porous plug on the damaged surface, where the factors of the extrinsic pathway become sheltered.

Leiderman and Fogelson (2011) [142] developed the first spatial-temporal mathematical model of platelet aggregation and blood coagulation under flow which included the coagulation system, chemical activation and deposition of blood platelets, as well as the two-way interaction between the fluid dynamics and the growing platelet mass. Figure 3.30a shows an example of simulation of thrombus growth performed with the model of Leideran and Fogelson. For this model, Leiderman and Fogelson introduced the reaction rates of Kuharsky and Fogelson (2001)[134] (commented in Sec. 3.3) as the source terms of a set of transport equations, which was solved by the finite difference method (FDM) in 2-D. The coupling of flow and thrombosis happen in one way

with near-wall enhanced platelet concentration and diffusion, and in the other way with the porous nature of the platelet aggregate. The higher convection rate caused higher rates of platelet to surface adhesion and platelet to platelet aggregation. As aggregation grew, the space inside it became porous, which decreased the transport of coagulation enzymes, and affected the growth of the thrombus at different stages and spatial locations.

Jordan and Chaikof (2011) [114] attempted to evaluate the importance of the spatial distribution of tissue factor (TF) and activated protein C (APC) to regulate the production of thrombin (IIa) in a microchannel. In contrast to the work of Leiderman and Fogelson, this transport-reaction model, simulated by the finite element method (FEM), lacked the effects of platelets and RBCs to control thrombus formation and growth. However, in the simulations of Jordan and Chaikof, there were prothrombotic surface patches, representing injuries, interspersed between antithrobotic patches, representing unharmed endothelium. On prothrombotic surfaces, TF activated the extrinsic pathway, whereas on the antithrobotic surfaces, the thrombomodulin (TM) complex with IIa (TM-IIa) activated APC. Therefore, the TF-coated surfaces produced a plume of IIa, whose size depended on injury length and flow rate. The relationship between the magnitude of the effective prothrombotic plume and the interval distance between TF sites dictated the net response of the system. Multiple TF sites, which individually failed to activate the coagulation pathway, were able to interact in an additive manner to activate IIa. On the other hand, activation of APC due to TM, in the regions between TF sites, downregulated IIa activation at subsequent TF sites. Because the Jordan and Chaikof ignores the transport effects of platelets and RBCs, the validity of their results for a whole blood flow is highly questionable.

Bark and Ku (2013) [20] simulated the thrombus formation over a ruptured atherosclerotic plaque cap on stenotic vessels, using FEM (Fig. 3.30b). They used a similar approach to Leiderman and Fogelson (2011) [142], where the thrombus is modelled as

a porous medium. They applied the field potential near-wall excess model for platelets of Hund and Antaki (Eq. 3.33), but they assumed a similar distribution potential for the haematocrit, instead of simulating its dynamics with a mixed-phase model. Bark and Ku applied a local shear-dependent version Zydney and Colton's EDM (Eq. 3.40), although the original version of this EDM accounts the wall shear rate $\dot{\gamma}_w$ instead of local shear rate $\dot{\gamma}$. Platelet adhesion was modelled as first order kinetics (Table 3.4) with a fixed rate constant, where activation occurred due to contact with either the atherosclerotic plaque cap or the porous thrombus. The porosity grew with the local volume fraction of aggregated platelets, and it completely occluded the element cell once the volume fraction got over 80%. The results indicated that thrombus growth rates are limited by platelet transport to the wall for shear rates up to $6000\,\mathrm{s}^{-1}$. Above $7000\,\mathrm{s}^{-1}$, the thrombus growth rate was likely limited by the binding kinetic rate constant. Both the thrombus locations and occlusion times obtained by the simulations correlated with experimental observation obtained with similar conditions.

3.4 Modelling SIPA

This section introduces the current development of the mathematical modelling of SIPA. More details are thoughtfully presented in Chapter 4, where a more sophisticated model for SIPA is proposed and analysed.

Platelet aggregation can be simulated either by particle dynamics or by statistical mechanics [157]. In particle dynamics, the velocities and positions of a group of randomly distributed platelets are integrated in a flow field; collisions occur where positions occupied by two particles coincide. This method yields more details of the microscopic level, but it is computationally very expensive when too many particles have to be included in the simulation. In a statistical mechanics method, the particles are considered uniformly distributed inside a control volume. The many individual

probabilities of collision and aggregation can be averaged by the central limit theorem (CLT) of statistics. The CLT states that for a sufficiently large number of iterations of independent random variables, the system is approximated by a normal distribution, whose variance decreases with the number of random variables. Hence, for a large number of particles, the state of each individual particle can be averaged into a physical state of the system as a whole, where state transitions are formulated as rate equations [179].

In the statistical mechanics approach, the colloid particle population is distributed by mass (or size) in a cluster mass distribution (CMD). The CMD evolves according to a population balance equation (PBE) which satisfies the principle of mass conservation. Smoluchowski (1916, 1917) was the first to apply statistical mechanics for aggregation of colloid particles [222, 223]. However, in processes where hydrodynamic forces are dominant, fragmentation may occur. Simultaneous aggregation and fragmentation by fluid shear is encountered in a number of processes, such as polymerization, emulsification and waste-water treatment [22]. Blatz and Tobolsky (1945) were the first to solve a reversible PBE for a polymerization process [31]. A breakup PBE for colloid aggregates was formulated by Pandya and Spielman (1982, 1983) [168, 169] based on the experiments conducted by Kao and Mason (1975) [119]. Aggregate breakup occurs by two mechanisms: erosion and splitting. Erosion is the detachment of small particles from an aggregates's surface, and splitting is the breakup in pieces of size comparable to the parent aggregate's. Both these mechanisms have been observed in platelet aggregates [161].

Huang and Hellums (1993) are the only researchers to date to employ a PBE including the effects of both aggregation and breakup for platelets. In a series of three papers, they analysed the PBE dynamics [102], obtained experimental parameters [103], and tested the system reversibility under varying shear stresses [104]. The calculated aggregation efficiency was so low that Huang and Hellums argued that breakup

need not be modeled [104]. However, the complete PBE, with breakup as well as aggregation, is expected to be more realistic than the aggregation-only version because it naturally predicts steady states, whereas the aggregation-only PBE can only reach steady state when all primary particles are contained in a single cluster. Furthermore, the experimental CMDs obtained by these authors were bimodal, contrary to what is mathematically expected by either the aggregation-only or the aggregation-breakup PBE at steady state. This may have occurred because they classified the aggregates by size, but assumed a fixed void fraction, within the porous aggregates, independent of the aggregate size. Yet, when measuring the aggregate size, Huang and Hellums used a Coulter counter without correcting the void fraction. The Coulter counter detects the volume of primary particles in the aggregates, which is lower than the apparent volume of porous aggregates.

Other experimental studies on SIPA have applied two-body collision theory to calculate the aggregation efficiency of freshly activated platelets [42, 26, 236, 80]. In this approach, experimental data is correlated with the theoretical aggregation rate of free platelet to platelet, but it ignores the aggregation of free platelets to aggregates and of aggregates to aggregates. The two-body collision model is a simplified version of the Smoluchowski coagulation equation (Eq. 4.15) in which only aggregation between free platelets is considered, but aggregation between free platelets and platelet aggregates is not. Another problem with the two-body collision model is that its theoretical steady state does not correspond with the experimental data. In contrast, the aggregation-breakup PBE is more general than the two-body collision model, and is theoretically capable of representing the experimental steady-state condition.

3.4.1 Two-Body Collision Model

The two-body collision model states the inital rate by which the concentration of free platelets C aggregate under shear rate G. It is given by

$$\frac{dC}{dt} = -\eta \, \frac{32}{3} \, G \, R_p \, C^2 \ , \tag{3.78}$$

where R_p is the mean radius of platelets, $\frac{32}{3} \, G \, R_p \, C^2$ is the platelet collision ratio, and η is the empirical parameter called aggregation efficiency. Aggregation efficiency accounts the ratio of aggregation events to the shear induced platelet collision events. Collisions between clusters, and between free platelets and clusters, are ignored in this approach. The level of platelet aggregation is assessed by comparing the initial ($C(t=0) \equiv C_p$) and current concentration of free platelets ($C(t)$). This model coincides with the present aggregation-PBE model when the system is controlled by the aggregation rate alone, and it is not very accurate when either shear rate is large or a steady state is reached. Without any limitation mechanism, aggregates would grow indefinitely.

In previous works, discrepancies between the measured and expected depletion of free platelets were attributed to a shear-dependent aggregation efficiency $\eta = \eta(G)$ [42, 26, 102, 103, 104, 236, 80]. Aggregation efficiency was believed to decrease with increasing shear rate because higher shear rates would result in shorter platelet-platelet interaction times than required for connecting membrane receptors [80]. Using this assumption, Bell *et al.* reported the aggregation efficiency dropping from $\eta = 0.26$ at $G = 41.9\,\mathrm{s}^{-1}$ to $\eta = 0.17$ at $G = 335\,\mathrm{s}^{-1}$, and further to negligible levels ($\eta < 0.001$) at $G = 1335\,\mathrm{s}^{-1}$ [26]. Xia and Frojmovic confirmed a similar trend and postulated an empirical relation for the shear-dependent aggregation efficiency [236]

$$\eta(G) = 59 \, G^{-1} \ . \tag{3.79}$$

Xia and Frojmovic [236] studied SIPA of human activated platelets in a rheometer under Couette flow. They presented their data in terms of the fraction of aggregated

platelets

$$PA(t) = 1 - \frac{C(t)}{C_p} \ . \tag{3.80}$$

Because their results showed an inverse-exponential trend, they assumed a first-order ODE approximation, and applied a curve fit to

$$PA(t) \approx PA_{\max}(1 - e^{-k\,t}) \ . \tag{3.81}$$

Finally, the experimental aggregation efficiency is obtained by comparing the derivatives of Eqs. 3.80 and 3.81 at $t = 0$,

$$\eta \approx \frac{PA_{\max}\,k}{\frac{32}{3}\,G\,R_p^3\,C_p} \ . \tag{3.82}$$

In Eq. 3.82, Xia and Frojmovic obtained the rate parameter k and steady-state parameter $PA_{\max}$ of Eq. 3.81 from a curve fit to the experimental data. Theoretically, $PA_{\max}$ should be equal to 1, according to the two-body collision model (Eq. 3.78) in Eq. 3.80. Yet, the authors could not force $PA_{\max} = 1$ to the curve fitting because the data had a steady-state PA in the range 0–1. This means that in the formulation of Eq. 3.79 the shear rate G could be influencing $PA_{\max}$ more than k. Moreover, in a first order ODE, like Eq. 3.81, parameter k is the inverse of the equation's characteristic time ($k = t_a^{-1}$). If the aggregation characteristic time is used in Eq. 3.81, the only parameter to be fitted would be $PA_{\max}$. Nevertheless, a steady-state PA in the range 0–1 would be theoretically correct if the aggregation-breakup PBE was considered.

3.5 Concluding Remarks

The complexity of blood rheology, in terms of how RBCs distribute themselves in the flow, has a great impact in the formation of thrombi. Platelets are much higher concentrated near walls of narrow vessels, because there RBCs aggregate and migrate away from the walls. This effect is even more significant in sudden widening of vessel

diameter, a feature that is common in biomedical devices. Furthermore, the flow of suspended RBCs augment the apparent diffusivity of species in blood, including platelets and WBCs. This effect is very important for platelets and WBCs to adhere to thrombotic surfaces. On thrombotic surfaces, a series of chemical reactions occur. The kinetics of the coagulation cascades have been modelled with sets of ODEs since the 1960's. Earlier, kinetic models of a few reactions were used to test the dynamic effects of negative and positive feed-back loops. Later, the complexity of these models grew in terms of both the number of reactions and species, which comprise more than 100 of each. Complex models also include the effects of platelets, surfaces, and transport of species. The most recent models of thrombosis, devised in the last 10 to 15 years, include the transport equation of those species in flowing medium. In this case, the spatio-temporal formation of thrombi is analysed, and the rheology of blood has been shown to play an important part. Finally, the current state of SIPA models is presented. Shear induced platelet aggregation is a mode of thrombogenesis that lack rigorous modelling in the literature, because it is normally not detected at the site of platelet activation, but far away downstream of it. Therefore, the next chapters will focus in the mathematical modelling and simulation of SIPA. In Chapter 4, a PBE model for platelet aggregation and breakup is explained in detail, along with the its dynamical aspects clearified by computer simulation. In Chapter 5, the aggregation and breakup PBE model is extended with the transport of aggregates in complex flows obtained from computational fluid dynamics (CFD). Lastly, a protocol for obtaining experimental data of SIPA in real time is presented in Chapter 6.

Chapter 4

Analysis of Shear Induced Platelet Aggregation and Breakup

One aspect that is normally neglected in the mathematical models of thrombosis is the aggregation of activated platelets in the bulk, away from a thrombotic surface. Therefore, we (Hellmuth, Bruzzi and Quinlan, 2015) [97] have developed and analysed a comprehensive model of the dynamics of shear-induced platelet aggregation (SIPA). This chapter is an extended version of the published article. In our model, shear rate regulates a mass-conservative population balance equation (PBE) which computes the aggregation and disaggregation of platelets in a cluster mass distribution (CMD). Aggregation is modeled by the Smoluchowski coagulation equation, and disaggregation is incorporated using the aggregate breakup model of Pandya and Spielman. Previous experimental data for SIPA have been correlated with a special case of this model where only the two-body collision of free platelets was considered. However, the two-body collision theory is oblivious to the steady-state condition, and it required the use of a shear-dependent aggregation efficiency parameter to fit it to experimental data. Our method not only predicts steady states but also correlates with literature data without employing a shear-dependent aggregation efficiency.

4.1 Platelet Aggregation

From the point of view of chemistry, platelets are colloid particles that may clump together at specific conditions to form larger particles. A single colloid particle is known as a singlet and a larger particle is known either as a multiplet or as an aggregate. There are many mechanisms that can clump colloids together, such as the ones depicted in Fig. 4.1. IUPAC classifies each mechanism by different names [200]:

- *Agglomeration* is the reversible weak adhesion of particles.
- *Aggregation* is the interconnection of particles by chemical bouds.
- *Coagulation* is the irreversible formation of aggregates in which particles are in physical contact.
- *Coalescence* is the disappearance of the boundary between two particles in contact followed by changes of shape leading to a reduction of the total surface area.
- *Flocculation* is the reversible formation of aggregates in which the particles are not in physical contact.

The IUPAC definition is used in this thesis in the sense that activated platelets may aggregate using specific proteins as bridges between membrane receptors, and they may coagulate once the fibrin mesh is polymerised around them.

Platelet dynamics can be simulated either by particle dynamics or by a stochastic approach. The first is more efficient at a microscopic level, but it is computationally expensive when too many particles have to be included in the simulation. This thesis will focus on the former approach, where the many events can be averaged by the central limit theorem (CLT) of statistics [179]. The CLT states that for a sufficiently large number of iterates of independent random variables, the arithmetic mean will be approximately normally distributed, whose variance decreases with the number of

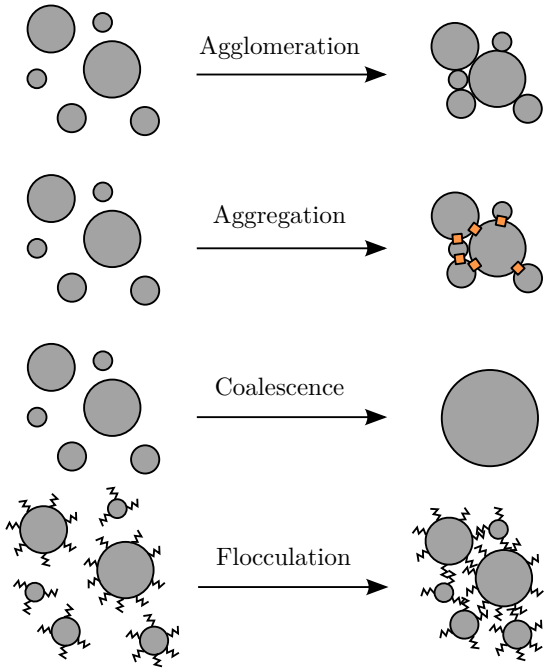

Fig. 4.1: IUPAC definitions for physical combination of colloidal particles.

random variables. Hence, for a large number of particles, the physical conditions can accurately be summarised into physical states. These states are here called aggregate classes.

4.1.1 Cluster Mass Distribution

The cluster mass distribution (CMD) is a distribution of concentrations of clusters of a certain colloid. The CMD can be modelled as a continuous function $C(m,t)$, where m is mass and t is time, or as discrete function $C_i(w_i,t)$, where w_i is the number of primary particles (or monomers) in the cluster of class i, see Fig. 4.2a. The particles are assumed to be uniformly distributed in a control volume V. The continuous CMD is more general than the discrete CMD, because it can consider the variation in monomer sizes. Experimental measurements will give continuous distributions. However, the discrete CMD is more tractable in terms of numerical integration. As shown by Fig.

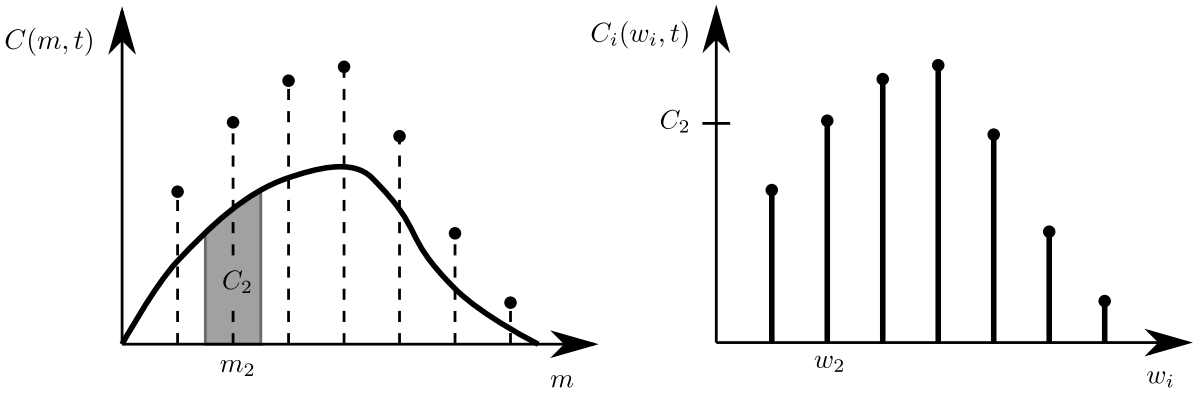

(a) Continuous CMD. (b) Discrete CMD.

Fig. 4.2: Cluster mass distribution.

4.2, the number of particles lumped around the mass point m_i is obtained by the integration

$$C_i(w_i,t) = \int_{\frac{w_{(i-1)}+w_i}{2}m_1}^{\frac{w_i+w_{(i+1)}}{2}m_1} C(m,t)\,dm \ , \tag{4.1}$$

where m_1 is the mass of the monomer. In a special case, the primary particle can be considered as the first mass point, when it is sufficiently large in comparison to the formed clusters. The total mass M of the colloid, a conserved quantity, is thus

$$\int_0^\infty C(m,t)\,m\,dm = m_1 \sum_{i=1}^{n} C_i w_i = M \ , \quad \forall t \in \mathbb{R}^+ \ . \tag{4.2}$$

From Eq. 4.2 it is possible to obtain the total concentration of monomers in the system, regardless if they are aggregated or not. The total concentration of monomers (e.g. platelets)

$$C_p \equiv C_1 = \sum_{i=1}^{n} C_i w_i = \frac{M}{m_1} \ , \quad \forall t \in \mathbb{R}^+ \tag{4.3}$$

is a conservative quantity.

Another useful distribution is monomer population distribution, which is here called platelet population distribution (PPD),

$$\tilde{C}_i = \frac{C_i\,w_i}{C_p} \ . \tag{4.4}$$

The PPD represents how proportionally populated by monomers each cluster class is.

4.1.2 Integral Quantities of the CMD

Integral quantities are single values which summarize some aspects of the state of the distribution. The moments of the CMD are defined as

$$M_j(t) := \frac{1}{M} \int_0^\infty C(m,t)\, m^j \, dm \ , \tag{4.5}$$

for the continuous case, or as

$$M_j(t) := \sum_{i=1}^{n} C_i(w_i,t)\, w_i^j \ , \tag{4.6}$$

for the discrete case, where the index j represents the order of the moment, and M without subscript is the total mass obtained by Eq. 4.2. The zeroth moment M_0 is the total number of particles in the suspension. The first moment M_1 represents the initial total number of primary particles in the suspension. The second moment M_2 is a measure of aggregation level. It follows that the mean number of monomers (e.g. platelets) per cluster is

$$\langle w \rangle(t) = \frac{M_1(t)}{M_0(t)} \ . \tag{4.7}$$

Some experimental techniques observe population averaged quantities of colloid mixtures. They are non-invasive techniques such as light scattering and sound spectroscopy. In light scattering, the intensity of the scattered light is measured as a function of the scattering angle with respect to the incident light beam. The zero angle intensity is the intensity of the scattered light extrapolated to a scattering angle of zero,

$$I_0 = I(\theta = 0, t) = C_{\text{inst}} \frac{M_2(t)}{M_1(t)} \ , \tag{4.8}$$

where θ is the scattering angle, and C_{inst} is a constant of proportionality [140, 201]. Another integral quantity measurable by light scattering is the root mean square radius of gyration

$$\langle R \rangle_{rms}(t) = \sqrt{\frac{\sum_{i=1}^{\infty} C_i(t)\, w_i^2\, R_i^2}{\sum_{i=1}^{n} C_i(t)\, w_i^2}} = R_p \sqrt{\frac{M_{2-2/D_F}}{M_2(t)}} \ , \tag{4.9}$$

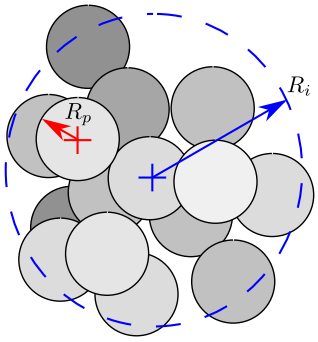

Fig. 4.3: Colloid aggregate and its radius of gyration.

where R_p is the mean radius of the monomer (e.g. platelet). The radius of gyration of a colloid cluster is defined in Eq. 4.10.

4.1.3 Fractal Structure of Aggregates

Colloid aggregates are ramified non-dense clusters with self-similar characteristics typical of a fractal structure [202]. The radius of gyration of a discrete aggregate cluster formed by w_i primary particles (e.g. platelets) of radius R_p is calculated by

$$R_i = w_i^{1/D_F} R_p \ . \tag{4.10}$$

In Eq. 4.10, D_F is the fractal dimension of the structure, which is lower than the Euclidian dimension $D_E = 3$ (i.e. $0 < D_F < D_E$) [6, p. 8]. The structure consists of fractal branches with voids between themselves. The structure grows only at the edges, where other colloids or clusters are attached to. Therefore, the radius of gyration of a fractal ball, see Fig. 4.3, is larger than the radius of a sphere of the same volume.

In a system where the motion of colloid particles is primarily Brownian, the fractal dimension of the aggregates is $D_F \approx 1.8$, if aggregation is limited by diffusion, or $D_F \approx 2.1$, if it is limited by chemical reaction [144]. The fractal dimension $D_F = 2.2$ for platelet aggregates forming under Brownian diffusion was measured by laser light scattering technique [50], which corrresponds to the magnitude of 2.0–2.5 predicted for

reaction limited aggregation by the light scattering theory [139]. The fractal dimension for SIPA could be higher because breakup and restructuring may make the aggregate more compact [206]. However, there is no experimental data reporting the fractal dimension of SIPA. Therefore, the $D_F = 2.2$ is used as a lower bound reference in this work.

The mean platelet radius R_p can be calculated from either the radius of the mean platelet volume (i.e. $\langle R\rangle = \sqrt[3]{3/4\pi\,\langle V\rangle}$), or the geometric mean of the mean discoid radii of a platelet (i.e. $\langle R\rangle = \sqrt[3]{R_{\min}R_{\max}^2}$). The volume distribution of healthy platelets resembles a gamma distribution, with $V = \langle V\rangle \pm \sigma_V = (6.6 \pm 2.1)1.16\,\mu\text{m}$ [171]. Nonactivated platelets are 99% discoid in shape, with the smallest and largest radii 0.6 µm and 1.6 µm, respectively [69]. Using either of these methods, $R_p \equiv \langle R\rangle \pm \sigma_R = (1.16 \pm 0.25)\,\mu\text{m}$. Although the size distribution of a single platelet is not normal, but log-normal, the size distribution for aggregates converges to a normal distribution due to the central limit theorem (CLT) of statistics. The CLT also yields greater accuracy for the radius of gyration of larger clusters because the variance of the platelet radius s_R^2 is normalized by the number of platelets in the cluster ($s_R^2 \to \sigma_R^2/w_i$). Figure 4.4 presents Eq. 4.10 for $R_1 = (1.16 \pm 0.25)\,\mu\text{m}$ and $D_F = 2.2$ inside a confidence band.

Equation 4.10 takes the voids between the fractal branches into account, so the radius of gyration of a fractal ball is larger than the radius of a sphere of the same material volume. The void fraction is

$$\phi_i = \frac{\tilde{V}_i - V_i}{\tilde{V}_i} = 1 - w_i^{1-3/D_F} = 1 - \left(\frac{R_i}{R_p}\right)^{D_F-3}\ , \tag{4.11}$$

where $\tilde{V}_i = \frac{4}{3}\pi R_i^3$ is the apparent volume, and $V_i = w_i\frac{4}{3}\pi R_p^3$ is the volume occupied by particles. The fractal structure naturally produces a void fraction that grows alongside with its size, as shown in Fig. 4.5. This has been observed in platelet aggregates, where the maximum void fraction ranged from 60 to 90% [37].

In the previous work of Huang and Hellums (1993) [102, 103, 104], platelets were assumed to be coalescing instead of aggregating. Coalescence is the fusion of initially

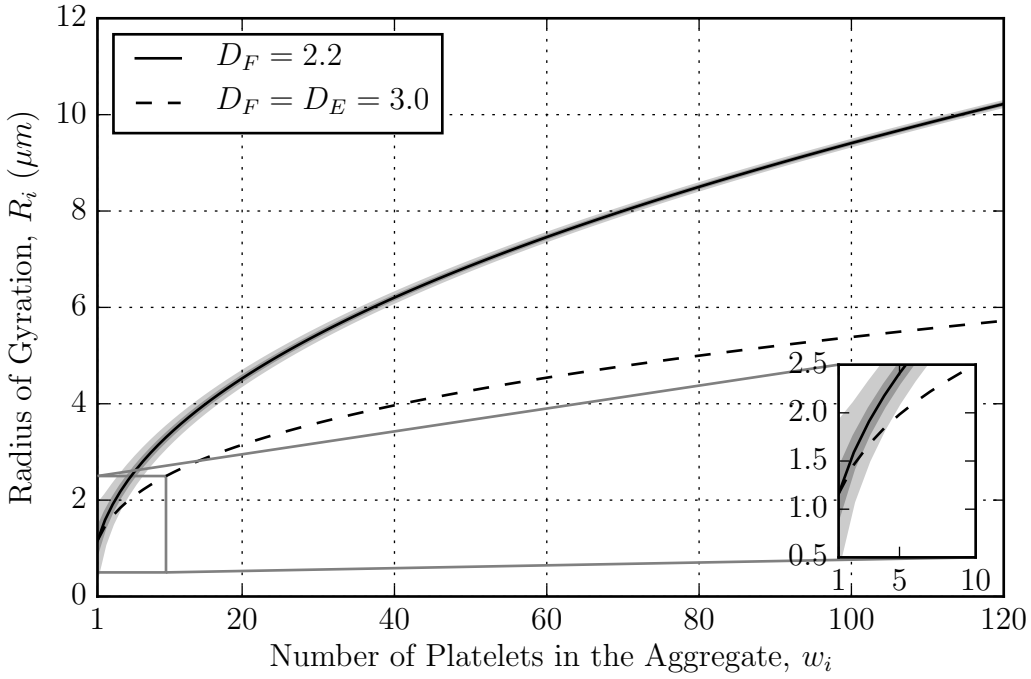

Fig. 4.4: Radius of gyration for aggregate clusters whose primary particle radius is $R_1 = (1.16 \pm 0.25)\,\mu\text{m}$. The continuous line shows particles of fractal dimension $D_F = 2.2$, enclosed by confidence bands of 68.3% ($\pm 1\sigma_{R_i}$, dark grey) and 99.7% ($\pm 3\sigma_{R_i}$, light grey). Comparatively, the dashed line shows particles of Euclidian dimension $D_E = 3$.

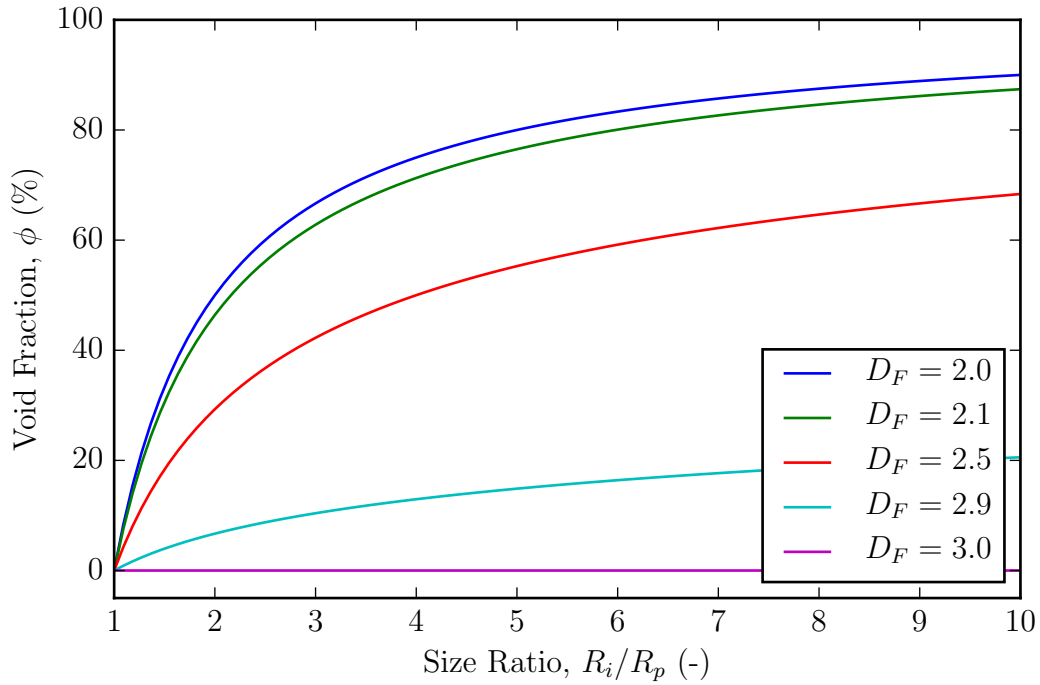

Fig. 4.5: Aggregate void fraction (ϕ) to size ratio (R_i/R_p) for different fractal dimensions (D_F).

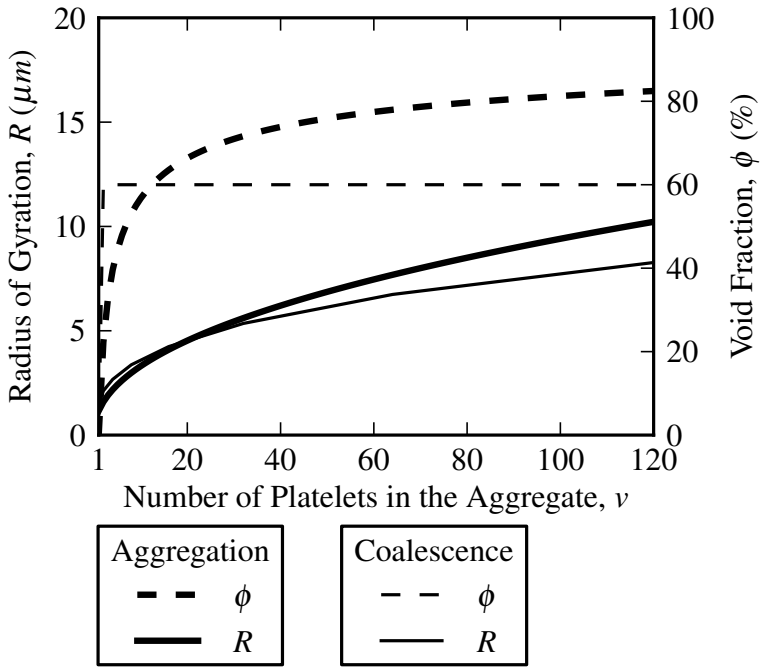

Fig. 4.6: Radius of gyration (solid lines) and void fraction of aggregates (dashed lines). The thick lines refer to $R_p = 1.16\,\mu\text{m}$ and $D_F = 2.2$ (aggregation). The thin lines to $R_p = 1.4\,\mu\text{m}$, $D_F \equiv D_E = 3.0$ (coalescence), and a fixed void fraction of 60% for $w \geq 2$, as assumed by Huang and Hellums [102, 103, 104].

distinct particles, followed by changes of shape leading to a reduction of the total surface area (e.g., fusion of liquid drops). On the other hand, aggregation is the interconnection of particles by chemical bonds [200]. Huang and Hellums scaled the cluster sizes with the Euclidian dimension, which characterizes coalescence instead of aggregation. Because the Euclidian dimension yields compact structures, they had to correct the size of their aggregates with a constant void fraction, which overestimates and underestimates the void fraction of smaller and larger aggregates, respectively. The aggregate size and void fraction obtained by both the fractal theory and constant void fraction are compared in Fig. 4.6.

4.1.4 Population Balance Equation

The population balance equation (PBE) is a conservation equation for a compound distributed among certain species [101]. The PBE is formulated as a first order integro-differential equation of the CMD, whose right hand side describes the PBE's laws of evolution. The PBE is an integro-differential equation because the CMD's time derivative is equal to integrations over the CMD space. In the case of an aggregation-breakup system, the PBE for cluster size class i is

$$\frac{\partial C_i}{\partial t} = A_i + B_i \ , \tag{4.12}$$

where $A_i = A_i(\boldsymbol{C}, \boldsymbol{w})$ and $B_i = B_i(\boldsymbol{C}, \boldsymbol{w})$ are the aggregation and breakup rates, respectively. The aggregation-breakup PBE is reversible, which means that aggregates can breakup and reaggregate. The PBE is also mass-conservative, which means that platelets are not destroyed upon aggregate breakup. The steady state ($\frac{\partial C_i}{\partial t} = 0$) is the physical point where both the aggregation and breakup rates are in equilibrium. Blatz and Tobolsky (1945) [31] were the first to solve a PBE of the form of Eq. 4.12. In their case, it was a reversible polymerisation process. Recently, the same approach has been used to model and simulate the formation of fibrin fibres (coagulation) under flow [94].

4.1.5 Smoluchowski Coagulation Equation

The Smoluchowski coagulation equation describes colloidal particles clumping together forming larger particles. This equation is used in different fields of science to describe any of the clumping mechanisms previously mentioned, because they all have the same kinetics, as illustrated in Fig. 4.7.

Smoluchowski (1916) derived his coagulation equation from statistical physics [222, 223]. The Smoluchowski coagulation equation is formulated by the interaction between the different particle classes, as in Fig. 4.7. It is then used as the aggregation function

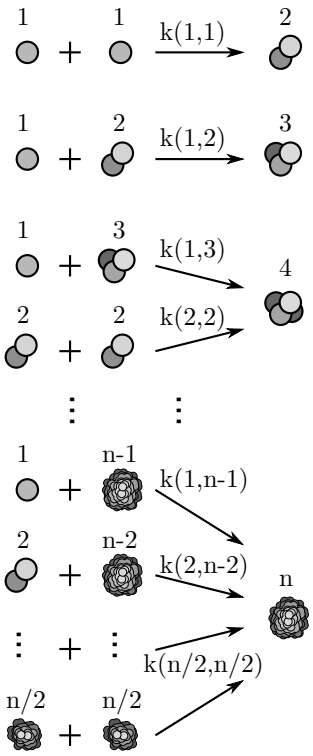

Fig. 4.7: Kinetics of the Smoluchowski Coagulation Equation for n aggregate classes.

of the PBE (Eq. 4.12),

$$A_i(\boldsymbol{R}, \boldsymbol{C}) = \frac{1}{2}\sum_{j=1}^{i-1} f_a(R_i - R_j, R_j) - \sum_{j=1}^{n} f_a(R_i, R_j) \tag{4.13a}$$

$$= \frac{1}{2}\sum_{j=1}^{i-1} k_a(R_i - R_j, R_j) C_{(i-j)} C_j - \sum_{j=1}^{n} k_a(R_i, R_j) C_i C_j \ , \tag{4.13b}$$

for $i, j = [1, ..., n] \in \mathbb{N}$. Aggregates of class i are formed by w_i primary particles (or monomers), and they have a radius of gyration (or size) R_i. The maximum n of the subsets i, j is arbitrary, which can be defined as $n = \infty$ in the extreme case, but usually the maximum chosen is the transition to gel state (gelation). In Eq. 4.13a, the function $f_a(R_i, R_j)$ denotes the aggregation rate at which particles of size R_i clump together with particles of size R_j.

The aggregation rates are second order rate functions (see Tab. 3.4), as shown

in the second version, Eq. 4.13b. The aggregation rate operator $k_a(R_i, R_j)$ is known as the coagulation kernel. The kernel functions are derived according to the physics involved in bringing particles in contact with each other. Smoluchowski derived kernel functions for spherical particles colliding due to Brownian motion (diffusion), external field forces (gravity, electrical fields, etc.), and velocity gradients [222]. Other kernel functions can be formulated for other situations, e.g. electrical charged particles or long-shaped particles.

Although collision rates $f_c(R_i, R_j)$ can be derived by statistical mechanics, not all collisions will result in aggregation. Aggregation depends on the balance of attraction and repulsion forces acting on the particles. Thus, there is an aggregation efficiency

$$\eta = \frac{f_a(R_i, R_j)}{f_c(R_i, R_j)} = \frac{k_a(R_i, R_j)}{k_c(R_i, R_j)} \tag{4.14}$$

that gives Eq. 4.13 in terms of collision rates

$$A_i(\boldsymbol{R}, \boldsymbol{C}) = \eta \left[\frac{1}{2} \sum_{j=1}^{i-1} k_c(R_i - R_j, R_j) C_{(i-j)} C_j - \sum_{j=1}^{n} k_c(R_i, R_j) C_i C_j \right] . \tag{4.15}$$

4.1.6 Derivation of Some Collision Kernels

Collision kernels are a measure of the volumetric collision rate between particles of class i and particles of class j. Taking a reference particle of class i placed on the origin of the spacial coordinates, there will be a flux

$$\boldsymbol{j}_{n_j} := C_j \, \boldsymbol{v}_{\text{rel}} = C_j \, (\boldsymbol{v}_j - \boldsymbol{v}_i) \tag{4.16}$$

of particles of class j coming towards it. The shocks occur at the distance $R_{ij} = R_i + R_j$ from the reference particle, where R_i and R_j are the particles' respective radii (see Fig. 4.8). Hence, the collision rate at a particle of class i is obtained by the integration of the flux $\boldsymbol{j}_{n_j}$ over the surface of the sphere of radius R_{ij},

$$\oint_{\text{sphere}} (-\boldsymbol{j}_{n_j} \cdot \hat{\boldsymbol{n}}) \, H(-\boldsymbol{v}_{rel} \cdot \hat{\boldsymbol{n}}) \, dS = -C_j \oint_{\text{sphere}} (\boldsymbol{v}_{\text{rel}} \cdot \hat{\boldsymbol{n}}) \, H(-\boldsymbol{j}_{n_j} \cdot \hat{\boldsymbol{n}}) \, dS \ , \tag{4.17}$$

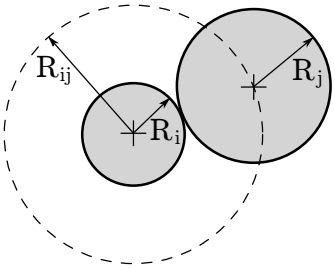

Fig. 4.8: Particles of radii R_i and R_j colliding at a distance R_{ij} $(= R_i + R_j)$.

where $\hat{\boldsymbol{n}}$ is the normal vector of the spherical surface, and

$$H(x) := \begin{cases} 0 & \text{, if } x < 0 \\ 1 & \text{, if } x \geq 0 \end{cases} \tag{4.18}$$

is the Heaviside step function. As the fluid is incompressible, the conservation of mass requires that net flow through a closed surface be a zero integral. Therefore, the Heaviside step function is necessary for integrating the influxes $(\boldsymbol{j}_{n_j} \cdot \hat{\boldsymbol{n}} < 0)$ solely, ignoring outfluxes, because they do not cause collisions.

To obtain the collision rate of all particles in a control volume, Eq. 4.17 is multiplied by the concentration C_i,

$$f_c(R_i, R_j, C_i, C_j) := -C_i C_j \oint_{\text{sphere}} (\boldsymbol{v}_{\text{rel}} \cdot \hat{\boldsymbol{n}})\, H(-\boldsymbol{v}_{rel} \cdot \hat{\boldsymbol{n}})\, dS \ . \tag{4.19}$$

Hence, the general collision kernel function is

$$k_c(R_i, R_j) := \frac{f_c(R_i, R_j, C_i, C_j)}{C_i C_j} = -\oint_{\text{sphere}} (\boldsymbol{v}_{\text{rel}} \cdot \hat{\boldsymbol{n}})\, H(-\boldsymbol{v}_{rel} \cdot \hat{\boldsymbol{n}})\, dS \ . \tag{4.20}$$

Because of the spherical shape of the particles, it is appropriate to consider a spherical coordinate system

$$\begin{cases} x = r\, cos\theta\, sin\phi \\ y = r\, sin\theta\, sin\phi \\ z = r\, cos\phi \end{cases} \text{, where } \begin{cases} r = \sqrt{x_1^2 + x_2^2 + x_3^2} \\ \theta = arctan(y/x) \\ \phi = arccos(z/r) \end{cases} . \tag{4.21}$$

The integration is performed over $r \equiv R_{ij}$, $\theta \in [0, 2\pi[$, $\phi \in [0, \pi[$. The normal vector of a sphere in Cartesian coordinates is

$$\hat{\boldsymbol{n}} \equiv \frac{\boldsymbol{r}}{\|\boldsymbol{r}\|} = sin\theta\, cos\phi\, \hat{\boldsymbol{e}}_x + sin\theta\, sin\phi\, \hat{\boldsymbol{e}}_y + cos\theta\, \hat{\boldsymbol{e}}_z \ . \tag{4.22}$$

Particle Collision Rate by Diffusion

Particle aggregation by diffusion is known as Brownian coagulation or perikinetic coagulation. Collisions occur when particles of class j moving randomly (Brownian motion) come to the distance R_{ij} from particles of class i. The influx of particles is defined by Fick's law of diffusion

$$\boldsymbol{j}_{n_j} = -D_j \frac{\partial C_j}{\partial r} = C_j \boldsymbol{v}_{rel} \ . \tag{4.23}$$

The diffusion of particles towards the reference sphere is given by the partial differential equation (PDE)

$$\frac{\partial C_j}{\partial t} = D_j \nabla^2 C = D_j \left(\frac{\partial^2 C_j}{\partial t^2} + \frac{2}{r} \frac{\partial C_j}{\partial r} \right), \tag{4.24}$$

where D_j is the diffusivity of particles j. The boundary conditions for Eq. 4.27 are illustrated in Fig. 4.9, and are defined by the Heaviside step function

$$\begin{cases} C_j = 0 & , \text{ for } r \leq R_{ij} \\ C_j = C_j & , \text{ for } r > R_{ij} \end{cases} \tag{4.25}$$

at $t = 0$. The time integration of Eq. 4.27 with these boundary conditions results in the concentration field

$$C_j(r,t) = C_j \left[1 - \frac{R_{12}}{r} + \frac{R_{12}}{r} \operatorname{erf}\left(\frac{r - R_{12}}{2\sqrt{Dt}} \right) \right] \ , \tag{4.26}$$

whose partial derivative in respect to coordinate r is

$$\frac{\partial C_j(r,t)}{\partial r} = C_j \left\{ \frac{R_{ij}}{r^2} \left[1 - \operatorname{erf}\left(\frac{r - R_{ij}}{2\sqrt{Dt}} \right) \right] + \frac{2R_{ij}}{r\sqrt{\pi Dt}} \exp\left(\frac{r - R_{ij}}{2\sqrt{Dt}} \right) \right\} \ . \tag{4.27}$$

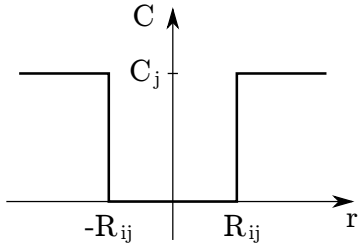

Fig. 4.9: Concentration of particles of class j around the reference particle at time $t = 0$.

The spatial derivative in Eq. 4.27 is applied to Eq. 4.23 to obtain the diffusion flux. In reality, the reference particle is not fixed, but diffusing itself similar to the other particles. Thus, the total diffusivity constant is the sum of each particle type diffusivity constant, $D_{ij} = D_i + D_j$. The diffusion flux (Eq. 4.23) is used to derive the diffusion collision kernel

$$\begin{aligned} k_d(R_i, R_j) &:= \oint_{\text{sphere}} \left[\frac{D_{ij}}{C_j} \frac{\partial}{\partial r} C_j(r = R_{ij}, t > 0)\, \hat{\boldsymbol{n}} \cdot \hat{\boldsymbol{n}} \right] H(\hat{\boldsymbol{n}} \cdot \hat{\boldsymbol{n}})\, dS \\ &= 4\pi\, R_{ij}^2\, \frac{C_j}{R_{ij}}\, \frac{D_{ij}}{C_j} \\ &= 4\pi (R_i + R_j)(D_i + D_j)\ . \end{aligned} \tag{4.28}$$

For collision by Brownian motion, the diffusion kernel (Eq. 4.28) can be written in terms of Brownian diffusivity model of Einstein and Smoluchowski (Eq. 3.38),

$$k_d(R_i, R_j) = \frac{2k_B T}{3\mu}(R_i + R_j)\left(\frac{1}{R_i} + \frac{1}{R_j}\right) = \frac{2k_B T}{3\mu}\frac{(R_i + R_j)^2}{R_i R_j}\ . \tag{4.29}$$

Collision Rate by Differential Sedimentation

The sedimentation velocities of particles dragged by a gravitational field are determined by their weights and sizes. Taking colloid cluster of i primary particles falling in a viscous fluid, its velocity is obtained by the force balance between the weight F_g

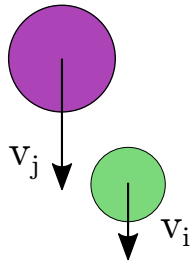

Fig. 4.10: Relative velocities of sedimenting particles.

and Stokes' drag force F_d,

$$F_g = F_d \quad \Rightarrow \quad (\rho_c - \rho_f)\, w_i \left(\frac{4\pi}{3} R_p^3\right) g = 6\pi\, \mu\, R_i\, v_i \quad \Leftrightarrow \quad v_i = \frac{2}{9} \frac{(\rho_c - \rho_f)\, g}{\mu} R_p^3 \frac{w_i}{R_i} \ , \tag{4.30}$$

where ρ_c and ρ_f are the densities of the colloid and the fluid, respectively; R_i and R_p are the radius of a cluster of class i and the radius of the primary particles, respectively; g is the gravitational acceleration, and μ is the viscosity of the fluid.

A cluster of w_j primary particles has a different velocity than a cluster of w_i primary particles. This creates a flux $\boldsymbol{j}_{n_j}$ of clusters of w_j primary particles towards the cluster of w_i primary particles, as illustrated in Fig 4.10. The relative flux of particles between clusters of class j and i is

$$\boldsymbol{j}_{n_j} = C_j (v_i - v_j) \hat{\boldsymbol{e}}_z = C_j \frac{2}{9} \frac{(\rho_c - \rho_f)\, g}{\mu} R_p^3 \left(\frac{w_i}{R_i} - \frac{w_j}{R_j}\right) \hat{\boldsymbol{e}}_z \ , \tag{4.31}$$

which is applied to Eq. 4.20 yields the sedimentation collision kernel

$$\begin{aligned} k_g(R_i, R_j, w_i, w_j) &:= \oint_{\text{sphere}} [-(v_i - v_j)\, \hat{\boldsymbol{e}}_z \cdot \hat{\boldsymbol{n}}]\, H[-(v_i - v_j)\, \hat{\boldsymbol{e}}_z \cdot \hat{\boldsymbol{n}}]\, dS \\ &= \int_{\text{disk}} |v_i - v_j|\, dS_z \\ &= \int_0^{2\pi} \int_0^{R_{ij}} |v_i - v_j|\, r\, dr\, d\theta \\ &= \frac{2}{9} \frac{(\rho_c - \rho_f)\, g}{\mu} R_p^3 \left|\frac{w_i}{R_i} - \frac{w_j}{R_j}\right| \pi (R_{ij})^2 \\ &= \frac{2\pi}{9} \frac{(\rho_c - \rho_f)\, g}{\mu} R_p^3 \left|\frac{w_i}{R_i} - \frac{w_j}{R_j}\right| (R_i + R_j)^2 \ . \end{aligned} \tag{4.32}$$

The integration in Eq. 4.32 is performed on a cross-sectional disc of a sphere of radius R_{ij}, whose unitary normal vector is opposed to $\hat{\boldsymbol{e}}_z$ (i.e. $\hat{\boldsymbol{n}}_{\text{disk}} \cdot \hat{\boldsymbol{e}}_z = -1$).

The sedimentation collision kernel (Eq. 4.32) can also be normalized by the radius of gyration (Eq. 4.10). Thus, Eq. 4.32 becomes a function of just the radii of the colliding clusters,

$$k_g(R_i, R_j) = \frac{2\pi}{9} \frac{(\rho_c - \rho_f)\, g}{\mu} R_p^{3-D_F} \left| R_i^{D_F-1} - R_j^{D_F-1} \right| (R_i + R_j)^2 \ . \tag{4.33}$$

Collision Rate by Simple Shear Flow

For this derivation, particles are assumed to have neutral buoyancy, therefore inertial effects can be ignored. Inertial effects can be ignored when Stokes' number

$$Stk_i := \frac{\hat{t}_{p_i}}{\hat{t}_f} = \frac{2}{9} \frac{(\rho_c - \rho_f) R_i^2}{\mu} \frac{v}{L} < 0.01 \ , \tag{4.34}$$

where $\hat{t}_{p_i}$ and $\hat{t}_f$ are the characteristic times of the particle and the fluid, respectively; ρ_c and ρ_f are the densities of the colloid and the fluid, respectively; R_i is the radius of the particle, μ is the viscosity, v is velocity, and L is the dimension of the flow obstacle. In laminar flow the velocity field occurs as a continuous gradient. Assuming a reference particle of class i being dragged by a laminar flow stream, as in a Lagrangian reference frame, particles of class j moving in streams adjacent to the reference particle will have different velocities, as illustrated in Fig. 4.11. The flux of particles j towards the reference particle i shall be

$$\boldsymbol{j}_{n_j} = C_j\, \boldsymbol{v}_{\text{rel}} = C_j \frac{\partial v_y}{\partial z} z\, \hat{\boldsymbol{e}}_y = C_j\, \dot{\gamma} z\, \hat{\boldsymbol{e}}_y \ , \tag{4.35}$$

where $\dot{\gamma}$ is the shear rate of the fluid. Equation 4.35 is applied to Eq. 4.20 to yield the shear collision kernel

$$\begin{aligned} k_s(R_i, R_j) &:= \oint_{\text{sphere}} (-\dot{\gamma} z\, \hat{\boldsymbol{e}}_y \cdot \hat{\boldsymbol{n}})\, H(-\dot{\gamma} z\, \hat{\boldsymbol{e}}_y \cdot \hat{\boldsymbol{n}})\, dS \\ &= \int_{\text{disk}} |\dot{\gamma} z|\, dS_y \\ &= 4 \int_0^{R_{ij}} (\dot{\gamma} z) \sqrt{R_{ij}^2 - z^2}\, dz \\ &= 4\, \dot{\gamma} R_{ij}^3 \int_0^{\pi/2} \sin\phi \sqrt{1 - \sin^2\phi}\, \cos\phi\, d\phi \\ &= 4\, \dot{\gamma} R_{ij}^3 \int_0^{\pi/2} \sin\phi\, \cos^2\phi\, d\phi \\ &= \frac{4}{3} \dot{\gamma}\, R_{ij}^3 \\ &= \frac{4}{3} \dot{\gamma}\, (R_i + R_j)^3 \ . \end{aligned} \tag{4.36}$$

Because the flow is symmetric (even function about the z-axis and odd about the x-axis), the integration in Eq. 4.36 could be performed on one forth of the sphere projection, where $\boldsymbol{j}_{n_2} \cdot \hat{\boldsymbol{n}} < 0$. The shear collision rate is proportional to the cube of the collision radius R_{ij} which demonstrates a strong dependence on the particle size for shear induced aggregation. This implies that larger particles have greater collision frequency and the aggregation growth rate increases as the aggregation proceeds.

Collision Rate in a General Laminar Field

In the general laminar flow field, the direction on the flow is arbitrary in space. Therefore, the integration of the particle flux cannot be simply done on the projection plane, as in Eq. 4.36, but it has to be done on the actual surface of the sphere of radius R_{12}. In the general case, the relative velocity is

$$\boldsymbol{v}_{\text{rel}} = \boldsymbol{L}\boldsymbol{r}\ , \tag{4.37}$$

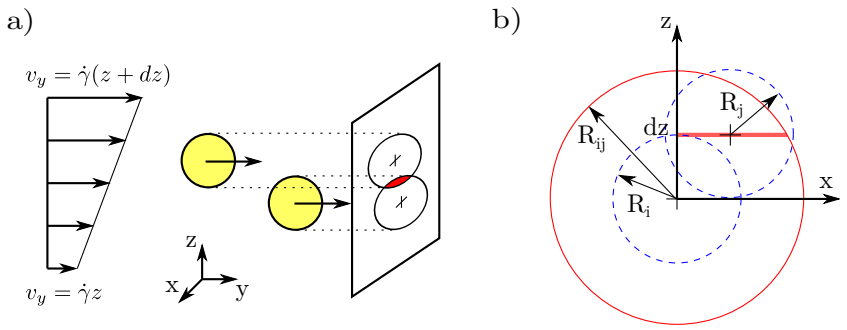

Fig. 4.11: Scheme of particle collision rate by a velocity gradient $\dot{\gamma} = \frac{\partial v_y}{\partial z}$. **a)** Projection of colliding particles on a plane x–z. **b)** Reference particle with radius R_i and colliding particles with radius R_j; R_{ij} is the maximum distance between hitting particles.

where $\boldsymbol{L} = \frac{\partial v_i}{\partial x_j}\hat{\boldsymbol{e}}_i \otimes \hat{\boldsymbol{e}}_j$ is the velocity-gradient tensor. The strain rate tensor has be decomposed in a sum of a symmetric and an antisymmetric tensor,

$$\boldsymbol{L} = \boldsymbol{E} + \boldsymbol{W} = \frac{1}{2}(\boldsymbol{L} + \boldsymbol{L}^T) + \frac{1}{2}(\boldsymbol{L} - \boldsymbol{L}^T) \ . \tag{4.38}$$

The symmetric tensor $\boldsymbol{E} = \frac{1}{2}(\boldsymbol{L} + \boldsymbol{L}^T)$ is the strain-rate tensor, and the antisymmetric $\boldsymbol{W} = \frac{1}{2}(\boldsymbol{L} - \boldsymbol{L}^T)$ is the rigid-body rotation tensor. The strain-rate tensor causes physical distortion of the fluid element that moves the particles along $\boldsymbol{r}$, but the rotation tensor can be ignored because rotations do not contribute to the collision rate ($\boldsymbol{W}\boldsymbol{r} \cdot \hat{\boldsymbol{n}} = 0$).

The integration of the fluxes becomes simpler when performed on the basis of the principal directions of the flow (eigenvectors), see Fig. 4.12. The eigenvalues of the strain-rate tensor form the principal strain-rate tensor

$$\tilde{\boldsymbol{E}} = \begin{bmatrix} \tilde{E}_1 & 0 & 0 \\ 0 & \tilde{E}_2 & 0 \\ 0 & 0 & \tilde{E}_3 \end{bmatrix} \ , \tag{4.39}$$

where $\tilde{E}_1 \geq \tilde{E}_2 \geq \tilde{E}_3$, $\tilde{E}_1 \geq 0$ and $\tilde{E}_3 \leq 0$, and $\tilde{E}_2 = -(\tilde{E}_1 + \tilde{E}_3)$. Using this definition it is possible to show the following flow types:

- *Uniaxial extension*, when $\tilde{E}_1 = -2\tilde{E}_2 = -2\tilde{E}_3$;

- *Planar extension*, when $\tilde{E}_1 = -\tilde{E}_3$, and $\tilde{E}_2 = 0$;
- *Equal biaxial extension*, when $\tilde{E}_1 = \tilde{E}_2 = -\tilde{E}_3/2$.

The continuity equation ($\tilde{E}_1 + \tilde{E}_2 + \tilde{E}_3 = 0$) implies that when $|\tilde{E}_1| > |\tilde{E}_3| \Rightarrow \tilde{E}_2 < 0$, and when $|\tilde{E}_1| < |\tilde{E}_3| \Rightarrow \tilde{E}_2 > 0$. Therefore,

$$|\tilde{E}|_{max} := max(|\tilde{E}_1|, |\tilde{E}_2|, |\tilde{E}_3|) = \frac{1}{2}(|\tilde{E}_1| + |\tilde{E}_2| + |\tilde{E}_3|) \tag{4.40}$$

is a tensor invariant of $\boldsymbol{E}$ which quantifies the flux upper bound. The eigenvalues of $\boldsymbol{E}$ can be scaled by $|\tilde{E}|_{max}$ as

$$\begin{aligned} \tilde{E}_1 &:= \alpha\, |\tilde{E}|_{max} \\ \tilde{E}_2 &:= (1-\alpha)\, |\tilde{E}|_{max} \ , \\ \tilde{E}_3 &:= -|\tilde{E}|_{max} \end{aligned} \tag{4.41}$$

where $\alpha \in [0, 1] \subset \mathbb{R}$ [172]. The influx of particles is depicted in Fig. 4.13 for different α's.

The collision kernel (Eq. 4.20) with the definitions in Eqs. 4.37 and 4.41, and integrated in spherical coordinates (Eqs. 4.21 and 4.22), yields

$$\begin{aligned} k_l(R_i, R_j) &:= \oint_{\text{sphere}} (-\boldsymbol{E}\boldsymbol{r} \cdot \hat{\boldsymbol{n}})\, H(-\boldsymbol{E}\boldsymbol{r} \cdot \hat{\boldsymbol{n}})\, dS \\ &= \int_0^{2\pi} \int_0^{\pi} (-R_{ij} \boldsymbol{E}\hat{\boldsymbol{n}} \cdot \hat{\boldsymbol{n}})\, H(-R_{ij} \boldsymbol{E}\hat{\boldsymbol{n}} \cdot \hat{\boldsymbol{n}}\, R_{ij}^2 sin\phi)\, R_{ij}^2 sin\phi\, d\phi\, d\theta \\ &= |\tilde{E}|_{max} R_{ij}^3 \int_0^{2\pi} \int_0^{\pi} \frac{1}{2} |\alpha\, sin^2\phi\, cos^2\theta + (1-\alpha)\, sin^2\phi\, sin^2\theta - cos^2\phi|\, sin\phi\, d\phi\, d\theta \\ &= F(\alpha)\, |\tilde{E}|_{max} (R_i + R_j)^3 \ , \end{aligned} \tag{4.42}$$

where $F(\alpha)$ is the trigonometric integral in the third step of the derivation of Eq. 4.42. The integration $F(\alpha)$ is too complicated to be integrated analytically because of the modulus operator. Nevertheless, it can be obtained numerically by Simpson's

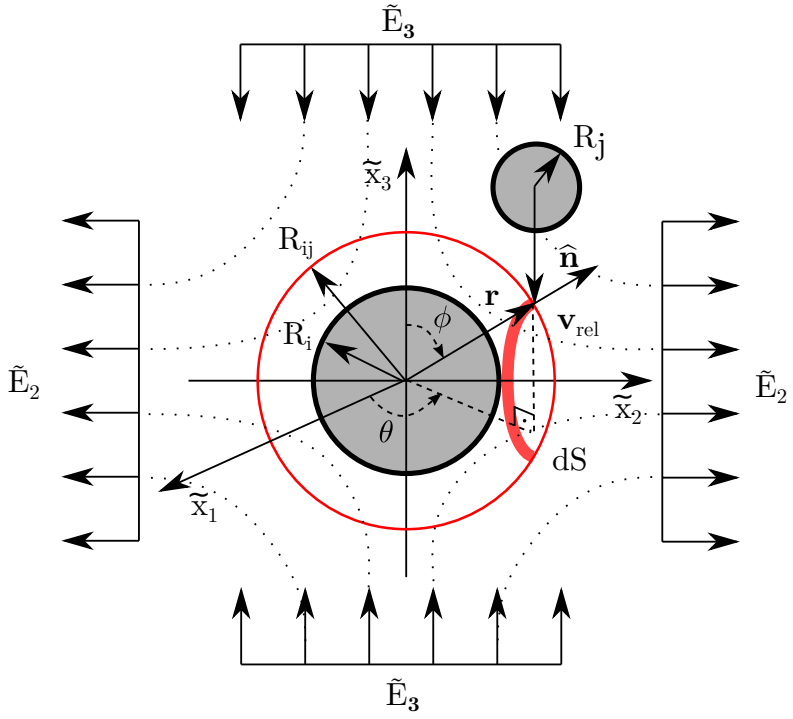

Fig. 4.12: Integration scheme of the general laminar flow on the principal directions.

method. The graph of $F(\alpha)$ is plotted in Fig. 4.14. The function $F(\alpha) \in [\frac{8}{3}, \frac{4\pi}{3\sqrt{3}}] \subset \mathbb{R}$ $(\forall \alpha \in [0,1] \subset \mathbb{R})$.

An alternative way for obtaining the collision kernel for general laminar flow (Eq. 4.42) was proposed by Camp and Stein (1945) [40]. They generalized the collision kernel for simple shear (Eq. 4.36) by introducing an absolute shear rate

$$G = \sqrt{\frac{\Phi}{\mu}} = \sqrt{\dot{\gamma}_{12}^2 + \dot{\gamma}_{13}^2 + \dot{\gamma}_{23}^2} \; . \tag{4.43}$$

where Φ is the viscous energy dissipation function. Camp and Stein proposed the use of the power input (equal to Φ) to predict the flocculation time industrial processes. However, Kramer and Clark (1997) [131] proved that the power input cannot be used to monitor flocculation in heterogeneous shear fields. Although Eq. 4.43 would be measuring the root-mean-square shear gradient in industrial equipment, local flocculation rates would differ a lot from the expected average. They proposed a similar

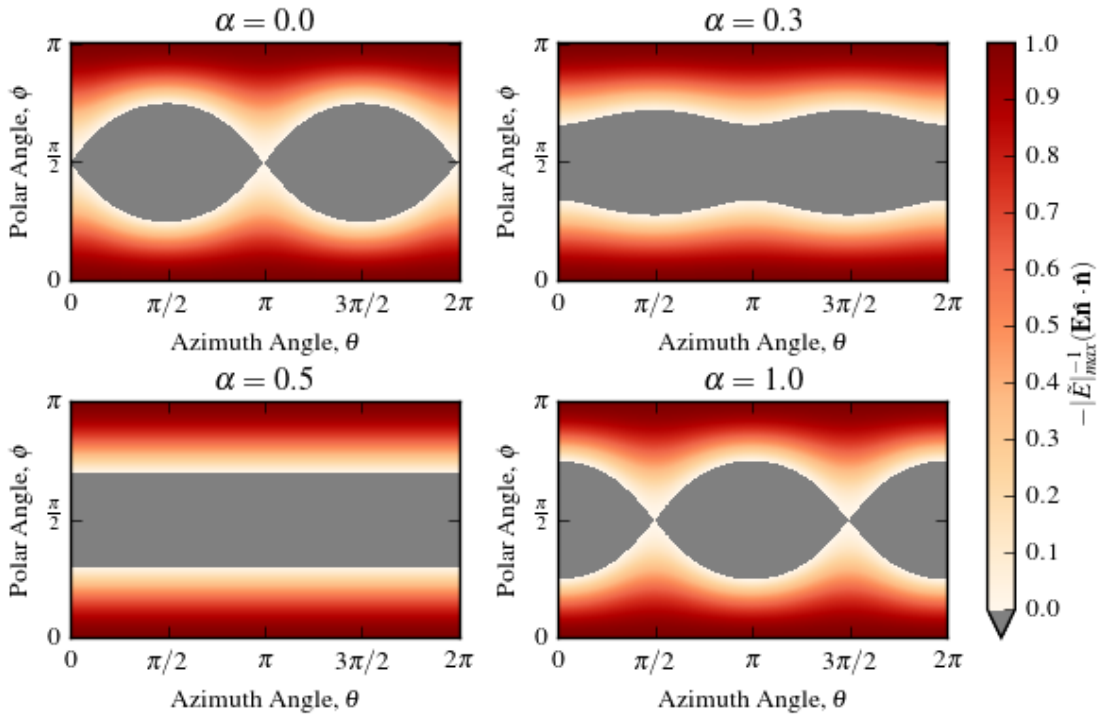

Fig. 4.13: The influx of particles due to general flow according to the scheme in Eq. 4.41. The effect of the influx mode was scaled to keep it bound to $[-1, 1] \subset \mathbb{R}$, but the outflux (negative part) was masked out in grey.

derivation as in Eq. 4.42, but they considered only the maximum inflow direction ($\tilde{\boldsymbol{E}}_3$ in Eq. 4.41). Because only one principal direction was considered, their integration resulted in $F = \frac{4\pi}{3}$. Later, the same authors performed a CFD simulation of a flocculation process between two eccentric cylinders using Eq. 4.42, which correlated with experimental data but not with the root-mean-square shear rate as proposed by Camp and Stein [130].

Pedocchi and Piedra-Cueva (2005) [172] noted that the dissipation function for an incompressible Newtonian fluid is defined as

$$\Phi = 2\mu\, tr(\boldsymbol{E}^2) = 2\mu\, \boldsymbol{E} : \boldsymbol{E} \ , \tag{4.44}$$

where $tr(\boldsymbol{E}^2)$ is an invariant of $\boldsymbol{E}$. They expanded this invariant with principal strain

rates in Eq. 4.41,

$$tr(\boldsymbol{E}^2) = tr(\tilde{\boldsymbol{E}}^2) = \tilde{E}_1^2 + \tilde{E}_2^2 + \tilde{E}_3^2 = 2(\alpha^2 - \alpha + 1)|\tilde{E}|_{max} \ . \tag{4.45}$$

Hence, using the definition of Eqs. 4.43 and 4.44 yields

$$|\tilde{E}|_{max} = \frac{1}{2\sqrt{\alpha^2 - \alpha + 1}} G = F'(\alpha) G \ . \tag{4.46}$$

By coupling Eq. 4.46 to Eq. 4.42, the collision kernel for general flow becomes

$$k_l(R_i, R_j) = F(\alpha)\, F'(\alpha)\, G\, (R_i + R_j)^3 = F''(\alpha)\, G\, (R_i + R_j)^3 \ . \tag{4.47}$$

The functions $F(\alpha)$, $F'(\alpha)$ and $F''(\alpha)$ are plotted in Fig. 4.14. It is important to notice that $F''(\alpha) \in [\frac{4}{3}, \frac{4}{3}\frac{\pi}{3}] \subset \mathbb{R}$ ($\forall \alpha \in [0,1] \subset \mathbb{R}$). A difference in ratio $\pi/3 \approx 1.047$ is negligible compared to the physical uncertaintes of a shear induced aggregation system, therefore the function F'' can be approximated as a constant for all kinds of laminar flow [172], i.e. $F''(\alpha) \approx 4/3$ ($\forall \alpha \in [0,1] \subset \mathbb{R}$).

In conclusion, although the Camp and Stein did not prove mathematically that the kernel equation

$$k_l(R_i, R_j) = \frac{4}{3} G\, (R_i + R_j)^3 \tag{4.48}$$

correctly computed the collision rate in general laminar flow, their insight of approximating Eq. 4.36 was proved to be fairly accurate by Pedocchi and Piedra-Cueva. However, Kramer and Clark proved that using an average shear rate is not suitable to monitor the aggregation process. Shear induced aggregation has to be resolved locally by CFD to be accurate. Finally, the absolute shear rate G is a better parameter to evaluate the general laminar kernel than the maximum strain-rate $|\tilde{E}|_{max}$, because the former case does not require the computation of eigenvalues. It is computationally cheaper to compute $G = \sqrt{2\, \boldsymbol{E} : \boldsymbol{E}}$ (Eq. 3.11).

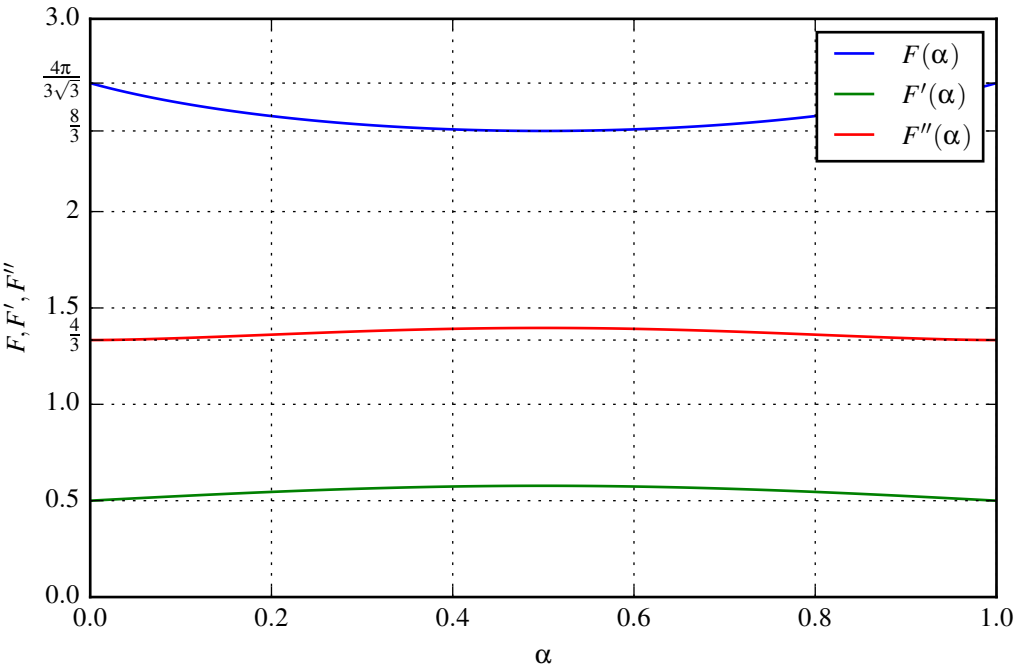

Fig. 4.14: Graph of the functions $F(\alpha)$, $F'(\alpha)$ and $F''(\alpha)$ defined in Eqs. 4.42, 4.46 and 4.47, respectively.

Collision Rate in Isotropic Turbulent Flow

Turbulence is statistically isotropic when the turbulent motions have no preferential direction in space. Isotropic turbulence is, however, an idealization never encountered in nature, because flows with a particular orientation introduce anisotropies. Although turbulence isotropy and homogeneity are violated close to boundary layers and jet streams, they still hold there at small scales and away from sources of turbulence.

Saffman and Turner (1956) [181] developed a theory to explain the speed of rain formation in turbulent clouds at high altitudes. Condensed water must have a critical mass to fall as rain drops. The mass of condensed water drops increase primarily by coalescense. Initially, when drops are little, collision rate is controlled by diffusion, but shear becomes more important as drops grow. Finally, differential sedimentation

causes the drops to grow a little bit more, shortly, as rain falls. Saffman and Turner noticed that neither the effects of condensation from the vapor phase or differential sedimentation alone would be sufficiently rapid for the small water droplets to grow to raindrop sizes in the times usually available. Therefore, they considered the effect of random motion in turbulence as the cause of drop collision.

The theory considers particles smaller by at least an order of magnitude than the length scale of the small eddies of the turbulence, therefore the relative motion between colliding particles is governed by the small scale flows. This theory is suitable for large Reynolds numbers, because the similarity theory of turbulent motion holds for the small scales. This implies that for scales of motion sufficiently small compared to the energy-containing eddies, the motion is isotropic and the mean values of quantities related to the turbulence depend only on the kinematic viscosity ν and the rate of energy dissipation ϵ. Similarly to Eq. 4.37, the root-mean-squeare relative velocity between particles of class i and j is

$$\langle \boldsymbol{v}'_{\mathrm{rel}} \rangle_{rms} = \langle \boldsymbol{L}' \rangle_{rms} \boldsymbol{r} \ , \tag{4.49}$$

where the $\boldsymbol{v}'$ and $\boldsymbol{L}'$ are turbulence random fluctuations of the velocity vector and the velocity-gradient tensor, respectively. Saffman and Turner considered the particles to be on the same length scale of the Taylor microscale, because it is the length scale where turbulence fluctuations are noticed, yet it is still larger than the Kolmogorov legth scale, where dissipation occurs. The Taylor microscale gives a convenient estimation for fluctuating strain rate field,

$$\langle \boldsymbol{L}' \rangle_{rms} \hat{\boldsymbol{n}} = \sqrt{\frac{\epsilon}{15\,\nu}} \hat{\boldsymbol{n}} \ . \tag{4.50}$$

The collision kernel (Eq. 4.20) with the definitions in Eqs. 4.49 and 4.50, and by

integrating in spherical coordinates (Eqs. 4.21 and 4.22), it yields

$$\begin{aligned} k_t(R_i, R_j) &:= \oint_{\text{sphere}} (-\langle \boldsymbol{L'} \rangle_{rms} \boldsymbol{r} \cdot \hat{\boldsymbol{n}})\, H(-\langle \boldsymbol{L'} \rangle_{rms} \boldsymbol{r} \cdot \hat{\boldsymbol{n}})\, dS \\ &= \frac{1}{2} \oint_{\text{sphere}} |-R_{ij} \langle \boldsymbol{L'} \rangle_{rms} \hat{\boldsymbol{n}} \cdot \hat{\boldsymbol{n}}|\, dS \\ &= 2\pi R_{ij}^3 \sqrt{\frac{\epsilon}{15\,\nu}} \\ &= 2\pi \sqrt{\frac{\epsilon}{15\nu}}\, (R_i + R_j)^3 \ . \end{aligned} \tag{4.51}$$

The second derivation step of Eq. 4.51 implies that the integral is symmetric, therefore the modulus can be computed instead of the Heaviside function. Equation 4.51 is similar to the laminar collision kernels (Eqs. 4.36 and 4.48), where the mean fluctuation of shear rate is obtained by Eq. 4.50 at the Taylor microscale.

4.1.7 Breakup Equation of Pandya and Spielman

To effectively model the overall coagulation process the effects of aggregate breakup must be included. The break-up function of the PBE (Eq. 4.12) can be formulated as

$$B_i(\boldsymbol{C}, \boldsymbol{R}, \boldsymbol{w}) = -k_b(R_i) C_i + \sum_{j=i+1}^{n} g(w_i, w_j)\, k_b(R_j)\, C_j \ , \tag{4.52}$$

where the first term on the right hand side accounts for the break-up rate of particles of class i and the second accounts for the formation of this particle class by the breaking up of larger aggregates. Equation 4.52 is a reformulation of the PBE proposed by Pandya and Spielman (1982, 1983) [168, 169]. The disaggregation rates are first order rate functions (see Tab. 3.4), whose disaggregation rate operator $k_b(R_i)$ is known as the break-up kernel, and $g(w_i, w_j)$ is the fragment mass distribution. The fragment mass distribution gives stoichiometric balance for the breakup of a cluster of w_j monomers to form a cluster of w_i monomers.

Both the break-up kernel k_b and the fragment mass distribution $g(w_i, w_j)$ in Eq. 4.52 depend on the manner by which the aggregate structure fails. The location of

the failure is computed in Eq. 4.52 by the fragment mass distribution $g(w_i, w_j)$. The breakup occurs either within the body (splitting) or on the surface (erosion) of the aggregate [129]. Usually, the fragmentation of an aggregate occurs at the bonds between monomers. However, the primary colloid unit itself can break when the medium's shear stress its material strength. The material strength of both the colloid monomers and their bonds can change in time due to chemical transformations influenced by the environment's temperature and reactivity. If either the broken bonds cannot be reestablished or primary particles are destroyed, the total number of viable primary particles in the volume of control is decreased.

Fragment Mass Distribution

In order to guarantee the conservation of mass, the fragment mass distribution is defined as

$$g(w_i, w_j) = P(w_i|w_j) + P(w_j - w_i|w_j) \ , \tag{4.53}$$

where $P(w_i|w_j)$ is the conditional probability mass function (PMF) for the breakup of a cluster of w_j monomers to form a cluster of w_i monomers. Whenever a break-up event occurs, two clusters are formed with the same probability, one with w_i platelets and the other with $(w_j - w_i)$ platelets. The PMF has to have the following characteristics in relation to the value of breaking-up cluster of size w_j:

$$\begin{aligned} &P(w_i|w_j) > 0 \quad \Leftrightarrow \quad 1 < w_i < \frac{w_j}{2} \ , \text{ and} \\ &\sum_{w_i=1}^{n} P(w_i|w_j) = 1 \ , \quad \forall w_j \in [2, ..., n] \ . \end{aligned} \tag{4.54}$$

The second probability function term in Eq. 4.52 computes the same probability function (Eq. 4.54) for forming the particle of class $(w_j - w_i)$. The summation of these two probabilities form a symmetric distribution along the variable w_j, which also guarantees the stoichiometry when $w_j = 2w_i$. Both these probability equations can be

combined in the fragment mass distribution $g(w_i, w_j)$, where

$$\sum_{w_i=1}^{n} g(w_i, w_j) = 2 \ , \quad \forall w_j \in [2, ..., n] \ , \tag{4.55}$$

and

$$\sum_{w_i=1}^{n} w_i \, g(w_i, w_j) = w_j \ , \quad \forall w_j \in [2, ..., n] \ , \tag{4.56}$$

respectively demonstrate that two particles are being formed each time a fragmentation event occurs, and that mass conservation is being obeyed.

Pandya and Spielman (*idem*) proposed the use of a log-normal and a normal probability distribution (Eq. 4.54) for erosion and splitting, respectively. They preferred a log-normal distribution for splitting because this distribution is slender and never yields negative particles. The erosion distribution is fixed, and the splitting distribution is scaled to the parent aggregate class. The standard deviation of the normal distribution can be scaled by

$$\sigma_j = \frac{w_j}{2\,\lambda} \tag{4.57}$$

for splitting, where the larger the value of the parameter λ, the narrower is the fragment-size distribution [205], as illustrated in Fig. 4.15c. Pandya and Spielman (*idem*) found that most of the fragments produced by splitting were about half of the size of the parent aggregate.

In extreme cases, these distributions converge to either a uniform distribution (when $\sigma \to \infty$), or to a degenerate distribution (when $\sigma \to 0$). In an uniform distribution $P_u(w_i|w_j)$, a particle w_j has the same chance of breaking up into a couple of pieces of any size. Thus,

$$P_u(w_i|w_j) = \begin{cases} \frac{1}{floor(w_j/2)} & \text{, if } 1 < i \leq w_j/2 \\ 0 & \text{, if } w_i > w_j/2 \end{cases} \ , \tag{4.58}$$

where $floor(\cdot)$ maps a real number to the largest previous integer. In a degenerate distribution $P_d(w_i|w_j)$, a particle w_j has just the chance of breaking up into a couple

of pieces of a specific sizes. Thus,

$$P_d(w_i|w_j) = \begin{cases} 1 & \text{, if } w_i = w_k \ , \ w_k \leq w_j/2 \\ 0 & \text{, if } w_i \neq w_k \end{cases} , \tag{4.59}$$

where w_k is the particle class being formed. A special case for the degenerate distribution is the binary splitting, when an aggregate breaks into a couple clusters of the same size

$$P(v_i|v_j) = \begin{cases} 1 & \text{, if } v_i = floor(\frac{v_j}{2}) \\ 0 & \text{, otherwise} \end{cases} , \tag{4.60}$$

For the sake of simplicity, Fig. 4.15 shows matrices $g_{ij} = g(w_i, w_j)$ generated by these two probability functions (Eq. 4.54).

Break-up Kernel

Many models for aggregate failure have been proposed in the literature [129]. Some account for the chemical factors, but most of them account for mechanical factors only. Some of these models predict the material failure out of the internal stresses caused by the fluid's shear stress on the aggregate's surface. Even though, there has been some effort to characterize the material strength of aggregates depending on the fractal structure [210, 58], the way material strength translates to disaggregation is still unknown. The failure of some internal bonds may lead to reorganisation of the internal structure, which is the same as plastic deformation, instead of definitive fracture.

Therefore, the most convenient way of formulating the breakup kernel would be with a constitutive equation, where both the flow's shear stress and the aggregate size are variables. The parameters of this kernel can be observed in the aggregate mixture, without any information about the aggregate's microstructure. A power-law model was proposed by Pandya and Spielman (1982, 1983) [168, 169]:

$$k_b(G, R_i) = a\, G^b\, R_i^c \ , \tag{4.61}$$

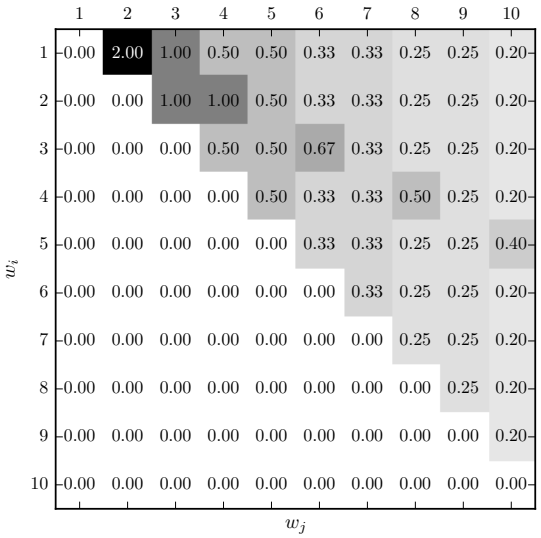

(a) Splitting with either uniform distribution or normal distribution ($\lambda \to 0 \Rightarrow \sigma_j \to \infty$).

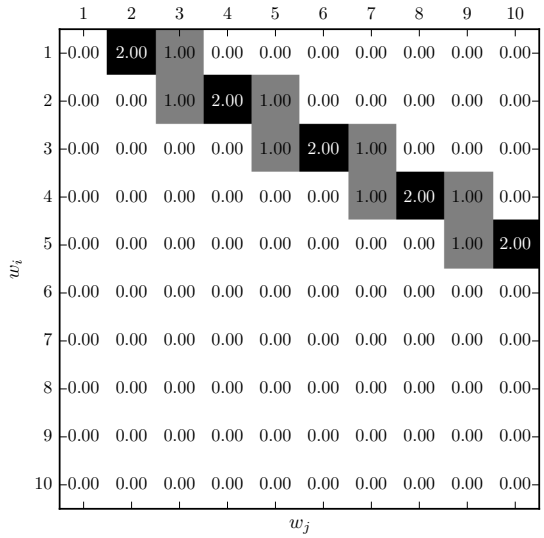

(b) Binary splitting with either degenerate distribution ($w_k = w_j/2$) or normal distribution ($\lambda \to \infty \Rightarrow \sigma_j \to 0$).

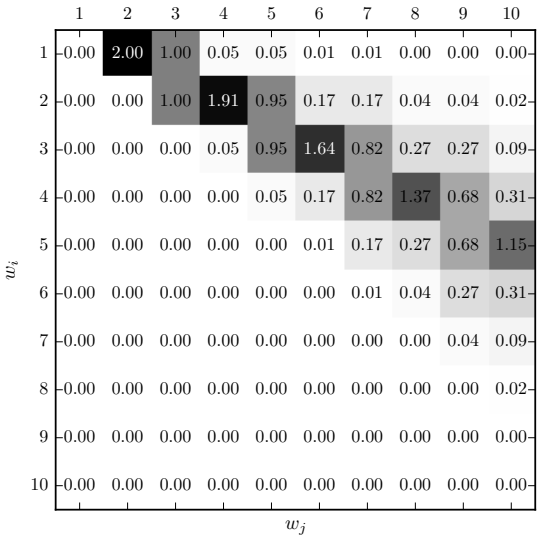

(c) Splitting with normal distribution ($\lambda = 4$).

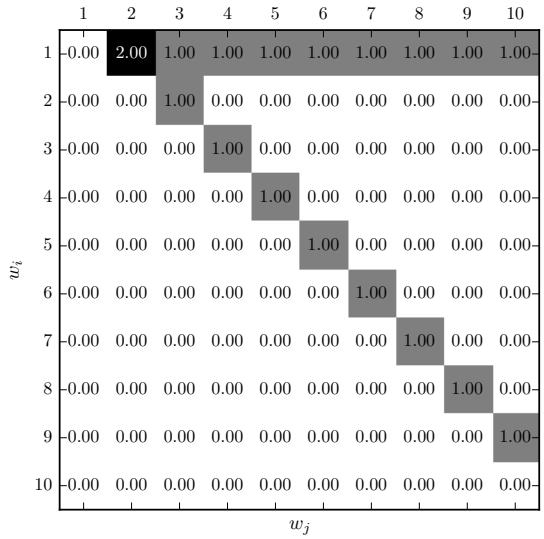

(d) Erosion with degenerate distribution ($w_k = 1$).

Fig. 4.15: Fragment mass distributions $g(w_i, w_j)$.

where G is a measure of flow strain rate, R_i is the aggregate radius, and a, b and c are constitutive parameters. Equation 4.61 holds for laminar flow, and for isotropic turbulent flow if the aggregates are larger than the Kolmogorov length scale l_K,

$$R_j \gg l_K = \left(\frac{\nu^3}{\epsilon}\right)^{1/4} . \tag{4.62}$$

Because the physical magnitude of parameter a depends on the values of parameters b and c, which are empirical, it is suitable to normalize Eq. 4.61 as

$$k_b(\tau, R_i) = a' \left(\frac{G}{G^*}\right)^b \left(\frac{R_i}{R_p}\right)^c , \tag{4.63}$$

where $a' = 1\,\mathrm{s}^{-1}$ is a constant used to match the dimensions of both sides of the equation [129]. The parameter characteristic shear rate G^* in Eq. 4.63 is an empirical parameter which gives the value above which the breakup grows exponentially with shear rate. The characteristic shear rate is defined as

$$G^* = \left(\frac{a'}{a\, R_p^c}\right)^{1/b} \tag{4.64}$$

regarding to the parameters of Eq. 4.61.

The parameters of Eq. 4.61 may change if the aggregates are immersed in a different fluid. The parameters of Eq. 4.61 would be different because it is shear stress, not shear rate, that causes aggregate breakup. Other physico-chemical properties of the fluid may interfere with the aggregation-breakup system. The chemical affinity of colloids and polymers can be strongly affected by pH and chemical potential. If the chemistry factors are steady, but only viscosity changes (for instance, in a non-linear fluid), Eq. 4.61 can be normalised to shear stress for translating the parameters obtained in fluids of different viscosity. Considering, for instance, the power-law constitutive equation (eq. 3.14) for the effective viscosity, Eq. 4.61 can be transformed to

$$k_b(\tau, R_i) = a''\, \tau^{b'}\, R_i^c , \tag{4.65}$$

where $a'' = a/K^{b'}$ and $b' = b/(n-1)$. Equation 4.65 can have its linear parameter a'' normalised as in Eq. 4.63 regarding to Eq. 4.61,

$$k_b(\tau, R_i) = a' \left(\frac{\tau}{\tau^*}\right)^{b'} \left(\frac{R_i}{R_p}\right)^{c} . \tag{4.66}$$

In Eq. 4.66, a' is the same unity constant as found in Eq. 4.63, and the characteristic shear stress

$$\tau^* = K \left(\frac{a''}{a\, R_p^c}\right)^{\frac{(n-1)}{b}} \tag{4.67}$$

is also an empirical parameter analogous to the characteristic shear rate G^* in Eq. 4.63.

Pandya and Spielman [168, 169] based the formulation of Eq. 4.61 in experiments with single colloid aggregates trapped in a simple extensional flow field, and earlier experiments conducted by Kao and Mason (1975) [119]. In the experiments with trapped aggregates, erosion frequency was quasi-continuous, whereas splitting was inconstant and highly dependent on the aggregate's internal microstructure. Moreover, erosion rate was linearly dependent to the aggregate's apparent volume, whereas splitting rate was dependent to the power $\frac{1}{3}$. Translating these results for the radius of gyration in Eq. 4.61, one obtains $c = 3$ for erosion, and $c = 1$ for splitting. Finally, in a Newtonian fluid, the erosion rate was linearly dependent to shear rate ($b = 1$), whereas splitting was dependent to a lesser extent ($b = 0.71$). In another experiment, Spicer and Pratsinis (1996) obtained $b = 1.6$, considering only splitting and $c = 1$ [205]. Barthelmes *et al.* (2003) reported b ranging in $1.75 - 6.5$ from a series of articles [22].

Splitting is dependent on the way in which the particles are arranged within the structure. The external loads are distributed within aggregates by acting on aggregate bonds. In a continuous solid, the internal stresses decrease as cross-sectional area increases. However, the void fraction of a fractal structure increases with aggregate size, see Figs. 4.6 and 4.5. Equation 4.11 shows that the lower the fractal dimension is, the weaker the material strength becomes with respect to an increase of aggregate size

[210]. This fact supports the parameter $c = 1$ for splitting obtained by Pandya and Spielman [168, 169]. However, this parameter should have some sort of dependence to the fractal dimension, which is included in the assumption $c = 3/D_F$ [22]. Using this assumption for platelets, with $D_F = 2.2$ one obtains $c = 1.36$.

The break-up behaviour of inorganic aggregates is qualitatively similar to the one of platelet aggregates. Nesbitt *et al.* (2009) [161] observed platelet aggregates with vWF adhering to a solid surface. These aggregates were continuously losing platelets from their outer layer, and sporadically losing large chunks of themselves. In spite of the apparent universality of the break-up behaviour, the dependence of aggregate size for platelet aggregates has never been measured.

4.2 Scaling Analysis

Scaling analysis is a systematic method for nondimensionalizing the variables of the equation describing physical processes. The unique aspect of this nondimensionalization technique is that it is done to ensure that the variables and their derivatives are bounded of order one, which implies that their magnitudes range between zero and one. When this scaling to order one is done, the magnitudes of the resulting dimensionless groups are used to evaluate the relative importance of the various terms in the describing equations, which are primordial for simplifying approximations [132].

The scaling process henceforth developed was published by Bäbler and Morbidelli (2007) [16]. The PBE (Eq. 4.12) with the Smoluchowski aggregation equation (Eq. 4.13b) and the breakup equation of Pandya and Spielman (Eq. 4.52) becomes

$$\frac{\partial C_i}{\partial t} = \eta \left[\frac{1}{2} \sum_{j=1}^{i-1} k_c(R_i - R_j, R_j) C_{(i-j)} C_j - \sum_{j=1}^{n} k_c(R_i, R_j) C_i C_j \right] - k_b(R_i) C_i + \sum_{j=i+1}^{n} g(w_i, w_j)\, k_b(R_j)\, C_j \ . \tag{4.68}$$

Equation 4.68 is scaled by the following dimensionless variables:

$$\hat{C}_i := \frac{C_i}{C_p} \ , \quad \text{and} \quad \hat{t} := \frac{t}{t_a} \ ; \tag{4.69}$$

where C_p is the absolute concentration of primary particles, and t_a is the aggregation characteristic time of free platelets. The absolute concentration of platelets C_p is chosen to scale concentration, because it is the maximum possible concentration of particles in the system. The aggregation characteristic time t_a is chosen as the time scale, because the aggregation rates must be faster than the breakup rates for any aggregation to occur.

The aggregation characteristic time is obtained by scaling just the initial aggregation rate of free platelets, i.e. $R_i = R_j = R_p$ and $D_i = D_j = D_p$ at $t = 0$ in Eq. 4.15. Hence,

$$\begin{aligned} \frac{1}{t_a} &= \eta \left[k_s(R_p, R_p) + k_d(R_p, R_p) \right] C_p \\ &= \eta \frac{4}{3} G \left(2R_p\right)^3 C_p \left(1 + \frac{1}{Pe} \right) \ , \end{aligned} \tag{4.70}$$

where

$$Pe := \frac{t_d}{t_s} = \frac{k_s}{k_d} = \frac{\frac{4}{3} G \left(2R_p\right)^3}{4\,\pi\,(2\,R_p)(2\,D_p)} = \frac{2\,G\,R_p^2}{3\pi\,D_p} \tag{4.71}$$

is the Péclet number, determined by the advection-diffusion ratio of platelet aggregation. Therefore, diffusion is significant in Eq. 4.70 only if $Pe \lesssim 100$. Considering Brownian diffusion (Eq. 3.38) only,

$$Pe = \frac{2\,G\,R_p^2}{3\pi\,\frac{k_B\,T}{6\pi\,\mu\,R_p}} = \frac{4\mu\,G\,R_p^3}{k_B\,T} \ , \tag{4.72}$$

for SIPA in platelet-rich plasma[1] (PRP) Brownian diffusion becomes insignificant at

$$G \gtrsim \frac{k_B\,T\,Pe}{4\mu\,R_p^3} = \frac{(1.38 \cdot 10^{-23})\,(3.1 \cdot 10^2)\,(10^2)}{4(1.2 \cdot 10^{-3})\,(1.16 \cdot 10^{-6})^3} = 57\,\mathrm{s}^{-1} \ . \tag{4.73}$$

[1] $k_B = 1.38 \cdot 10^{-23}\,\mathrm{J\,K}^{-1}$, $T = 310\ K$, $\mu = 1.2\,\mathrm{mPa\,s}$, and $R_p = 1.16\,\mu\mathrm{m}$.

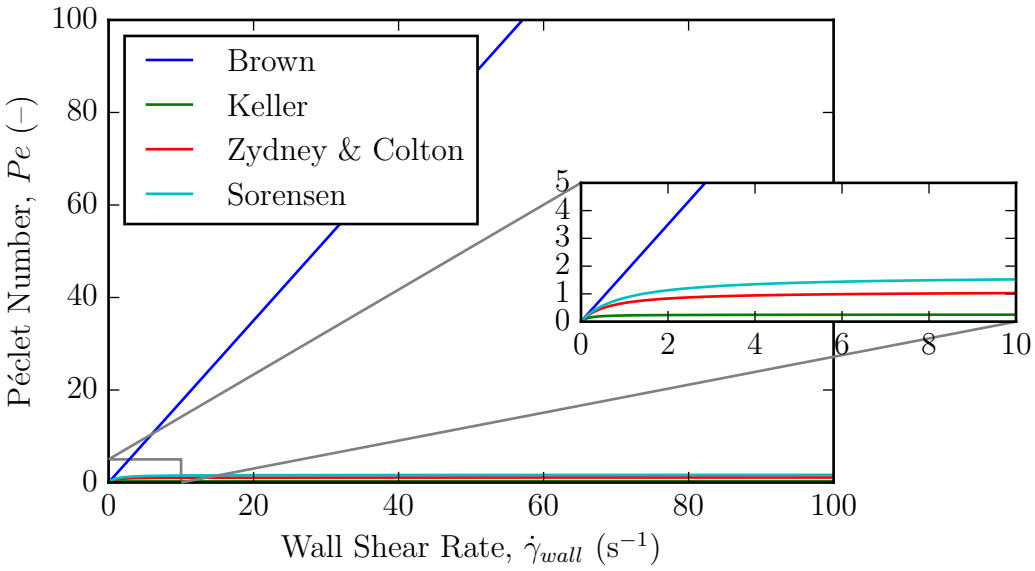

Fig. 4.16: Péclet number in function of shear rate for different diffusivity models. For Brownian diffusion, Péclet number rises steadily, becoming $Pe \gtrsim 100$ for $G \gtrsim 57\,s^{-1}$. However, augmented diffusion in whole blood ($Ht = 0.45$) causes $Pe \approx 1$ for $G \gtrsim 2\,s^{-1}$.

In contrast, for SIPA in whole blood, the augmented diffusivity effect takes place. All enhanced diffusivity models (Eqs. 3.39 to 3.44) are linear to G. Therefore, they would all result in a constant Pe, for $Pe \gtrsim 100$, which depend on the model parameters, see Fig. 4.16. In Case of Sorensen EDM (Eq. 3.41), $Pe \approx 1.40$ for $G \gtrsim 57\,s^{-1}$, independently of shear rate. Therefore, RBC-enhanced diffusion would increase the SIPA rate (Eq. 4.70) by a constant factor of 72% compared to shear collision alone.

In order to interpret how the collision rates vary with aggregate size, it is useful to consider the scaled collision kernel

$$\begin{aligned}\hat{k}_c(w_i, w_j) :=& k_c\, t_s \\ =& (w_i^{1/D_F} + w_j^{1/D_F})^3 + \frac{1}{Pe}\left[2 + \left(\frac{w_i}{w_j}\right)^{1/D_F} + \left(\frac{w_j}{w_i}\right)^{1/D_F}\right] . \end{aligned} \tag{4.74}$$

In Eq. 4.74 one can see that even for small Pe, diffusion is more significant for colliding clusters with a large difference in sizes. On the other hand, shear collision rate is not

sensitive to differences in cluster size, and yet it grows at a power of 3 as clusters become larger. This is an important remark because breakup is stronger for larger clusters, see Eq. 4.63. Therefore, although diffusion can contribute to aggregation rate, the shape of the CMD at steady state is determined by the equilibrium of shear and breakup rate [16].

Similar to Eq. 4.74, the break-up kernel function (the version of either Eq. 4.61 or Eq. 4.63) is scaled as

$$\hat{k}_b(w_j) := k_b(w_j)\, t_a = \frac{1}{K_{ab}}\, w_j^{c/D_F} \ , \tag{4.75}$$

where

$$\begin{aligned} K_{ab} := \frac{t_b}{t_a} =& \frac{32}{3}\, \eta\, C_p \left(1 + \frac{1}{Pe}\right) \frac{R_p^{(3-c)}}{a\, G^{(b-1)}} \\ =& \frac{32}{3}\, \eta\, C_p \left(1 + \frac{1}{Pe}\right) \frac{R_p^3\, G^{*b}}{a'\, G^{(b-1)}} \end{aligned} \tag{4.76}$$

is the ratio of aggregation and breakup rates of free platelets. The dependence of the break-up rate to c and D_F is evidenced in the scaled form of the break-up kernel (Eq. 4.75 and Fig. 4.18). For $c/D_F = 1$ the relation of w_j to k_b is linear.

The scaled aggregation-breakup PBE takes the dimensionless form

$$\begin{aligned} \frac{\partial \hat{C}_i}{\partial \hat{t}} = \Bigg[& \frac{1}{2} \sum_{j=1}^{i-1} \hat{k}_c(i-j, j) \hat{C}_{(i-j)} \hat{C}_j - \sum_{j=1}^{n} \hat{k}_c(i, j) \hat{C}_i \hat{C}_j \\ & - \hat{k}_b(i) \hat{C}_i + \sum_{j=i+1}^{n} g(i, j)\, \hat{k}_b(j)\, \hat{C}_j \Bigg] \ , \end{aligned} \tag{4.77}$$

where all quantities are in range 0–1, and the scaled aggregation ($\hat{k}_c$) and breakup ($\hat{k}_b$) kernels are given by Eqs. 4.74 and 4.76, respectivelly. Since, the time was scaled with the inverse of the highest aggregation rate (Eq. 4.69), t_a determines the system's aggregation speed. At a certain point, as the aggregates grow in size, the system's aggregation rates find equilibrium with the breakup rates. The equilibrium of these two rates is given by the aggregation-breakup ratio K_{ab}, which is analogous to the

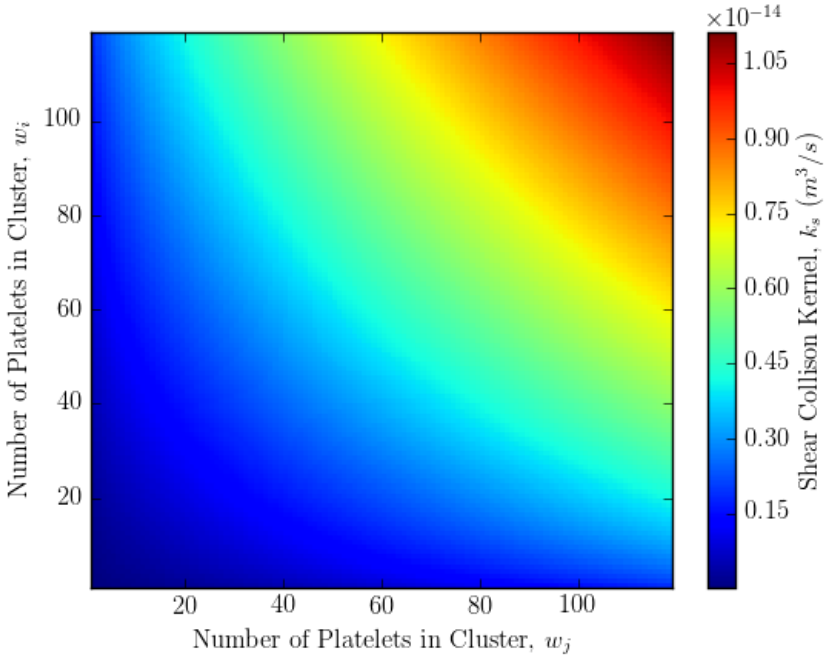

(a) Shear collision kernel at $G = 1.0\,\mathrm{s}^{-1}$.

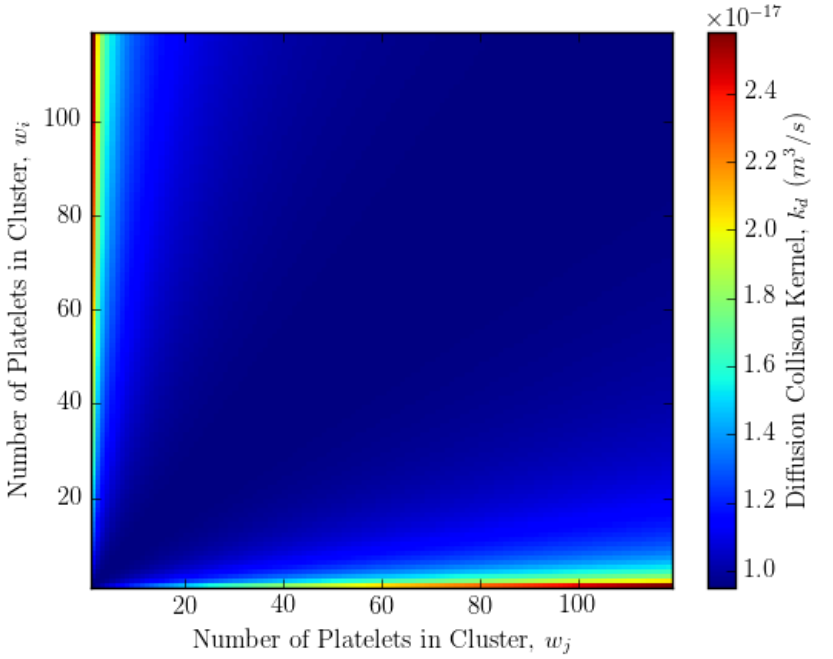

(b) Brownian diffusion collision kernel at $T = 37\,°\mathrm{C}$.

Fig. 4.17: Values of collision kernel between different platelet clusters.

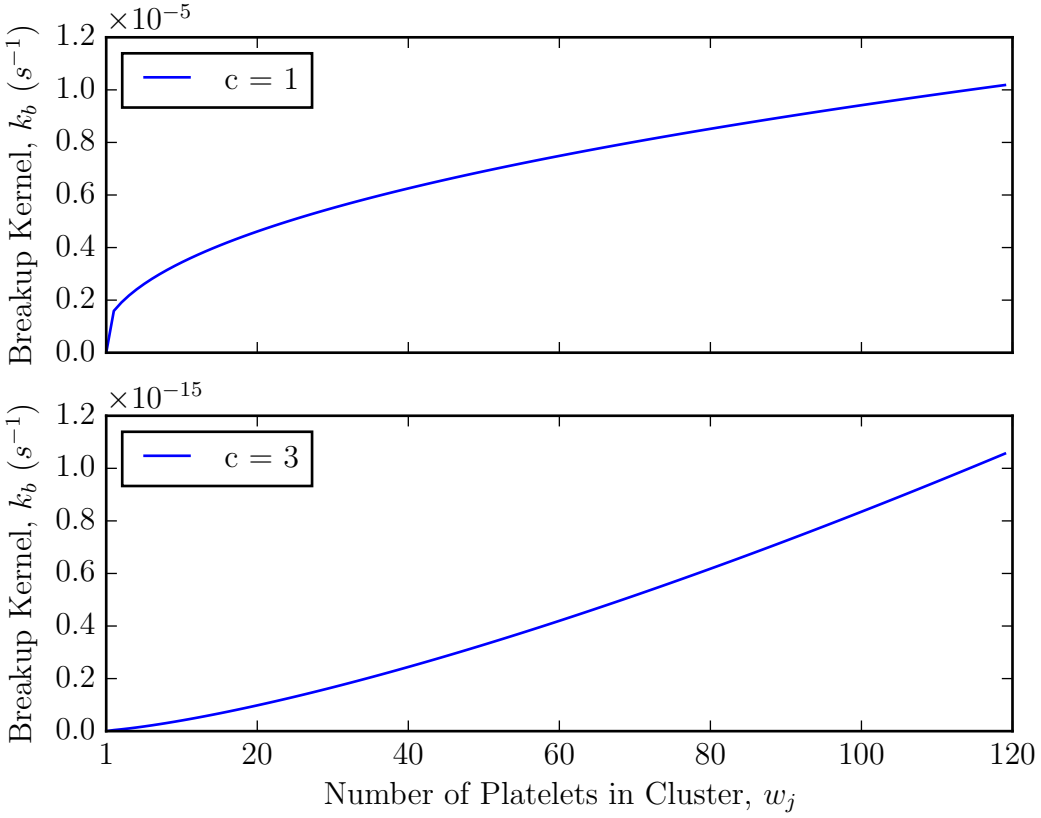

Fig. 4.18: The break-up kernel as a function of the number of colloids per cluster w_j. Shear rate was set $G = 335\,\mathrm{s}^{-1}$, and fractal dimension was set $D_F = 2.2$. On the top, $c/D_f < 1$; and on the bottom, $c/D_f > 1$.

dissociation constant K_d (Eq. 3.48) of molecules binding to multiple sites (see Sec. 3.2.3). The dissociation constant describes a statistical state of equilibrium between many molecules dynamically coupling and uncoupling.

4.3 Steady State Analysis

The dynamic behavior of the aggregation-breakup PBE (Eq. 4.12) was investigated both experimentally (for polystyrene particles) and numerically by Spicer, Pratsinis *et al.* (1996) [205, 207]. They showed that after a transient start, the CMD achieves

a steady state which reflects the equilibrium between aggregation and breakup. Moreover, the shape of the CMD is self-preserving at the steady state for any $K_{ab} > 1$ (i.e. the shape is preserved when normalized by the average number of platelets per aggregate $\langle w \rangle$, Eq. 4.7). Although higher shear rates shift the curve to smaller sizes, any steady-state distribution collapses to the same line when scaled at the mean aggregate size. This distribution is universal if the shear rate is low enough to keep less than 5% of primary particles unaggregated. This is accomplished when aggregation rate is higher than breakup rates for small cluster sizes, i.e. $K_{ab} > 1$ (Eq. 4.76). Additionally, the transient time decreases exponentially with decreasing K_{ab} because breakup halts the development of the CMD at smaller clusters [207].

A more rigorous mathematical analysis was performed by Kostoglou and Karabelas (1999). They derived an approximate analytical solution for the CMD at steady state assuming a log-normal distribution [128]. Their analysis shows that as the fractal dimension D_F decreases, or breakup exponent c (in Eq. 4.61) increases, the CMD becomes wider. The same occurs if the dispersion of the fragment mass distribution is increased, as Spicer and Prasinis had observed numerically [205]. Kostoglou and Karabelas obtained an analytical approximation for the steady-state mean number of particles per cluster

$$\langle w \rangle \propto K_{ab}^{\frac{D_F}{D_F+c-3}} \tag{4.78}$$

along with the condition

$$D_F + c - 3 > 0 \tag{4.79}$$

for the existence of a steady state. Otherwise, aggregation dominates for all shear rates. Later, Bäbler and Morbidelli (2007) proved both numerically and experimentally that the approximation of Kostoglou and Karabelas is very good for many integral quantities of the CMD, such as the RMS radius of gyration

$$\langle R \rangle_{\mathrm{RMS}} \propto K_{ab}^{\frac{1}{D_F+c-3}} \ , \tag{4.80}$$

if $K_{ab} > 1$ [16], despite the steady-state CMD not really being log-normal. It is important to notice that at the steady state, the mean number of platelets per cluster (Eq. 4.78) and the RMS radius of gyration (Eq. 4.80) rise exponentially with decreasing ratio of breakup and aggregation rates. The exponential growth rate of these equations is inversely dependent on the parameter c of the break-up kernel (Eq. 4.61).

4.4 Numerical Integration

The fixed pivot method (FPM) of Kumar and Ramkrishna was applied to solve the PBE numerically [136]. In this method the CMD is represented by discrete pivot points i, as described for Eq. 4.12. The FPM guarantees the conservation of mass by interpolating aggregation and breakup rates of particles at the pivot points. The CMD is discretized by a geometric series of pivot points

$$w_i = 2^{i-1} \ , \quad i \in [1, ..., n] \ . \tag{4.81}$$

In comparison with an uniform discretization, such as

$$w_i = i \ , \quad i \in [1, ..., n] \ , \tag{4.82}$$

Eq. 4.81 requires few discretization points, and thus facilitates a large choice for maximum cluster size, helping to avoid errors due to an artificial upper bound.

The disadvantage of the FPM lays on conserving just two moment rates, which are normally the particle number and mass (zeroth and first moments, respectively). The error is evidenced in non-uniform grid-spacing, such as ours, which shifts the simulation results towards aggregation [16]. However, there is no ideal method in the literature which conserves all moments accurately [127].

These arrays are recursively called to calculate the PBE at each discrete cluster size. The PBE yields an ordinary differential equation (ODE) for each cluster size, which is solved numerically at each time step. We coded our ODE system in Python

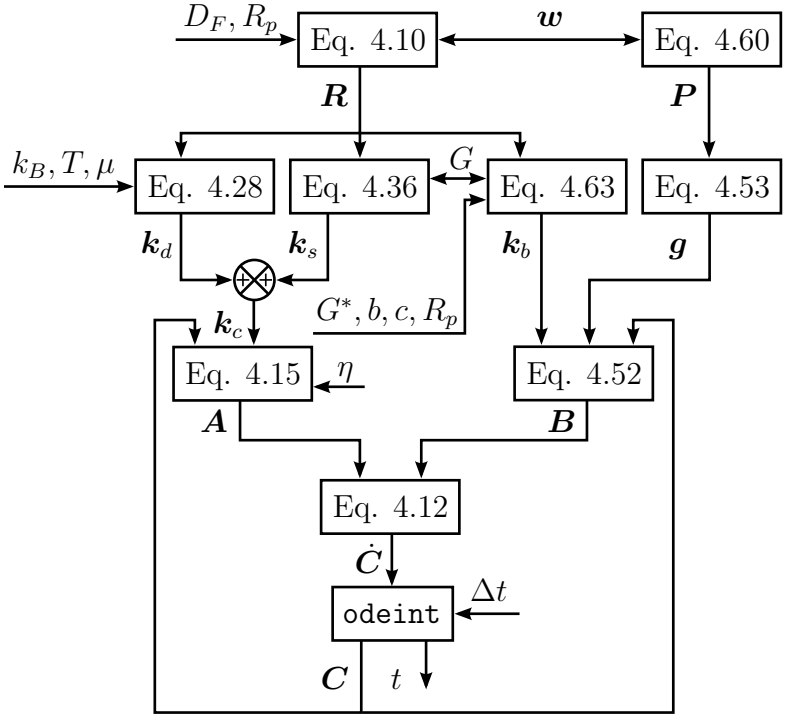

Fig. 4.19: Algorithm flowchart for building and integrating the PBE over time.

using the `scipy.odeint` function [167], which runs the Adams method (predictor-corrector) in the non-stiff case, and Backward Differentiation Formula (BDF) methods (the Gear methods) in the stiff case.

4.4.1 Algorithm Overview

The algorithm that computes the evolution of the CMD is summarised in Fig. 4.19. The PBE (Eq. 4.12), which expresses the development of the CMD as the sum of the aggregation rate (Eq. 4.15) and the breakup rate (Eq. 4.52), yields an ODE set that is numerically integrated by the `odeint` algorithm. The time integration is an iterative operation since the CMD vector $\boldsymbol{C}$ is updated at each time step. The aggregation rate depends on the collision rate of platelets, which can occur by diffusion or advection, and the collision efficiency parameter η which relates to the availability of active binding receptors on the cellular wall. The diffusion and flow shear effects are

computed by the diffusive (Eq. 4.28) and advective kernels (Eq. 4.36), respectively. The importance of each of these effects on the collision rate can be evaluated by the Péclet number (Eq. 4.71). The breakup rate equation includes a breakup kernel (Eq. 4.63), as well as a fragment mass distribution (Eq. 4.53). In the simulations presented next, we use the binary splitting PMF (Eq. 4.60) to compose the fragment mass distribution. Both the advective (Eq. 4.36) and the breakup (Eq. 4.63) kernels are regulated by the shear rate G. Therefore, the steady state of the CMD depends on G, as stipulated by the aggregation-breakup ratio K_{ab} (Eq. 4.76). All kernel functions (Eqs. 4.28, 4.36, and 4.63) require the size of the aggregates given by the radius of gyration (Eq. 4.10). The numerical system is discretized by the clusters classified by platelet number in the vector $\boldsymbol{w}$.

4.5 Results

First, the PBE dynamics is presented with the results of a few simulations. These results illustrate the dynamics discussed previously in Sections 4.2 and 4.3. Next, the PBE is correlated with experimental data of Xia and Frojmovic (1994) [236].

4.5.1 Dynamics

Figures 4.20 and 4.21 show the evolution of the aggregation-breakup PBE (Eq. 4.12) in time, starting from a state of zero aggregation ($PA = 0$) to steady state condition. The parameters of the aggregates are: concentration of activated platelets $C_p = 300{\cdot}10^{12}\,\mathrm{m}^{-3} = 300\,000\,\mu\mathrm{L}^{-1}$, platelet radius $R_p = 1.16\,\mu\mathrm{m}$, and fractal dimension $D_F = 2.2$. Platelets aggregation occurs due to collision by velocity gradient $G = 500\,\mathrm{s}^{-1}$ (Eq. 4.36), with aggregation efficiency $\eta = 0.3$. Aggregate splitting is binary (Eq. 4.60, with the constitutive parameters of the breakup kernel (Eq. 4.63) being: $b = 2$, $c = 3$, and $G^* = 8004\,\mathrm{s}^{-1}$. Mass conservation was guaranteed after 30 s of simulation.

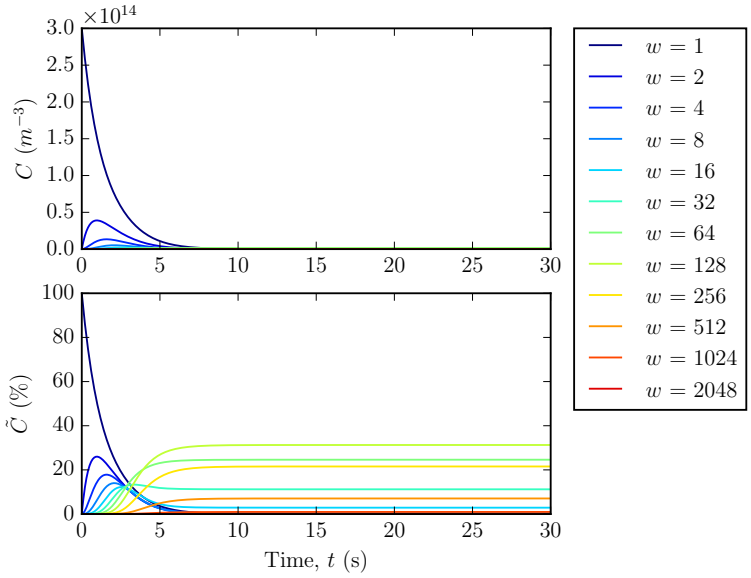

Fig. 4.20: Evolution of the aggregation-breakup PBE. The *top* graph shows the concentrations C_i of different clusters formed by w_i platelets. The *bottom* graph show the PPD $\tilde{C}_i$ (Eq. 4.4) in each of those clusters.

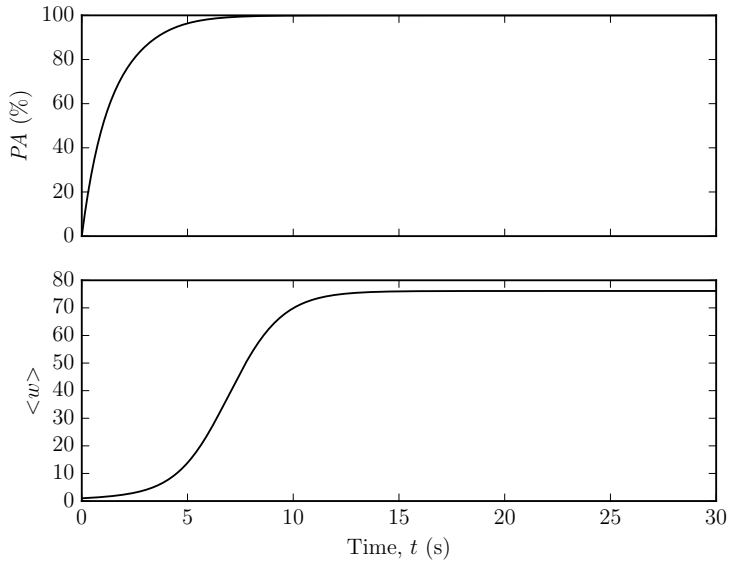

Fig. 4.21: Evolution of the aggregation-breakup PBE. The *top* graph shows the fraction of aggregated platelets PA (Eq. 3.80). The *bottom* graph show the mean number of platelets per aggregate $\langle w \rangle$ (Eq. 4.7).

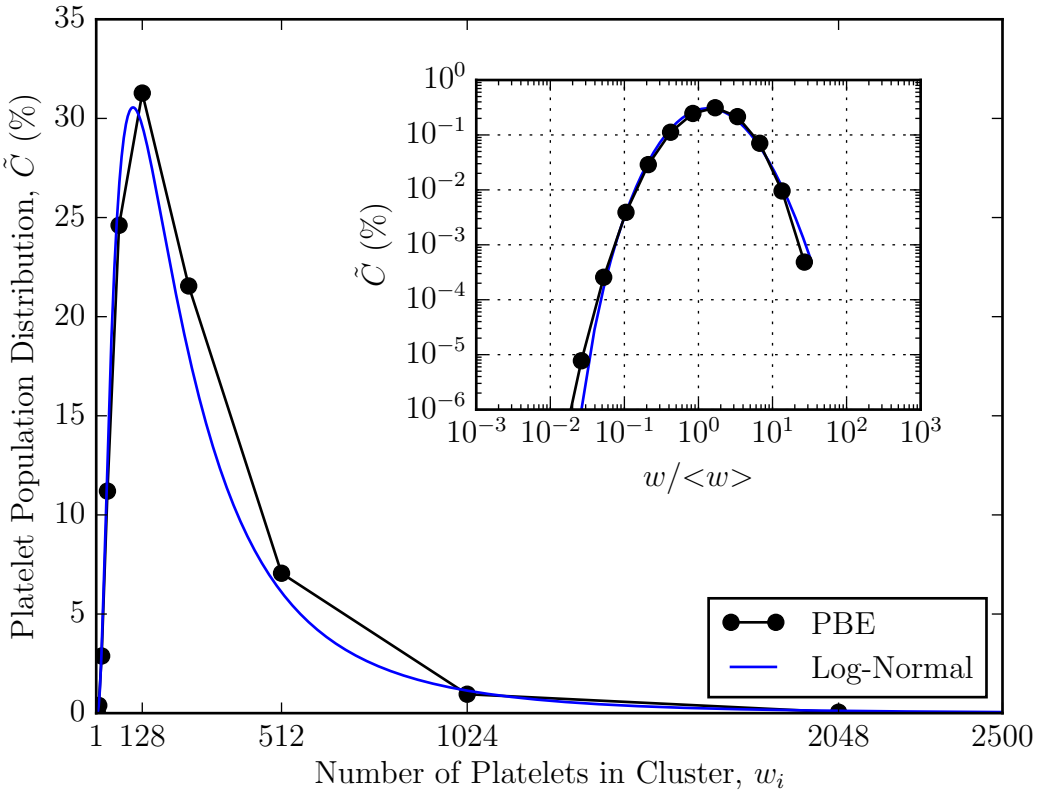

Fig. 4.22: Steady state of the PPD shown in Fig. 4.20. The *inset* shows the log-log graph of the PPD with normalized number of platelets per aggregate ($w/\langle w \rangle$). The blue line is a log-normal distribution that approximates the steady-state PPD.

Figure 4.22 shows the platelet population distribution (PPD) at the steady state. Figure 4.22 can be interpreted as a perpendicular slice of Fig. 4.20 after steady state is reached. The log-normal approximation for the PPD is indicated in Fig. 4.22.

Next, both the shear rate G and the sensitivity of breakup to shear rate G^* are varied in order to maintain the same aggregation-breakup ratio K_{ab}. Figure 4.23 shows these two simulation conditions converging to the same steady state. The condition where $G = 1000$ has an aggregation characteristic time t_a (Eq. 4.70) which is half the t_a of the condition where $G = 500$. Therefore, aggregation occurs in half the time for the former, compared to the later case.

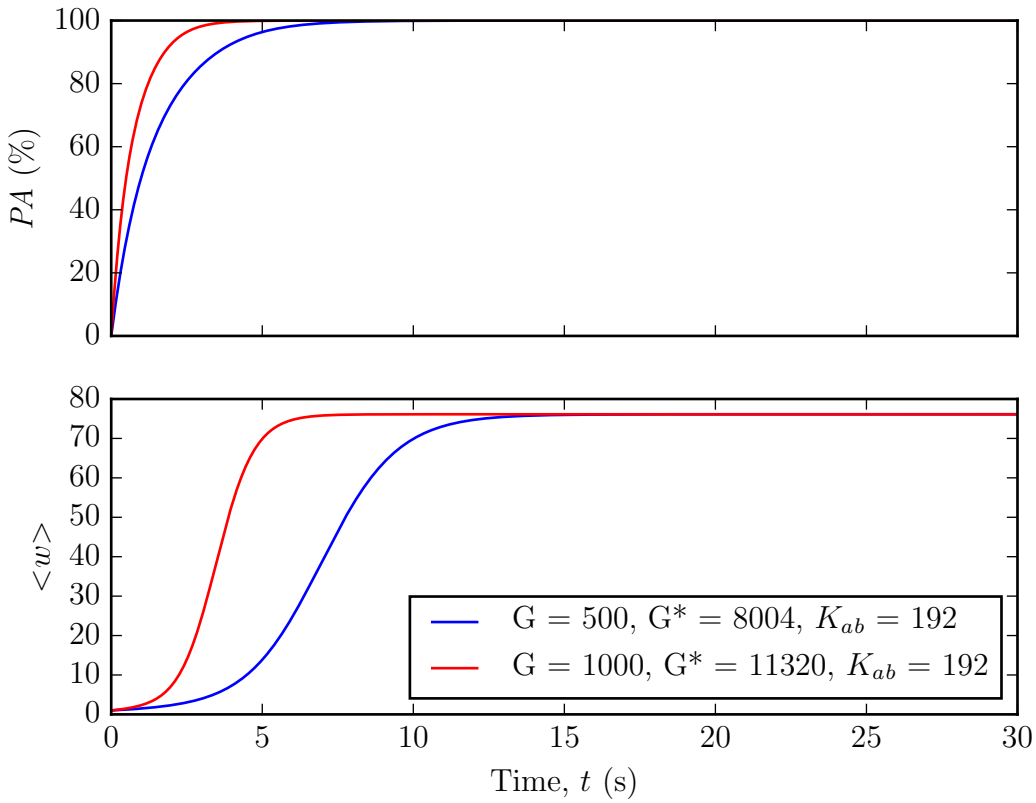

Fig. 4.23: Evolution of the aggregation-breakup PBE with two different conditions, but the same aggregation-breakup ratio K_{ab}.

Finally, the diffusion collision kernel (Eq. 4.28) is turned on. In Fig. 4.24 the evolution of the PBE system is displayed, comparing the diffusivity models of Brown and Sorensen to no diffusion condition. Because Péclet number (Eq. 4.71) is high ($Pe = 872 > 100$) for Brownian diffusivity at $G = 500\,\mathrm{s}^{-1}$, the simulation yields the same results whether Brownian diffusion is turned on or not. However, the Péclet number for the Sorensen EDM (Eq. 3.41) is low ($Pe = 1.66 < 100$), which nearly doubles the aggregation speed (or it nearly halves t_a). Nevertheless, the EDM is able to influence just the aggregation speed, but not the steady state. This occurs, because the diffusion kernel produces higher collision rates for the smallest aggregates, but the balance between the aggregation and breakup rates is achieved at the level of the largest aggregates, where the shear collision kernel is more potent (see Eq. 4.74, and Fig. 4.17).

4.5.2 Correlating with Experimental Data

To determine the effectiveness of our aggregation-breakup PBE model to correlate experimental data, we use the data of Xia and Frojmovic [236], because of the nature of the test flow and the clarity of the data presentation. Although Xia and Frojmovic applied the two-body collision model for the analysis of their experiments, their experimental data are suitable for estimation of the parameters of the new aggregation-breakup PBE model. Their experiments were conducted in Couette flow, which guarantees that all sampled platelets underwent the same shear rate (and stress) history, whereas other experiments were done in Poiseuille flow [25, 26, 80]. Although they have not recorded the whole CMD, we show in the following that the fraction of aggregated platelets PA has an unique association with the state of the CMD. A sensitivity analysis of the aggregation-breakup PBE model demonstrates how the different parameters affect the initial aggregation rate or the steady state. We show that PA_{max} can show an inverse relationship with shear rate G using the aggregation-breakup PBE, as

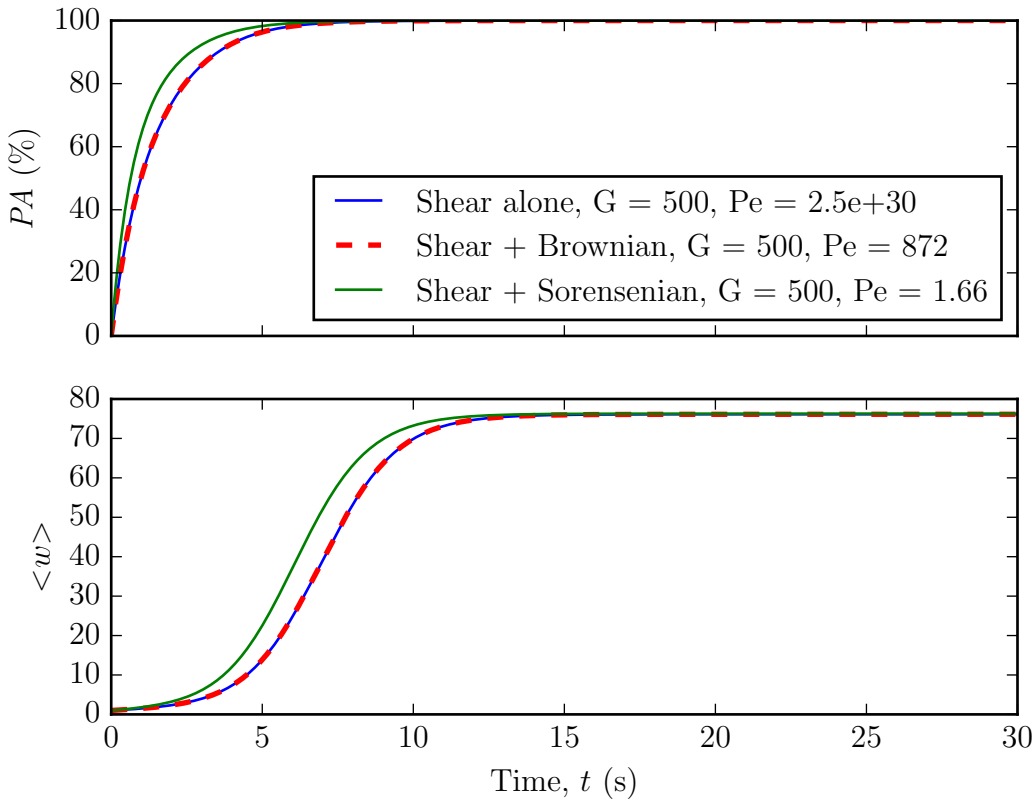

Fig. 4.24: Evolution of the aggregation-breakup PBE comparing the diffusivity models of Brown and Sorensen to no diffusion condition.

should have occurred for the formulation of Eq. 3.79. Finally, we demonstrate that the aggregation-breakup PBE model presents two distinct physical states: *low aggregation* and *high aggregation*. The characteristics of these two states are presented.

To show that SIPA correlates to the second order kinetics, as predicted by Eq. 4.15, Xia and Frojmovic ran tests at three distinct concentrations, as shown in Fig. 4.25. These samples were diluted ten-fold to increase the aggregation characteristic time, Eq. 4.70. The curve fitting obtained by Eq. 3.80 resulted in the same aggregation efficiency $\eta = 0.24 \pm 0.07$ (Eq. 3.82) for the three data sets. The curve-fitting precision was obtained from the correlation matrix of the weighted least-squares method. The error estimation of about 30% occurred due to the limited number of points as well as the significant experimental uncertainty.

The aggregation-breakup PBE was applied using aggregation efficiency $\eta = 0.3$, which is technically the same as the value obtained by the curve fitting, within experimental uncertainty. The break-up kernel parameters were adjusted so that the simulated curves would approximate the data points. Parameter b, which scales the power of shear to aggregate break-up in Eq. 4.63, was fixed as $b = 2$ in order to impose $K_{ab} \propto G^{-1}$ in Eq. 4.76. This was done because the steady state parameter $PA_{\max}$ in the curve-fitting equation (Eq. 3.81) was used by Xia and Frojmovic to scale the aggregation efficiency ($\eta \propto PA_{\max}$ in Eq. 3.82), which was then used to formulate Eq. 3.79 (where $\eta \propto G^{-1}$). Although aggregation efficiency itself is not necessarily related to shear rate, those empirical relations indicate that $PA_{\max} \propto G^{-1}$. Using the aggregation-breakup PBE, the steady-state PA varies directly with K_{ab}. With $b = 2$, $PA(t \to \infty) \propto K_{ab} \propto G^{-1}$. We tested two values for parameter c: $c = 1$ and $c = 3$. Because this parameter regulates the intensity of breakup to the aggregate size, the parameter G^* that regulates the breakup of the whole CMD to shear rate had to be adjusted to each case of parameter c. Consequently, the curve fit of the PBE was performed with the parameter pairs $c = 1$ and $G^* = 928\,\mathrm{s}^{-1}$, and $c = 3$ and

$G^* = 1540\,\mathrm{s}^{-1}$. These two pairs of arguments along with $\eta = 3$ and $b = 2$ are able to fit the experimental data of the three concentrations of activated platelets C_p in Fig. 4.25.

The simulations in Fig. 4.25 are compared with the fitted inverse-exponential curves using Eq. 3.81. The initial aggregation rate $\frac{d}{dt}PA(t = 0)$ was the same in all cases because they all used the same aggregation parameters. However, the state at $t = 60\ s$, which was not necessarily steady in all cases, was sensitive to parameter c. The fraction of aggregated platelets was more sensitive to variations of C_p for $c = 1$ than $c = 3$. This is expected, since the parameter c regulates aggregate growth by being the exponent of aggregate size in Eq. 4.63.

In order to investigate the sensitivity of the simulated results to physical uncertainties, we varied the aggregation-breakup ratio K_{ab} (Eq. 4.76) and the aggregation characteristic time t_a (Eq. 4.70) by $\pm 10\,\%$. Figure 4.26a shows that the steady-state fraction of aggregated platelets PA depends on K_{ab}, and Fig. 4.26b shows that the initial aggregation rate $\frac{d}{dt}PA(t = 0)$ depends on t_a. Figure 4.26b also shows that the PBE steady state was not achieved for platelet concentrations $40\,000\,\mu\mathrm{L}^{-1}$ and $60\,000\,\mu\mathrm{L}^{-1}$ at 60 s. We analysed the relation of K_{ab} to PA_{max}, and we found the linear relations $PA_{max} = 2.50\,K_{ab}$ and $PA_{max} = 1.12\,K_{ab}$ for $c = 1$ and $c = 3$, respectively. Thus, for an unknown value of c ranging in 1–3, the sensitivity of PA_{max} to K_{ab} varies by maximally a factor of approximately 2. The linear relationship of PA_{max} to C_p, for C_p ranging from 20 000–60 000 $\mu\mathrm{L}^{-1}$, was reported by Xia and Frojmovic [236]. The same relationship occurs in our model, since $K_{ab} \propto C_p$.

Similarly to parameter c, the fractal dimension D_F regulates the aggregation and breakup ratios to the size of the aggregates (see Eq. 4.74 and 4.74). Figures 4.27a and 4.27b present the sensitivity of PA_{max} to D_F for $c = 1$ amd $c = 3$, respectively. In these figures, the base value of D_F is $D_F = 2.2$ for Brownian diffusion [50], $D_F = 2.4$ is an intermediate value, and $D_F = 3.0$ is the value for coalescence (compact aggregates).

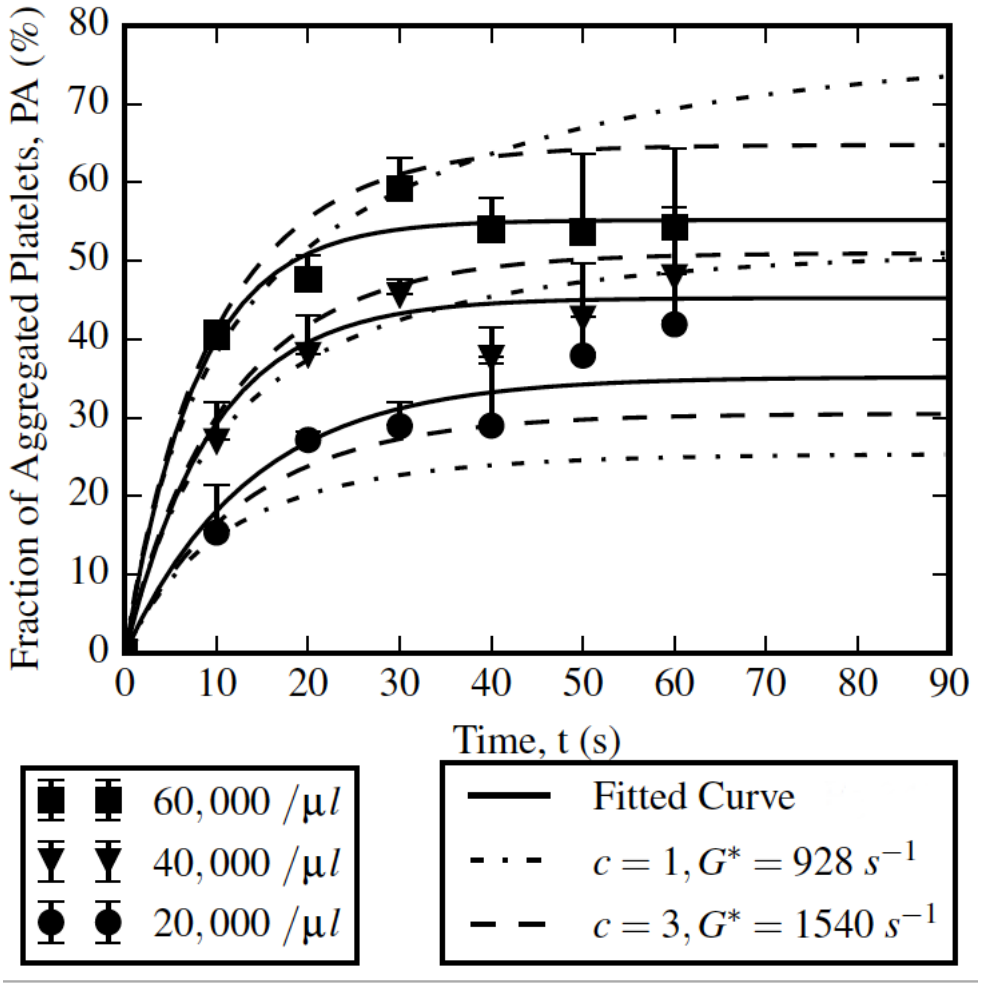

Fig. 4.25: Dependence of platelet concentration on the aggregation rate at $G = 250\,\mathrm{s}^{-1}$. Data from Xia and Frojmovic (1994) [236] showing fraction of aggregated platelets (PA). The solid lines represent the curve fitting with Eq. 3.81 [236]. All simulations were run with parameters $\eta = 0.3$ and $b = 2$. The dash-dotted lines represent the present aggregation-breakup PBE with parameters $c = 1$ and $G^* = 928\,\mathrm{s}^{-1}$. For this case, K_{ab} was 0.10, 0.21 and 0.31, for platelet concentration (C_p) $20\,000\,\mu\mathrm{L}^{-1}$, $40\,000\,\mu\mathrm{L}^{-1}$ and $60\,000\,\mu\mathrm{L}^{-1}$, respectively. The dashed lines represent the present aggregation-breakup PBE with parameters $c = 3$ and $G^* = 1540\,\mathrm{s}^{-1}$. For this case, K_{ab} was 0.28, 0.57 and 0.85, for platelet concentration (C_p) $20\,000\,\mu\mathrm{L}^{-1}$, $40\,000\,\mu\mathrm{L}^{-1}$ and $60\,000\,\mu\mathrm{L}^{-1}$, respectively.

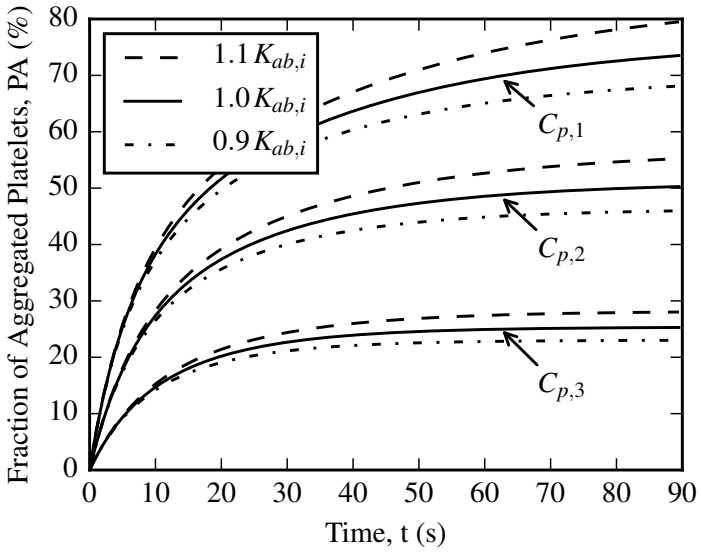

(a) Variations of the aggregation-breakup ratio $K_{ab,i}$ ($t_{a,i}$ constant).

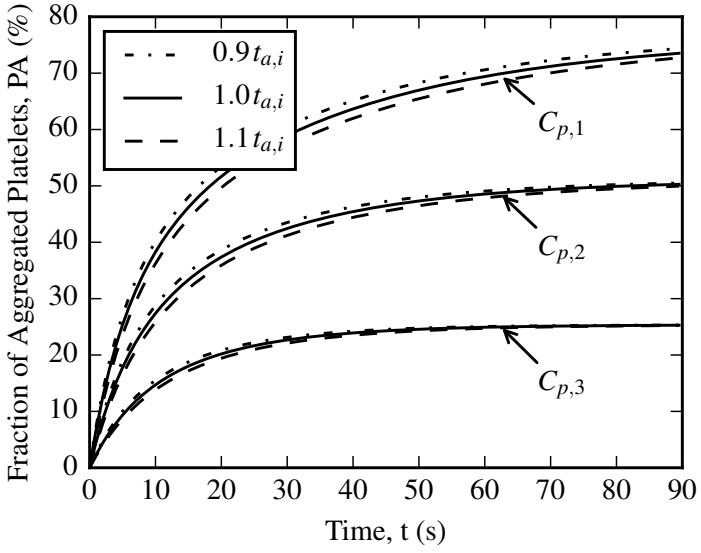

(b) Variations of the aggregation characteristic time $t_{a,i}$ ($K_{ab,i}$ constant).

Fig. 4.26: Sensitivity of the aggregation-breakup PBE to K_{ab} and t_a. The subscript i in $K_{ab,i}$ and $t_{a,i}$ denotes values of K_{ab} and t_a corresponding to platelet concentrations $C_{p,1} = 60\,000\,\mu\text{L}^{-1}$, $C_{p,2} = 40\,000\,\mu\text{L}^{-1}$ and $C_{p,3} = 20\,000\,\mu\text{L}^{-1}$, respectively. Solid lines show simulations of the PBE model with the same $K_{ab,i}$ and $t_{a,i}$ depicted in Fig. 4.25 for $c = 1$ and $G^* = 928\,\text{s}^{-1}$. Dashed and dash-dotted lines show variations of K_{ab} and t_a of $\pm 10\%$ about the reference conditions $K_{ab,i}$ and $t_{a,i}$, respectively. The steady state is controlled by K_{ab}, and the initial transient rate is controlled by t_a.

Interestingly, PA_{max} decreases as D_F increases for $c = 1$. These trends are related to the the number by which the number of platelet in the clusters (v_i) are powered in Eqs. 4.74 and 4.75. They are powered by $3/D_F$ and c/D_F for aggregation and breakup, respectively. Therefore, aggregation rate decreases more than breakup as D_F increases, if $c \neq 3$. However, for $c = 3$, aggregation and breakup rates are equal in power, then aggregation rate increases slightly more than breakup just because it encloses a sum of two numbers $v_i \geq v_j \geq 1$, instead of just one number $v_j \geq 1$ of the breakup kernel.

Figure 4.28 shows the dependence of the steady state of the aggregation-breakup PBE on the aggregation-breakup ratio K_{ab} (Eq. 4.76). The sensitivity of PA_{max} to K_{ab} is seen as the slope of the continuous lines in Fig. 4.28, both for $c = 1$ and $c = 3$. As the inset in Fig. 4.28 shows, the relation of PA_{max} and K_{ab} is linear for $K_{ab} \ll 1$, and it becomes asymptotic to 1 as $K_{ab} \to 1$. The same behaviour was reported by Xia and Frojmovic on the relation of η and G^{-1} [236]. The fact that our PBE model obtains the same behaviour as the experimental data, by following the rule $K_{ab} \propto G^{-1}$ with $b = 2$, it supports the hypothesis that the aggregation efficiency η could be modeled as a shear-independent constant when breakup is considered. A high count of free platelets in a shearing sample could not necessarily mean that they were not aggregating. If our hypothesis is correct, then those free activated platelets were aggregating for short intervals, but the aggregates were being broken up by shear forces. The equilibrium is the point where aggregation and breakup rates have the same intensity, not where both cease to exist.

The relation of $PA_{\max}$ and K_{ab} breaks down for $K_{ab} \gtrsim 1$, and $PA_{\max} \approx 100\%$. At this point, the mean number of platelets per aggregate $\langle w \rangle$ becomes a better metric for platelet aggregation, and the CMD becomes similar to a log-normal distribution with self-similar shape regardless of K_{ab}, see Fig. 4.30. As expected by Eq. 4.78, for $K_{ab} \gtrsim 1$, $\frac{dlog\langle w \rangle}{dK_{ab}}$ is 11 and 1 for $c = 1$ and $c = 3$, respectively, as depicted by the inset in Fig. 4.28.

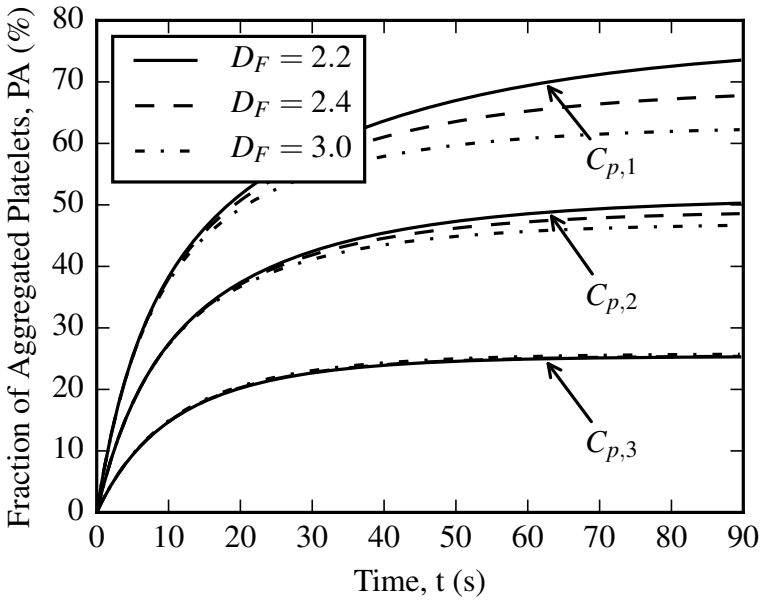

(a) Parameters $c = 1$ and $G^* = 928\,\mathrm{s}^{-1}$.

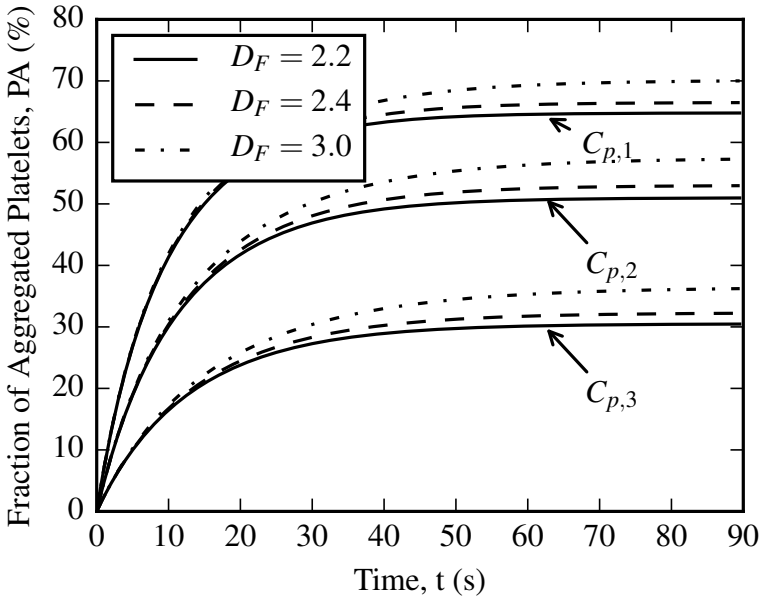

(b) Parameters $c = 3$ and $G^* = 1540\,\mathrm{s}^{-1}$.

Fig. 4.27: Sensitivity of the aggregation-breakup PBE to fractal dimension D_F. Solid lines show the same results presented in Fig. 4.25 for platelet concentration $C_{p,1} = 60\,000\,\mu\mathrm{L}^{-1}$, $C_{p,2} = 40\,000\,\mu\mathrm{L}^{-1}$ and $C_{p,3} = 20\,000\,\mu\mathrm{L}^{-1}$.

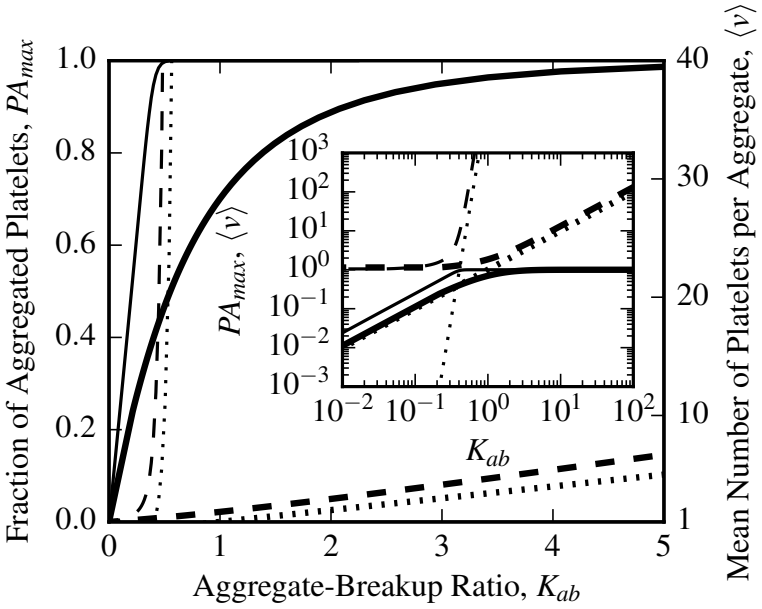

Fig. 4.28: Dependence of the steady state on the aggregation-breakup ratio K_{ab}. Solid lines represent the fraction of aggregated platelets $PA_{\max}$, and dashed lines represent the mean number of platelets per aggregate $\langle w \rangle$. Dotted lines represent the approximation by Eq. 4.78. Thin and thick lines represent parameter $c = 1$ and $c = 3$, respectively. The inset shows the same data in log-scale.

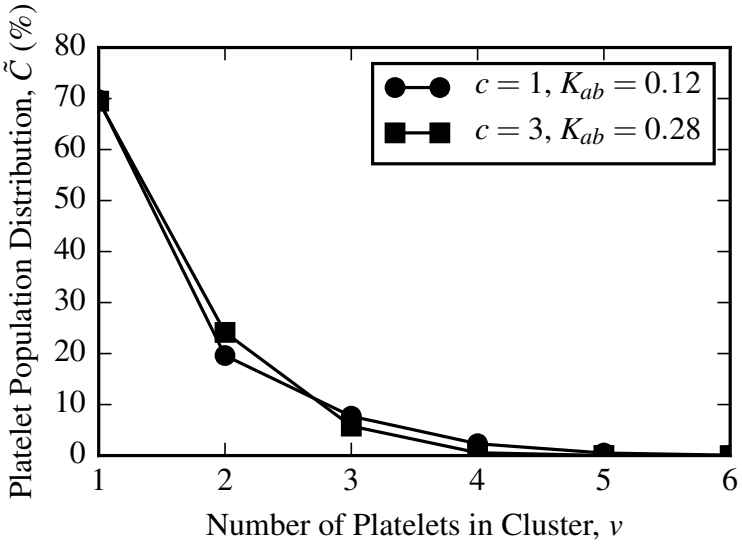

Fig. 4.29: Platelet population distribution at 30 % of fraction of aggregated platelets (PA).

The aggregation-breakup PBE model presents two steady-state physical phases, a low-aggregation phase when $K_{ab} \ll 1$, and a high-aggregation phase when $K_{ab} \gg 1$. Figure 4.28 shows a sharper phase transition occurring for $c = 1$ around $0.3 \lesssim K_{ab} \lesssim 0.5$, and a smoother phase transition for $c = 3$ around $1.0 \lesssim K_{ab} \lesssim 4.0$. When the aggregation-breakup ratio is lower than the transition region, there is a very low number of aggregated platelets. However, when the ratio is higher, there are very few free platelets. There are no aggregates at $K_{ab} \approx 0$. Doublets and a few triplets are formed as K_{ab} increases towards the transition region. The population distribution (Eq. 4.4) of the unaggregated phase is seen in Fig. 4.29. It corresponds to early microaggregation of activated platelets observed experimentally [236]. The parameter c as well as the fractal dimension D_F have minimal influence on the CMD shape in the unaggregated phase, since aggregates are small.

Larger aggregates are formed only in the high-aggregation phase ($K_{ab} \gg 1$). The population distribution in the aggregated phase resembles the log-normal distribution, as shown in Fig. 4.30. In Fig 4.30 the steady-state CMD is normalized at the mean

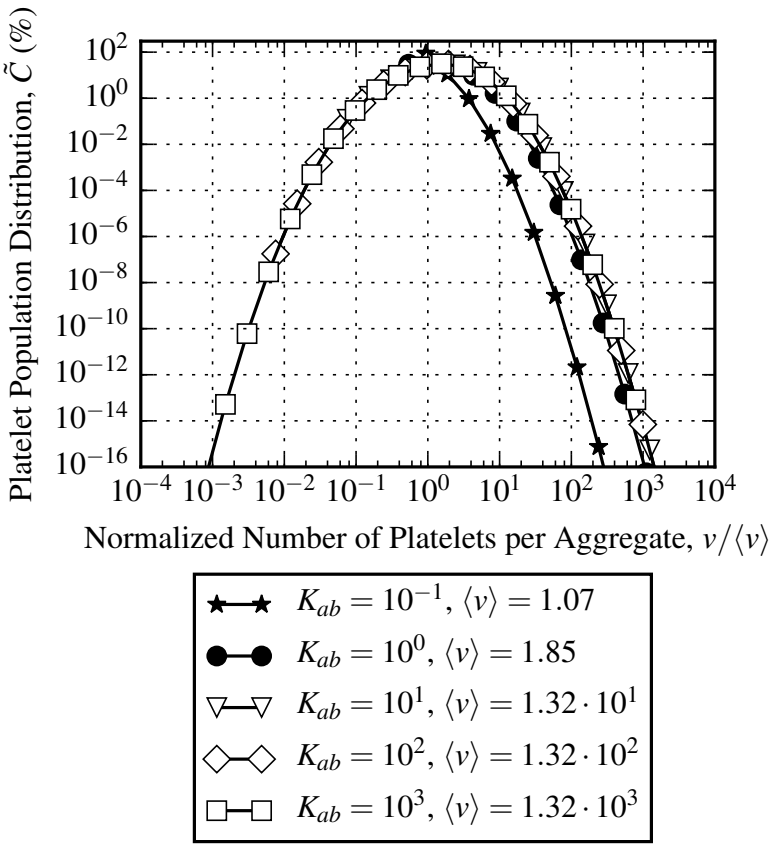

Fig. 4.30: Steady-state CMD shown over normalized platelets per aggregate. The markers represent the discretization classes of the CMDs. The CMD is self-similar for $K_{ab} \gg 1$ when normalized by $\langle w \rangle$. In this case, $\langle w \rangle \propto K_{ab}$ because $c = 3$ (see Eq. 4.78).

number of platelets per aggregate $\langle w \rangle$ to highlight the self-similarity of the distribution at different $K_{ab} \gg 1$. For $K_{ab} \lesssim 1$ the logarithm of the CMD does not resemble the normal distribution. The mean number of platelets per aggregate is proportional to the aggregation-breakup ratio as demonstrated by Eq. 4.78. It is also possible to observe in Fig. 4.30 that most of platelets form aggregates ranging $0.1\langle w \rangle$–$10\langle w \rangle$, other aggregate sizes are very rare. The mean cluster size is obtained by Eq. 4.80. The steady-state CMD becomes narrower with increasing D_F or c [16], which is related to the decrease in power of aggregation compared to breakup, as seen in Figs. 4.27a and 4.27b.

4.6 Discussion

Previous authors [42, 26, 102, 103, 104, 236, 80] have considered hydrodynamic effects inhibiting platelet aggregation, and incorporated this in models of aggregation efficiency. However, this approach only delays aggregation by prolonging the transient phase, as indicated in Eq. 4.70. Any model involving only the effect of aggregation would inevitably yield to a steady state where all platelets are clumped together in a single aggregate. A realistic theoretical steady state can only occur when two opposite rates come to equilibrium. Our model, incorporating aggregation and breakup processes, implies that aggregates are less noticed at higher shear rates because they break apart very quickly instead of building up at a slower pace. The scaling analysis shows that the equilibrium level of aggregation depends only on one dimensionless number, the aggregation-breakup ratio K_{ab}. The only physical quantities not appearing in K_{ab} are the fractal dimension D_F and the breakup parameter c, both of which control the power of aggregation and breakup along the CMD. At $K_{ab} \ll 1$, PA_{max} is linearly dependent on K_{ab}, with a low sensitivity to D_F and c. At $K_{ab} \gg 1$, $PA_{max} = 1$ and $\langle w \rangle$ becomes a more suitable parameter of aggregation, following the power-law relation in Eq. 4.78 which is much more sensitive to D_F and c.

The trend embodied in the empirical formula (Eq. 3.79) of Xia and Frojmovic for shear-dependent aggregation efficiency can be reproduced by our aggregation-breakup model with shear-independent aggregation efficiency, as seen in Fig. 4.28. In our simulations, we apply the fixed aggregation efficiency $\eta = 0.3$ because it is approximetely the highest value ($\eta = 0.29 \pm 0.01$) reported by Xia and Frojmovic, for their lowest shear rate ($G = 100\,\mathrm{s}^{-1}$) [236]. Although they presented a lower value for the data in Fig. 4.25 ($\eta = 0.24 \pm 0.07$ at $G = 250\,\mathrm{s}^{-1}$), our $\eta = 0.3$ is still a good value as our simulations show. It is important to stress that η affects primarily the steepness of the curves in Fig. 4.25, but the steady state depends also on the balance with the breakup parameters. This is illustrated in Figs. 4.26a and 4.26b, where parameters

of aggregation and breakup parameters were varied. Interestingly, Chang and Robertson reported $\eta = 0.368 \pm 0.175$ and 0.301 ± 0.051 for Brownian aggregation of rabbit platelets using two different methods [42]. If aggregation efficiency is considered to be independent of shear rate, it would be better to measure it in the absence of shear forces breaking aggregates up. Thus, measuring aggregation efficiency from Brownian aggregation should be more accurate than measuring from SIPA. Moreover, the aggregation efficiency reflects the ratio of the chemical rate for platelet-platelet bond formation to the collision rate. Because both a platelet collision and receptor chemical reaction must occur to consummate an aggregation event, the slowest rate controls the speed of this process. A low Brownian aggregation efficiency means that the chemical rate is slower than Brownian collision rate. Another evidence showing that platelet aggregation is controlled by the chemical rate is the observed fractal dimension $D_F = 2.2$ for aggregates formed out in Brownian motion [50]. A $D_F \approx 2.2$ is typical of aggregation controlled by chemical reaction. Aggregates controlled by the collision from Brownian motion are less compact, with $D_F \approx 2.2$, because generally monomers aggregate to the first contact with the fractal structure [144].

Xia and Frojmovic [236] conducted their experiments at concentration of activated platelets C_p equivalent to 1/10 of physiological platelet concentration. There are at least three reasons for this. First, it is very unlikely to have all platelets activated in natural conditions. Second, aggregation characteristic time is inversely proportional to the concentration of activated platelets ($t_a \propto C_p$, Eq. 4.70). Therefore, if C_p was equivalent to the physiological concentration of platelets, steady state would be achieved in less then 5 s at $G = 250\,\mathrm{s}^{-1}$, which is less than the 10 s sampling period. Third, the aggregation-breakup ratio would be ten times higher, because $K_{ab} \propto C_p$ (Eq. 4.76), which would result in a $K_{ab} > 1$. We show that $PA_{max} \propto K_{ab}$ only for $K_{ab} \ll 1$, and $\langle w \rangle \propto K_{ab}^{\frac{1}{D_F+c-3}}$ for $K_{ab} \gg 1$. Thus, it is only possible to use PA_{max} to quantify platelet aggregation if $K_{ab} \ll 1$. Nonetheless, the experimental data of Huang and

Hellums [102, 103, 104] indicates a log-normal CMD if the concentration of particles whose size is similar to free platelets is disconsidered. It seems that the samples of Huang and Hellums contained a mixture of activated and unactivated platelets, whereas the experiment of Xia and Frojmovic contained only activated platelets. Despite the theoretical expectation that the present PBE model is valid for $K_{ab} > 1$ (i.e. high platelet concentration) there is not yet any conclusive experimental evidence to confirm it.

It has been shown in a previous work that the concentration of ADP in platelet-rich plasma was linearly proportional to aggregation rate, whereas the concentration of prostaglandin E_1 (PGE_1) was inversely proportional [42]. Similarly, in a mixture of fully activated platelets with resting platelets, the aggregation efficiency was linearly related to the proportion of activated platelets [236]. This linear relationship to the concentration of activated platelets suggests that there are two distinct states (*resting* or *activated*) instead of a continuous transition between both states. A platelet would exert its full potential to aggregate if it is activated, but there would not be any half-activated state where it would have half the potential to aggregate. On the basis of this hypothesis, different platelets could have different sensitivity to activation stimuli. Once the pro-activation stimuli overcomes the power of the anti-activation stimuli, resting platelets would flip to the activated state. Hence, when dealing with a mixture of activated and resting platelets the two populations should be split into separate groups, each with its own concentration. Stimuli of distinct intensities would be able to transfer a certain portion of resting platelets to the activated platelets group. This is the the approach normally found in the literature to formulate models of platelet activation, where a rate function transforms resting platelets into a single class of activated platelets proportionally to chemical and mechanical stimuli present in the system [142, 134, 203]. Accordingly, as the concentration of activated platelets C_p increases, so does the characteristic aggregation rate ($1/t_a$) and aggregation-breakup

ratio K_{ab}, as seen in Eqs. 4.70 and 4.76. A change in K_{ab} would immediately change the CMD's steady state.

The PBE model presented in this chapter attempts to rationalize the observations that the steady state of SIPA is inversely proportional to shear rate. We note that SIPA modeled as a one-way process is unable to explain the steady states detected experimentally. We apply this PBE model because it succeeds in describing shear-induced aggregation of non-biological colloids. This model is also capable of separating the shear rate from other physicochemical aspects of SIPA, such as platelet activation and platelet to platelet chemical bonding. This is important for better interpreting SIPA experiments in complex flows, such as in platelet aggregometry (in a stirred cuvette) or in biomedical devices. Nevertheless, this is not a conclusive model for SIPA, mainly because the binding mechanism between platelets was not elucidated. The presence of a linking protein, such as fibrinogen or vWF, is required in platelet aggregation. Therefore, the concentration of such molecules in the plasma is an important factor in SIPA, which was not addressed in this paper. Either the lack or the excess of such molecule in plasma can decrease aggregation efficiency η, because the lack of these molecules reduces the chance of bond formations and the excess results in the saturation of membrane receptors [236, 138]. Another important aspect is to model how these molecules interact with enzymes when they are connected to membrane receptors. Furthermore, if the aggregate bonds are stronger than the platelet membrane a breakup would possibly damage platelets, rendering breakup irreversible. These types of interactions could also have important roles in the steady state of SIPA. Finally, the maturation of the aggregates into stable thrombi reinforced by a fibrin mesh was not considered. Possibly, after a time span, platelet aggregates loose their ability to aggregate and breakup. Thus, stable thrombi would not breakup at the high shear stresses present in microvessels.

Chapter 5

Shear-Induced Platelet Aggregation in Non-Uniform Flow

Shear induced platelet aggregation (SIPA) naturally occurs in non-uniform flows, where both the velocity and shear rates vary in space and time. Shear induced platelet aggregation is present in light transmission platelet aggregometry (LTPA), a technique used in medical laboratories to test the effectiveness of patient platelet function. Non-uniform SIPA has also been experimentally observed in flow inside tubes. These non-uniform flow systems are discussed below. To simulate SIPA in non-uniform conditions, the method presented in Chapter 4 was extended. The population balance equation (PBE) for aggregation and breakup (Eq. 4.12) was included as the reaction term (or source term) in the transport equations (Eq. 3.1) for each cluster type discretised in a cluster mass distribution (CMD). The velocity field obtained is from a computational fluid dynamics (CFD) simulation, whose gradient is used to calculate the shear rate field. The effects of non-uniform flow on SIPA are analysed, and simulations are compared with experiments documented in the literature.

5.1 Numerical Modelling

The transport equation (Eq. 3.1) of each aggregate cluster class i, including the aggregation-breakup PBE (Eq. 4.12) as the source term, is given by

$$\frac{\partial C_i}{\partial t} = D_i \boldsymbol{\nabla}^2 C_i - \boldsymbol{\nabla} \cdot (\boldsymbol{v} C_i) + A_i + B_i \ , \tag{5.1}$$

where $\boldsymbol{v}$ is the velocity vector, D_i is the diffusivity constant, A_i is the Smoluchowski aggregation equation (Eq. 4.15), and B_i is the breakup equation of Pandya and Spielman (Eq. 4.52). By expanding A_i and B_i, Eq. 5.1 is written as

$$\begin{aligned} \frac{\partial C_i}{\partial t} =& D_i \boldsymbol{\nabla}^2 C_i - \boldsymbol{\nabla} \cdot (\boldsymbol{v} C_i) \\ &+ \eta \left[\frac{1}{2} \sum_{j=1}^{i-1} k_c(R_i - R_j, R_j) C_{(i-j)} C_j - \sum_{j=1}^{n} k_c(R_i, R_j) C_i C_j \right] \\ &- k_b(R_i) C_i + \sum_{j=i+1}^{n} g(w_i, w_j)\, k_b(R_j)\, C_j \ , \end{aligned} \tag{5.2}$$

where η is the aggregation efficiency, R_i is the radius of gyration of the aggregate, w_i is the number of platelets clustered in the aggregate, $g(w_i, w_j)$ is the fragment mass distribution, and $k_c(R_i, R_j)$ and $k_b(R_j)$ are the collision and breakup kernels, respectively. The diffusivity constant of the aggregates is given by the Stokes-Einstein relation (Eq. 3.38), which is inversely proportional to the aggregate radius of gyration (Eq. 4.10). For simplicity, the fragment mass distribution $g(w_i, w_j)$ (Eq. 4.53) used in this work is the binary splitting (Eq. 4.60), where aggregates break up into two clusters of half the number of platelets of the original cluster. Bäbler and Morbidelli (2007) [16] showed that different fragment mass distribution can move the steady state of the PBE by two to four orders of magnitude in terms of mean number of platelets per cluster $\langle w \rangle$ (Eq. 4.7) and root-mean-square (RMS) radius of gyration $\langle R \rangle_{\mathrm{rms}}$ (Eq. 4.9). However, different fragment mass distributions barely change the shape of the steady-state CMD, and this difference is compensated by the constants of the breakup

kernel, which are obtained from the correlation of the steady-state CMD, as it was demonstrated in Chapter 4.

5.1.1 Implementation

Equation 5.2 is a set of partial differential equations (PDEs), whose general solution can be obtained by discretising the space in a finite number of cells. This sets a finite boundary value problem, which can be solved by different numerical methods. The finite volume method (FVM) was used to integrate the spatio-temporal evolution of Eq. 5.2, because it is the most estabilished method in computational fluid dynamics (CFD) [61]. The computer library OpenFOAM®(Open Field Operation and Manipulation) [226] was applied to implement Eq. 5.2 in FVM. OpenFOAM is an open source library of FVM written in C++, which is widely used in both academia and industry to solve PDE problems, including anything from complex fluid flows involving chemical reactions, turbulence and heat transfer, to solid dynamics and electromagnetism. By being open, OpenFOAM offers users complete freedom to customise and extend its existing functionality. Thus, a solver named `aggBreakupFoam` was written to integrate Eq. 5.1, given any velocity field obtained by a steady-state CFD solver. It is possible to run this solver in parallel using domain decomposition and message passing interface (MPI) [92]. The process of parallel computation involves three steps: (1) decomposition of mesh and fields, (2) running `aggBreakupFoam` in parallel, and (3) reconstruction of mesh and fields for post-processing.

The velocity field $\boldsymbol{v} = \boldsymbol{v}(x, y, z)$ is obtained from the integration of the Navier-Stokes equation (Eq. 3.9). Normally, the integration of steady-state velocity and pressure fields is performed by the SIMPLE algorithm [170], which is an acronym standing for *Semi-Implicit Method for Pressure Linked Equations*. The SIMPLE algorithm is essentially an iterative loop, where the pressure and velocity fields are independently solved and used to correct one another, so that the algorithm converges to the steady-

state solution of the Navier-Stokes equation [61, p. 168]. OpenFOAM provides a solver named `simpleFoam`, which runs the SIMPLE algorithm.

The solver `aggBreakupFoam` takes the steady-state velocity field and solves the transient states of the PBE both in space and time. It is assumed that the platelet aggregates do not significantly interfere with the velocity field because the volume fraction of platelets is less than 1% (see Tab. 3.1). This assumption could appear to be unphysical once aggregates become as large as the mesh cells, although does not become invalid. This model computes average results that exclude random field distortions made by passing particles, since it deals with concentration of particles instead of discrete particles. Even though large aggregates could locally distort the flow field, these distortions would be sparse and local, due to the fact that the volume fraction of platelets is very low.

5.1.2 Spatial Analysis of SIPA Dynamics

The CMD forms a field of too many degrees of freedom to be simultaneously visualised in the post-processing. Therefore, integral quantities are used to interpret the state of the CMD without having to compare each pivot point of the discretised CMD individually (see Section 4.1.2). Integral quantities include the moments of the CMD M_j (Eq. 4.6), and other integral quantities derived from these moments, such as the mean number of platelets per cluster $\langle w \rangle$ (Eq. 4.7), the zero angle intensity of scattered light I_0 (Eq. 4.8), and the RMS radius of gyration $\langle R \rangle_{rms}$ (Eq. 4.9). A quantity that is commonly used to represent the proportion of aggregated platelets in the system is the fraction of aggregated platelets PA (Eq. 3.80), which is not an integral quantity because it only provides information about the free platelets. All these quantities are easily calculated over the whole space occupied by the system, so that they form a summarised display of the state of the CMD in space.

Similarly, the characteristic times for aggregation t_a (Eq. 4.70) and breakup t_b

(Eq. 4.76) are used to interpret the evolution rate of the system. The characteristic times display the time-scales in which transformations occur. Characteristic times can be used to compare rate intensities in the form of dimensionless numbers. For instance, the intensity of two mechanisms of platelet aggregation, shear-induced and diffusion-induced, are compared by the aggregation Péclet number Pe (Eq. 4.72). If one of these mechanisms is many orders of magnitude larger than the other, the slowest mechanism can be ignored, because the transformation it produces is too weak, relatively. On the other hand, aggregation and breakup rates are opposed conversion rates. Thus, the dimensionless number that compares these rates, the aggregation-breakup ratio K_{ab} (Eq. 4.76), features the equilibrium state of the system, for it is the dissociation constant (Eq. 3.48) of the aggregation-breakup system.

Other characteristic times are introduced when dealing with spatial differences. Flow rate introduces an advection characteristic time

$$t_{adv} := \frac{L}{v} \ , \tag{5.3}$$

where L is the transported distance, and v is the local velocity of the fluid. The diffusion characteristic time over the same distance L is given by

$$t_{diff} := \frac{L^2}{D} \ , \tag{5.4}$$

where D is the diffusivity constant. Thus, the Péclet number defined to evaluate the transport ratio over the distance L is

$$Pe_L := \frac{t_{diff}}{t_{adv}} = \frac{Lv}{D} \ . \tag{5.5}$$

This Péclet number Pe_L is equivalent to the Péclet number previously defined in Eq. 4.72, if the mean velocity and mean distance between particles are applied as v and L, respectively.

For the numerical solution of a transient PDE, normally both space and time are divided in discrete segments. The space is divided in cells forming a mesh, and time

is divided in time steps. In order to obtain a reliable solution, a constraint must be imposed between the spatial and temporal meshes. In essence, the temporal steps must be short enough in order to capture information travelling from one mesh point to its next neighbour mesh point. The numerical integration becomes unreliable if the time integration of a flux is longer than the distance between mesh points. This numerical constraint is known as the Courant–Friedrichs–Lewy (CFL) condition, and it is satisfied if

$$Co := \frac{\Delta t}{t_{adv}} = \frac{v\,\Delta t}{\Delta x} \leq 1 \ , \tag{5.6}$$

is guaranteed at every mesh point of the mesh. The dimensionless number Co is known as the Courant number, Δt is the time step, and Δx (L in Eq. 5.3) is the distance between mesh points [61].

The dimensionless number which relates the conversion rate of any substance to the transport rate is the Damköhler number (Da) [65]. It is widely used to get estimates of the production or consumption of substances in a chemical reactor, given a certain residence time. The Damköhler number for SIPA is defined as

$$Da := \frac{t_{adv}}{t_a} = \frac{L}{v}\eta\frac{4}{3}G\,(2R_p)^3 C_p \left(1 + \frac{1}{Pe}\right) \ , \tag{5.7}$$

where t_{adv} is the advection characteristic time defined in Eq. 5.3, and t_a is the aggregation characteristic time defined in Eq. 4.70. Like the Courant number, cell Damköhler numbers are evaluated at each mesh cell (so, $L \equiv \Delta x$) in order to give a constraint to the numerical integration method. Even though the CFL condition remains a necessary condition, it is not sufficient for a reliable integration of the numerical method if $Da \gg 1$. In this case, conversion rates at grid points are far higher than the transport between grid points, and eventual changes in conversion rates would not be resolved if the time step is close to the limit imposed by the CFL condition. A solution for that is to solve the conversion of substances (or aggregation) in substeps between the transport time steps, rather than solving the whole transport equation many times at

the conversion time-scale. Another possible solution is to give an automatic update to the steady state of the CMD, as a state equation, if the steady state is known.

On the other hand, if $Da \ll 1$, the transformation rate is far slower than the transport rate. In this case, the CFL condition is a sufficient condition, and the conversion rates given by the state of the last step can be safely given as source terms in the transport equation. Evidently, physical systems with multiple time-scales are complex to solve numerically.

5.2 User Guide to `aggBreakupFoam`

In the `aggBreakupFoam` solver, each discretised aggregate concentration of the CMD is solved independently at every time step. The concentration fields of the CMD are named as `C_w`, where `w` is the number of platelets (monomers) contained in those aggregates. Hence, the boundary conditions of each cluster concentration are independent of the other cluster concentrations, which makes it possible to set the whole CMD as a fixed-value boundary condition. Since it might be tedious for setting the boundary values of the many discretised concentrations of the CMD, the user is able to set default boundary conditions (named `Cdefault`) to all aggregate concentrations, whose boundary conditions are the same. All the `aggBreakupFoam` options are set by the user in the dictionary `aggBreakupProperties`. These options are:

isPBEcoupled (Boolean switch)

Coupled PBE is updated at every time step and included as explicit source term in the transport equations of the CMD. Otherwise, the PBE is solved separately by an ordinary differential equation (ODE) solver at each cell independently, after solving the transport equation.

odeSolver (subdictionary)

The ODE solver and its options are set here, if `isPBEcoupled = false`.

solver (string label)

Sets the solving method.

relTol (scalar)

Relative convergence tolerance per step.

absTol (scalar)

Absolute convergence tolerance per step.

subDeltaT (scalar)

Initial time substep size.

isGridUniform (Boolean switch)

Specify the bin structure of the discretised CMD. If true, then a linear bin structure is used (Eq. 4.82), and the PBE is solved in standard form. Otherwise, the bin structure is geometrically spaced (Eq. 4.81), and the PBE is solved using the fixed pivot method (FPM) of Kumar and Ramkrishn [136].

nBins (integer)

Number of discretization points of the CMD (n in Eqs. 4.81 and 4.82).

Rp (dimensioned scalar)

Monomer mean radius in meters (R_p in Eq. 4.10).

DF (scalar)

Cluster fractal dimension (D_F in Eq. 4.10).

isBrowninanAggOn (Boolean switch)

Whether the Brownian diffusion model (Eq. 4.29) is computed for the collision rate of the aggregates.

isShearAggOn (Boolean switch)

Whether the shear model (Eq. 4.48) is computed for the collision rate of the aggregates.

isSorensenianAggOn (Boolean switch)

Whether the Sorensenian diffusion model (Eq. 4.28 with diffusivity constant defined by Eq. 3.41) is computed for the collision rate of the aggregates.

isBreakupOn (Boolean switch)

Whether the aggregate breakup model of Pandya and Spielman (Eq. 4.52) is computed.

T (dimensioned scalar)

Base absolute temperature in degrees Kelvin used to obtain the Brownian diffusivity constant defined by the Stokes-Einstein relation (T in Eq. 3.38).

muMedium (dimensioned scalar)

Base dynamic viscosity in Pa.s used to obtain the Brownian diffusivity constant defined by the Stokes-Einstein relation (μ in Eq. 3.38).

eta (scalar)

Aggregation efficiency (η in Eq. 5.2).

Gstar (dimensioned scalar)

Characteristic shear rate for breakup in s^{-1} (G^* in Eq. 4.63).

b (scalar)

Constitutive parameter in Eq. 4.63.

c (scalar)

Constitutive parameter in Eq. 4.63.

writeFields (subdictionary)

Includes a number of post-processing fields that can be computed at every saved time step. None of these options alter the solution of the PBE, they only help the analysis of the results.

t_s (Boolean switch)

Shear aggregation characteristic time ($t_s = [k_s(R_p, R_p)]^{-1}$ in Eq. 4.70).

t_d (Boolean switch)

Diffusion aggregation characteristic time ($t_d = [k_d(R_p, R_p)]^{-1}$ in Eq. 4.70).

Pe (Boolean switch)

Aggregation Péclet number (Eq. 4.71).

t_b (Boolean switch)

Breakup characteristic time ($t_b = [k_b(w_1)]^{-1}$ in Eq. 4.75).

K_ab (Boolean switch)

Aggregation breakup ratio (Eq. 4.76).

PA (Boolean switch)

Fraction of aggregated monomers in % (Eq. 3.80).

M_0 (Boolean switch)

Zeroth moment of the CMD (Eq. 4.6 with $j = 0$).

M_1 (Boolean switch)

First moment of the CMD (Eq. 4.6 with $j = 1$).

M_2 (Boolean switch)

Second moment of the CMD (Eq. 4.6 with $j = 2$).

v_mean (Boolean switch)

Mean number of monomers per cluster (Eq. 4.7).

R_mean (Boolean switch)

Mean RMS radius of gyration (Eq. 4.9).

I0 (Boolean switch)

Zero angle light scater intensity (Eq. 4.8).

t_adv (Boolean switch)

Advection characteristic time (Eq. 5.3).

Da (Boolean switch)

Aggregation Damköhler number inside the mesh cell (Eq. 5.7).

The switch *isPBEcoupled* gives an option on the method for solving the PBE. The PBE can either be given as explicit source terms in the transport equation, or solved separately by an ODE solver. The coupled solution is inherently less computationally expensive than the uncoupled solution, because the uncoupled solution requires extra computation in substeps. However, the coupled solution becomes unreliable if the aggregation characteristic time t_a is much shorter than the transport characteristic time t_{adv}. This situation is monitored by the Damköhler number Da (Eq. 5.7) calculated for each individual cell of the mesh. If all cells in the mesh have $Da < 0.01$, it means that it is safe to solve the aggregation-breakup PBE as explicit source terms. Otherwise, changes in conversion rates that occur between time steps would not be solved, and could intrinsically introduce cumulative errors. In this case, instead of decreasing the computation time steps of the transport equation to the scale of the aggregation characteristic time (i.e. $\Delta t \approx t_a \ll t_{adv}$) to achieve accuracy, it takes much less computational time to use an ODE solution method to solve the PBE between the transport time steps.

The solver `aggBreakupFoam` is basically a temporal loop, where an object of class `aggBreakup` is iterated. Once the class `aggBreakup` is initiated, it reads the velocity field and the dictionary `aggBreakupProperties`. The parameters given in the dictionary `aggBreakupProperties` are used to set the CMD as well as the basis of the collision and breakup kernels that do not change in time. As mentioned before, all `C_w` fields that are given by the user are loaded, and those `C_w` not given by the user are copied from `Cdefault`. In order to avoid computation of the PBE kernels for every mesh cell, the common basis of the kernels are computed at the initialisation, and stored in arrays. Only the shear rate varies among the numerous cells, which makes it more efficient to store the quotient of all kernel parameters, excluding shear rate,

and reuse these quotients by multiplying with the shear rate at every cell. The shear rate field `G` is computed as $G = \sqrt{2\,\boldsymbol{E} : \boldsymbol{E}}$ (Eq. 3.11), because it is computationally cheapr to compute the double-dot operator ($\boldsymbol{A} : \boldsymbol{B} = A_{ij}B_{ij}$), than to compute the trace operator on an intermediate matrix $\boldsymbol{E}^2$ in $G = \sqrt{2\,\mathrm{tr}\boldsymbol{E}^2}$.

Finally, at every time step, the *isPBEcoupled* switch dictates the solving method. At every saved time step, the post-processing fields listed in the *writeFields* subdictionary are calculated and saved. The fields given on the saved time steps are used for post-processing. Post-processing is performed using OpenFOAM post-processing utilities, ParaView [15] and python scripts.

5.3 Simulated Cases

Several cases have been simulated to show the capabilities of the spatial solution for the aggregation-breakup PBE. First, in order to guarantee that the 3-D solver was yielding the same calculation as the 0-D solver presented in Chapter 4, a Couette flow case was run as a verification procedure. Second, a flow through a constrained microchannel aperture was simulated in order to demonstrate the effect of high shear followed by low shear in SIPA. Third, flow of activated platelets passing by a crevice was simulated in order to demonstrate the effect of SIPA in regions of recirculating flow. Fourth, a LTPA test case was simulated for validation of the SIPA model. Fifth, a simulation of Poiseuille flow was also run for validation purposes. Lastly, a case where recirculation occurs in a contained mixing vessel was simulated.

When not explicitly specified, the aggregation and breakup parameters were the same as those obtained from the experiments of Xia and Frojmovic [236], which were presented in Chapter 4. These general parameters are displayed in Tab. 5.1. The kinematic viscosity considered in the simulations is the kinematic viscosity of blood plasma $\nu = 1.2 \cdot 10^{-6}\,\mathrm{m^2\,s^{-1}}$ (Section 3.1.3).

Table 5.1: General aggregation and breakup parameters applied on most simulations.

Parameter	Symbol	Value
Aggregation efficiency	η	0.30
Breakup characteristic shear rate	G^*	$1540\,\mathrm{s}^{-1}$
Shear exponent in the breakup kernel	b	2
Size exponent in the breakup kernel	c	3

The simulations were performed in a 4 core Intel Xeon 2.8 GHz desktop, with 8 GB of RAM. All cases were simulated in parallel. The computational time was limited by the CFL condition for the transport of species, because aggregation characteristic time for the simulated platelet concentrations was longer than the transport characteristic time. The computational time varied from a couple of minutes, for the case with less cells, to a couple of days, for the largest mesh grid.

5.3.1 Couette Flow

The simulation of SIPA in Couette flow was used to verify that the `aggBreakupFoam` solver was yielding the same results as the 0-D solver presented in Chapter 4. The 0-D solver solves only the PBE as an ODE, disregarding the transport of aggregates in space. The 0-D solver was written in python, which is a scripted language, and thus is less computationally efficient than a compiled solver. However, the 0-D solver was verified against published data for the similar aggregation-breakup PBE [16], and was verified against experiments on SIPA in Couette flow [236].

The mesh of the Couette flow case has 20×20 cells, in a 2-D square of height $h = 50\,\mu\mathrm{m}$. The upper side moves at $v_x = h\,G$, where G is the expected shear rate, and the lower side is static ($v_x = 0$). The left and right walls have cyclic boundary conditions to make them physically connected to each other. The tested cases were the same three correlated cases in Chapter 4. Shear rate was fixed at $G = 250\ \mathrm{s}^{-1}$, and platelet concentrations C_p were $20\,000$, $40\,000$, and $60\,000\,\mu\mathrm{L}^{-1}$ ($1\,\mu\mathrm{L}^{-1} = 10^9\,\mathrm{m}^{-3}$).

The kinematic viscosity of the sample is considered the same as blood plasma, $\nu = 1.2 \cdot 10^{-6}\,\mathrm{m^2\,s^{-1}}$. With these conditions, the Reynolds number of the Couette flow is

$$Re = \frac{v_x\,h}{\nu} = \frac{G\,h^2}{\nu} = \frac{250\,(50 \cdot 10^{-6})^2}{1.2 \cdot 10^{-6}} = 0.52\ , \tag{5.8}$$

demonstrating a laminar flow regime.

5.3.2 Nesbitt Microchannel

The microchannel geometry used by Nesbitt *et al.* (2009) [161] in their SIPA experiments (showed in Fig. 2.11) was simulated using the aggregation-breakup PBE (Eq. 5.2). This was done in order to investigate whether the SIPA mechanism in that experiment was the same as the SIPA mechanism modelled by Eq. 5.2. The mesh geometry was reproduced from Fig. 2.11 using ImageJ [4] and Gmsh [75]. First, the scale of the microchannel photograph was calibrated with the scale bar, then the gap distance, nozzle curvature, and ramp inclination angle were measured. Then, a structured mesh of hexahedra was produced with those measurements in Gmsh. The mesh mas more refined near the walls, as shown in Fig. 5.1. The kinematic viscosity of blood plasma is considered $\nu = 1.2 \cdot 10^{-6}\,\mathrm{m^2\,s^{-1}}$. The inlet velocity was uniform, with $v_i = 10^{-4}\,\mathrm{m\,s^{-1}}$, on a channel width of $Y_i = 60\,\mu\mathrm{m}$. According to the continuity equation (Eq. 3.3), the mean fluid velocity at the narrowing is $\bar{v}_g = 6 \cdot 10^{-4}\,\mathrm{m\,s^{-1}}$, because the channel width at the narrowing is $Y_g = 10\,\mu\mathrm{m}$. The Reynolds number is

$$Re = \frac{\bar{v}_g\,Y_g}{\nu} = \frac{(6 \cdot 10^{-4})\,(10^{-5})}{1.2 \cdot 10^{-6}} = 8 \cdot 10^{-3}\ , \tag{5.9}$$

demonstrating a laminar flow regime.

5.3.3 Crevice

When the flow boundary layer separates from part of the fluid, a recirculation zone appears. In laminar flow, advection is largely contained in the recirculation zone

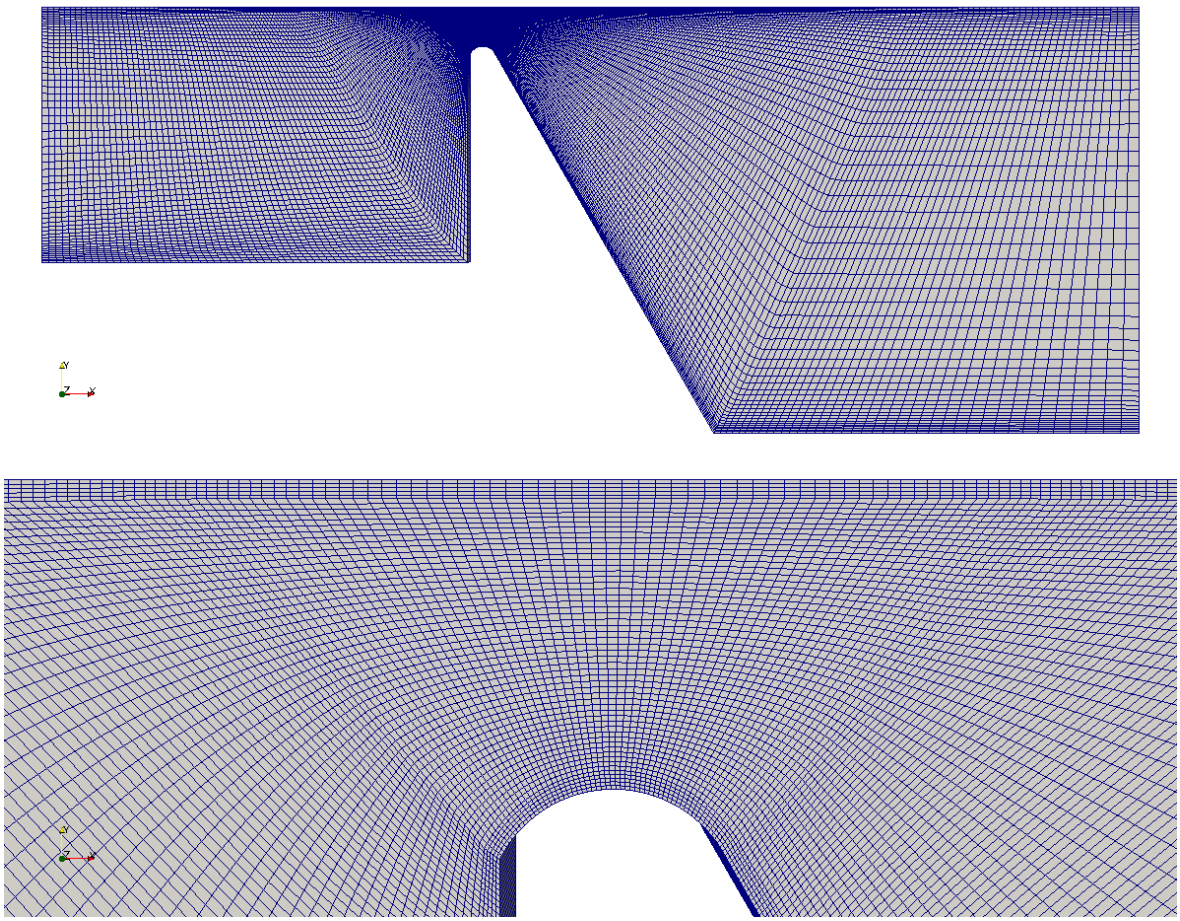

Fig. 5.1: Mesh of microchannel constriction of Nesbitt *et al.* (2009) [161]. Insight at the nozzle.

and the transport of substances in and out this region occurs by diffusion. On one hand, shear rate is comparatively lower in the recirculatory zone that in the boundary layer of the main flow region, which produces a lower aggregation rate. On the other hand, platelets get confined inside the recirculation zones, making their residency times significantly longer than the residency times of platelets flowing in the main flow. Theoretically, large aggregates could be formed locally inside these secondary flow patterns. Recirculation occurs only in pathological situations in the circulatory system, such as downstream of acute stenosis [232], anastomoses [95], and aneurysms [33]. In biomedical devices, separation normally occurs at tube connections, where sharp diameter expansion [121] and crevices [235] may exist.

A simulation of flow over a wall crevice was run, because the size of the recirculation zone is the same for a large range of Reynolds number. The objective of this simulation was to see whether the aggregates would continue growing inside the crevice, even though shear rate is very low there. In this simulation, a square crevice of $100 \times 100\,\mu\text{m}$ is located at the wall of a microchannel, whose width is much larger than the crevice size. The flow in the microchannel is laminar (Poiseuille flow), which produces a parabolic velocity profile. Because flow in the crevice is affected only by the flow near the wall, the control volume of the simulation was limited to the region near the wall, close to crevice location. Therefore, the fluid velocity profile was linearised, i.e. Poiseuille flow was approximated by Couette flow (Sec. 5.3.1). Fluid velocity at $50\,\mu\text{m}$ distance from the wall has the same velocity as the moving wall of the Couette flow case, $v_x = 1.25 \cdot 10^{-2}\,\text{m}\,\text{s}^{-1}$, producing a wall shear rate of $G \approx 250\,\text{s}^{-1}$. If the crevice size is used to obtain a Reynolds number, the velocity near the wall should be used as characteristic velocity. Hence, the Reynolds number of the crevice is many orders of magnitude less than the Reynolds number of the microchannel, whose average velocity and width are both orders of magnitude greater than the characteristic velocity and length of the crevice, respectively. The mesh was generated in Gmsh, like

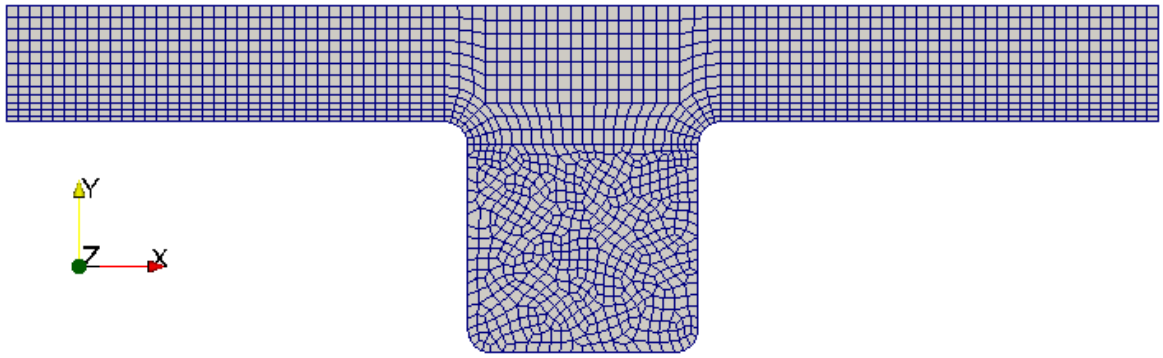

Fig. 5.2: Mesh of the crevice case.

the to Nesbitt microchannel case (Sec. 5.3.2), see it in Fig. 5.2.

5.3.4 LTPA

The LTPA geometry was created based on the design parameters of the commercial product model AggRAM System [96], from Helena Laboratories. The dimensions of the cuvette and the stir bar are displayed on the scheme illustrated in Fig. 5.3. The height of the liquid sample was obtained from the standard sample volume (225 µL of PRP, plus 25 µL of activator agonist dilution), the volume of the stir bar and the cuvette diameter,

$$h_{\text{sample}} = \frac{V_{\text{sample}} + V_{\text{stir bar}}}{\frac{\pi}{4} D^2_{\text{cuvette}}} = 5.7\,\text{mm} \ . \tag{5.10}$$

The standard rotational velocity of the stir bar is $\omega = 1000\,\text{rpm} = 104.7\,\text{rad}\,\text{s}^{-1}$, which yields a Reynolds number

$$Re = \frac{(\omega \frac{L_{\text{stir bar}}}{2})\, L_{\text{stir bar}}}{\nu} = \frac{104.7 \cdot 0.004^2}{2 \cdot 1.2 \cdot 10^{-6}} = 698 \ , \tag{5.11}$$

indicating that the system's flow regime could be slightly turbulent. However, this turbulence was ignored in the simulation because it has not been characterised. Moreover, it was considered that the stir bar was rotating at the exact centre of the cuvette, at a fixed distance from the cuvette's bottom, and with the stir bar axis parallel to the

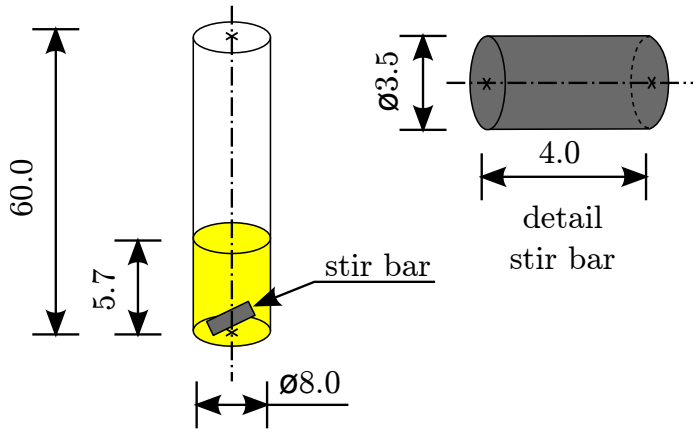

Fig. 5.3: Dimensions of the AggRAM System in millimetres.

bottom surface. This is very unlikely to happen since the body forces of a magnetic field are not linear to the distance of its poles, and lift forces are likely to rotate the axis of the stir bar around.

A 3-D mesh was created with the `snappyHexMesh` OpenFOAM mesh application. This application sculpts the desired surfaces from a block mesh, also performing some regional mesh refinement. The mesh was defined with as a vertical cylinder, representing the PRP sample, with a cylindrical hole inside, representing the stir bar (See Fig. 5.4). The mesh is more refined at the walls, where velocity and shear gradients are higher. The flow was solved at steady state by imposing a rotation reference frame fixed to the stir bar on the cells around stir bar wall.

The volume averaged absolute shear rate

$$\bar{G} = \frac{\sum_{i=1}^{N_{\text{cells}}} G_i \, V_i}{\frac{1}{N_{\text{cells}}} \sum_{i=1}^{N_{\text{cells}}} V_i} \tag{5.12}$$

was calculated to compare the results in the 3-D simulation with the results from a 0-D simulation, where only the PBE is solved, and all fields are considered homogeneous. In Eq. 5.12, V_i is volume of cell i.

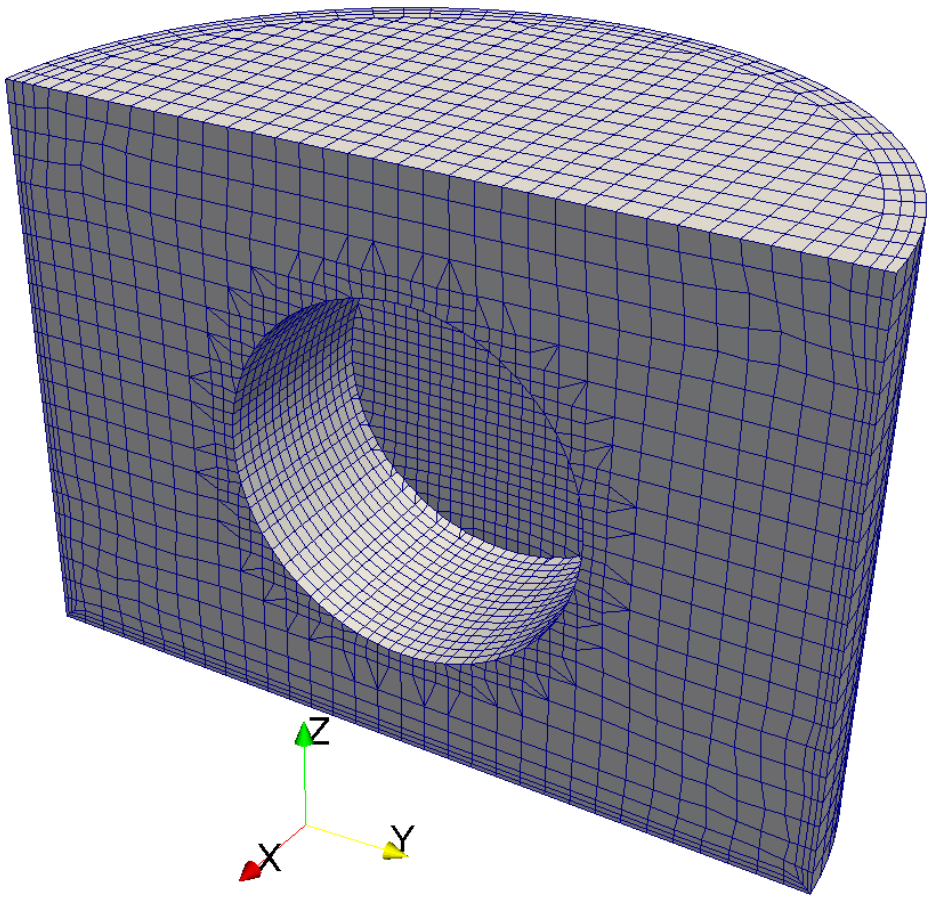

Fig. 5.4: Sectioned view of the mesh for simulating the platelet aggregometer AggRAM System.

5.3.5 Poiseuille Flow

Poiseuille flow is the denomination of laminar flow along tubes. It creates a parabolic velocity profile (Eq. 2.5) and a linear shear rate profile (Eq. 2.8). The experiments of Bell *et al.* (1989) [25] were simulated as axisymmetric flows. The simulated tube radius and length are $R = 595\,\mu\text{m}$ and $L = 9\,\text{m}$, respectively. The mesh is a wedge of 10×6438 cells, and it is more refined at the inlet, where flow is not developed. The inlet velocity was calculated in order to yield mean shear rate (Eq. 2.9) $\bar{\dot{\gamma}} = 335\,\text{s}^{-1}$, a value tested by Bell *et al.*

To quantify SIPA in Poiseuille flow, Bell *et al.* sampled platelet aggregates at the exit of tubes of different lengths. If volume samples are collected from the exit of the tube, the sample concentration will be influenced by both the concentration profile and the velocity profile. Velocity profile is not uniform, but parabolic and faster at the centre. Concentration profile depends on the evolution of the CMD, which is related to shear rate, whose profile is linear and higher at the walls. Therefore, in volume samples collected at the exit of the tube, more is sampled from platelets moving close to the centre, which have experienced less shear rates; and less is sampled from platelets moving close to the wall, which have experienced high shear rates. To simulate this sampling, the computed CMD flow was integrated at the cross-sections representing these points. After the processing of the `aggBreakupFoam` solver had finished, an OpenFOAM application called `sample` was run to sample planes at the cross-sections. These planes were saved as VTK files [189]. The VTK sampled cross-sections contained the velocity $\boldsymbol{v}(r)$ and aggregate concentration $C_i(r)$ profiles in planar cells. The areas of these planar cells were calculated based on the cell geometry, and they were used to integrate the aggregate concentration flow on that cross-section, in order to obtain the sampled concentration

$$\bar{C}_i = \frac{\int\int C_i(r)\,\boldsymbol{v}(r)\cdot d\boldsymbol{A}}{\int\int \boldsymbol{v}(r)\cdot d\boldsymbol{A}} \approx \frac{\sum_j C_{i,j}\,\boldsymbol{v}_j\cdot\boldsymbol{A}_j}{\sum_j \boldsymbol{v}_j\cdot\boldsymbol{A}_j}\ . \tag{5.13}$$

Platelet aggregate samples collected from the exit of the tube would have a CMD according to Eq. 5.13, where $\boldsymbol{A}_j$ and $\boldsymbol{v}_j$ are the respective area and velocity vectors of a plane cell j, and $C_{i,j}$ is the concentration of aggregate class i in that same cell.

5.3.6 Eccentric Cylinders

Large aggregates take a long time to form at low shear rates. At high shear rate, however, velocities are normally very high too. In an open system, like in a tube or channel, large aggregates are formed only far downstream along the tube, which can be out of the observation area. If high advection occurs evenly in a closed aggregation system, then CMD of different shear histories may quickly mix, which would create a homogeneous CMD field. Therefore, Kramer and Clark [130] performed simulations of shear induced aggregation and breakup of a simple closed system of non-uniform flow fields. This system consisted of a couple of eccentric cylinders, where the outer cylinder is fixed and the inner cylinder rotates at constant speed about its own centre line. The rotation of the inner cylinder creates a flow field between the two cylinders. These authors showed that a non-uniform distribution of aggregates was formed in the simulation.

A couple of cases of eccentric cylinders were simulated using the `aggBreakupFoam` solver. The two cases had the same geometrical parameters and boundary conditions. The geometrical parameter were: outer radius $R_o = 15\,\mathrm{cm}$, inner radius $R_i = 10\,\mathrm{cm}$, and eccentricity $e = 2.5\,\mathrm{cm}$. The inner cylinder rotated at $\omega = 10\,\mathrm{rad\,s^{-1}}$. The aggregation parameters were obtained from the experiments of Xia and Frojmovic [236], see Tab. 5.1. The only difference between the simulations was that breakup was turned off in one of them. A 2-D structured mesh was produced in `Gmsh`, and the rotation field was solved using a rotating reference frame.

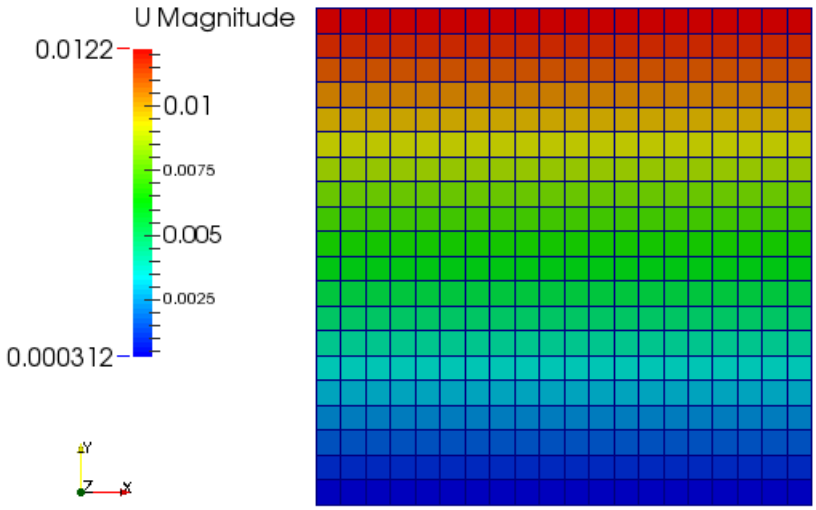

Fig. 5.5: Velocity field and mesh of Couette flow case.

5.4 Results

5.4.1 Couette Flow

The mesh and the velocity field are presented in Fig. 5.5. Figure 5.6 shows the field of cell Damköler number. Cell Damköler numbers are very low where velocity is high, but they are still less than 0.01 in the cell layer adjacent to the wall. Low cell Damköler number demonstrate that the PBE can be accurately solved as source terms of independent transport equations, given that the CFL condition is obeyed. Higher cell Damköler numbers could be achieved only with finer meshes, because both advection and aggregation speeds are linearly related to velocity. However,

Figure 5.7 depicts graphs of the velocity and shear rate along the gap height (y-direction). The resulted shear rate was not as accurate as the velocity, because the numerical method imposed convergence only in the velocity and pressure fields. The velocity gradient, seen as generalised shear rate, was not monitored for convergence, but it was derived from both the velocity field and the mesh topology. Nevertheless, the error of the shear rate is less than 1%, which is admissible. Figure 5.8 shows the

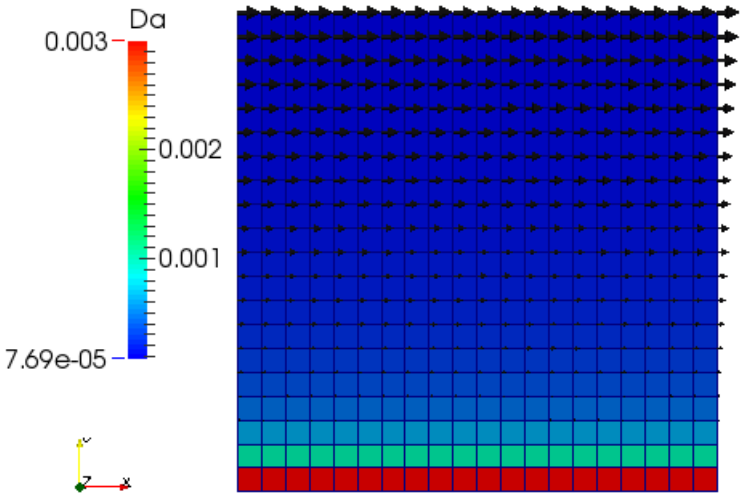

Fig. 5.6: Damköhler number and velocity vectors

first moment of the CMD and the Péclet number along the gap height (y-direction), at 90 s of simulated time. The first moment calculates the total concentration of primary particles (platelets), regardless whether they are aggregated or free. Thus, the first moment is informing that mass was conserved in this simulation. The aggregation Péclet number is not highly accurate, because it is calculated with the shear rate of each cell, which are not converged values as shown in Fig 5.7. The error of the Péclet number is as negligible as the error of the shear rate.

The time series of a cell from the centre of the mesh was extracted from the 3-D Couette flow case. This result was compared with the time series obtained from the 0-D case written on a python script. Both the results of the 0-D and 3-D solver are shown in Fig. 5.9. This verification test demonstrated that the C++ solver is computing the same PBE as the python script.

5.4.2 Nesbitt Microchannel

An example of a simulation of the `aggBreakupFoam` solver with the microchannel geometry published by Nesbitt *et al.* (2009) [161] is depicted in Fig. 5.10. The inlet

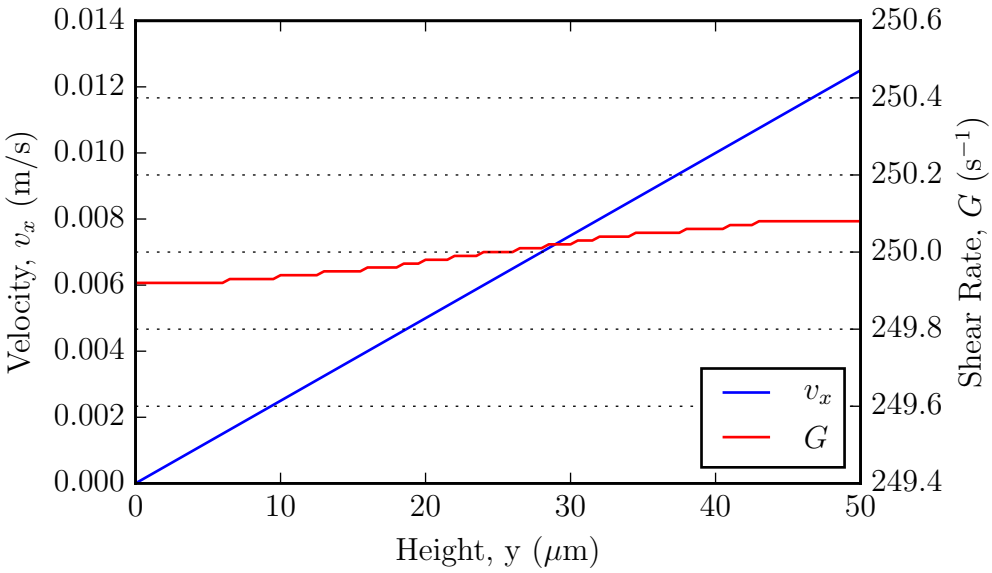

Fig. 5.7: CDF simulation of Couette flow. Velocity and shear rate.

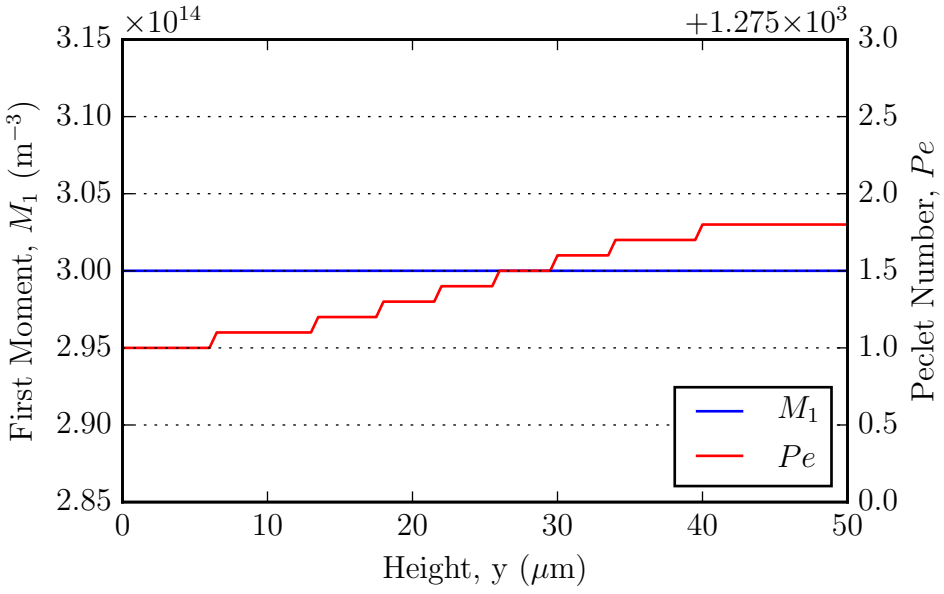

Fig. 5.8: CDF simulation of Couette flow at 90 s of simulated time. First moment of the CMD and aggregation Péclet number.

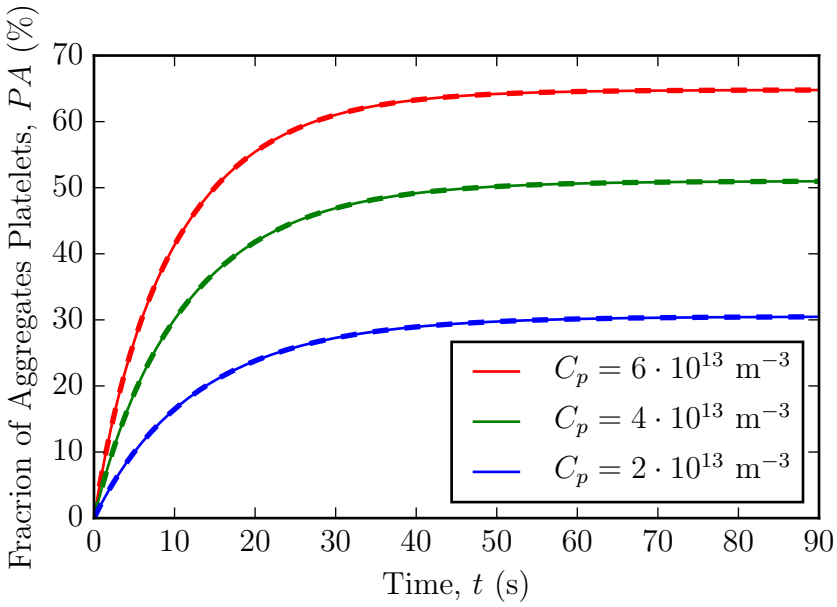

Fig. 5.9: Simulation of the aggregation-breakup PBE in 0-D (continuous lines) and in 3-D Couette flow (dashed lines).

is at the left-hand side, and the outlet at the right-hand side. Free activated platelets ($C_p = 4 \cdot 10^{14}\,\mathrm{m}^{-3}$) aggregate near the walls, where shear rate is higher. Then, at the nozzle shear rate is very high, and breakup becomes stronger than aggregation. Just downstream from the nozzle, platelets begin to aggregate again. This transient simulation reaches apparent steady state very soon (approx. 5 s), but both velocity near the wall and shear rate are very low, which makes aggregation very slow there. Large aggregates are only formed far from the nozzle. Clearly, the simulation (Fig. 5.10) does not reproduce the experiment presented in Fig. 2.11. Qualitatively, the experiment produced a large aggregate just downstream from the nozzle, and no aggregate far downstream from it. In the simulation, aggregates were never large, they formed only near the wall, and they were convected downstream without disappearing.

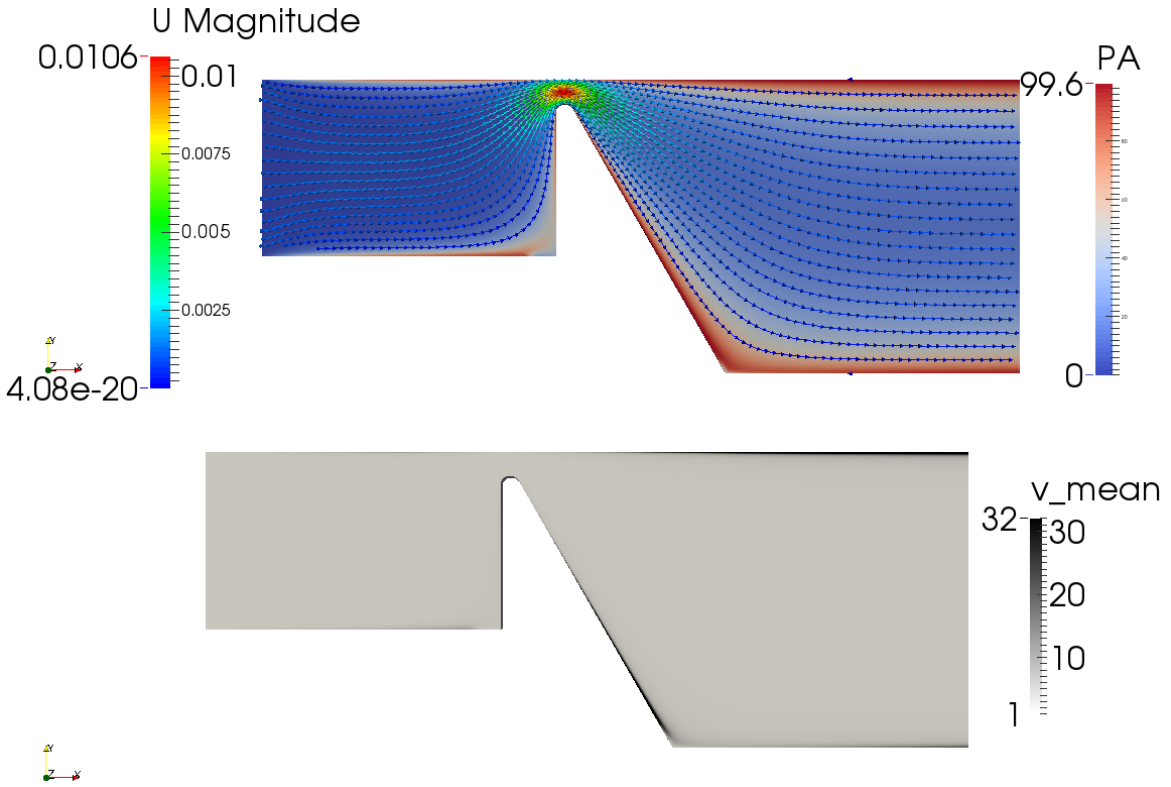

Fig. 5.10: Simulation of the aggregation-breakup PBE in the microchannel nozzle of Nesbitt *et al.* [161]. Top: velocity streamlines (U Magnitude) and fraction of aggregated platelets (PA). Bottom: mean number of platelets per aggregate (v_mean).

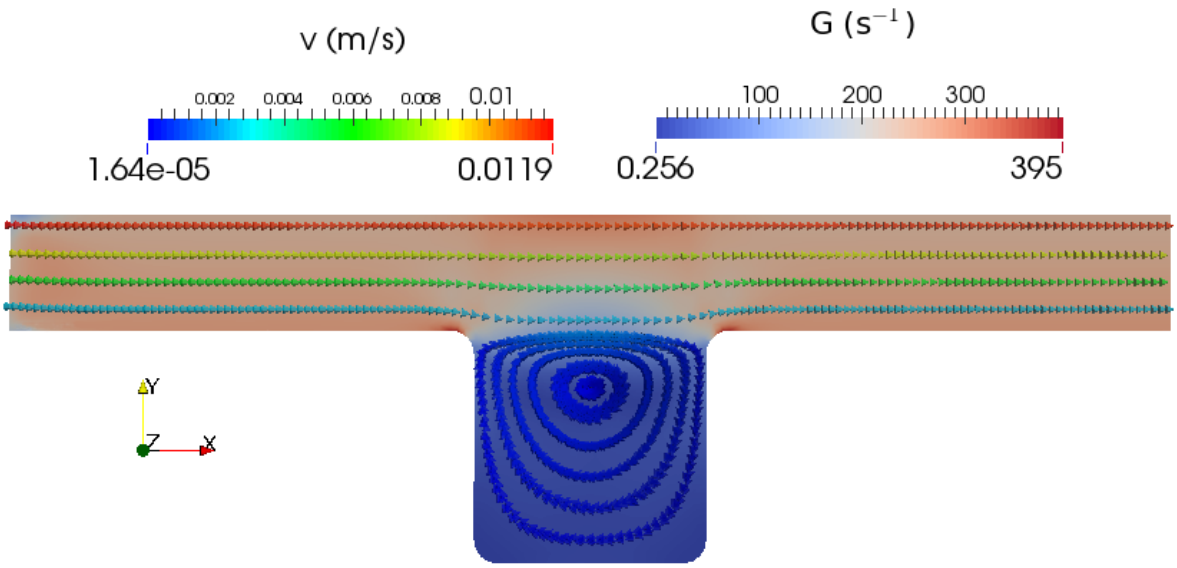

Fig. 5.11: Simulation of flow over a crevice. Streamlines of the velocity field (v), and the shear rate field (G).

5.4.3 Crevice

Both the velocity field and the shear rate field are seen in Fig. 5.11. Velocities inside the recirculation zone are very slow compared to the main flow. Shear rate is nearly constant ($G \approx 250\,\mathrm{s}^{-1}$) in the main flow, and it peaks at the edges of the crevice $G \approx 250\,\mathrm{s}^{-1}$). Shear rate is very low inside the crevice ($G \lesssim 100\,\mathrm{s}^{-1}$).

Figure 5.12 shows the steady state fraction of aggregated platelets (PA), which is achieved in about 40 s. The fraction of aggregated platelets is increasing since the inlet. The aggregates enter the crevice recirculation by diffusion at the region of flow separation. Therefore, fraction of aggregated platelets inside most of the crevice is the same as outside, just upstream from it. The peak of aggregates occur at the centre of the recirculation zone, where the streamlines are more distant from the main flow. Therefore, the aggregates in the centre of the recirculation zone remain trapped for longer times than the aggregates circulating at the outer rims. Once they are convected outside the recirculation zone, aggregation is resumed almost at the same level as it

was before the crevice.

The particle collision Péclet number in Fig. 5.13 is showing that almost no shear induced aggregation is occurring inside the crevice, because it is comparable with diffusion induced aggregation. Some SIPA occurs at the height of the crevice edges, where it is crossed by the recirculation streamlines in Fig. 5.11.

The cell Damköhler number shows that the points of highest aggregation to advection ratio occur at the bottom of the crevice, where flow is almost inexistent. Relatively significant levels of cell Damköhler number are seen at the walls of the main channel. However, these levels of cell Damköhler number are still low ($Da < 0.01$), indicating that aggregation rates are far slower than advection rates.

The aggregation-breakup ratio in Fig. 5.15 indicate the positions where the larger aggregates have more potential to be formed. The meaning of this quantity was explained in full extension in Chap. 4. In theory, the crevice could be a good environment to form aggregates. However, the aggregation-breakup ratio is a quantity that ignores the transport of these particles, which is very significant in this case, given that steady state is achieved after 40 s of simulated time.

5.4.4 LTPA

The simulation of the LTPA using the design parameters of the AggRAM system are presented. The topology of the velocity field, together with the shear rate on the wall of the stir bar, is displayed in Fig. 5.16. Shear rate is highest on the rotor wall. It is possible to see in Fig. 5.16 that the velocity field, although laminar, is intermingled. This characterises a well mixing system. In order to evaluate the convection mixing time, a scalar transport simulation was run, see Fig 5.17. The scalar diffusivity was set to zero, in order to check the power of advection alone. As initial condition, the scalar value at the top layer of the sample volume ($V_{\text{top}} = 25\,\mu\text{L}$, or 10% of total volume) was set to 1. The top volume represents the volume of activation agonist, which is

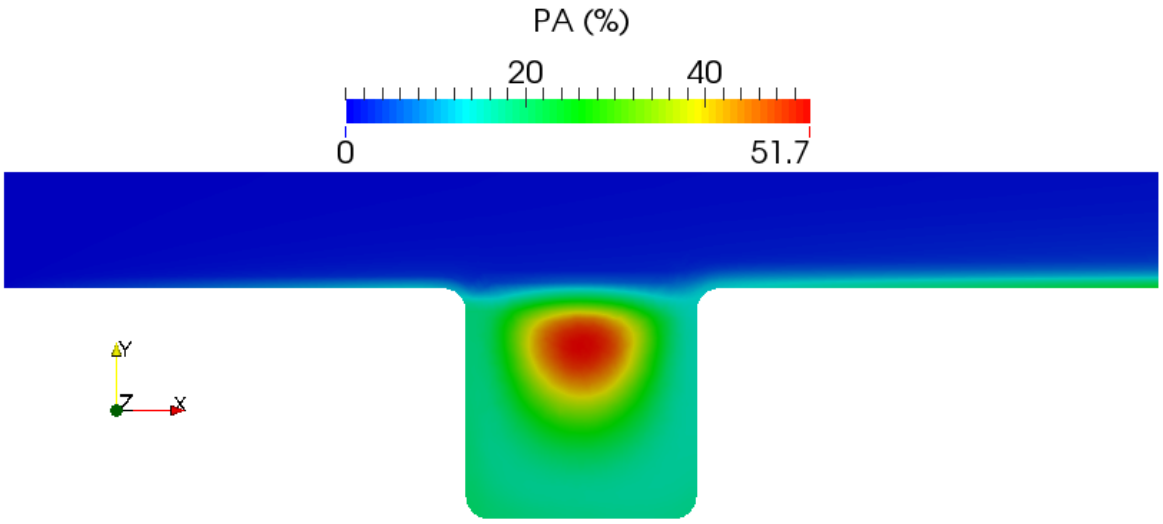

Fig. 5.12: Simulation of flow over a crevice. Fraction of aggregated platelets (PA) at steady state, at 120 s of simulated time.

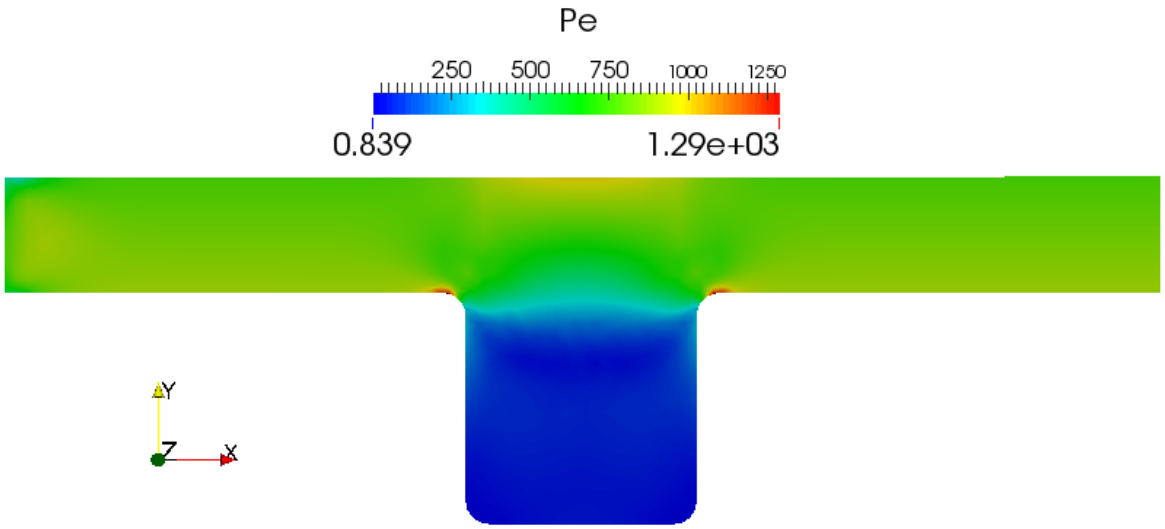

Fig. 5.13: Simulation of flow over a crevice. Particle collision Péclet number (Pe).

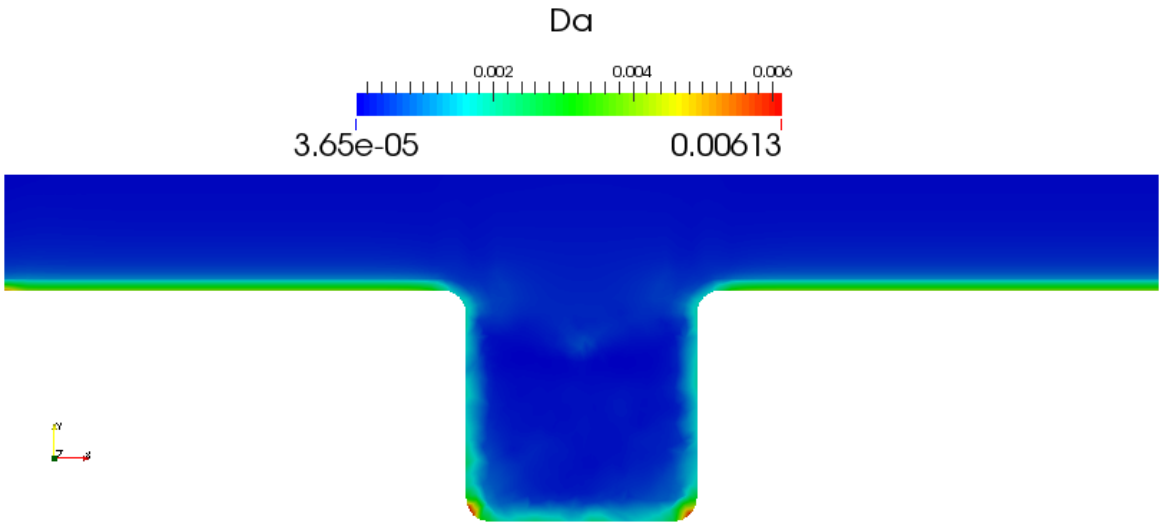

Fig. 5.14: Simulation of flow over a crevice. Cell Damköhler number (Da).

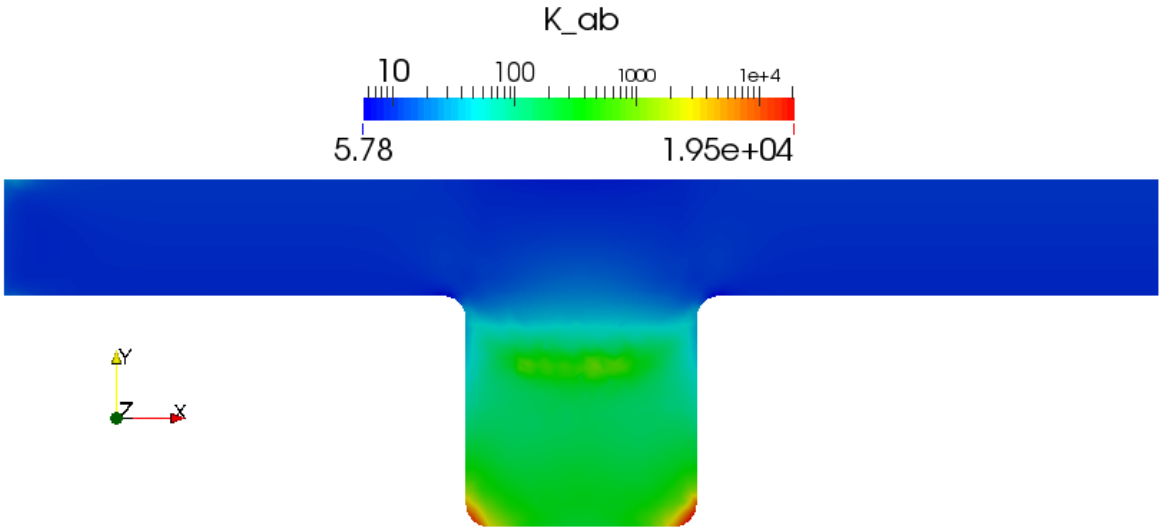

Fig. 5.15: Simulation of flow over a crevice. Aggregation-breakup fraction (K_ab) in log-scale.

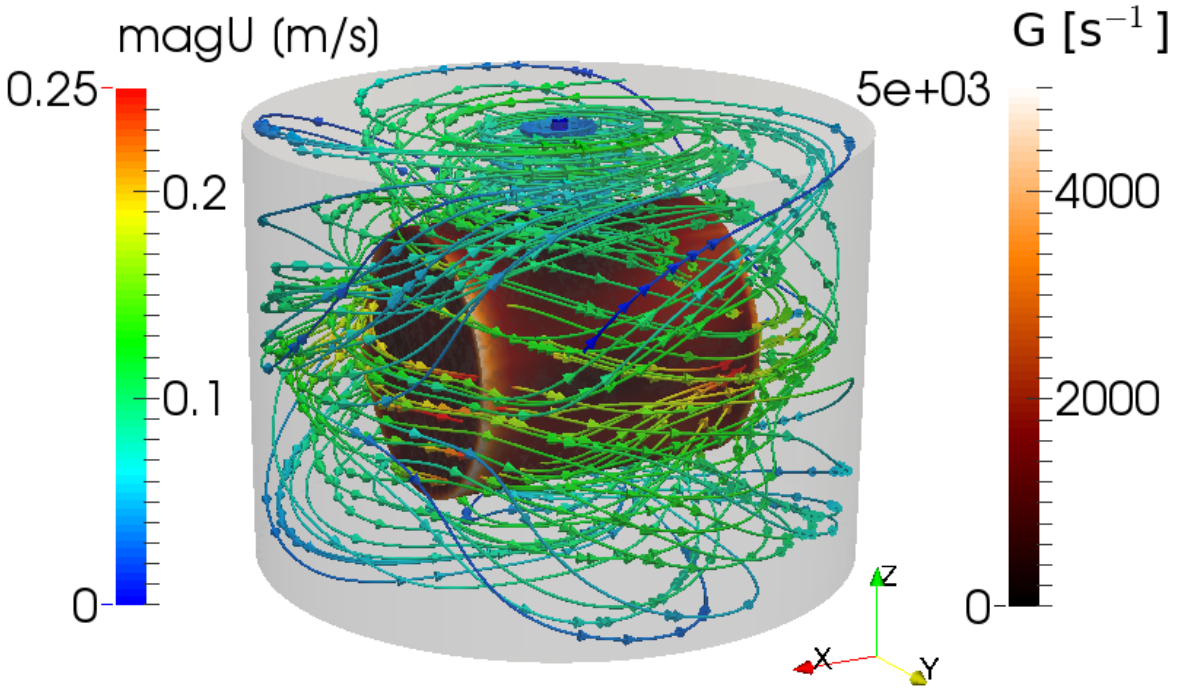

Fig. 5.16: Simulation of LTPA. Velocity on stream lines, and shear rate on the stir bar wall.

added to the PRP sample in a volume ratio of 1:9, in order to achieve the total volume of 250 µL. Figure 5.17 is showing that the agonist mixing time is of the order of 5 s in LTPA, which should not interfere with the normal aggregation time registered by LTPA, which is of the order of 2 min.

In Fig. 5.18 the distribution of cell Damköhler number is displayed. Cell Damköhler number is maximum at the walls of the cuvette, where $Da \approx 0.01$, and it is about one or two order of magnitude lower elsewhere. Although the highest shear rates are at the stir bar surface (Fig. 5.16), fluid velocity is also very high there. Therefore, Da is about one order of magnitude lower at the stir bar than at the cuvette walls. Cell Damköhler number is lowest in the bulk of the flow, where it is about two orders of magnitude lower than at the cuvette walls.

The evolution of the CMD in space and time was evaluated both with and without

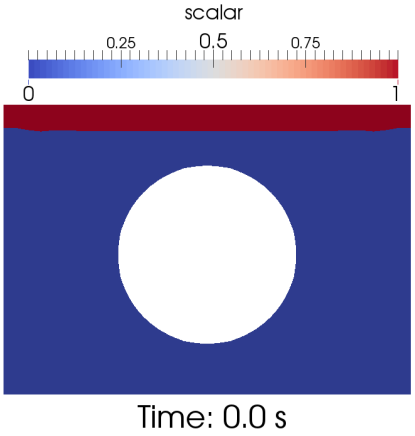

(a) Initial state, scalar concentration 1.0 in the top layer ($V_{\text{top}} = 25\,\mu\text{L}$, or 10% of total volume).

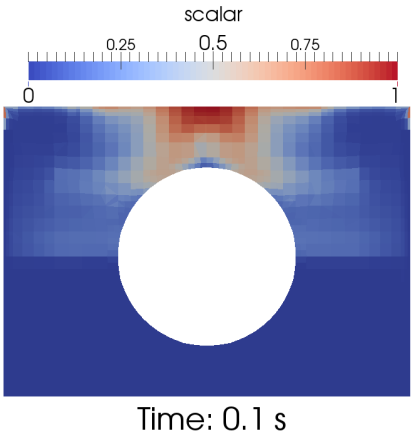

(b) Initial mixing.

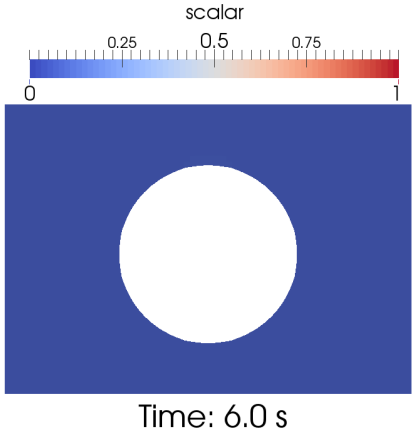

(c) Mixed state, scalar concentration is 0.1 everywhere.

Fig. 5.17: Mixing in the AggRAM system. Figures show scalar concentration on a cross-section of the mesh.

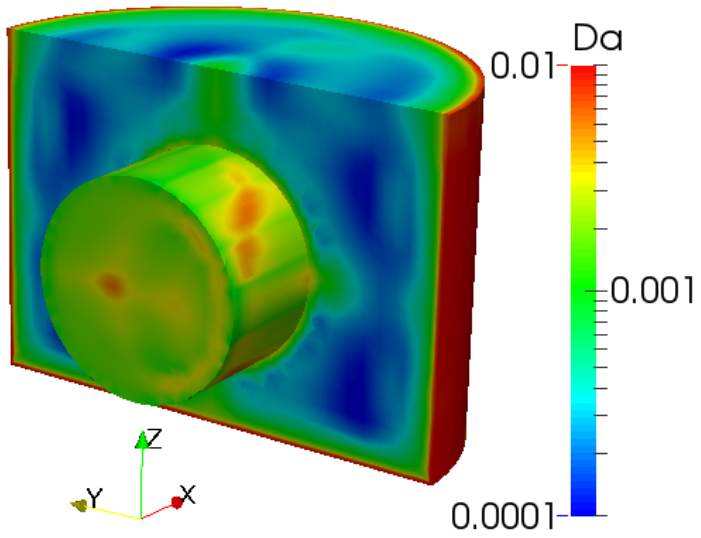

Fig. 5.18: Cell Damköhler number in LTPA.

breakup. Breakup caused the simulation to reach steady state at $t \approx 40\,\mathrm{s}$, which did not happen for the case where breakup was turned off. Regardless whether breakup was on or off, mixing was very strong, as stated before, and the CMD did not differ much spatially. Figure 5.19 compares the CMD state by two integral quantities: mean number of platelets per aggregate $\langle w \rangle$, and zero angle light intensity I_0. These two quantities are presented for both cases where breakup is on or off. The images are shown at $t = 60\,\mathrm{s}$, because at this time the breakup on has already reached steady state. The case with breakup turned off cannot reach steady state. All colour bars in Fig. 5.19 were scaled to the data presented in the respective picture. Therefor, the maximum and minimum numbers on the scale bar represent the maximum and minimum numbers of that data set. It is important to notice that there is a very tiny spatial variation of the values represented in Fig. 5.19, because space is almost homogeneous. It is easy to notice the contrast between the maximum and minimum spatial values between the two cases. With breakup on, the aggregation level is lowest at the walls, where shear rates are highest. With breakup off, the opposite occurs, because shear rate functions only to increase aggregation.

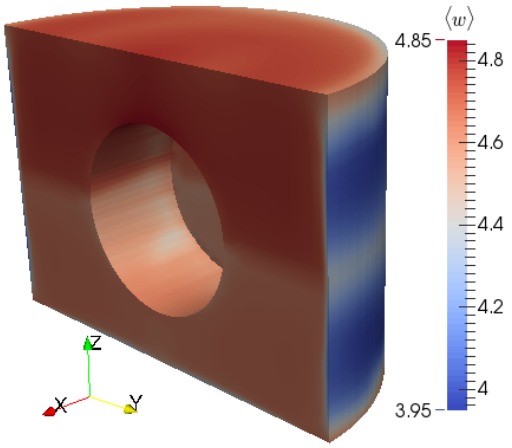

(a) Breakup on, $\langle w \rangle$.

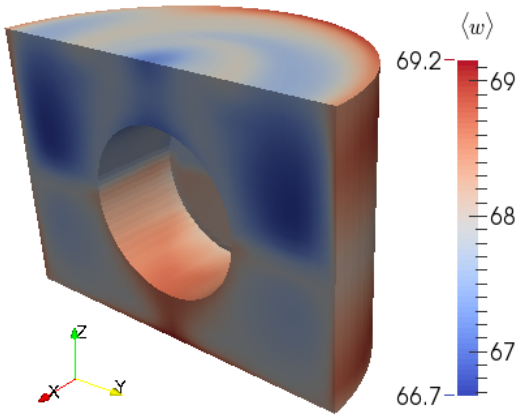

(b) Breakup off, $\langle w \rangle$.

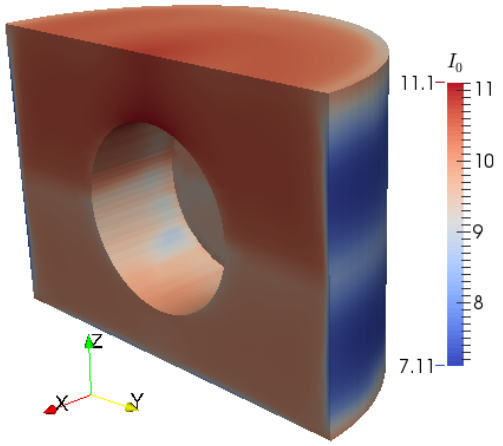

(c) Breakup on, I_0.

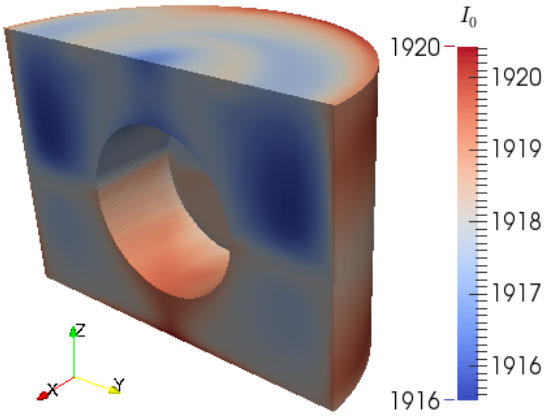

(d) Breakup off, I_0.

Fig. 5.19: Spatial distributions of mean number of platelets per aggregate $\langle w \rangle$, and zero angle light intensity I_0, at $t = 60\,\mathrm{s}$.

Since the spatial distribution is practically uniform, the CMD evolution of the 3-D case was compared with the solution of the PBE alone, named 0-D model (See Chapter 4). The shear rate field in the 3-D case is not uniform. The distribution of shear rate over all the cells of the mesh is depicted as an histogram in Fig. 5.20. From this distribution, the average shear rate $\bar{G} = 191\,\mathrm{s}^{-1}$ was obtained using Eq. 5.12. A simulation of the 0-D model with breakup off was run with $G \equiv \bar{G} = 191\,\mathrm{s}^{-1}$. In Fig. 5.21, it is possible to compare 0-D and 3-D simulations with breakup turned on or off. For the 3-D AggRAM system, the simulations with and without breakup were similar but not exactly the same as the 0-D simulation, which is equivalent to Couette flow. As expected by the results in Chapter 4, there is no maximum aggregation state when breakup is off. The aggregates grow in size indefinitely. The maximum absolute numbers for both zero angle light intensity I_0 and mean number of platelets per aggregate $\langle w \rangle$ are two orders of magnitude larger in Fig. 5.21b than in Fig. 5.21a, at the end of simulation time ($t = 180\,\mathrm{s} = 3\,\mathrm{min}$). The level up of I_0 in Fig. 5.21b is a numerical artefact, which occurs when many aggregates form at the ceiling of the discretised CMD. In this simulation, the ceiling of the discretised CMD was an aggregate formed by $w_{n=12} = 2^{11} = 2048$ platelets. Although the ceiling of the discretised CMD is increasing in concentration, the mean number of platelets per aggregate $\langle w \rangle$ is still growing monotonically in Fig. 5.21b after $t = 20\,\mathrm{s}$. When breakup is on, steady state was obtained at $t = 30\,\mathrm{s}$. The aggregation efficiency was $\eta = 0.3$, and with breakup parameters were $b = 2$, $c = 3$ and $G^* = 1540\,\mathrm{s}^{-1}$, as in the simulations correlating the SIPA experiments of Xia and Frojmovic [236] (Fig. 4.25).

Neither of the 3-D with mean shear rate $\bar{G} = 191\,\mathrm{s}^{-1}$ did perfectly match the 0-D cases with shear rate $G = 191\,\mathrm{s}^{-1}$ (see Fig. 5.21). Therefore, shear rate of the 0-D solver was adjusted for best fitting the 3-D results. For the breakup on case, shear rate was adjusted for $G = 285\,\mathrm{s}^{-1}$ (Fig. 5.21a), and, for the breakup off case, shear rate was adjusted for $G = 160\,\mathrm{s}^{-1}$ (Fig. 5.21b). When adjusted for $G = 160\,\mathrm{s}^{-1}$, the breakup

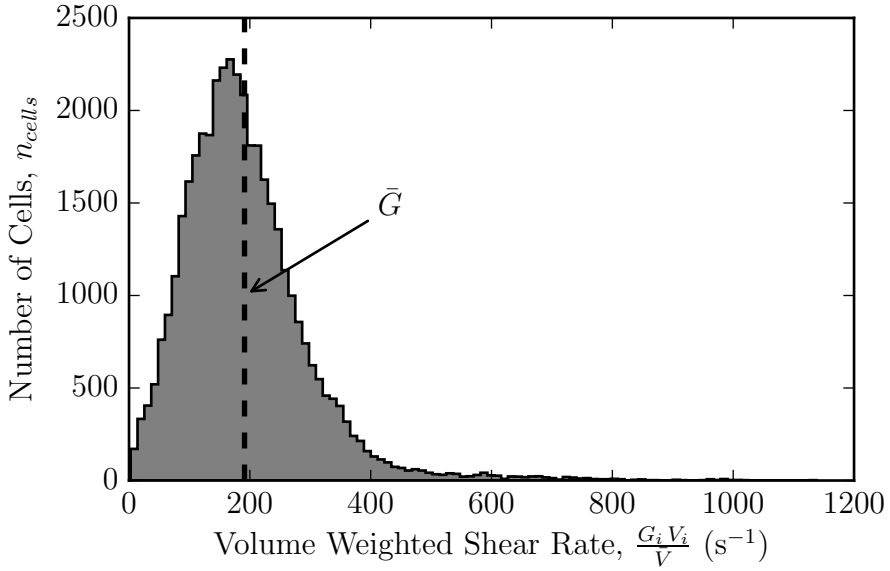

Fig. 5.20: Histogram of volume weighted shear rate per mesh cells for the LTPA simulation. Volume averaged shear rate $\bar{G} = 191\,s^{-1}$ is highlighted.

off 0-D simulation perfectly matched the 3-D simulation with $\bar{G} = 191\,s^{-1}$. However, when adjusted for $G = 285\,s^{-1}$, the breakup on 0-D simulation could not perfectly match its respective 3-D simulation with $\bar{G} = 191\,s^{-1}$. Even though these differences, the curves of the adjusted 0-D breakup on case were very close to the curves of the 3-D LTPA case. The differences between those results would certainly fall within the margin of error of an eventual experiment.

The curves for zero angle light intensity I_0 in Fig. 5.21 were very similar to the ones obtained by real data of LTPA. It is important to restress that the shape of the I_0 curve that is important, not the absolute values. The maximum and minimum points of the LTPA curves are calibrated with values of I_0 from PPP and unactivated PRP, respectively. In Fig. 5.22 simulation results, with and without breakup, are compared with a LTPA experiment with high final concentration of ADP ([ADP] = 10 µM). Moreover, the I_0 values from Eq. 4.8 are also relative, thus they have to be experimentally calibrated, which could not be done for the simulations. Experimental

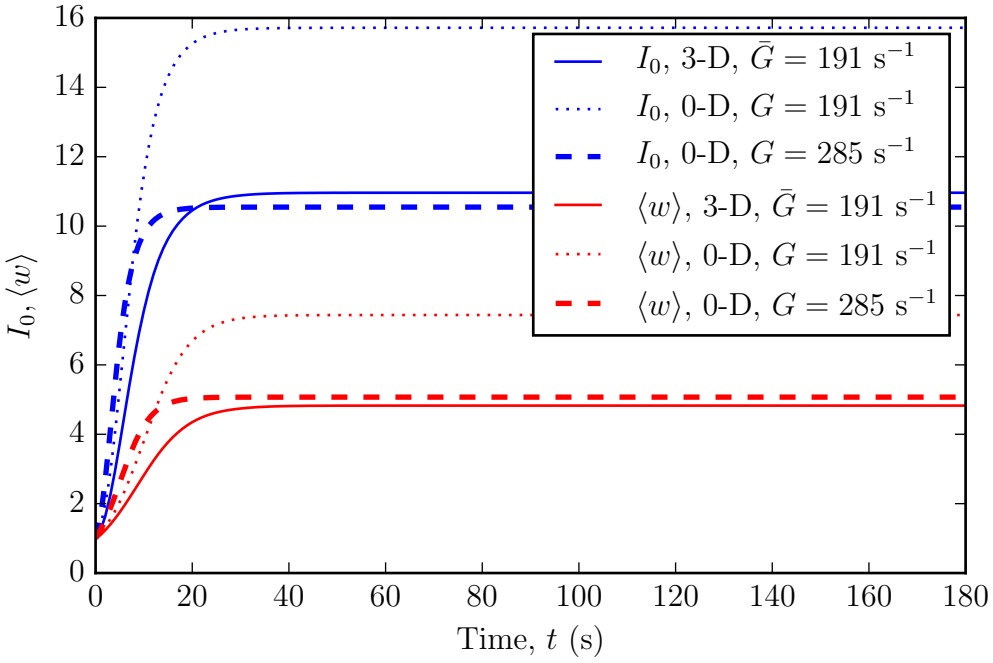

(a) Breakup on.

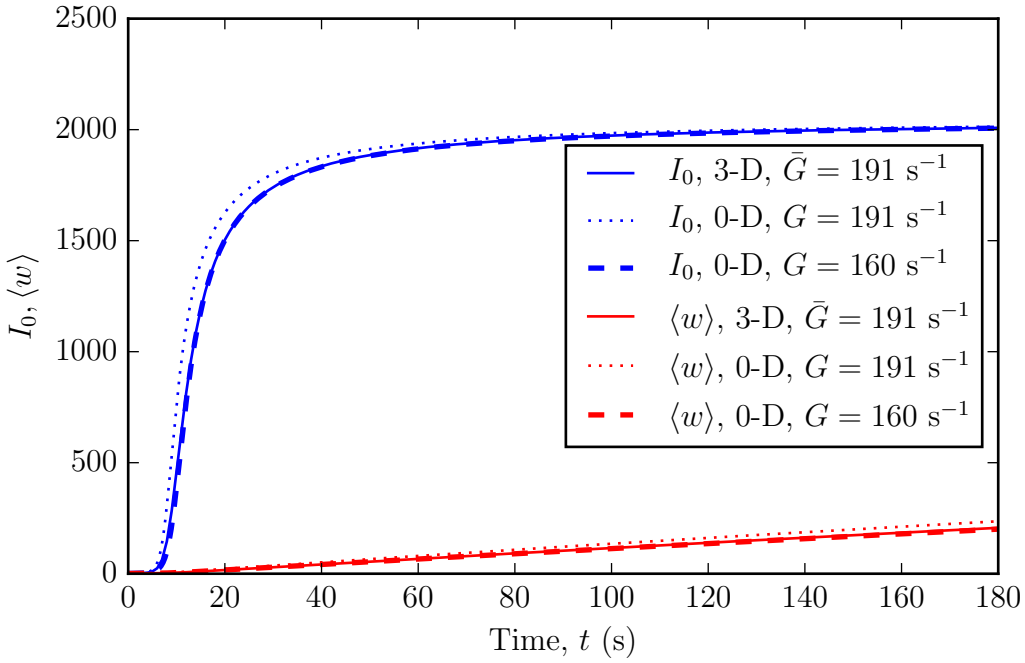

(b) Breakup off.

Fig. 5.21: Comparing results 0-D and 3-D solvers for the aggregation-breakup PBE. The 3-D results are time samples from a single cell of the LTPA case, and $\bar{G}$ is the generalised shear rate averaged from all cells in the mesh.

data from a routine LTPA test was obtained in the Aemostasis Laboratory, University College Hospital Galway. The correlation between experiment and simulation was better when breakup was on. With breakup off, there is a delay in the rise of I_0, which is sensitive to aggregation efficiency η. This delay made the I_0 curve to be S-shaped when breakup is off, but simply similar to an inverse exponential curve when breakup was on. Light transmission platelet aggregometry presents no initial delay, which indicates that breakup is present. Aggregation efficiency $\eta = 0.01$ gave the best correlation when breakup was on, although $\eta = 0.01$ at $\bar{G} = 191\,\mathrm{s}^{-1}$ is lower than $\eta = 0.30$ at $G = 250\,\mathrm{s}^{-1}$ obtained by Xia and Frojmovic [236] in Couette flow. The settling down of the aggregation curve is faster in the simulation than in the experiment, probably due to longer breakup characteristic time t_b (in Eq. 4.76), than predicted form the experiments of Xia and Frojmovic.

5.4.5 Poiseuille Flow

Figure 5.23 shows the velocity and shear rate fields developing at the inlet of the tube, where the mesh is more refined on the x-direction. The mesh does not have to be very refined on the x-direction once the flow profile is developed, because there are no flow gradients on this direction, and the gradients of aggregate concentrations are very low. Cell refinement in the x-direction is such that maximum cell Damköhler number is of order 0.01 ($Da \approx 0.01$). A peak of shear rate occurs at the inlet wall ($G = 3610\,\mathrm{s}^{-1}$, and in the developed region it is highest at the cells that border ($G_{\mathrm{wall}} = 609\,\mathrm{s}^{-1}$).

Figure 5.24 shows the aggregation evolution along the tube. This simulation used the aggregation and breakup parameters obtained from the experiments of Xia and Frojmovic (1994) [236], see Tab. 5.1. Fraction of aggregated platelets (PA) is shown at three points along the tube: $x = 0$, 2 and 8 m. Initially, significant aggregation is seen near the wall, where shear rate is highest, although aggregation is occurring everywhere at different rates. At $x = 2\,\mathrm{m}$, aggregation is higher at an annular region away from

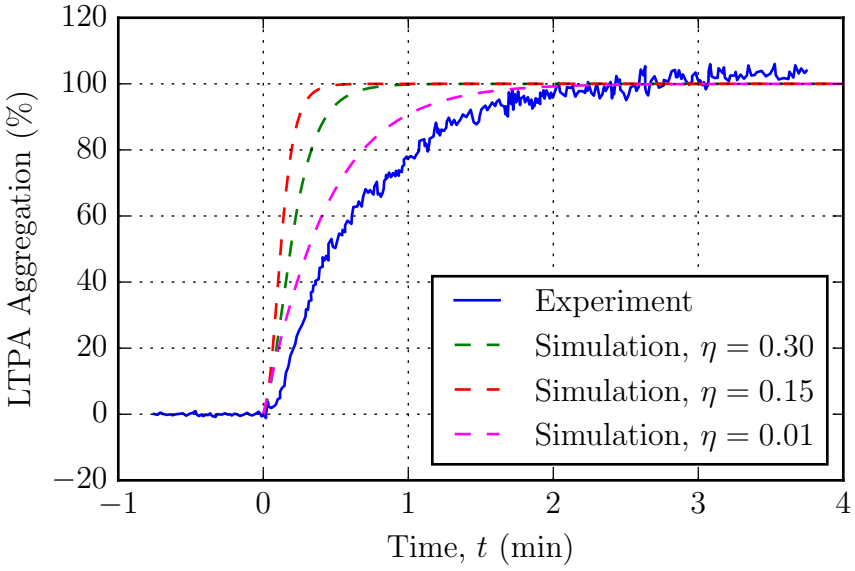

(a) Breakup on.

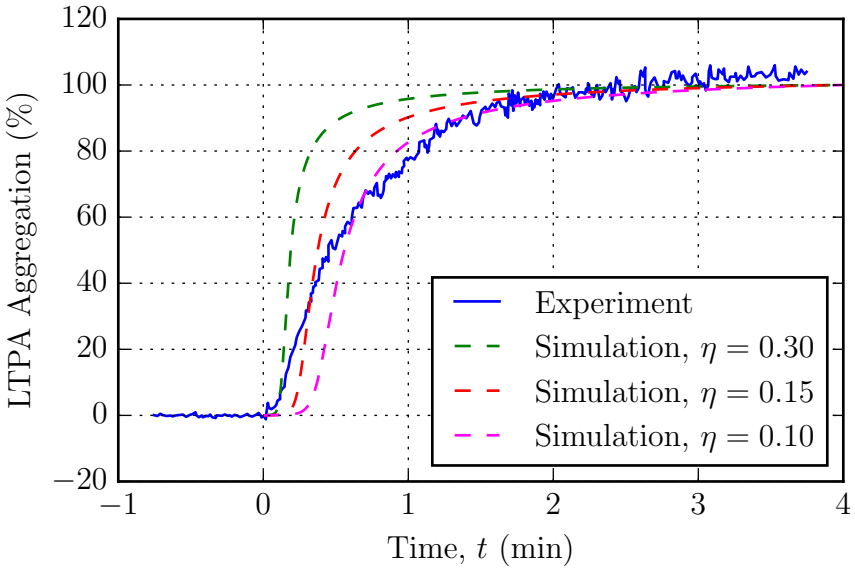

(b) Breakup off.

Fig. 5.22: Comparing experimental and simulation results of LTPA. Aggregation efficiency η of the simulation was adjusted for better comparison. Experiment $t = 0$ is the time when ADP was added to PRP (final concentration [ADP] = 10 µM).

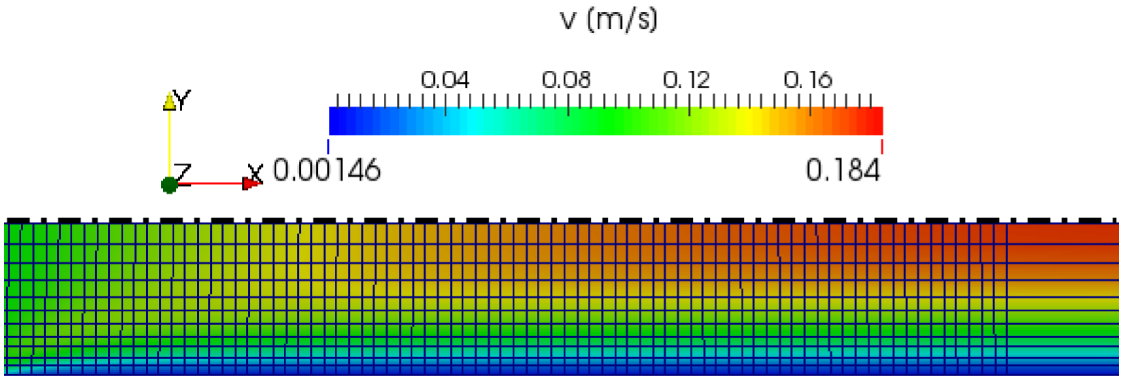

(a) Velocity field.

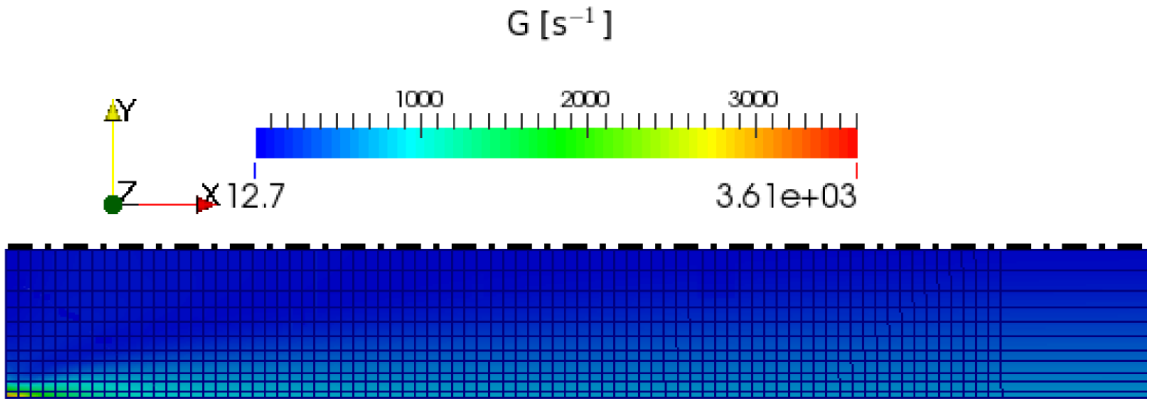

(b) Shear rate.

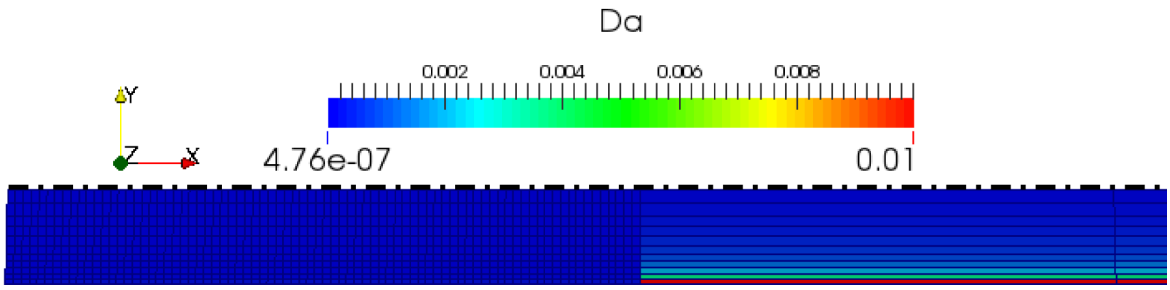

(c) Cell Damköhler number.

Fig. 5.23: Inlet of axisymmetric tube. Flow field develops inside the refined mesh region. Symmetry line (-··-).

the wall. Aggregation is still low at the centre of the tube, where aggregation rates are lowest. However, at $x = 2\,\mathrm{m}$, aggregation is lower near the wall, where breakup is high enough to limit further aggregation. At $x = 8\,\mathrm{m}$, aggregation reached near steady state. All platelets are forming aggregates at the centre part of the flow, but about 25% of platelets are free near the wall, where breakup is highest.

This situation, in which the highest aggregation levels are seen first at the wall, but then migrate towards the centre of the tube, is only observed if breakup is switched on in the simulation. If breakup is switched off, aggregation is always higher at the wall, because the aggregation rate is linearly dependent on shear rate. A sample of the fraction of aggregation field without any breakup is shown in Fig. 5.25.

The methodology described in Section 5.3.5, was used to obtain the sampled concentrations of sampled volumes at the exit of tubes of different lengths. Equation 5.13 was used to calculate the CMD in the collected volume samples. Cluster mass distributions were sampled at different cross-sections along the tube's length. The collected platelets take an average transit time $\bar{t}$ (Eq. 2.4) between the inlet and the sampling point. The evolution of the PPD (Eq. 4.4) is shown in Fig. 5.26 for two cases. In the first case, the aggregation-breakup PBE is solved with model parameters obtained from the experiments of Xia and Frojmovic (1994) [236], see Tab. 5.1. The results of this numerical simulation were not similar to the results of the experiment conducted by Bell *et al.* (1984) [24] (see Fig. 5.27). Therefore, a new simulation was run, in which the breakup part of the PBE was turned off, and aggregation efficiency was adjusted to obtain a result similar to that of Bell *et al.*

The fact that aggregation efficiency $\eta = 0.02$ was adjusted in the case without breakup had only the effect to retard the growth of aggregates, which was expected according to the experimental data in Fig. 5.27. The effect of different η is seen by following the decrease in concentration of $C_{w=1}$ (in Figs. 5.26 and 5.27), which is the same as the growth of PA. In the absence of breakup, the distribution of platelets be-

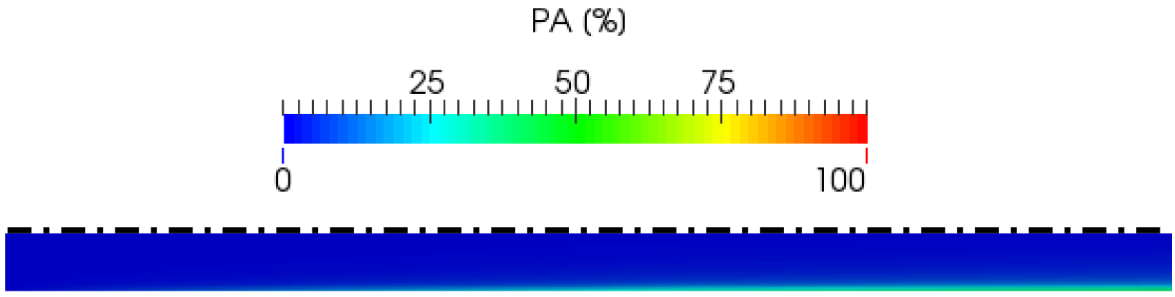

(a) $x \approx 0\,\mathrm{m}$, or inlet.

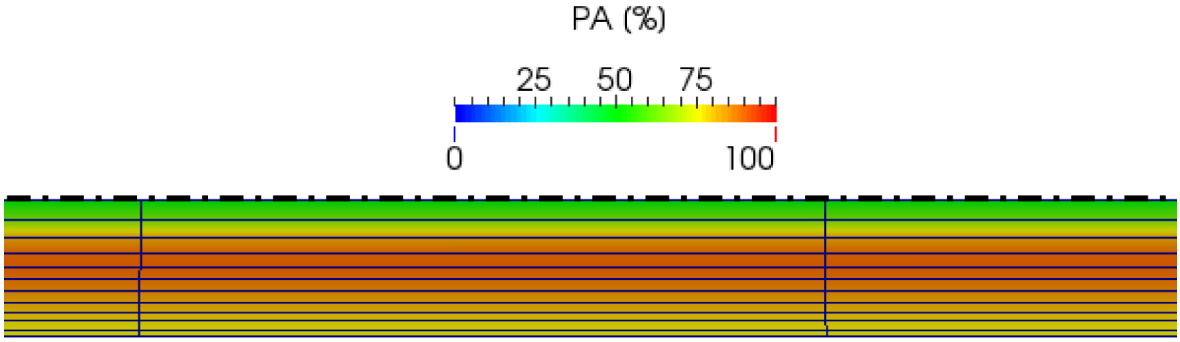

(b) $x \approx 2\,\mathrm{m}$.

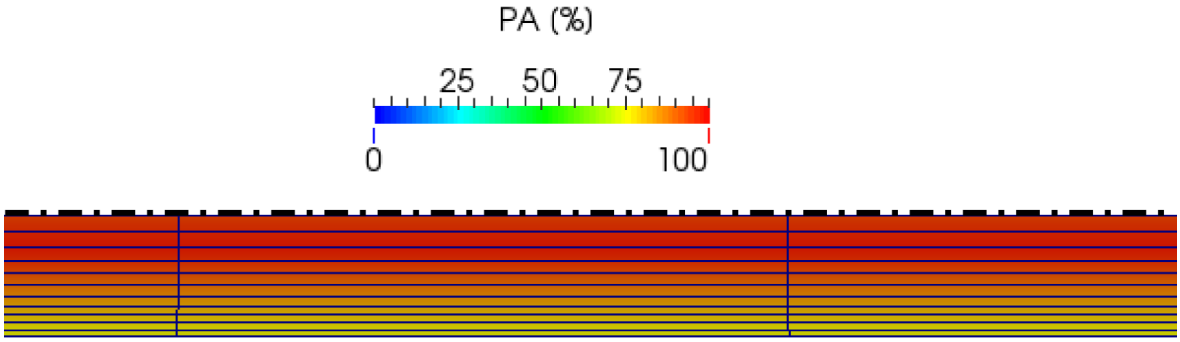

(c) $x \approx 8\,\mathrm{m}$.

Fig. 5.24: Fraction of aggregated platelets (PA) at different positions of the tube. Breakup is on, and aggregation efficiency is $\eta = 0.30$. Symmetry line (-··-).

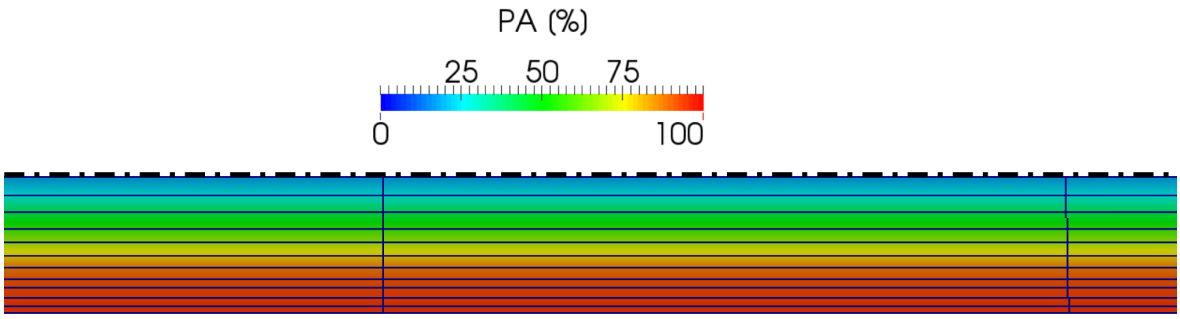

Fig. 5.25: Fraction of aggregated platelets (PA) at 8 m when breakup is off. Symmetry line (-··-).

tween aggregate sizes is very wide, i.e. the population of platelets in large aggregates is almost as high as in small aggregates (Fig. 5.27). There is no actual limitation for aggregate growth, so the discretised CMD easily ends up with many platelets forming the largest aggregate defined in the discretisation. However, the experiment shows a physical limit in aggregate size, which is in disagreement with the breakup off simulation. Hence, the PPD shape obtained by the simulation is different than the PPD obtained in the experiment. In the experiment, the PPD is bimodal, with a peak of clusters of one or two platelets, and a greater peak of clusters of about 500 platelets. In the simulation with breakup on, there was only one peak of clusters of two to eight platelets.

5.4.6 Eccentric Cylinders

The velocity and shear rate fields are represented in Fig. 5.28. The velocity field is nearly linear along the inner cylinder radius, and there is a flow recirculation where the cylinder walls are more distant from each other. The flow recirculation is a secondary flow field, such as a swirl in a pipe flow, with lower velocity and shear rates than the primary flow around the inner cylinder.

Figure 5.29 compares the aggregation state of the two cases, at $t = 120\,\mathrm{s}$. The

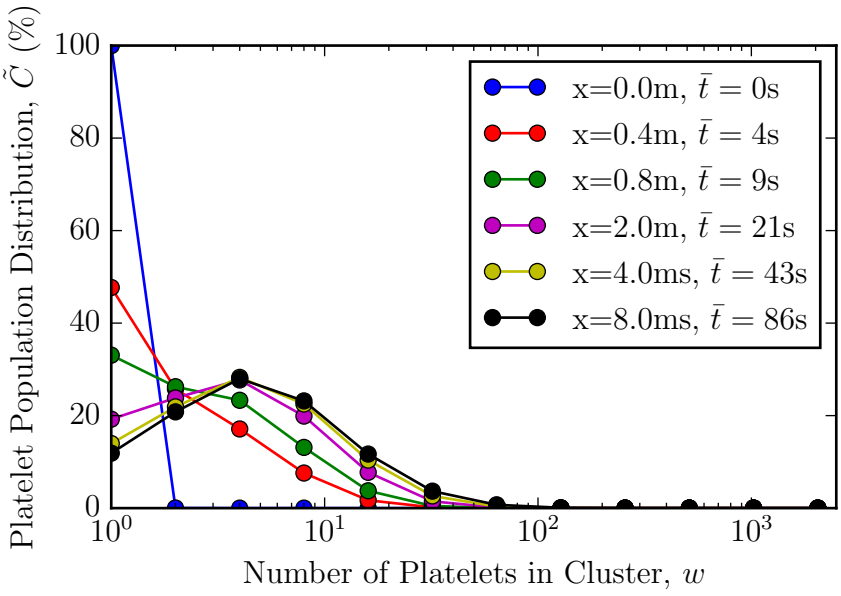

(a) Breakup on, $\eta = 0.30$.

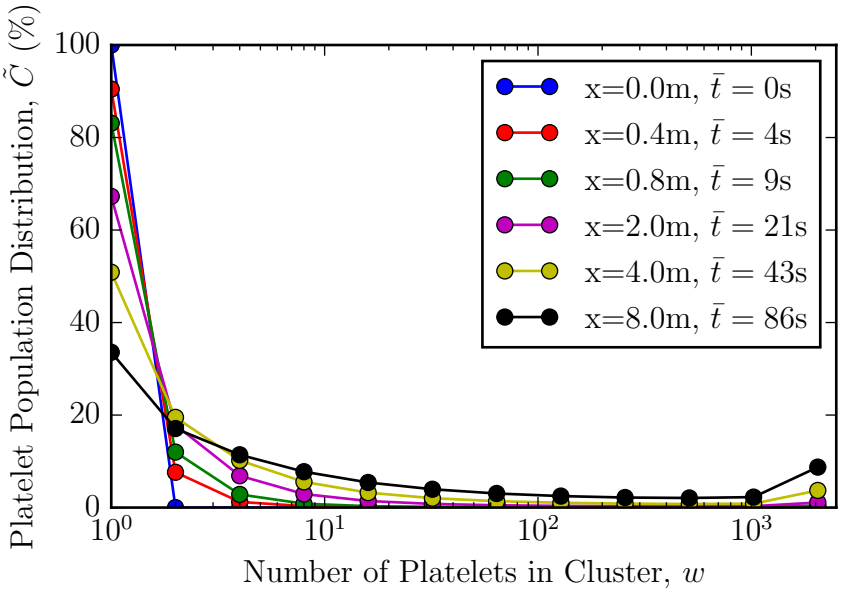

(b) Breakup off, $\eta = 0.02$.

Fig. 5.26: Platelet population distribution of the CMD flow sampled at several points along the tube.

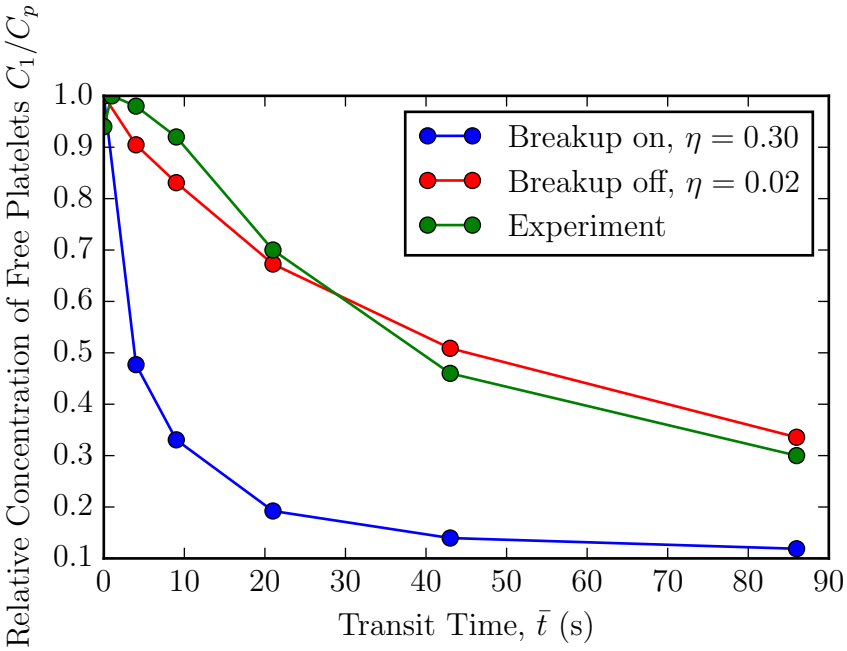

Fig. 5.27: Aggregation along the tube. Experimental points are reproduced from Bell *et al.* (1984) [24].

integral quantities $\langle w \rangle$ and I_0 are shown in Fig. 5.29 to summarize the state of the CMD in scalar terms. When breakup is on, the mean number of platelets per aggregate $\langle w \rangle$ is larger, than when breakup is off. In contrast, breakup is off, zero angle light intensity I_0 is larger, than when breakup is on. The reason for that can be seen in the graph displayed in Fig. 5.26. Very large aggregates can normally form only when breakup is turned off. This shifts the values of I_0 up, because I_0 is scaled by the square of the number of platelets in the aggregate, see Eq. 4.8. However, the higher is the concentration of large aggregates, the lower is the concentration of particles in general, because large aggregates are formed by many platelets (monomers). Consequently, the aggregation rate of small aggregates sharply decreases, which makes the CMD dispersion large, and its mean value $\langle w \rangle$ low.

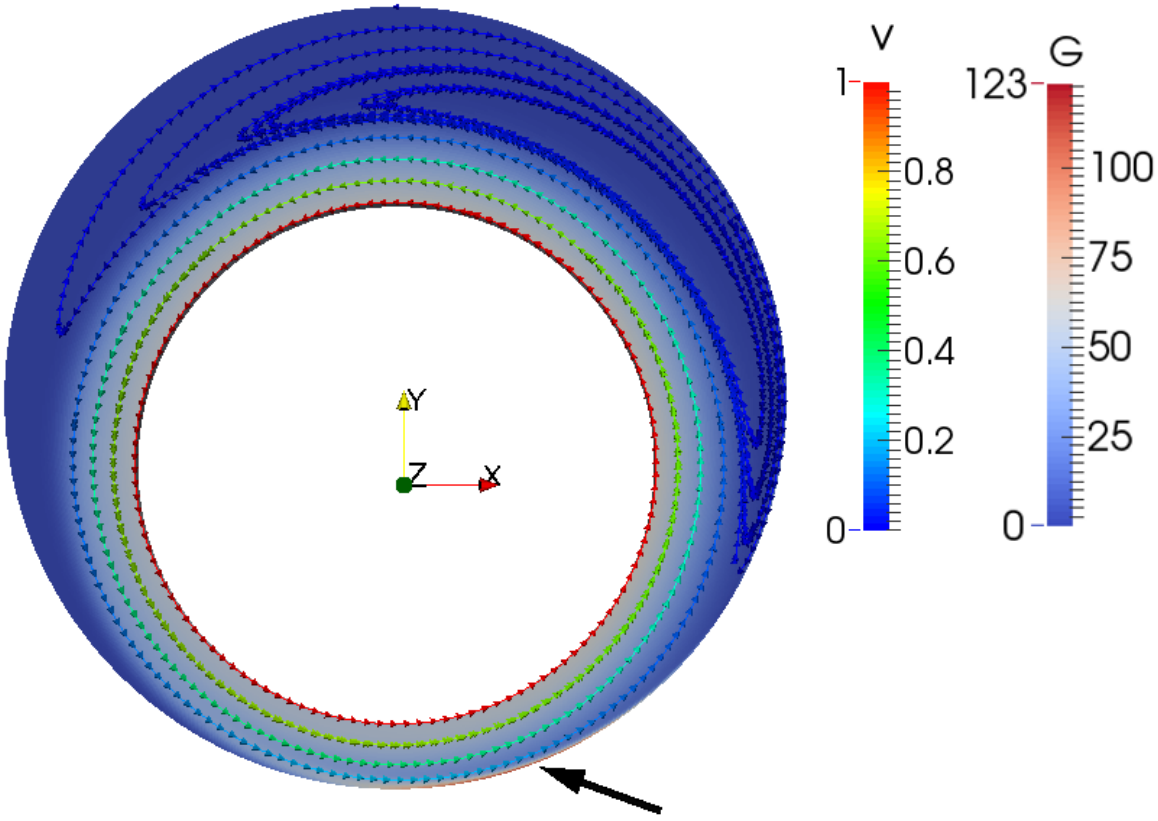

Fig. 5.28: Velocity v ($\mathrm{m\,s^{-1}}$) on streamlines and shear rate field G ($\mathrm{s^{-1}}$) between two eccentric cylinders. The arrow indicates the position of maximum shear rate.

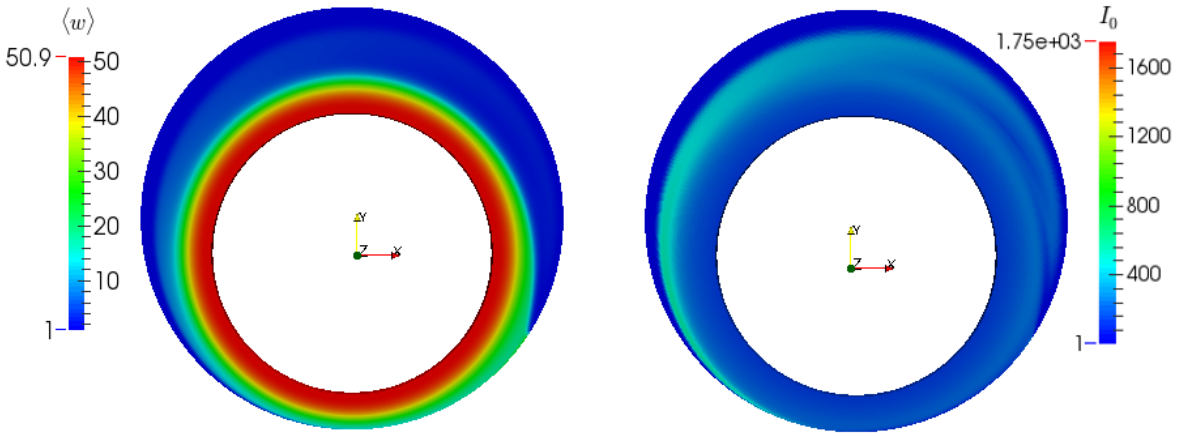

(a) Breakup on.

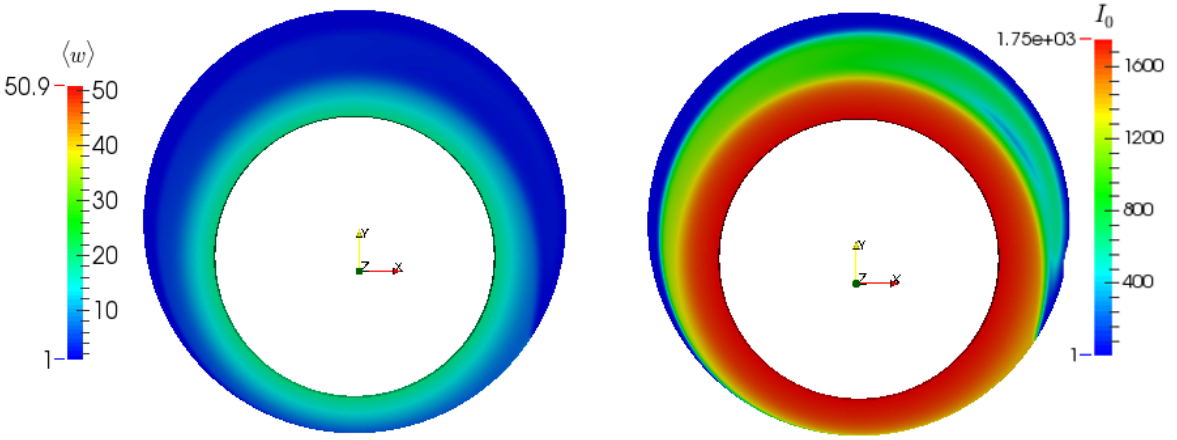

(b) Breakup off.

Fig. 5.29: Comparison between cases where breakup was switched on or off, at $t = 120$ s. Showing mean number of aggregates per cluster $\langle w \rangle$, and zero angle light intensity I_0.

5.5 Discussion

Flow rate plays two roles in SIPA: shear regulates aggregation rate, and fluid velocity regulates platelet advection. Shear rate is normally highest near walls, where the no-slip condition creates a velocity gradient, and fluid velocity is normally highest far away from the wall, where the non-slip condition is less influential. Although the maximum and minimum of these two fields are inversed in space, they are both linearly related to flow rate. An increase in overall flow rate generates a proportional increase of both shear rate and velocity fields. Damköhler number (Eq. 5.7) is the dimensionless number that compares the aggregation and advection rates. Since both aggregation and advection rates are linearly proportional to the flow rate, Damköhler number becomes independent of flow rate in a given geometry. Locally, Damköhler number depends on the distance from the wall, and the length of the characteristic length by which it is being calculated. Equation 5.7 refers to the cell Damköhler number, or the Damköhler number whose characteristic length is the finite volumes cell length. In Fig. 5.14, the pure dependence of Da on distance from the wall is evident, because it has practically the value near the wall, regardless of the shear rate and velocity at that location. The pattern of Damköhler number is the same inside and outside the crevice, and it is highest at the corners of the crevice. The insensitivity of Da to flow rate limits the power of local flow features, such as recirculation zones and flow obstructions, in significantly changing the aggregation state locally. The change of the aggregation state is going to be significantly noticed only far away downstream from those features.

This fact is not only noticed in the crevice case, but in all simulated cases. Moreover, the maximum cell Damköhler number is always $Da \leq 0.01$, which evidences that advection is much stronger than aggregation rates for SIPA. In channel flows, aggregation builds up near the walls at long distances relative to the distance between walls. In the constriction case (Fig. 5.10), the narrowing breaks up the large aggregates, which slowly form back downstream near the wall. In the tube case (Fig. 5.26), aggregation

takes about 5 m to reach steady state, when breakup is present, in a tube of $\sim 1\,\mathrm{mm}$ in diameter. In the crevice case (Fig. 5.12), aggregation occurs only at the channel wall, and continues with similar rate on the crevice mouth. Some of the aggregates formed near the wall, fall inside the recirculation zone, and some of the aggregates in the recirculation zone return to the main flow in the microchannel. The transport rate of the aggregates in and out the crevice is higher for the outer layers of the recirculation zone, than for the inner layers. Therefore, the centre of the recirculation region presents more aggregates than elsewhere. Those aggregates remain in the system for longer periods, because it takes more time for them to travel outside the recirculation zone. All these results demonstrate that SIPA is a slow process compared to advection. Thus, the gradients of aggregate concentrations are very low for SIPA, differences are noticed after long travelled distances.

In closed systems, such as a stir tank or a rheometer, the produced aggregates do not exit the system, while fresh new PRP enter the system. Light transmission platelet aggregometry is an example of stir tank, and Couette flow is the type of flow present in rheometers. In closed systems, aggregation is not limited by advection rate, because platelets eventually return to places where they have already passed by. Both in Fig. 5.9 and Fig. 5.19 it is evident that advection has no effect in the system state, because these systems are nearly homogeneous throughout the whole domain. Aggregation grows with time, and it is limited only by breakup. Zero angle light intensity (I_0) is very uniform in the LTPA simulation, because the system is well mixed. It is evident to conclude that in a very well mixed system, the spatial distribution of velocity and shear rate does not significantly interfere in the evolution of the CMD. Again, the reason for this is the low Damköhler numbers in all cells of the mesh, see Fig. 5.18. Low cell Damköhler numbers indicate that the local conversion rates are insignificant compared to advection. As advection in a closed system is related to the mixing speed, low Damköhler number indicate that the conversion rate is slower than the mixing rate.

An well mixed system is spatially homogeneous, and, thus, could in theory be treated as a 0-D model. However, when comparing the 3-D model with the 0-D PBE model (Fig. 5.21), the volume averaged shear rate $\bar{G}$ of the 3-D model did not yield exactly the same result as the 0-D model with the same shear rate. The 0-D model yielded the same result as the 3-D model only when shear rate was adjusted for matching the 3-D results. The fitting was perfect when only aggregation was occurring, but no breakup. Yet, when brekup was on, the fitting was was not perfect, but it was still very accurate if compared to experiments. This means that the aggregation dynamics is not altered by the non-uniform field, but breakup dynamics is.

The eccentric cylinder system is an example of a closed system with spatial heterogeneity (Fig 5.28). The recirculation zone, created where the outer cylinder is more distant from the inner cylinder, limits the growth and transport of aggregates. This case functions more or less as an hybrid between the Couette flow and the crevice case. Aggregation achieves steady state in the main flow around the inner cylinder, but it takes a long time to flow inside the recirculation zone, see Fig 5.29. Aggregation has the potential to grow more, but at lower rate, in the recirculation zone, because of the lower shear rate. Eventually, the larger aggregates end up moving out of the recirculation zone back to the main flow.

In the Poiseuille flow experiments of Bell *et al.* [25, 26], the slow aggregation rate compared to advection rate is evident. The tubes in those experiments were very thin (order of millimetres) and very long (order of 10 metres). The result show that platelets enduring SIPA have to travel through long distances to become significantly aggregated. These distances might be too long for SIPA to be a real problem in the circulatory system. Furthermore, it is very unlikely that all platelets in blood would be activated, if activation is a local effect instead of a systemic reaction. Therefore, those experiments of SIPA with Poiseuille flow recreated aggregation rates that are possibly stronger than what would occur in the circulatory system.

One situation that could potentially increase the rate of SIPA, but was not analysed either in experiments or in simulations, is SIPA in turbulent flow. Turbulence causes random local gradients of velocity that would induce additional aggregation of platelets. The effect of turbulence in colloid aggregation was modelled by Saffman and Turner (1956) [181]. Assuming that turbulence cause much more collisions than laminar shear, the cell Damköhler number for turbulence is given by

$$Da_t := \frac{t_{adv}}{t_a} = \frac{\Delta x}{v}\,\eta\,2\pi\sqrt{\frac{\epsilon}{15\,\nu}}(2\,R_p)^3 C_p\ , \tag{5.14}$$

where the aggregation characteristic time t_a is derived from the the turbulence kernel (Eq. 4.51). Kinematic viscosity is a constant $\nu \approx 10^{-6}\,\mathrm{m^2\,s^{-1}}$. Whether or not turbulence could significantly change the local state of aggregation, also depends on the local fluid velocity. The energy dissipation associated with haemolysis is $\epsilon \gtrsim 10^3\,\mathrm{m^2\,s^{-3}}$ at fluid velocity $v \approx 10\,\mathrm{m\,s^{-1}}$ [112]. Turbulence strong enough to cause thrombosis is an extreme flow situation, which might occur in leakage jets from mechanical heart valves [175]. Using these parameters with mesh cells of size $\Delta x = 10\,\mu\mathrm{m}$, and physiological mean platelet radius and platelet concentration, $R_p = 1.16\,\mu\mathrm{m}$ and $C_p = 300 \cdot 10^{12}\,\mathrm{m^{-3}}$, respectively, the cell Damköhler number becomes $Da_t \approx 10^{-4}$. Such low cell Damköhler number indicate that even in turbulent flow, local aggregation can not be observed, because fluid velocity is too high ($v \approx 10\,\mathrm{m\,s^{-1}}$). SIPA rates are always related to fluid velocity, therefore, strong local aggregation would only be observed if platelet concentration C_p is many orders of magnitude higher than physiological values.

5.6 Conclusions

The similarity between the results 3-D and 0-D simulations of closed systems demonstrate that experimental data could be accurately be fitted to a 0-D PBE model. Spatially homogeneous models can be solved only on time by an ODE solver, as demonstrated in Fig. 5.21. Although the average shear rate $\bar{G}$ in the 3-D simulation does

not yield exactly the same result in the 0-D, shear rate values close to $\bar{G}$ yield very close results in the 0-D simulation. The differences might be inferior to experimental uncertainties of real cases. In this case, it is unnecessary to process a 3-D solution with transport, which is computationally much more expensive than the 0-D solution.

In open systems, the local Damköhler numbers Da are always lower than 1, which indicates very low gradients of aggregate concentration. Although aggregation rates increase with higher flow rates, so do the advection rates, which keep Da orders of magnitude lower than 1. Damköhler number are also orders of magnitude inferior to 1 in turbulent flow, because turbulence occurs in high shear rates. For observing significant SIPA in open systems, the simulated geometry must have large dimensions, and too many cells, because the CFL condition still has to be attended. This makes SIPA simulations of open systems computationally expensive.

Hybrid cases, where a closed system has secondary flows, such as recirculation zones, are more interesting for 3-D solution of SIPA. In these cases, fast aggregation occurs in the main flow, where mixing is high, and slow local aggregation occurs in the zones of secondary flow.

Chapter 6

Experiments on Shear-Induced Platelet Aggregation in Couette Flow

This chapter describes a series of experiments conducted in 2013 and 2014 in McGowan Institute of Regenerative Medicine, University of Pittsburgh, Pittsburgh, Pennsylvania, USA. The experiements had the objective of recording the dynamics of shear-induced platelet aggregation (SIPA) in real time, recording pictures of platelet-rich plasma aggregating in a rheometer running at different shear-rate profiles. The statistics of the platelet samples, including free platelets and aggregates of different sizes, were obtained from image processing technique in order to demonstrate the dynamics of SIPA.

6.1 Introduction

To date, there is no experiment that measures SIPA in real time, where the shear rate is uniform. Normally, SIPA is experimentally observed in a cone-and-plate

[38, 42, 90, 103, 107, 156, 193, 190, 242] or a concentric-cylinder rheometer [236], because shear rate is uniform in Couette flow. However, platelets are sampled out after discrete intervals larger than 10 s, and the state of the sample is assessed elsewhere by cytometry. Two limitations exist in this approach. First, there is a time interval between the stress test and the sample's evaluation, which will thus measure not only aggregates induced by stress but also aggregates induced by degranulated factors. The amplification effect caused by degranulated factors in SIPA tests has been demonstrated by shearing samples of different platelet concentrations [190]. Second, transient aggregates forming in time scales of 0.1–5.0 s can only be detected in real time. Although Poiseuille flow gives non-uniform shear rate, flow in tubes has also been used to test SIPA [26, 24, 25]. In this case, an average shear rate was calculated, based on the shear profile and residence time.

Time-resolved observations of aggregation kinetics are usually conducted either *in vitro* in microchannels, or *in vivo* in mouse arterioles [161, 217, 227]. In both cases, more aggregates arise at places of steep decrease of shear stress than in places of constant over-threshold shear stresses. Although these experimental set-ups can highlight the phenomenon of post-stenotic thrombogenesis very well, the flow field developed there does not have an uniform shear profile, as in cone-and-plate rheometers. Different blood particles experience different stress histories, which makes it unsuitable for quantifying the relationship between shear stress and aggregation kinetics.

To analyse the micromechanics of cell aggregation, Goldsmith *et al.* [80, 81, 146, 84] have recorded platelets and neutrophils aggregating in a rheoscope. The rheoscope is an equipment composed of a rheometer with a transparent orifice and a microscope, which is normally connected to a CCD camera for video recordings. The microstructure of complex fluids can be observed at different shear rates in a rheoscope. Rheoscopes bring the ability for time-resolved observation of SIPA in uniform shear fields. However, there is a physical limitation to visualize the same cells on a sequence of recorded frames

when shear rate is high. At high shear rates, cells would be crossing the window of view faster than the camera is able to record. Therefore, the studies carried out by Goldsmith *et al.* have only reported results at low shear rates ($\dot{\gamma} < 500\,\mathrm{s}^{-1}$). At low shear rates, the authors could visualize cell collision, cell aggregation, aggregate rotation, and aggregate breakup. Those studies focused on the kinematics of SIPA in a shear-controlled environment, but they did not report the dynamics of SIPA. Nevertheless, the dynamics of SIPA can still be recorded with a rheoscope, if instead of tracking individual cells moving inside the microscope's window of view, the statistics of the whole population of cells is obtained. The experiment shown in this chapter follows this methodology.

6.2 Methodology

We employed the Linkam Optical Shearing System (CSS450), a plate and disc rheoscope produced by Linkam Scientific Instruments Ltd., Tadworth, Surrey, UK. This rheoscope is property of the laboratory of Dr. Kameneva, in McGowan Institute for Regenerative Medicine. The intrument's accuracy is reported based on its technical specifications. All blood samples were collected and processed in the McGowan Institute. Platelet-rich plasma was obtained according to the protocol stated below. In order to achieve higher levels of shear stress, plasma viscosity was increased by adding a polymer called Polyvinylpyrrolidone (PVP). Platelet and aggregate populations were assessed by image processing technique, which output the average concentration of diferent platelet clusters along time. Limitations of the protocol are also discussed.

6.2.1 Rheoscope

The Linkam CSS450 shearing stage has been used for measuring the deformability of red blood cells (RBC), but as far as we know it had never been used to test platelets

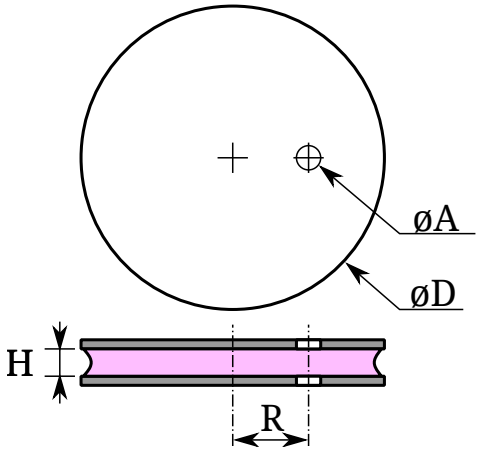

Fig. 6.1: Linkam CSS450 parallel-disc geometry. Aperture diameter (øA), disc diameter (øA), gap height (H), and aperture position (R).

before. The system produces a parallel-disc Couette flow [145], whose geometrical parameters are depicted in Fig. 6.1. The disc diameter is $D = 30\,\mathrm{mm}$, the gap height $H = 5$–$2500\,\mu\mathrm{m}$, aperture position $R = 7.5\,\mathrm{mm}$ from the disc centre, aperture diameter $A = 2.5\,\mathrm{mm}$, and angular velocity $\omega = 0.001$–$10.000\,\mathrm{rad\,s^{-1}}$. The resolution of the gap height is $\Delta H = 1\,\mu\mathrm{m}$, and the resolution of the angular velocity is $\Delta\omega = 0.001\,\mathrm{rad\,s^{-1}}$. The uncertainties of the device parameters were not disclosed in the manual, so they had to be assumed. As a conservative estimative, the uncertainty of both the gap height and the angular velocity were assumed to be as large as half of their respective resolutions, i.e. $\sigma_H \equiv \frac{\Delta H}{2}$ and $\sigma_\omega \equiv \frac{\Delta\omega}{2}$.

Throughout the experiments the gap height was fixed at $H = 25 \pm 1\,\mu\mathrm{m}$. In order to break any aggregate formed prior to the experiment, the shear rate profile was programmed to give a short high-shear phase for 5 s followed by a long low-shear phase phase for 30 s, as shown by Fig. 6.2. A CCD camera was coupled with a stroboscope in order to avoid blurred pictures. Pictures were taken at the maximum possible frequency (2.5 Hz, or one picture every 0.4 s). The high shear phase started right after the first five frames.

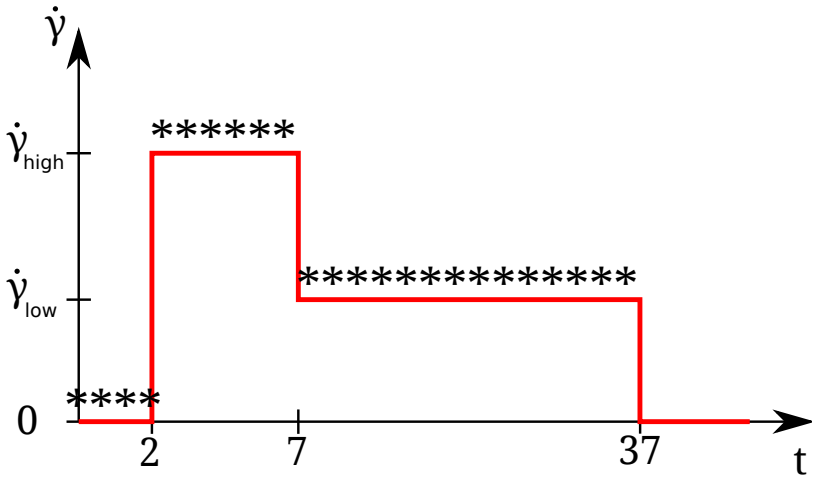

Fig. 6.2: Shear rate curve applied to the sample at R. The high shear phase starts after five photo shots, and persists for five seconds. The low shear phase lasts for 30 s. Asterisk marks (*) stand for photo shooting times.

The window of view is 260 µm wide and 194 µm high. So, the volume observed in the window of view is

$$V_{\text{view}} = 260 \times 194 \times 25 = (1.3 \pm 0.1) \cdot 10^6\,\mu\text{m}^3 = (1.3 \pm 0.1) \cdot 10^{-3}\,\mu\text{L}\ . \tag{6.1}$$

6.2.2 Viscosity-Raising Agent

For shearing RBCs it is common to add either Glycerol or Polyvinylpyrrolidone (PVP) to increase plasma viscosity in order to apply higher shear stresses at lower shear rates. Long PVP polymers (molecular weight 360 000, produced by Sigma Aldrich) were dissolved in phosphate buffered saline (PBS). Viscosity of diferent concentrations of PVP was measured using capillary glass viscosimeters. The relation of viscosity per mass concentration of PVP in PBS is shown in Fig. 6.3. A solution of 11.2% in mass concentration of PVP was later dissolved in platelet-rich plasma (PRP) to increase its viscosity. A graph of the viscosity of diferent volume fractions of this 11.2% PVP solution dissolved in plasma is shown in Fig. 6.4. For the experiment presented here,

a 20% volume fraction of this PVP solution was used. The final viscosity of the 20% PVP and 80% PRP solution was 6.3 $\pm$ 0.2 cP.

The 11.2% PVP solution was acidic ($pH = 5.44 \pm 0.03$), but blood plasma had the buffering capacity to turn pH back to normal. A $pH = 7.16$ was measured for 39.1% volume of PVP in plasma, $pH = 7.27$ for 17.6%, and $pH = 7.57$ for 0.0%. So, blood with 20% PVP has normal pH, which would not activate platelets because of acidity.

6.2.3 Flow Field

The flow field in a disc-plate rheometer is known as Couette flow. In Couette flow, one surface (the plate) is static, while the other surface (the disc) moves. The velocity field grows linearly between the two surfaces, which results in a constant shear rate.

Maximum Shear Rate

In disc-plate rheometer, the shear rate is given by:

$$\dot{\gamma} = \frac{v_\theta}{z} = \frac{\omega R}{H} \, . \tag{6.2}$$

The gap height H was fixed at 25 µm, and the angular velocity was limited to half the maximum speed in order not to overload the machine. Hence, the maximum shear rate obtained in the rheoscope was

$$\dot{\gamma} = \frac{5 \cdot 7.5 \cdot 10^{-3}}{25 \cdot 10^{-6}} = 1500\,\mathrm{s}^{-1} \, . \tag{6.3}$$

With this shear rate and viscosity $\mu = 6\,\mathrm{Pa\,s}$, the maximum shear stress was $\tau = 9.0\,\mathrm{Pa}$.

Uncertainty of Shear Rate

The uncertainty σ_f of a derived quantity $f = f(x_1, ..., x_n)$ can be obtained by

$$\sigma_f^2 = \left(\frac{\partial f}{\partial x_1}\sigma_{x_1}\right)^2 + ... + \left(\frac{\partial f}{\partial x_n}\sigma_{x_n}\right)^2 \, . \tag{6.4}$$

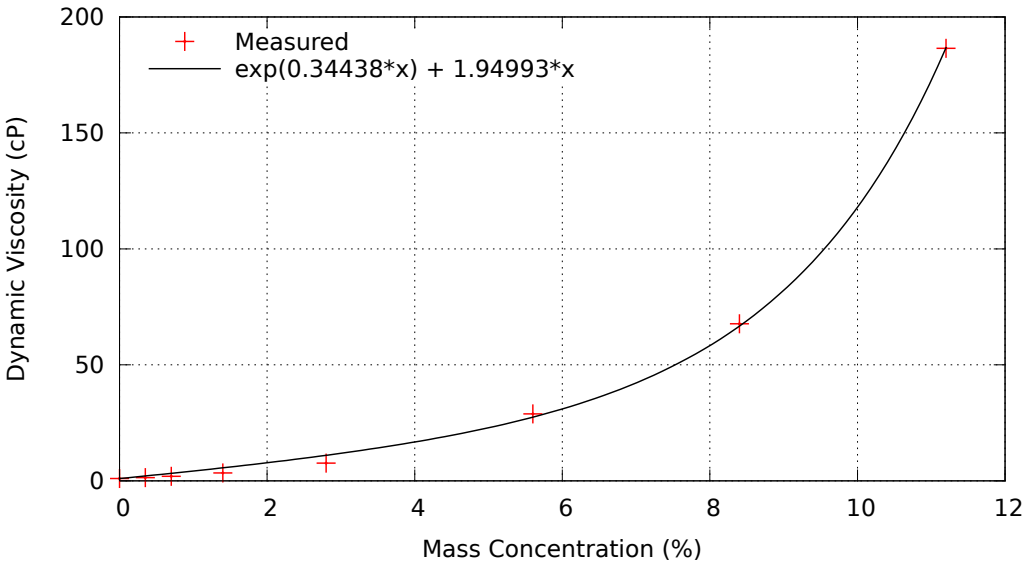

Fig. 6.3: Viscosity of PVP solution in PBS.

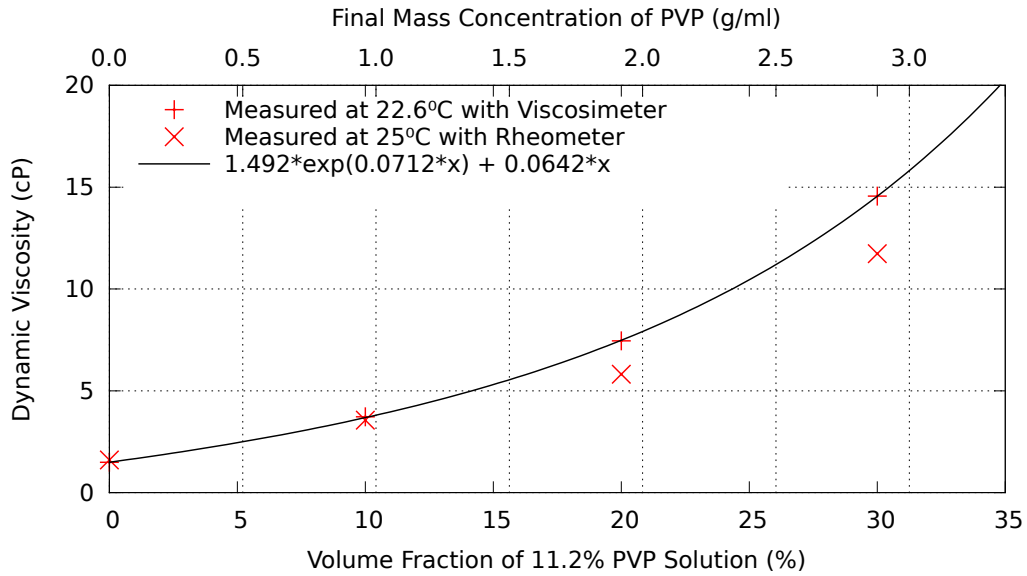

Fig. 6.4: Viscosity of 11.2% PVP solution in blood plasma. Lower axis shows the volume portion of PVP solution in the increased viscosity PRP solution, wheras the upper axis shows the actual PVP concentration.

Given Eq. 6.2, the uncertainty in $\dot{\gamma}$ is

$$\begin{aligned}\sigma_{\dot{\gamma}} &= \sqrt{\left(\frac{\partial\dot{\gamma}}{\partial\omega}\sigma_\omega\right)^2 + \left(\frac{\partial\dot{\gamma}}{\partial R}\sigma_R\right)^2 + \left(\frac{\partial\dot{\gamma}}{\partial H}\sigma_H\right)^2} = \\ &= \sqrt{\left(\frac{R}{H}\sigma_\omega\right)^2 + \left(\frac{\omega}{H}\sigma_R\right)^2 + \left(-\frac{\omega R}{H^2}\sigma_H\right)^2} = \\ &= \dot{\gamma}\sqrt{\left(\frac{\sigma_\omega}{\omega}\right)^2 + \left(\frac{\sigma_R}{R}\right)^2 + \left(\frac{\sigma_H}{H}\right)^2} \,. \end{aligned} \tag{6.5}$$

The uncertainty σ_ω is estimated as half the step motor's resolution, hence $\sigma_\omega = 5\cdot10^{-4}\,\mathrm{rad\,s^{-1}}$, and σ_H is the stage calibration precision, estimated to be $\sigma_H = 0.5\,\mu\mathrm{m}$. Since the aperture is much larger than the microscope's window of view, and there is no precise way of calibrating its positioning over the aperture, σ_R is estimated as half the aperture's diameter, i.e. $\sigma_R \equiv \frac{A}{2} = 1.25\,\mathrm{mm}$. From those relative uncertainties, the relative uncertainty of the microscope positioning ($\sigma_R/R = 17\%$) is far the largest. Therefore, the overall shear rate uncertainty is $\sigma_{\dot{\gamma}} = 0.17\,\dot{\gamma}$.

Shear Rate Variation in the Window of View

The window of view is $260\,\mu\mathrm{m}$ wide along the radius. The shear rate difference between the inner and outer edges of a picture frame is

$$\Delta\dot{\gamma} = \frac{\omega\,\Delta R}{H} = 52\,\mathrm{s^{-1}} \,. \tag{6.6}$$

Flow Regime

The maximum Reynolds number at our point of view was

$$Re = \frac{\omega R H \rho}{\mu} = \frac{5.0\,(7.5\cdot10^{-3})(25\cdot10^{-6})(1.025\cdot10^{3})}{6\cdot10^{-3}} = 0.16 \,. \tag{6.7}$$

That means that although inertial forces are lower than viscous forces, inertial forces are still significant ($Re > 0.01$); the velocity field is not purely potential.

Centrifugal forces

As PRP rotates inside the rheometer, centrifugal forces move platelets along the radial direction. Thererefore, the speed of this separation has to be known, in order to determine its significance for the experiement. Density of plasma is approximately $\rho = 1025\,\mathrm{kg\,m^{-3}}$, the density of blood cells is approximately $\rho_{Pl} = 1125\,\mathrm{kg\,m^{-3}}$, and mean platelet volume (MPV) is $V_{Pl} = (9.7\text{–}12.8)\cdot 10^{-18}\ \mathrm{m}^3$ [235]. So, the platelet mass can be estimated as $m = 1125 \cdot 12 \cdot 10^{-18} = 1.35 \cdot 10^{-14}$ kg.

Centrifugal force is given by

$$F_c = \frac{m\, v_\theta^2}{R} = m\,\omega^2\, R\,(z/H)^2\ . \tag{6.8}$$

Particle drag force according to Stokes flow is given by

$$F_s = 6\pi\,\mu\,(d/2)\,v_r\ . \tag{6.9}$$

At steady state the centrifugal force is equal to the drag force:

$$F_c = F_s \Rightarrow v_r = \frac{m\,\omega^2\,R\,(z/H)^2}{3\pi\,\mu\,d}\ . \tag{6.10}$$

Eq. 6.10 gives a maximum at $z = H$,

$$v_r = 2.2 \cdot 10^{-8}\ \mathrm{m\,s^{-1}} = 0.022\,\mu\mathrm{m\,s^{-1}}\ , \tag{6.11}$$

which is a negligible velocity.

Shear Stress in the Pipette Tip

Adjustable pipettes were used to transfer the samples from tubes to the rheoscope. They were also used to mix PVP with PRP. It is important to get an estimate of the shear stress levels in the pipette tip, in order to determine if it could be too high to damage the platelets. Velocity field in the pipette tip is parabolic, which gives the shear stress field

$$\tau(r) = \mu\dot{\gamma}(r) = \mu\frac{4Q}{\pi R^4}r\ . \tag{6.12}$$

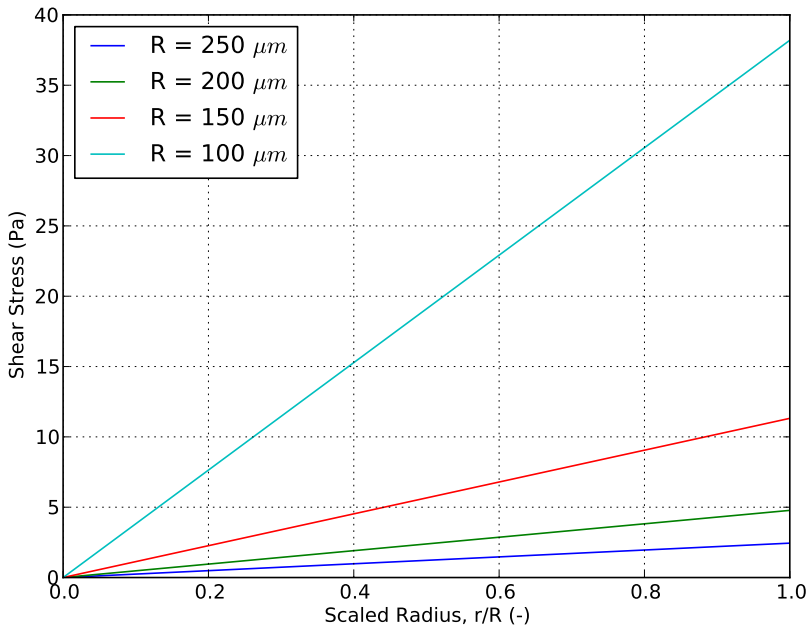

Fig. 6.5: Shear stress in the 10–100 µL pipette tip with flow $Q = 5\,\mu\mathrm{L\,s^{-1}}$. Each stress curve relates to one tip radius.

Pipettes for 10–100 µL were used to gently mix PVP in PRP, by sucking the mixture in and out at very low flow rates ($Q \approx 5\,\mu\mathrm{L\,s^{-1}}$). Equation 6.12 shows fourth order sensibility to the tip radius, whose exact value is not present in the manufacturer's (Eppendorf) manuals. In Fig. 6.5, shear stress is plotted for different tip radii close to the pipette tip radius measured with a calliper. The tip radius was estimated to be close to 250 µm, which would give a shear stress lower than the activation level ($\tau = 3.5 \sim 5.0$ Pa).

Shear Stress at the Closure of the Parallel Plates

Once 20% in volume of PVP is mixed with 80% in volume of PRP, a drop of 25 µL of this sample is is immediately pipetted on the rheometer's disc. When the rheoscope's plate closes parallely over the disc there is a squeeze flow field [60] whose

shear stress field is given by

$$\tau = \mu\dot{\gamma} = \mu\frac{3\dot{h}}{h^3}\sqrt{\frac{r^2z^2 + 3(h^2 - z^2)^2}{2}}\ , \tag{6.13}$$

where z is the vertical coordinate referenced at mid point between the plate and the disc, h is the plate position from the reference point $z = 0$ (also called as half height), $\dot{h}$ is the approximation velocity, and r is the radial coordinate. The shear field resultant from Eq. 6.13 is ilustrated in Fig. 6.6b. The shear stress at different half heights is shown in Fig. 6.7. Apparently, the shear stress levels caused by the squeeze flow are high enough to activate the platelets. There are two ways of overcoming this problem. One is to increase the gap height (H), and the other is to reduce the approximation speed ($\dot{h}$).

6.2.4 Image Processing

The images were recorded as 12-bit TIF files with 696×560 pixel resolution. In order to obtain the statistics of the aggregation state of the platelet population in time, the recorded image array was processed using ImageJ [4]. A script was used to run a pipeline of algorithms, which scaled the images, cleaned noise, segmented the particles, and counted and classified them according to their sizes. For reproductivity purpose, the ImageJ script displayed:

```
> Open Image Stack(Files)
> Set Scale(distance=2.672, known=1, pixel=1, unit=um, global)
> Image Differentiation(x, y)
> Gaussian Blur(sigma=1, stack)
> setAutoThreshold(method=Default, background=Dark)
> Fill Holes
> Analyze Particles(size=3.2-Infinity, circularity=0.00-1.00,
show=Ellipses, display, clear, include, in_situ, stack)
```

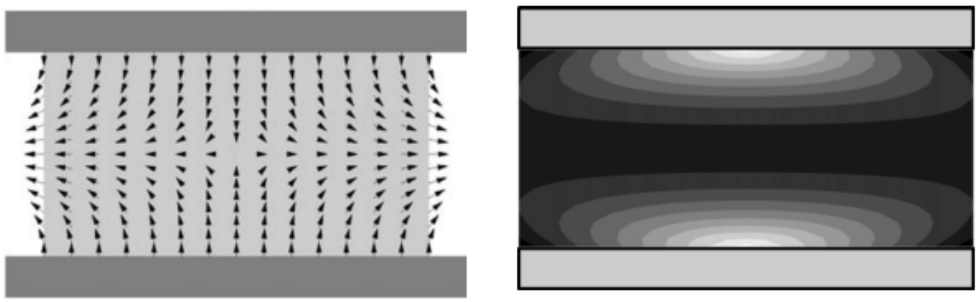

(a) Velocity Field. (b) Shear Field.

Fig. 6.6: Squeeze Flow images from Engmann *et al.* (2005) [60] computed from Eq. 6.13. In (b), darker shades correspond to higher shear stresses.

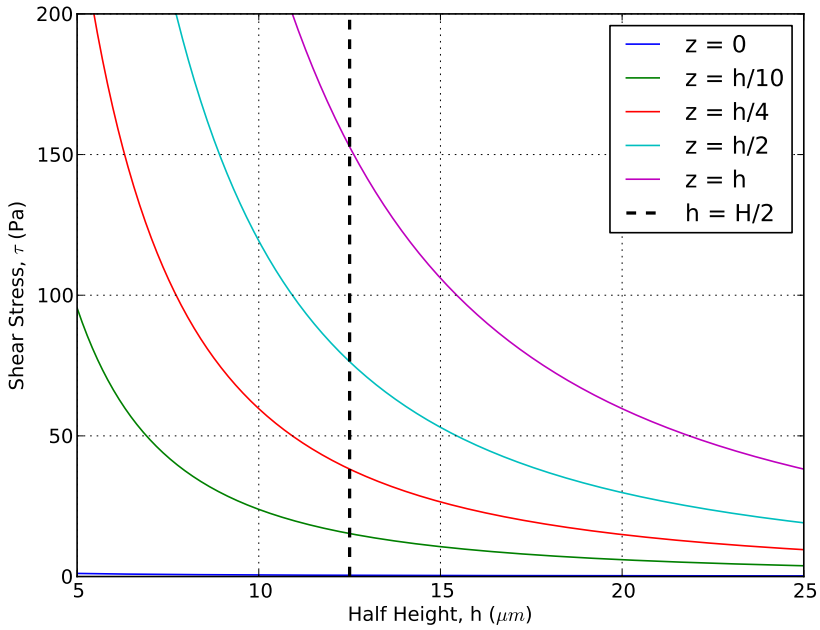

Fig. 6.7: Squeeze flow shear stress at different half heights. The curves demonstrate how shear stress varies along the z direction. The dashed vertical line marks the position where the experiments were run ($h = H/2$). The closure velocity was estimated as $\dot{h} \approx \frac{1}{2}(2,500\text{–}25)/5\,\mu\text{m}\,\text{s}^{-1} \approx 248\,\mu\text{m}\,\text{s}^{-1}$.

```
> Save Data
```

The stack of images is scaled as 1 pixel amonts 2.672 µm. Then, image differentiation gives the gradient of the pixel values on the pictures. This highlights the borders between dark and light regions compared with the background. Gaussian blur runs a Gaussian (normal) filter, which smooths the image noise. Autothreshold automatically sets a binary mask, where platelets and aggregates are present. However, the previous steps are not sufficient to autosegment the pictures, some pixels inside the segmented regions are remain unmasked. The holes in the mask are automatically filled. The mask is analysed, where the detected blobs are approximated by ellipses, which are numbered and saved along with their areas. An image sample showing of the detected particles is seen in Fig. 6.8. A histogram of particle sizes detected in the whole image array is presented in Fig. 6.9. After the data of the segmented particles is saved, the statistics is obtained by a python code.

6.2.5 Aggregate Classification

Platelets are colloid particles aggregating on contact. Colloid aggregates are often ramified non-dense clusters with self-similar characteristics. Therefore, the apparent mean radius of the detected by image process technique is the radius of gyration (Eq. 4.10), which relates to the aggregate real volume by the exponent constant known as fractal dimension D_F. Thus, Eq. 4.10 can give the average number of platelets inside an aggregate based on its mean radius. The fractal dimension $D_F = 2.2$ was used for estimating the number of platelets clustered in the aggregate, because this number was measured by a laser light scattering technique [50]. This number is inside the magnitude range of 2.0–2.5 theoretically predicted for aggregation rates controlled by the collision rates (i.e., chemical rates much larger than collision rates) [139].

The aggregates in Fig. 6.8 are more easily detected as ellipses than circles, because they are rolled by the rheoscope's disc rotation. the translation of aggregate size

Fig. 6.8: Snapshot highlighting the detected particles and their approximate sizes. The black smudge is a RBC being sheared at $\tau = 7\ Pa$.

to the number of platelets there clustered (Eq. 4.10) is still valid. The radius of gyration is an average radius of fuzzy object; therefore, the average radius of an ellipse ($A_{\text{circle}} = A_{\text{ellipse}} \Leftrightarrow \pi R_g 2 = \pi\, R_1\, R_2 \Leftrightarrow R_g = \sqrt{R_1\, R_2}$ is the radius of gyration of the detected aggregates. The aggregates are detected as ellipses, because this is the 2-D projection of 3-D ellipsoid aggregates. The geometric mean radius of an ellipsoid equals to the radius of a sphere of the same volume. This method sometimes underestimate and sometimes over estimate the radius of gyration of aggregates, because part of the aggregates are left out of the ellipses, and the aggregates contain voids between platelets. However, when considering a large number of aggregates, and the central limit theorem (CLT) of statistics implies that those measurement errors are largely mitigated when the average is taken.

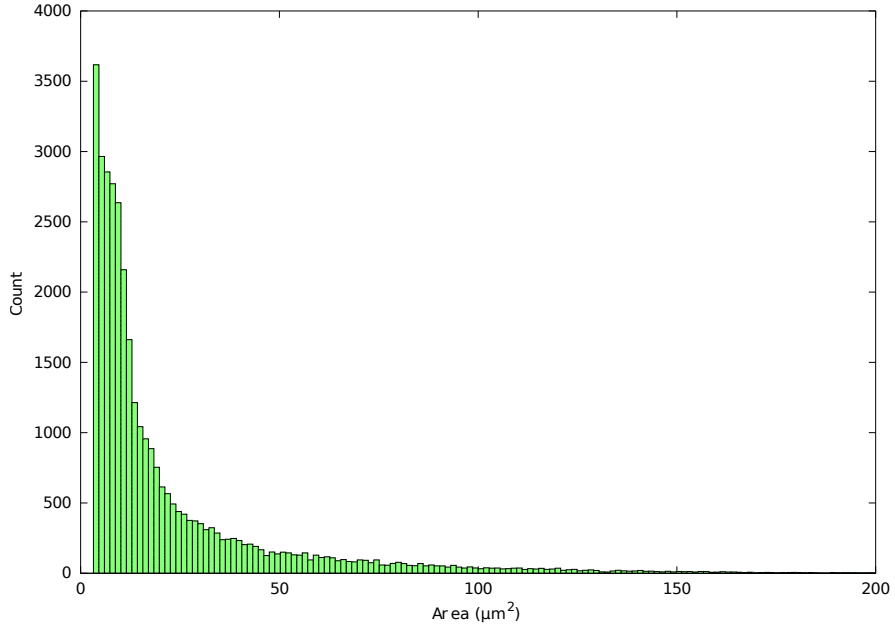

Fig. 6.9: Histogram of aggregate sizes detected from a sequence of images like Fig. 6.8. The histogram shows the particle size distribution in the whole sample instead of just on one image.

The detected aggregates were distributed in histograms classified by the number of platelets clustered in the aggregates detected by the `Analyze Particles` algorithm. In order to estimate the number of platelets clustered in those aggregates, Eq. 4.10 was transformed to give the cross-sectional area of fractal aggregates:

$$A = \pi R^2 = \pi (w^{1/D_F} R_p)^2 \ , \tag{6.14}$$

where R is the radius of gyration, R_p is the average radius of a single platelet, and w is the estimated number of platelets forming the aggregate. The histogram was formed by sampling the aggregates in a number of bins of a range of clustered platelets (w). The bins had higher resolution for the smallest aggregates, because it would give more precision on the measurement for the initial stages of SIPA, and because larger aggregates are sampled with much lower frequency than smaller aggregates (see Fig. 6.9) decreasing the count precision for larger aggregates. The histogram bins were defined as follows: singlets (free platelets), doublets, multiplets ranging 3–4 platelets,

5–15 multiplets, 16–36 multiplets, and 37–112 multiplets, see Fig. 6.10. For the singlets bin the lower and upper limits were defined as $A = \pi\,(R_p - \sigma_{R_p})^2$ and $A = \frac{1}{2}(\pi\,R_{w=2}^2 + \pi\,R_p^2)$, respectively. The upper limit of the singlet bin is the mid point between singlet bin and the doublet bin. The other bin limits were defined at the mid points between the largest and smallest aggregates defining those bins.

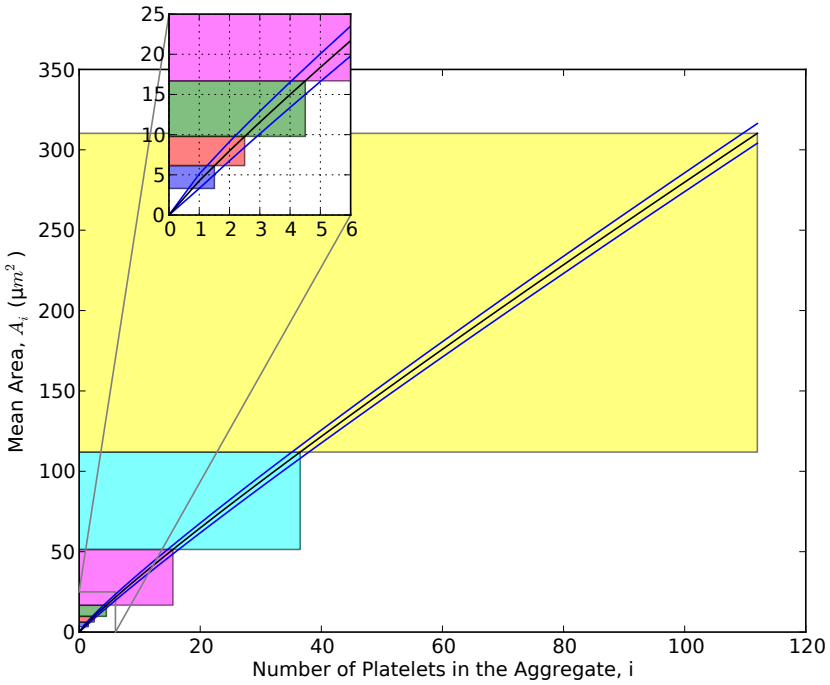

Fig. 6.10: Expected aggregate area by cluster of w platelets. Upper and lower lines enclose a 68.3% confidence band (1σ band) of the expected aggregate area (middle line). The coloured bars limit the multiplets' bins. Blue: singlets; red: doublets; green: 3–4 multiplets; magenta: 5–15 multiplets; cyan: 16-37 multiplets; and yellow: 37-112 multiplets.

6.2.6 Sample Preparation

Platelets become easily activated when outside their normal environment. Therefore, only fresh platelet samples would be viable for assessing platelet function in experiments. The viability of the platelets can be guaranteed to a maximum of six hours

[225].

Fresh whole blood was collected after informed consent from healthy donors, who had refrained from taking any platelet altering medications 14 days prior to collection, in accordance with Institutional Review Board guidelines of the University of Pittsburgh. The donors were healthy individuals who had not taken any anti-platelet drug, such as aspirin, for at least two weeks. Blood was drawn using silicon coated needles into clean polypropylene tubes containing one tenth volume of 3.2 % (w/v) trisodium citrate dihydrate anticoagulant (1:9 volume ratio of citrate to blood). This blood was always kept at room temperature of 22 °C.

The polypropylene tubes were centrifuged at 250 g for 15 min (soft spinning) to separate the cells. The top 2/3 of the transparent phase was denominated platelet poor plasma (PPP), and the bottom 1/3 including the buffy coat was denominated platelet rich plasma (PRP). The red blood cells were discarded. To increase platelet aggregation further, in order to normalise platelet concentration for the mixing with PVP, a second run of centrifugation is possible. In this case, a second spinning at 720 g for 10 min (hard spinning) is run. For a second centrifugation another anticoagulant has to be added in order to avoid platelet activation [225]. The anticoagulant successfully tested was prostaglandin E_1 (PGE_1, supplied by Sigma-Aldrich) at a final volume concentration of 1 µL per 1 mL of PRP. The molar concentration of PGE_1 was 1 mM before mixing with PRP, yielding a final concentration of 1 µM of PGE_1 in PRP. The hard spinning was done in 1.5 mL tubes, from which 1.0 mL was discarded and the bottom 0.5 mL was used to completely resuspend the platelet pallet by stirred and sucking in and out with a 100 µL pipette tip. The resuspended PRP from all 1.5 mL tubes was transferred into a single 1.5 mL tube. The hard spun PRP was visualised in the optical microscope, as seen in Fig. 6.11. Platelets were discoid and disaggregated. However, they aggregated after 30 min with 20% PVP mixed with them, as shown in Fig. 6.12. These aggregated platelets showed signs of activation, with spherical shape and pseudopods (Fig. 6.13).

Table 6.1: Average platelet count of different sample preparation protocols.

Sample	Count (μL^{-1})
PPP soft spinning	60,000
PRP soft spinning	350,000
PRP hard spinning	1,250,000
PRP soft spinning + 20% PVP	1,000,000

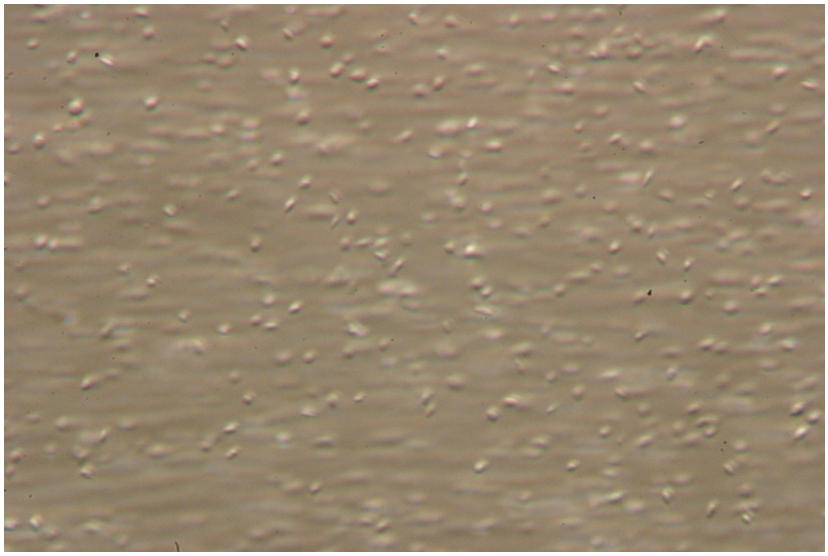

Fig. 6.11: PRP ($1\,000\,000\,\mu L^{-1}$) in the light microscope.

Platelets were counted in a Countess Automated Cell Counter, (Life Technologies Co.). Platelet concentration of different preparations are shown in Table 6.1.

In order to visualise the extent of platelet activation and aggregation caused by PVP, a test was made where two drops, one of PRP and the other of PVP, were placed adjacent to each other on a microscope slide. The drops merged when the slide was closed with the glass cover, creating a mixing layer of those two samples (see Fig. 6.14). No particles, besides dust from the slide, were seen on the PVP sample. Very few dust particles were present on the slide, but the picture of a dust particle is on Fig. 6.14 in order to demonstrate that the microscope was in focus. At the PVP side (left) of the mixing layer, no platelets are seen, but smaller colloid particles are seen adhered to the

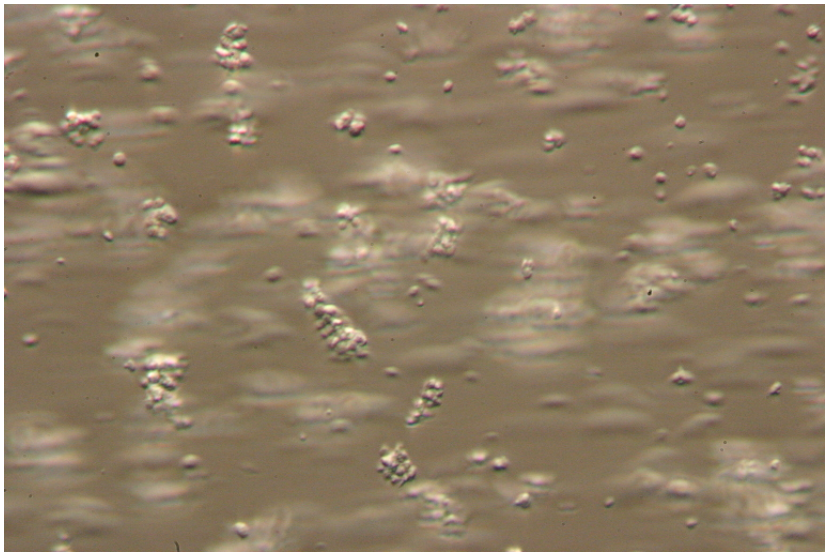

Fig. 6.12: PRP mixed with 20% PVP after 20 min.

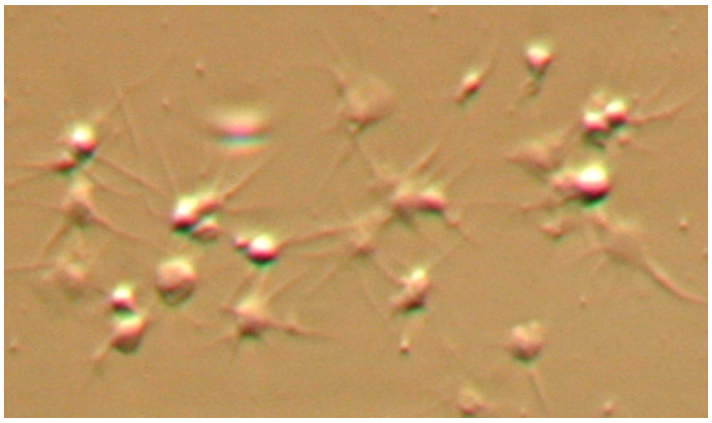

Fig. 6.13: Platelets 30 min after contact with PVP. Activated platelets become spherical and present pseudopods.

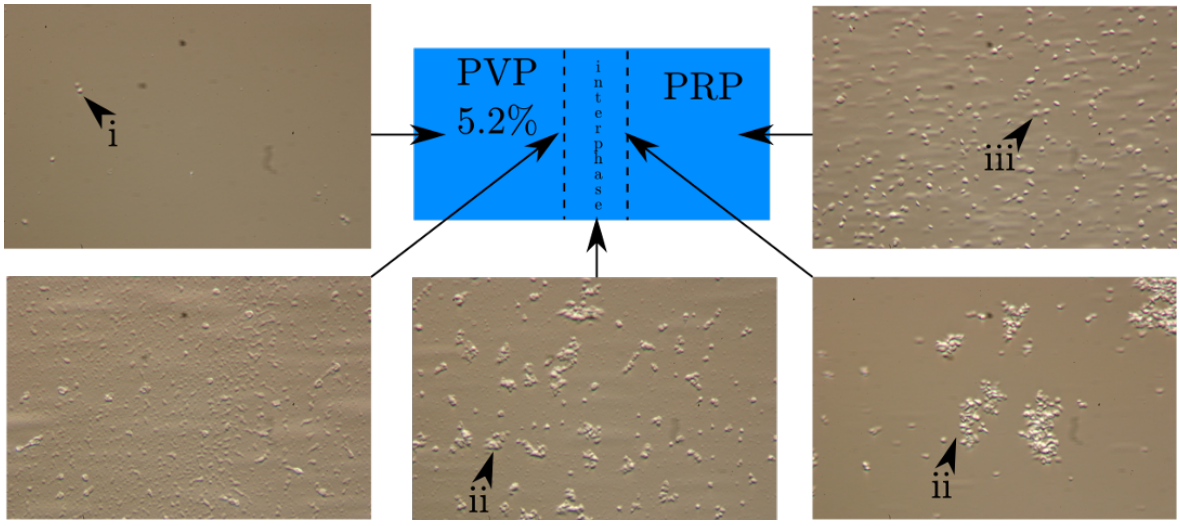

Fig. 6.14: PVP and PRP smeared together on a microscope slide, making a mixing layer. Arrows point to positions where pictures were taken. Arrow heads point to (i) dust particle in PVP, (ii) aggregates, and (iii) resting platelets. All pictures have the same enlargement factor.

glass slide, what looks like a rough surface. Both in the centre and at the PRP side (right) of the mixing layer, aggregates are spotted. Many medium-sized aggregates at the former, and a few large-sized aggregate at the latter. Finally, only resting platelets were seen in the PRP far from the mixing layer.

The colloid particles smaller than platelets that were apparent at the mixing layer were unexpected. Therefore, a similar experiment was done on a microscope slide, but using the plasma (or platler poor plasma, PPP) instead of PRP. Pictures of this experiment are shown in Fig. 6.15. No particles, besides dust from the slide, were seen on the PVP sample. At the PVP side (left) of the mixing layer, the same small colloid particles that were seen in Fig. 6.14 are present. They are either sparsely adhered to the glass slide (rough surface), or forming aggregates. These colloid aggregates in Fig. 6.15 resemble the platelet aggregates in Fig. 6.14. As in Fig. 6.14, the colloids adhered to the glass surface are more common at the PVP side (left) in Fig. 6.15. Again as in Fig. 6.14, the colloid aggregates are more common in the centre and at the PPP side

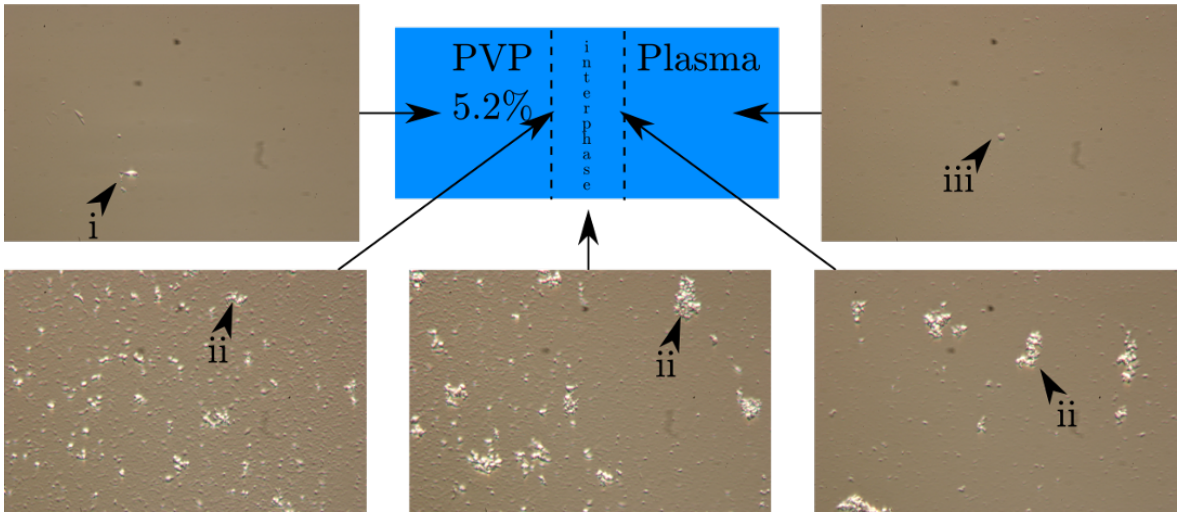

Fig. 6.15: PVP and plasma smeared together on a microscope slide, making a mixing layer. Arrows point to positions where pictures were taken. Arrow heads point to (i) dust particle in PVP, (ii) aggregates, and (iii) a remaining leukocyte. All pictures were taken with the same magnification factor.

(left) of the slide in Fig. 6.15. Figure 6.16 zooms in the precipitated particles. Finally, no particles, besides a few remaining cells that did not precipitate in the hard spinning centrifugation, were present in the PPP far from the layer. Very few cells were present on the slide, but the pictures with both a dust particle and leukocyte are displayed on Fig. 6.15 in order to demonstrate that the microscope was in focus and showing the right sample. Hence, it was demonstrated that PVP was precipitating microparticles from plasma.

Blood has normally a varying concentration of lipoprotein particles called chylomicrons that transport fat through the circulatory system. The colloids seen in Fig. 6.15 are not chylomicrons, because they are not apparent in PVP-free PPP, but it was hypothesised that PVP could be precipitating fat particles similar to chylomicrons. Therefore, PPP was again centrifuged at high spinning, and the supernatant, where fat should be, was discarded. Colloid particles did not precipitate from fat-skimmed plasma, when mixed with PVP. This demonstrated that PVP was precipitating fat

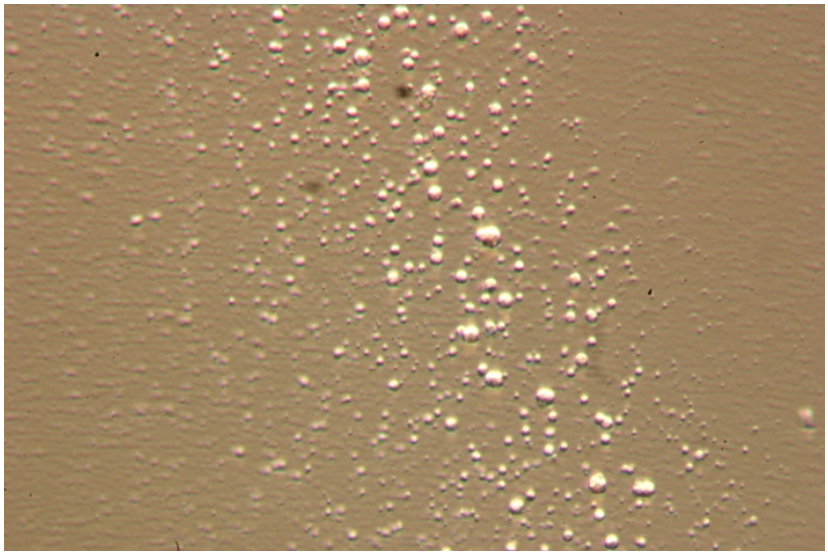

Fig. 6.16: Zoom in the colloid particles precipitated from plasma by PVP.

dissolved in blood. Next blood samples were taken from donors, who were fasting for at least 12h. The plasma of these samples did not present precipitation when mixed with PVP. Therefore, the next samples were obtained from fasting donors only.

6.2.7 Conservation of Mass

In order to check whether the number of platelets remain constant during the entire test time, the first moment of the CMD (Eq. 4.6) was computed. Because the histogram of aggregates show approximately a linear decrease of counts per aggregate size (in Fig. 6.9), the average aggregate size would be 1/3 (triangle centre of area) from the smallest to the largest size defining the group bin. The average number of platelets in each group relates to the average aggregate size by Eq. 6.14. Figure 6.17 shows the time series of the estimated number of platelets counted in the window of view. This time series presents statistically constant behaviour, with no apparent disturbances in the high shear phase. The time average mean of all trials is $(2.59 \pm 0.40) \cdot 10^3$ platelets, which can be compared to the concentration obtained by the cell counter, see Table

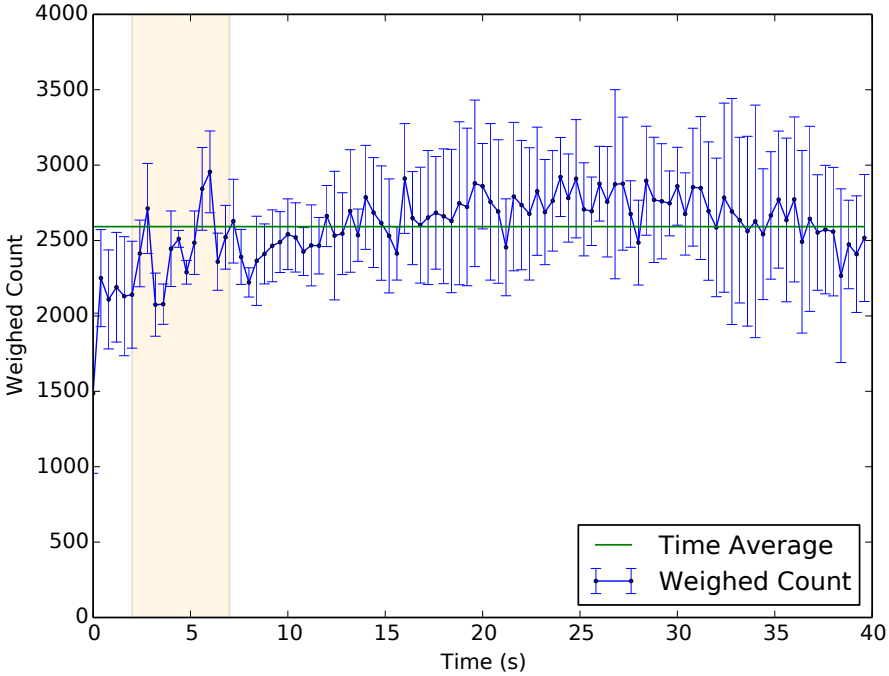

Fig. 6.17: Total number of platelets in time by weighed summation of multiplets. The orange area highlights the high shear stress phase ($\tau_{\text{high}} = 7.00\ Pa$) preceding the low shear stress phase ($\tau_{\text{low}} = 0.02\ Pa$).

6.1, in the volume of view obtained by Eq. 6.1. The theoretical number of platelets in the window of view is $(1.00 \pm 0.15) \cdot 10^6 \times (1.3 \pm 0.1) \cdot 10^{-3} = (1.3 \pm 0.2) \cdot 10^3$ platelets. Hence, the process was slightly overestimating the number of platelets, but the estimation is error is small – it is not even twice the theoretical number of platelets. The total mass estimation error could be occurring because it is adding up the mass of precipitated fat particles.

6.3 Results

Two experiment trials are presented here. The first, was held in 2013, was able to demonstrate the feasibility of the methodology. However, when the second trial has held, in 2014, it was noticed that the aggregation and breakup detected by the

Table 6.2: Performed tests (viscosity $\mu = 6 \cdot 10^{-3}$ Pa).

	High Shear Phase		Low Shear Phase	
Trials	$\dot{\gamma}$ (s^{-1})	τ (Pa)	$\dot{\gamma}$ (s^{-1})	τ (Pa)
2	33	0.20	17	0.10
1	67	0.40	33	0.20
1	133	0.80	100	0.60
1	167	1.00	133	0.80
2	500	3.00	3	0.02
3	1166	7.00	3	0.02
1	1166	7.00	8	0.05
1	1166	7.00	17	0.10
1	1166	7.00	167	1.00

methodology had the interference of fat particles. Fat particles were saturating in blood plasma after PVP was mixed in PRP. The second trial was run with blood from fasting donors, in order to prevent the precipitation of fat particles.

6.3.1 Aggregation and Breakup of Cluster of Platelets Mixed with Suspended Fat Particles

In 2013, the shear patterns listed in Table 6.2 were run a single time. Figure 6.18 show the results of the test case for $\tau_{\text{high}} = 7.00$ Pa and $\tau_{\text{low}} = 0.02$ Pa. In Fig. 6.18a the time series of all three repeats are present, but in Fig. 6.18b the mean time series are shown with the standard deviations for each data point. In Fig. 6.18b, the data points of the time series are fitted by the function

$$y(t) = (y_i - y_f)e^{-kt} + y_f \ , \tag{6.15}$$

where y_i and y_f are the initial and final count, respectively; and k is the inverse exponential constant. Equation 6.15 was fitted separately, both for the high and low shear phases.

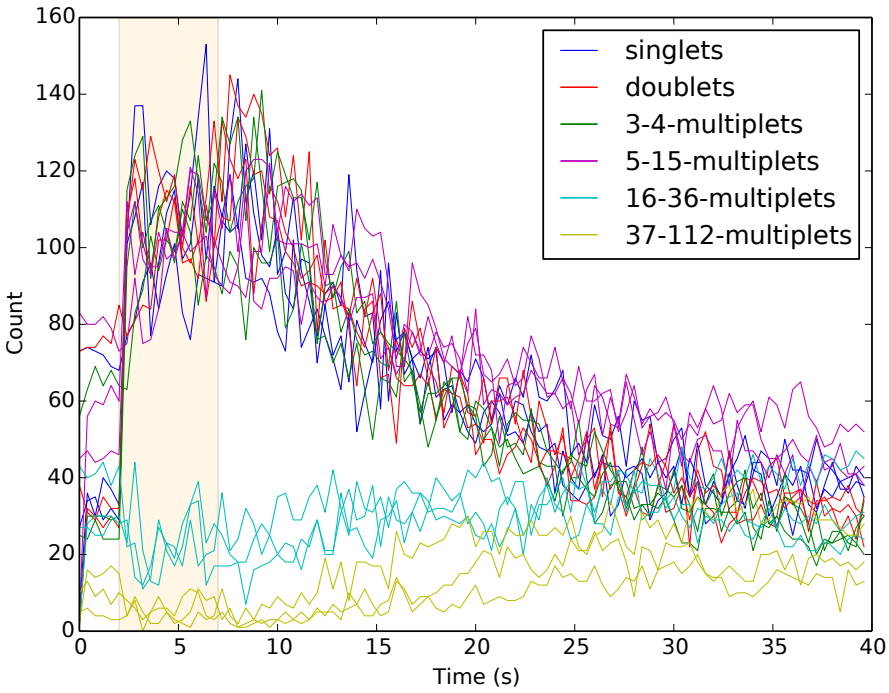

(a) Time series of three trials.

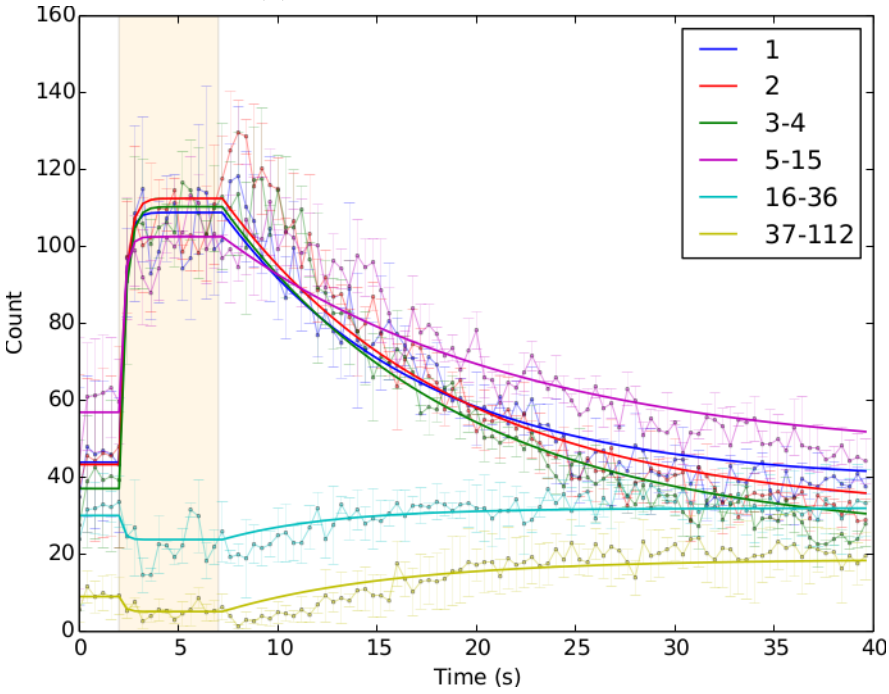

(b) Mean and standard deviation of three trials as well as curve fitting by Eq. 6.15.

Fig. 6.18: Counting of aggregate groups on time. The orange area highlights the high shear stress phase ($\tau_{\text{high}} = 7.00\ Pa$) preceding the low shear stress phase ($\tau_{\text{low}} = 0.02\ Pa$).

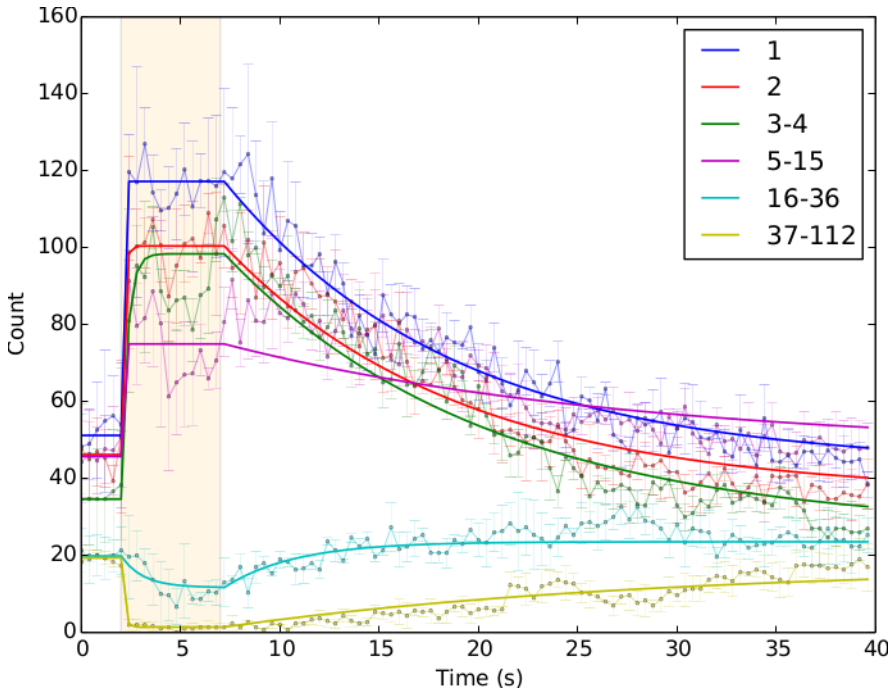

Fig. 6.19: Count of aggregate groups on time; showing mean and standard deviation of three trials as well as curve fitting by Eq. 6.15. The orange area highlights the high shear stress phase ($\tau_{\text{high}} = 3.00\ Pa$) preceding the low shear stress phase ($\tau_{\text{low}} = 0.02\ Pa$).

The inverse exponential curve fits the data very well for most time series, but one can see a transient growth instead of simple decay in the beginning of the low shear phase for doublets, 3–4 multiplets and 5–15 multiplets. This apparent second order behaviour was also observed for 3–4 and 5–15 multiplets in the $\tau_{\text{high}} = 3.00\ Pa$ and $\tau_{\text{low}} = 0.02\ Pa$ test, see Fig. 6.19. However, it was not clear whether the this observed trend is due to mass flux between aggregate orders or due to data noise.

In order to record the initial rates, which seemed contrary to Eq. 6.15, linear fittings were obtained at the shear phase transitions, as shown in Fig. 6.20a. However, the linear fitting is unreliable when signal-to-noise ratio is low, as it is evidenced in Fig. 6.20b.

A more serious problem with the linear fitting in Fig. 6.20b exist at the beginning

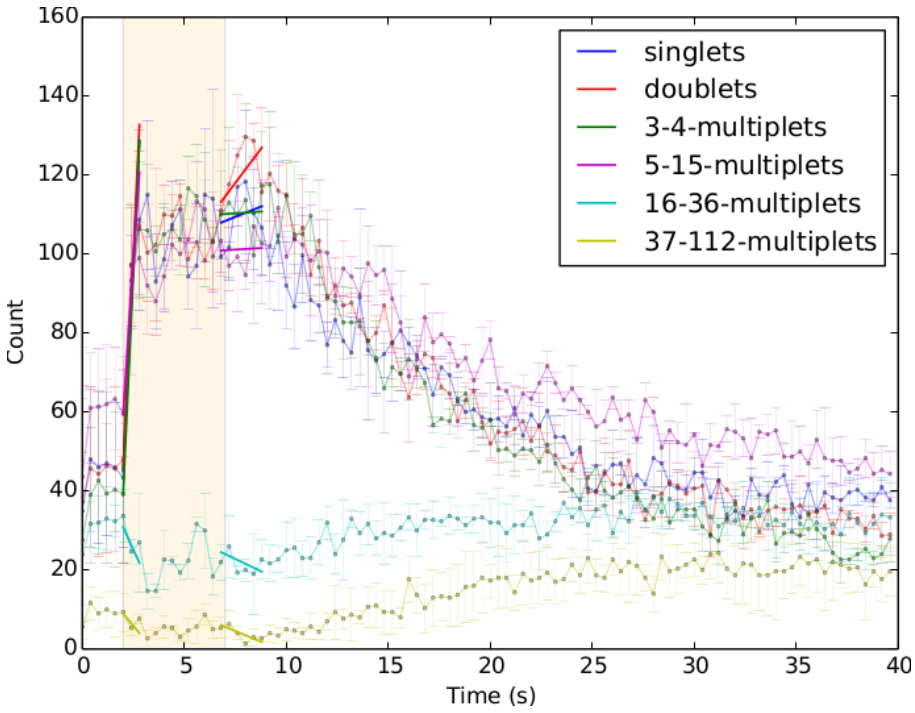

(a) $\tau_{\text{high}} = 7.00\ Pa$ and $\tau_{\text{low}} = 0.02\ Pa$. Good fitting.

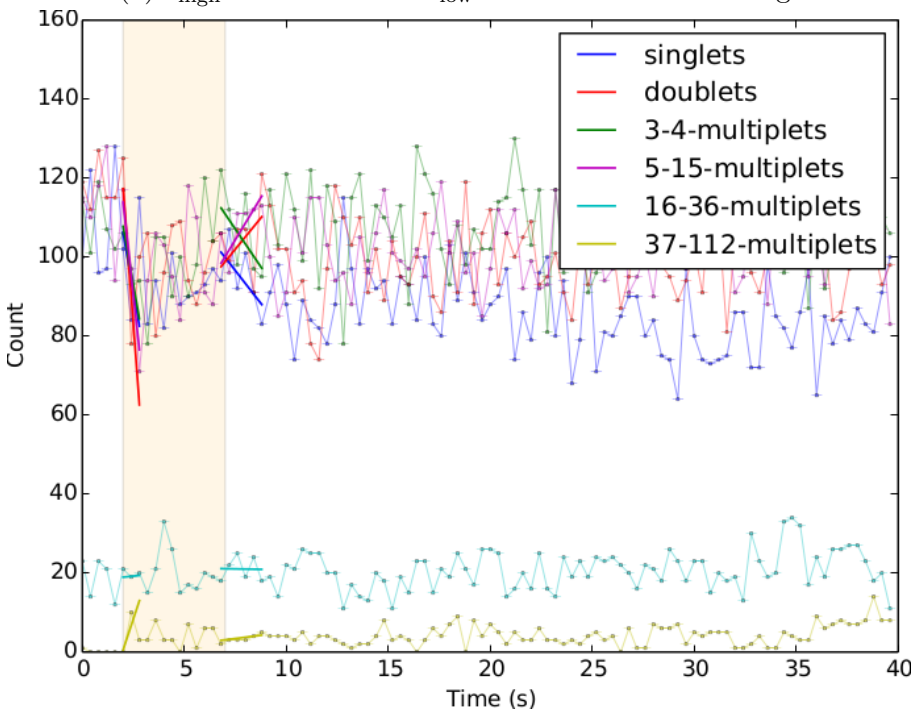

(b) $\tau_{\text{high}} = 0.40\ Pa$ and $\tau_{\text{low}} = 0.20\ Pa$. Bad fitting.

Fig. 6.20: Count of aggregate groups on time with linear curve fitting at phase transitions. The orange area highlights the high shear stress phase (τ_{high}) preceding the low shear stress phase (τ_{low}).

of the high shear phase. The sharp drops on the counting of low order multiplets are probably wrong because of improper estimation of initial count. Before starting the rotation of the disc, five pictures of the same scene were taken, which presented variations of ± 10 counts due to image noise. However, the image noise is lower than the variance between different scenes at the same physical condition. This is evidenced by the large differences between the initial 5 values of times series of the same group (see Fig. 6.18a). Although all samples should in theory have close initial counts, there is a large disparity between them, which would be greatly reduced if those pictures had been taken at different positions, because there would be more variation between the values, because the average of more positions should be closer to the average of all samples. The lack of parity of the initial counts impairs the statistical quality of the data on the transition to the high shear phase. A more accurate, but not ideal, way of obtaining a proper initial condition with this data is to take the average of each multiplet group exposed in Fig. 6.21. By this way, the multiplet counting in Fig. 6.20b would look constant in time.

It was not possible to attain significant statistical data that would differentiate the aggregation behaviour in function of shear, but two things could be observed. First, disaggregation occurred at 3.0 and 7.0 Pa, and no significant disaggregation under 1.0 Pa. Second, at the end of low shear phase, the concentrations returned to the initial condition before the high shear phase. The most significant statistical information that was obtained was the count difference of the low and the high shear phase. The difference of all valid tests can be seen in Fig. 6.22. However, it seems that the results of the trial $\{\tau_{high} = 7.00$ Pa, $\tau_{low} = 1.00$ Pa$\}$ are far off of the expected values.

6.3.2 Aggregation and Breakup of Platelets from Fasting Donors

Figure 6.23 displays a sample of the results from which PRP was obtained from fasting donors. The noise observed on the experiments was too high to detect any

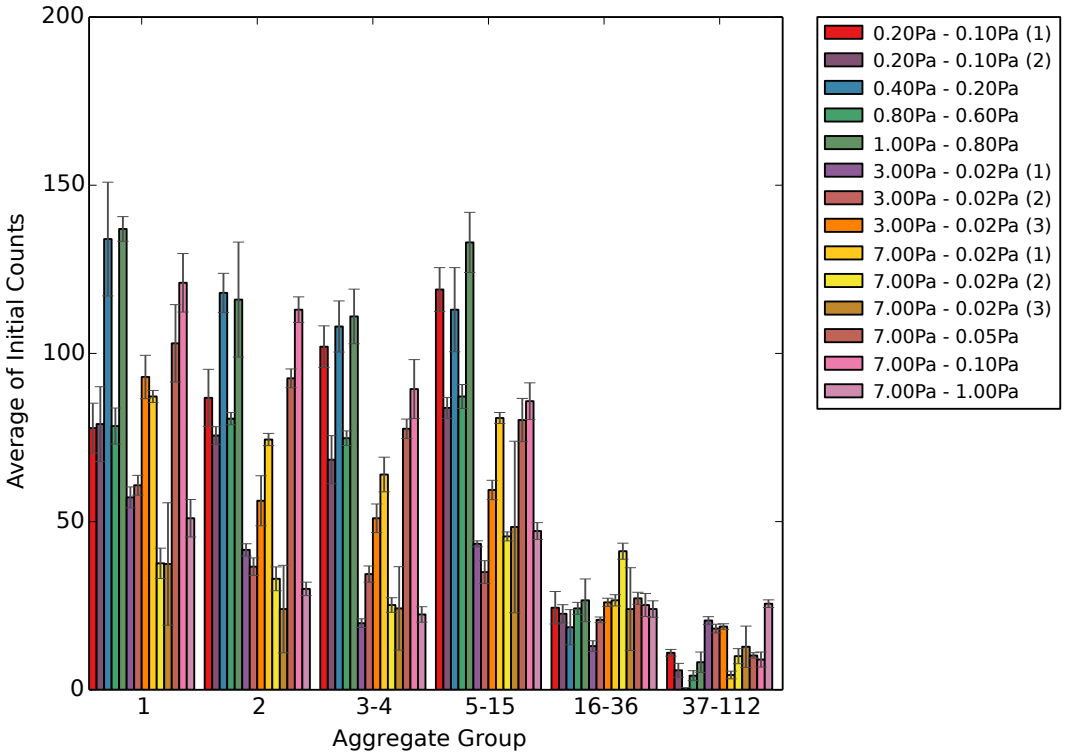

Fig. 6.21: Initial counts of all valid trials. Bars show average of first five pictures and error bars show standard deviation.

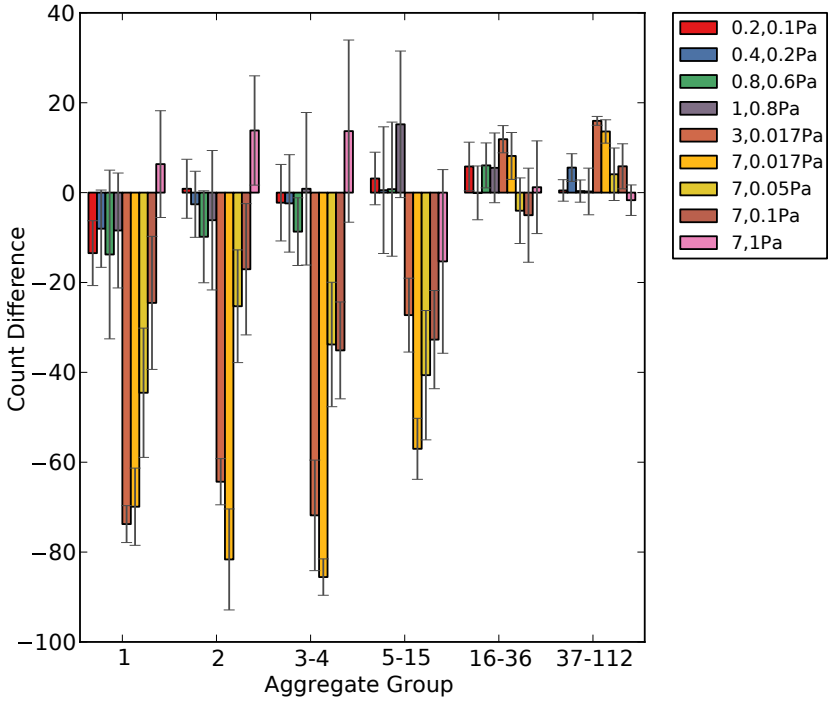

Fig. 6.22: Difference of the end of low and high shear phase ($\bar{y}_f^{LS} - \bar{y}_f^{HS}$).

significant change in the aggregate population. Therefore, no aggregate breakup could be observed when using blood free of precipitated fat. Similar results were obtained from from different shear profiles and different donnors. The results with high shear stress $\tau_{\text{high}} = 7\,\text{Pa}$ are presented here because this was the highest shear rate applied on platelet aggregates in the Linkam rheoscope. The shear protocol was the same as the one applied on PRP, whose fat containt had not been controlled. The initial aggregates were formed less than a minute after PVP was mixed in PRP, which indicates that platelets were very sensitive to PVP.

6.4 Concluding Remarks

The methodology for measuring time-resolved particle aggregation was successful. However, platelets did not react well with viscous polymer added to increase the shear

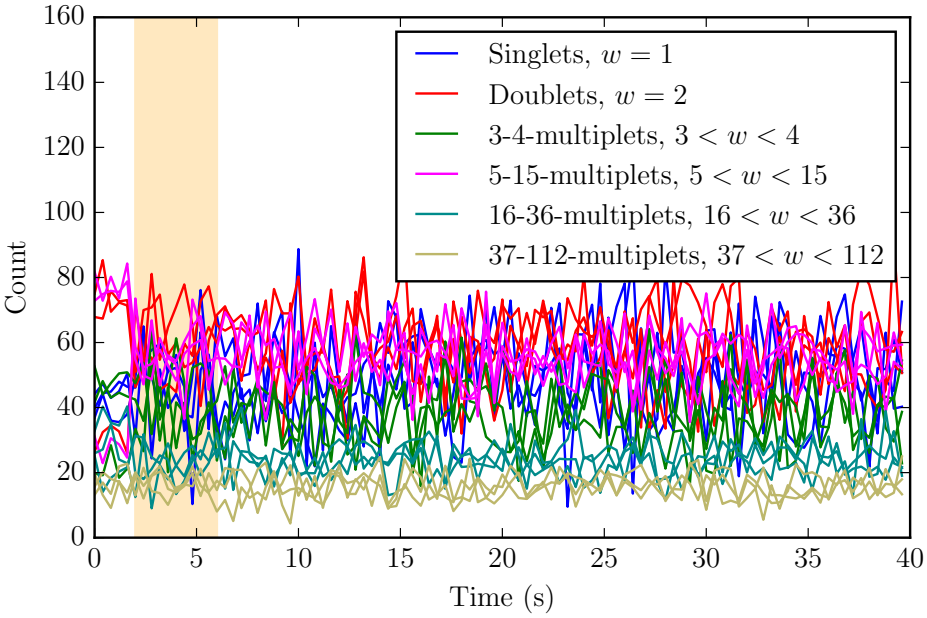

(a) Time series of three trials.

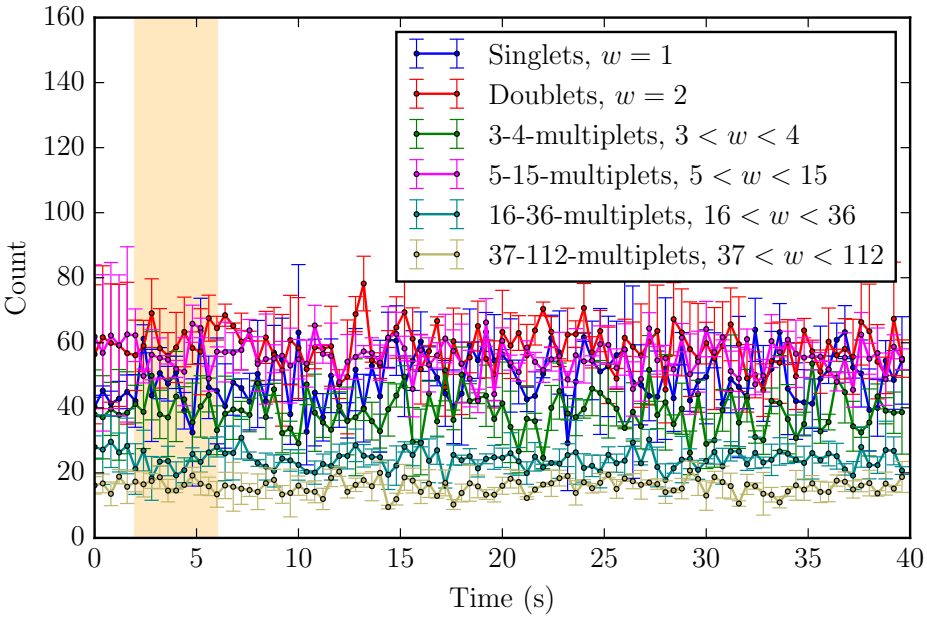

(b) Mean and standard deviation of three trials.

Fig. 6.23: Counting of aggregate groups on time. The orange area highlights the high shear stress phase ($\tau_{\text{high}} = 7.00\ Pa$) preceding the low shear stress phase ($\tau_{\text{low}} = 0.02\ Pa$). Fasting donors.

stress applied to PRP in the Linkam CSS450 rheoscope. Without higher viscosity it would be impossible to achieve the shear stress levels which would either induce aggregation via vWF activity, or break up aggregates. The viscosity raising polymer (PVP) caused two effects in PRP: the precipitation of fat particles present in plasma and the activation of platelets. The precipitation of fat particles caused a visual artefact, because they were first mistaken as platelets. Agglutinated fat particles were observed aggregating and disaggregating with platelets according to the expected theory. Figures 6.18 and 6.19 present groups (bins) of aggregates dynamicaly changing in time according to the applied shear rate/stress. Unfortunately, the dyanamics of aggregation and breakup (Eq. 4.12) was not observed from PRP obtained from donors who had fasted for more than 8 hours, as shown in Fig. 6.23. Platelet aggregates from fasting donors did not change in time in the range of shear stresses of the Linkam rheoscope ($\tau_{\max} = 7.0\,\mathrm{Pa}$). No statistically significant changes to the cluster mass distribution (CMD) were observed from the video frames of PRP obtained from fasting donors.

Other problems of this methodology have been addressed, such as the squeeze flow shear stress caused by the closing of rheoscope plate over the disc. If the closing is too fast, the shear stresses might be high enough to uncoil vWF, causing platelet aggregation before commencing the test. Closing the rheoscope either in low or normal speed did not modify the results of the experiment. After demonstrating that PVP was causing platelet activation even before supplying the rheoscope with PRP, the hypothesis that the closing was causing platelet aggregation was disregarded.

The experimental results for PRP with precipitated fat particles showed high breakup rate at shear stresses over a threshold of 1 Pa. Over this threshold, large aggregates broke up more easily than small aggregates. Figures 6.18b and 6.19 display small aggregates increasing in concentration during high shear phases of $\tau_{high} = 7.00$ Pa and $\tau_{high} = 3.00$ Pa, respectively. At the end of the low shear phase, the aggregate bins returned to their initial concentrations, showing that the aggregation and breakup

dynamics were reversible, according to the aggregation-breakup PBE (Eq. 4.12). The effect of the magnitude of the high shear phase for breakup is summarised illustrated in Fig. 6.22, where the steady-state concentration of each bin is displayed. It is possible to see the shear stress threshold in Fig. 6.22, because no significant concentration difference between the high and low shear is apparent. However, from all those tested cases, the result for the case of $\tau_{\text{high}} = 7.0$ Pa and $\tau_{\text{low}} = 1.0$ Pa did not have this behaviour. It is not clear, whether there was a systematic error specifically in that case, or if the above statement about the breakup threshold false, for not being statistically significant. It seems that the former hypothesis is true, because the shift in small particles count is very clear in the other high shear cases, but this could not be proved with the limited amount of data. In any case, this effect of colloid aggregation and breakup occurs only with the fat particles, since it is not observed in samples lacking them.

Chapter 7

Discussion

Chapter 1 highlighted the importance of developing reliable mathematical models to predict the formation and development of thrombosis in blood contacting medical devices. The biological aspects of thrombosis and haemostasis were reviewed in Chapter 2, and the existing mathematical models to simulate thrombosis were reviewed in Chapter 3. It was noted that models for the formation of platelet aggregates in the bulk of flow due to collision of activated platelets were very primitive. Therefore, in Chapter 4, a more sophisticated model for shear-induced platelet aggregation (SIPA) was proposed, calibrated with experimental data, and its dynamics were analysed. The model proposed in Chapter 4 could only solve SIPA for uniform flow fields, where the spatial dimensions of the control volume could be neglected. In Chapter 5, this model was coupled with the transport equation, whose advective term was solved by CFD in complex flow fields. Several simulation cases were used to test and validate the CFD-coupled model for SIPA. Finally, in Chapter 6, a new experimental setup for measuring the formation and evolution of SIPA with a rheoscope was proposed and executed. The aim of this chapter is to link the results obtained with proposed model and the experiments with the relevance of SIPA in critical blood trauma caused by medical devices.

The goal of mathematical models of thrombosis and haemostasis is to predict the intensity of the natural reaction of the coagulation system in closing a vessel where blood flows. There are many complex relations of cells and proteins that lead to the occlusion of vessels, one of which could be the formation of large platelet clusters in the bulk of the flow due to SIPA. Most of the mathematical models of thrombosis focus on platelet surface adhesion and chemical reactions of the coagulation cascades. These mathematical models can represent well the dynamics of the coagulation system, including effects of bifurcation of equilibrium state, waves of thrombin concentration, and effects of wall shear rate for regulating the procoagulation reactivity on biomaterials. However, very few attempts had been made to model the behaviour of platelets that flow close to the thrombotic region, but do not end up adhering to the procoagulant surface. Flowing activated platelets can eventually collide with other flowing activated platelets, and form aggregates. This process is known as SIPA. The lack of published models describing this special kind of kinetics, which is controlled by flow rates, has motivated the investigation reported in this thesis.

7.1 Distinctive Aspects of the New Model of SIPA

Shear-induced platelet aggregation is a phenomenon known since the 1960's, with the inception of light transmission platelet aggregometry (LTPA) by Born and co-workers. However, a rate equation for SIPA was only modelled in the 1990's using the two-body collision model of free aggregating platelets, which was used to quantify SIPA in shear-controlled experiments. The two-body collision model ignored the aggregation of platelets to already formed aggregates in the dynamics of SIPA, and publications using this model ceased to be published after the 1990's.

The work presented in this thesis can be seen as a continuation of this work. The two-body collision model for aggregation between free platelets was generalised

to include the aggregation kinetics between any size of platelet cluster. The platelet clusters were modelled as a cluster mass distribution (CMD), and kinetics of aggregate breakup was also included in the population balance equation (PBE). The model was formulated using the coagulation equation of Smoluchowski and the breakup equation of Pandya and Spielman. Dimensionless analysis demonstrated that shear rate controls both the aggregation and breakup rates, and that the steady state of the CMD can be monitored by a dimensionless number named aggregation-breakup ratio (K_{ab}), which is the ratio of aggregation to breakup rates. The aggregation-breakup ratio is a state quantity that represents the steady-state of the CMD. The aggregation rate was shown to depend not only on shear rate, but also on the overall concentration of activated platelets. At low concentration of activated platelets, no significant aggregation would ever be possible. This is an important finding because it is a physical fact that prevents SIPA to be dangerously high in the arteries of individuals. This physical fact was not noticed by the authors in the 1990's.

Previous authors had considered hydrodynamic effects inhibiting platelet aggregation, and incorporated this in models of aggregation efficiency. However, this approach is theoretically unphysical, because it only delays aggregation by prolonging the transient phase. The aggregate breakup included in new model of SIPA introduces the limitation of aggregate growth at high shear rates. Hence, the new model of SIPA operates with fixed aggregation efficiency η, which is a pure chemical parameter that does not vary with shear rates. The aggregation efficiency applied in the simulations of SIPA at high shear rates are the same as the one measured in diffusion-induced platelet aggregation (collision by Brownian motion). The argument that aggregation efficiency is a constant factor is also supported by the fractal dimension of platelet aggregates observed by light scatter technique. The aspect that would change platelet aggregation efficiency would be either an excess or lack of fibrinogen in plasma, because platelets should have both free and occupied membrane receptors, so that fibrinogen can become

the bridging link between aggregated platelets. Nevertheless, these situations of excess or lack of the bridging aggregation protein are very extreme and unlikely to naturally occur. Therefore, it is safe to assume aggregation efficiency constant, unless one of these extremes cases of either very high or very low fibrinogen concentration is being simulated.

Finally, the redistribution of platelets between different cluster sizes can be visualised in the new PBE model of SIPA. This is another significant advancement, as compared with the two-body collision model, because it allows an estimation of aggregate sizes within an experimental sample based on the shear rate history sustained by it.

7.2 Rate of SIPA in General Flow Fields

Even though there had been previous attempts to simulate SIPA in the simple shear state of Couette flow, the question of how SIPA behaved in general flow conditions had not been assessed. Platelets in general flow fields are convected by the flow through regions of different shear rates. The main work presented in this thesis tries to elucidate the dynamics of SIPA in general flow fields, such as inside the cardiovascular system.

As the SIPA model was extended to general flow conditions, by coupling it to a CFD solver, a new dimensionless number became a quantity of interest. The local Damköhler number (Da) expresses the ratio of aggregation to convection rates inside a discretised cell of a finite volume method mesh. Large gradients of aggregate concentration can form if the ratio of aggregation to convection is high ($Da \gg 1$), but these gradients are small if the ratio of aggregation to convection rates are low ($Da \lesssim 1$). In free flow conditions, the local Damköhler number is highest at solid walls, where shear rate is highest and velocity is near zero. However, the local Damköhler number is very low ($Da \ll 1$) at the centre of blood vessels, where shear rate is near zero and

velocity is highest. Even near solid walls, the local Damköhler number has a physical limitation, because both shear rate and velocity are directly proportional to flow rate.

All simulations have yielded low local Damköhler number, even close to the walls, which was $Da \leq 0.01$. The highest ratio of mean velocity to wall shear rate in open systems occurs in capillary tubes, according to the relation $\dot{\gamma}_w/\bar{v} = 4\,R^{-1}$ obtained from Eq. 2.8. Nevertheless, the capillary tubes had to be as long as 20 m for large aggregates to form in those simulations. Furthermore, in the LTPA simulation the Damköhler number was also low ($Da \leq 0.01$). In this closed stirred system, a low Damköhler number means that the mixing rate is at least 100 times faster than the aggregation rate. Thus, there was no significant gradient of aggregate concentration, and the 3-D simulation yielded aggregate concentrations very similar to the 0-D simulations modelled by ODE systems with no convective terms. The only simulation where SIPA was spatially inhomogeneous, i.e. with significant aggregate gradients, was the simulation of eccentric cylinders. In the eccentric cylinders simulation, the flow split in two regions, one rotating with the inner cylinder, and one recirculation flow zone where the distance between the walls of both cylinders was longest. The flow close to the inner cylinder had high aggregation and convection rates, and the recirculation zone had low aggregation and convection rates. The gradient in the recirculation zone became significantly high, because eventually the aggregates growing close the the inner cylinder escaped to the low convective recirculation zone. In all other simulated cases SIPA was too slow to form significant inhomogeneous spatial distribution of aggregates.

7.3 Platelet Activation and SIPA

The SIPA models would become even more realistic, if platelet activation models would have been included. Instead, in all simulations a fixed initial concentration of activated platelets was assumed. Activation models would have introduced another level

of complexity and uncertainty to the simulations, and they are discussed in Chapter 3. Activation would possibly delay SIPA in a couple of seconds, due to the physical transformations happening with the activating platelets. Furthermore, activating platelets release more activation factors that can produce a new wave of platelet activation.

7.4 Platelet Activation in Experiments

A new experimental method was invented to measure SIPA in real time. Platelets and platelet aggregates were visualised in a rheoscope with a microscope, while being sheared at different levels of shear rate. The images were recorded with a digital camera and processed by an algorithm which counted and classified platelets by size. The accuracy of this methodology was demonstrated mathematically as well as verified experimentally. The observed volume of particles was constant during the experiment, which indicated that the signal-to-noise ratio was low. However, the rheoscope had a physical limit to the maximum shear rate, and a viscosity-raising polymer had to be added to increase shear stress. The first goal was to observe platelets aggregating as they were being activated by high shear stress. Another goal was to observe aggregate breakup with higher levels of shear stress. At the first glance, this effect had been clearly seen with freshly obtained platelets. Nonetheless, after further examination, it was realized that the polymer thickening agent was precipitating fat particles in plasma, and those particles were aggregating to platelets as expected by the mathematical model of SIPA. Once fat-free blood samples were used in the experiment, no aggregate breakup was observed. Platelets that were already aggregated remained aggregated at the maximum shear stress of 7 Pa. Moreover, the viscosity thickening agent has proven to violently activate platelets. Because of that, it was impossible to measure SIPA with this viscosity thickening agent (polyvinylpyrrolidone, PVP). It remains unclear whether other viscosity thickening agent could be applied to this experimental methodology.

7.5 Theoretical Considerations

Although it was not possible to obtain significant spatial inhomogeneity of aggregate distribution with the simulations, those numerical experiments were very important to evidence important experimental and theoretical details of SIPA. The scaled equation of the mathematical model has demonstrated that the rate of SIPA cannot be high unless the concentration of platelets is also high; at least 100 times higher than the physiological concentration. This shows that the physiological concentration of platelets has been selected by biological evolution to have an optimum highest concentration which does not put the individual in danger of thrombosis, unless the endothelium is damaged and platelets aggregate there. Activated platelets would never form large aggregates by SIPA, even in a severely sick individual, because platelet concentration is not high enough for many activated platelets to collide with each other in the flow stream. Small aggregates made of two to four platelets can indeed form in the blood vessels of diseased individuals by SIPA, but those aggregates are more likely to be filtered in the spleen or in peripheral blood vessels, instead of continuing aggregating with other activated platelets.

7.6 Conclusions

The SIPA model and the simulations run with with it, both in 0-D and in 3-D with convection, are novel. The simulations were able to reproduce experiments conducted *in vitro*. These experiments included Couette flow in concentric cylinders, LTPA, and Poiseuille flow in capillary tubes. The results of the Couette flow experiment were used to calibrate the parameters of SIPA model, because it was an experiment with uniform shear rate, so aggregate concentration was considered homogeneously distributed in space. Once this model was coupled with a flow field from CFD, it was able to reproduce the experimental behaviour of both LTPA and Poiseuille flow experiment.

The aggregation curves obtained from the simulations had the same shapes and time response of the experiments. Unfortunately, the 3-D numerical experiments in general did not yield significant gradients of aggregate concentrations because aggregation rates were always at least 100-times higher than convection rates. Aggregates either got mixed with the rest of the fluid or were transported far downstream of the point of aggregation. Therefore, mathematical models of SIPA should be included in thrombosis analysis only in closed systems, when long time scales are important. This is the case of the LTPA simulation, where the spatial distribution could be neglected, because the system can be accurately solved in 0-D within a single control volume for a given average shear rate.

Chapter 8

Conclusions

A mathematical model of shear-induced platelet aggregation (SIPA) and breakup was derived, analysed, and simulated in both a 0-D system and in a spatially resolved system with the finite volume method (FVM). The intention of formulating this model was to include it in more complex models of thrombosis, in order to improve the prediction accuracy of blood damage in biomedical devices. Shear-induced platelet aggregation is a real phenomenon that occurs in stored blood and in the light transmission platelet aggregonometry (LTPA) test. An experimental methodology to obtain a temporal-resolved measurement of the cluster mass distribution (CMD) of platelets was also developed and tested. Important theoretical insights were achieved that contribute to the evolution of mathematical models of haemostasis and thrombosis.

The model of SIPA developed in this thesis is introduced and derived in Chapter 4. In order to analyse the dynamics of this model, the equations were scaled in terms of dimensionless numbers that summarise the effect of all the independent parameters of the model. The dimensionless numbers were calibrated with experimental data, and the effects of changing physical parameters are discussed in terms of characteristic times and steady-state aggregate distribution. Platelet aggregation rate is directly related with platelet concentration in blood, as well as shear rate. However, if shear rate is too

high, platelets do not seem to aggregate because large aggregates are more likely to break up. The concentrations of activated platelets used in the experiments to calibrate the model were about 10 % of the physiological platelet concentration. Therefore, only nearly half of the suspended platelets aggregated into doublets or triplets in about 20 s, as predicted by the SIPA model. However, when a simulation was run with about 100 % of the platelets activated, the results showed most of the platelets aggregating into clusters formed by 10–1000 platelets in about 2 s. This demonstrated the power of the new PBE model in describing SIPA, as compared to the more limited two-body collision model. Finally, the dynamics of aggregate growth are described in detail by the new SIPA model, because the full state of the CMD is available, and the mass transfer of platelets can be observed.

In Chapter 5, the mathematical model of SIPA was coupled with a computational fluid dynamics (CFD) solver, in order to study how SIPA and flow affects the spatial distribution of aggregates. A solver was developed using the finite volume method (FVM) in order to achieve this goal. Six completely different flow cases were simulated, including a Couette flow simulation used to verify the 3-D solver with the 0-D solver, and both a LTPA simulation and a flow through capillary tubes used to validate the model against experiments. The analysis of the simulation results with dimensionless numbers has demonstrated that, in most cases, the spatial distribution of aggregates is very homogeneous, because SIPA is a very slow effect compared to convection. Therefore, unless the platelet concentration is a couple of orders of magnitude higher than the normal, SIPA does not have to be discretized in space, and a 0-D simulation is sufficiently accurate to predict SIPA.

Lastly, in Chapter 6, a new experiment to measure SIPA with a time resolution of less than a second is described. The methodology was successful in accurately measuring the aggregate distribution of platelets mixed with fat particles, but it failed to visualise any dynamic transformation of SIPA due to the reaction of platelets with the

viscosity-raising agent applied to increase shear stress. Although it remained unclear if the experiment would have worked with a different viscosity-raising agent, important theoretical considerations were discussed.

The most important conclusion of this thesis results from mathematical analysis of this model and the analysis of the numerical simulations. This analysis revealed that SIPA is a very slow effect compared to convection. Therefore, SIPA does not form any significant inhomogeneous distribution of platelet aggregates in space, and it can be accurately solved with a single control volume. In a closed system, the distribution of aggregate sizes is directly dependent on the history of spatially average shear rate. In an open system, the distribution of aggregate sizes can be given as a boundary condition in the inlet, but in general the internal field will not be significantly altered by SIPA. Unless the shear rate is high and the blood vessel is very long, the internal field of the CMD would only be slightly altered by new platelets being activated (i.e., a source of activated platelets), or by activated platelets and aggregates adhering to surfaces (i.e., a sink of activated platelets). This is an important theoretical conclusion that is supported by experiments, mathematical analysis and simulation, which had not been explicitly addressed in the literature.

Bibliography

[1] P. A. Aarts, P. A. Bolhuis, K. S. Sakariassen, R. M. Heethaar, and J. J. Sixma. Red blood cell size is important for adherence of blood platelets to artery subendothelium. *Blood*, 62(1):214–7, jul 1983.

[2] P. A. Aarts, P. Steendijk, J. J. Sixma, and R. M. Heethaar. Fluid shear as a possible mechanism for platelet diffusivity in flowing blood. *Journal of Biomechanics*, 19(10):799–805, Jan. 1986.

[3] P. a. Aarts, S. a. van den Broek, G. W. Prins, G. D. Kuiken, J. J. Sixma, and R. M. Heethaar. Blood platelets are concentrated near the wall and red blood cells, in the center in flowing blood. *Arteriosclerosis, Thrombosis, and Vascular Biology*, 8(6):819–824, Nov. 1988.

[4] M. D. Abràmoff, P. J. Magalhães, and S. J. Ram. Image processing with imageJ. *Biophotonics International*, 11(7):36–41, 2004.

[5] P. C. Adams, V. Fuster, L. Badimon, J. J. Badimon, and J. H. Chesebro. Platelet/Vessel wall interactions, rheologic factors and thrombogenic substrate in acute coronary syndromes: Preventive strategies. *The American Journal of Cardiology*, 60(12):G9–G16, Oct. 1987.

[6] P. S. Addison. *Fractals and Chaos*. Institute of Physics, London, UK, 1977.

[7] M. Anand, K. Rajagopal, and K. R. Rajagopal. A Model Incorporating some of the Mechanical and Biochemical Factors Underlying Clot Formation and Dissolution in Flowing Blood. *Journal of Theoretical Medicine*, 5(3–4):183–218, 2003.

[8] M. Anand, K. Rajagopal, and K. R. Rajagopal. A model for the formation, growth, and lysis of clots in quiescent plasma. A comparison between the effects of antithrombin III deficiency and protein C deficiency. *Journal of theoretical biology*, 253(4):725–38, Aug. 2008.

[9] M. Anand and K. R. Rajagopal. A shear-thinning viscoelastic fluid model for describing the flow of blood. *International Journal of Cardiovascular Medicine and Science*, 4(2):39–68, 2004.

[10] J. Andersson, R. Larsson, R. Richter, K. N. Ekdahl, and B. Nilsson. Binding of a model regulator of complement activation (rca) to a biomaterial surface: surface-bound factor h inhibits complement activation. *Biomaterials*, 22(17):2435–2443, 2001.

[11] M. A. Arnaout. Structure and function of the leukocyte adhesion molecules cd11/cd18. *Blood*, 75(5):1037–1050, 1990.

[12] F. I. Ataullakhanov and M. A. Panteleev. Mathematical modeling and computer simulation in blood coagulation. *Pathophysiology of haemostasis and thrombosis*, 34(2-3):60–70, Jan. 2005.

[13] F. I. Ataullakhanov and M. A. Panteleev. Towards virtual coagulation. *Pathophysiology of haemostasis and thrombosis*, 34(2-3):58–9, jan 2005.

[14] P. Atkins and J. de Paula. *Atkins' Physical Chemistry*. Oxford University Press, 10 edition, 2014.

[15] U. Ayachit. *The Paraview Guide (Full Color Version): A Parallel Visualization Application*. Kitware, 2015.

[16] M. U. Bäbler and M. Morbidelli. Analysis of the aggregation-fragmentation population balance equation with application to coagulation. *Journal of colloid and interface science*, 316(2):428–41, Dec. 2007.

[17] L. Badimon, J. J. Badimon, V. T. Turitto, and V. Fuster. Thrombosis: Studies under Flow Conditions. *Annals of the New York Academy of Sciences*, 516(1 Blood in Cont):427–540, Dec. 1987.

[18] C. N. Bagot and R. Arya. Virchow and his triad: a question of attribution. *British journal of haematology*, 143(2):180–90, Oct. 2008.

[19] S. A. Baldwin and D. Basmadjian. A mathematical model of thrombin production in blood coagulation, Part I: The sparsely covered membrane case. *Annals of biomedical engineering*, 22(4):357–70, 1994.

[20] D. L. Bark and D. N. Ku. Platelet transport rates and binding kinetics at high shear over a thrombus. *Biophysical journal*, 105(2):502–11, July 2013.

[21] H. A. Barnes. The yield stressa review or $\pi\alpha\nu\tau\alpha$ $\rho\epsilon\iota$everything flows? *Journal of Non-Newtonian Fluid Mechanics*, 81(1-2):133–178, Feb. 1999.

[22] G. Barthelmes, S. Pratsinis, and H. Buggisch. Particle size distributions and viscosity of suspensions undergoing shear-induced coagulation and fragmentation. *Chemical Engineering Science*, 58(13):2893–2902, July 2003.

[23] D. Basmadjian, M. V. Sefton, and S. A. Baldwin. Coagulation on biomaterials in flowing blood: some theoretical considerations. *Biomaterials*, 18(23):1511–1522, Dec. 1997.

[24] D. N. Bell and H. L. Goldsmith. Platelet aggregation in poiseuille flow: II. Effect of shear rate. *Microvascular research*, 27(3):316–30, may 1984.

[25] D. N. Bell, S. Spain, and H. L. Goldsmith. Adenosine diphosphate-induced aggregation of human platelets in flow through tubes. I. Measurement of concentration and size of single platelets and aggregates. *Biophysical journal*, 56(5):817–28, nov 1989.

[26] D. N. Bell, S. Spain, and H. L. Goldsmith. Adenosine diphosphate-induced aggregation of human platelets in flow through tubes. II. Effect of shear rate, donor sex, and ADP concentration. *Biophysical journal*, 56(5):829–43, nov 1989.

[27] D. N. Bell, H. C. Teirlinck, and H. L. Goldsmith. Platelet aggregation in poiseuille flow: I. A double infusion technique. *Microvascular research*, 27(3):297–315, may 1984.

[28] E. Beltrami and J. Jesty. Mathematical analysis of activation thresholds in enzyme-catalyzed positive feedbacks: application to the feedbacks of blood coagulation. *Proceedings of the National Academy of Sciences of the United States of America*, 92(19):8744–8, Sept. 1995.

[29] G. M. Bernacca, M. J. Gulbransen, R. Wilkinson, and D. J. Wheatley. In vitro blood compatibility of surface-modified polyurethanes. *Biomaterials*, 19(13):1151–65, jul 1998.

[30] H. Bisswanger. *Enzyme Kinetics: Principles and Methods*. Wiley-Blackwell, 2 edition, 2008.

[31] P. J. Blatz and A. V. Tobolsky. Note on the Kinetics of Systems Manifesting Simultaneous Polymerization-Depolymerization Phenomena. *The Journal of Physical Chemistry*, 49(2):77–80, Feb. 1945.

[32] D. Bluestein, K. B. Chandran, and K. B. Manning. Towards non-thrombogenic performance of blood recirculating devices. *Annals of biomedical engineering*, 38(3):1236–56, mar 2010.

[33] D. Bluestein, L. Niu, R. T. Schoephoerster, and M. K. Dewanjee. Steady flow in an aneurysm model: correlation between fluid dynamics and blood platelet deposition. *Journal of biomechanical engineering*, 118(3):280–6, aug 1996.

[34] D. Bluestein, W. Yin, K. Affeld, and J. Jesty. Flow-induced platelet activation in mechanical heart valves. *The Journal of heart valve disease*, 13(3):501–8, may 2004.

[35] F. C. Boogerd, F. J. Bruggeman, J.-H. S. Hofmeyr, and H. V. Westerhoff. *Systems Biology*. Elsevier, Amsterdam, The Netherlands, 1 edition, 2007.

[36] G. V. Born and M. J. Cross. The Aggregation of Blood Platelets. *The Journal of physiology*, 168:178–195, Aug. 1963.

[37] G. V. R. Born and M. Hume. Effects of the Numbers and Sizes of Platelet Aggregates on the Optical Density of Plasma. *Nature*, 215(5105):1027–1029, Sept. 1967.

[38] C. H. Brown, L. B. Leverett, C. W. Lewis, C. P. Alfrey, and J. D. Hellums. Morphological, biochemical, and functional changes in human platelets subjected to shear stress. *The Journal of laboratory and clinical medicine*, 86(3):462–71, Sept. 1975.

[39] G. W. Burgreen, J. F. Antaki, Z. Wu, and A. J. Holmes. Computational Fluid Dynamics as a Development Tool for Rotary Blood Pumps. *Artificial Organs*, 25(5):336–340, May 2001.

[40] T. Camp and P. Stein. Velocity gradients and internal work in fluid motion. *Journal of the Boston Society of Civil Engineers*, 85:219–37, 1943.

[41] G. Cesarman-Maus and K. a. Hajjar. Molecular mechanisms of fibrinolysis. *British journal of haematology*, 129(3):307–21, 2005.

[42] H. N. Chang and C. R. Robertson. Platelet aggregation by laminar shear and Brownian motion. *Annals of Biomedical Engineering*, 4(2):151–183, jun 1976.

[43] J. C. Chapin and K. A. Hajjar. Fibrinolysis and the control of blood coagulation. *Blood reviews*, 29(1):17–24, jan 2015.

[44] W. W. Chen, M. Niepel, and P. K. Sorger. Classic and contemporary approaches to modeling biochemical reactions. *Genes & development*, 24(17):1861–75, Sept. 2010.

[45] D. E. Chenoweth. Complement activation during hemodialysis: clinical observations, proposed mechanisms, and theoretical implications. *Artificial organs*, 8(3):281–287, 1984.

[46] S. Chien. Shear Dependence of Effective Cell Volume as a Determinant of Blood Viscosity. *Science*, 168(3934):977–979, May 1970.

[47] S. Chien, S. Usami, R. J. Dellenback, and M. I. Gregersen. Shear-dependent deformation of erythrocytes in rheology of human blood. *The American journal of physiology*, 219(1):136–42, July 1970.

[48] T. W. Chow, J. D. Hellums, J. L. Moake, and M. H. Kroll. Shear stress-induced von Willebrand factor binding to platelet glycoprotein Ib initiates calcium influx associated with aggregation. *Blood*, 80(1):113–20, 1992.

[49] P. R. Craddock, J. Fehr, A. Dalmasso, K. Brighan, and H. Jacob. Hemodialysis leukopenia. pulmonary vascular leukostasis resulting from complement activation

by dialyzer cellophane membranes. *Journal of Clinical Investigation*, 59(5):879, 1977.

[50] P. David, A. C. Nair, V. Menon, and D. Tripathi. Laser light scattering studies from blood platelets and their aggregates. *Colloids and Surfaces B: Biointerfaces*, 6(2):101–114, Mar. 1996.

[51] A. Davies, A. G. H. Blakeley, and C. Kidd. *Human Physiology*. Churchill Livingstone, Philadelphia, USA, 1 edition, 2001.

[52] T. M. Devlin. *Textbook of Biochemistry with Clinical Correlations*. John Wiley & Sons Inc., Hoboken, USA, 7 edition, 2010.

[53] E. di Stasio and R. de Cristofaro. The effect of shear stress on protein conformation: Physical forces operating on biochemical systems: The case of von Willebrand factor. *Biophysical chemistry*, 153(1):1–8, dec 2010.

[54] S. L. Diamond. Systems biology of coagulation. *Journal of Thrombosis and Haemostasis*, 11(SUPPL.1):224–232, 2013.

[55] E. C. Eckstein and F. Belgacem. Model of platelet transport in flowing blood with drift and diffusion terms. *Biophysical journal*, 60(1):53–69, July 1991.

[56] E. C. Eckstein, J. F. Koleski, and C. M. Waters. Concentration profiles of 1 and 2.5 microns beads during blood flow. Hematocrit effects. *ASAIO transactions / American Society for Artificial Internal Organs*, 35(3):188–90, 1989.

[57] E. C. Eckstein, A. W. Tilles, and F. J. Millero. Conditions for the occurrence of large near-wall excesses of small particles during blood flow. *Microvascular research*, 36(1):31–9, July 1988.

[58] L. Ehrl, M. Soos, and M. Morbidelli. Dependence of aggregate strength, structure, and light scattering properties on primary particle size under turbulent conditions

in stirred tank. *Langmuir : the ACS journal of surfaces and colloids*, 24(7):3070–81, Apr. 2008.

[59] A. Einstein. Über die von der molekularkinetischen Theorie der Wärme geforderte Bewegung von in ruhenden Flüssigkeiten suspendierten Teilchen. *Annalen der Physik*, 322(8):549–560, 1905.

[60] J. Engmann, C. Servais, and A. S. Burbidge. Squeeze flow theory and applications to rheometry: A review. *Journal of Non-Newtonian Fluid Mechanics*, 132(1-3):1–27, dec 2005.

[61] J. H. Ferziger and M. Perić. *Computational Methods for Fluid Dynamics*. Springer Berlin Heidelberg, Berlin, Heidelberg, 2002.

[62] J. C. Fitch, S. Rollins, L. Matis, B. Alford, S. Aranki, C. D. Collard, M. Dewar, J. Elefteriades, R. Hines, G. Kopf, et al. Pharmacology and biological efficacy of a recombinant, humanized, single-chain antibody c5 complement inhibitor in patients undergoing coronary artery bypass graft surgery with cardiopulmonary bypass. *Circulation*, 100(25):2499–2506, 1999.

[63] A. L. Fogelson. Continuum Models of Platelet Aggregation: Formulation and Mechanical Properties. *SIAM Journal on Applied Mathematics*, 52(4):1089–1110, aug 1992.

[64] A. L. Fogelson and R. D. Guy. Platelet-wall interactions in continuum models of platelet thrombosis: formulation and numerical solution. *Mathematical medicine and biology : a journal of the IMA*, 21(4):293–334, Dec. 2004.

[65] H. Fogler. *Elements of Chemical Reaction Engineering*. Prentice Hall International Series in the Physical and Chemi. Pearson Education, 2016.

[66] R. Fåhræus. The Suspension Stability of the Blood. *Physiological Reviews*, 9(2):241–274, 1929.

[67] R. Fåhræus and T. Lindqvist. Viscosity of blood in narrow capillary tubes. *The American Journal of Physiology*, 96:562–568, 1931.

[68] K. H. Fraser, T. Zhang, M. E. Taskin, B. P. Griffith, and Z. J. Wu. A Quantitative Comparison of Mechanical Blood Damage Parameters in Rotary Ventricular Assist Devices: Shear Stress, Exposure Time and Hemolysis Index. *Journal of Biomechanical Engineering*, 134(8):081002, 2012.

[69] M. M. Frojmovic and J. G. Milton. Human platelet size, shape, and related functions in health and disease. *Physiological reviews*, 62(1):185–261, Jan. 1982.

[70] Y.-C. Fung. *Biomechanics: Mechanical Properties of Living Tissues*. Springer-Verlag, New York, EUA, 2 edition, 1993.

[71] Y.-C. Fung. *Biomechanics: Circulation*. Springer-Verlag, New York, EUA, 2 edition, 1996.

[72] B. Furie and B. C. Furie. Mechanisms of Thrombus Formation. *New England Journal of Medicine*, 359(9):938–949, aug 2008.

[73] G. P. Galdi, R. Rannacher, A. M. Robertson, and S. Turek. *Hemodynamical Flows*, volume 37 of *Oberwolfach Seminars*. Birkhäuser Basel, Basel, 2008.

[74] A. Gaspar-Rosas and G. B. Thurston. Erythrocyte aggregate rheology by transmitted and reflected light. *Biorheology*, 25(3):471–87, Jan. 1988.

[75] C. Geuzaine and J.-F. Remacle. Gmsh: A 3-D finite element mesh generator with built-in pre- and post-processing facilities. *International Journal for Numerical Methods in Engineering*, 79(11):1309–1331, sep 2009.

[76] P. L. F. Giangrande. Six Characters in Search of An Author: The History of the Nomenclature of Coagulation Factors. *British Journal of Haematology*, 121(5):703–712, June 2003.

[77] H. Goldsmith and J. Marlow. Flow behavior of erythrocytes. II. Particle motions in concentrated suspensions of ghost cells. *Journal of Colloid and Interface Science*, 71(2):383–407, Sept. 1979.

[78] H. L. Goldsmith. Red cell motions and wall interactions in tube flow. *Federation proceedings*, 30(5):1578–90, 1971.

[79] H. L. Goldsmith. The microrheology of human erythrocyte suspensions. In E. Becker and G. K. Mikhailov, editors, *Theoretical and Applied Mechanics. proc. 13th IUTAM congress*, pages 85–103. Springer Berlin Heidelberg, Berlin, Heidelberg, 1972.

[80] H. L. Goldsmith, D. N. Bell, S. Braovac, a. Steinberg, and F. McIntosh. Physical and chemical effects of red cells in the shear-induced aggregation of human platelets. *Biophysical journal*, 69(4):1584–95, oct 1995.

[81] H. L. Goldsmith, D. N. Bell, S. Spain, and F. A. McIntosh. Effect of red blood cells and their aggregates on platelets and white cells in flowing blood. *Biorheology*, 36(5-6):461–8, Jan. 1999.

[82] H. L. Goldsmith, G. R. Cokelet, and P. Gaehtgens. Robin Fåhraeus: evolution of his concepts in cardiovascular physiology. *The American journal of physiology*, 257(3 Pt 2):H1005–15, Sept. 1989.

[83] H. L. Goldsmith and J. Marlow. Flow Behaviour of Erythrocytes. I. Rotation and Deformation in Dilute Suspensions. *Proceedings of the Royal Society B: Biological Sciences*, 182(1068):351–384, Oct. 1972.

[84] H. L. Goldsmith, A. T. Quinn, G. Drury, C. Spanos, F. A. McIntosh, and S. I. Simon. Dynamics of neutrophil aggregation in couette flow revealed by videomicroscopy: effect of shear rate on two-body collision efficiency and doublet lifetime. *Biophysical journal*, 81(4):2020–34, oct 2001.

[85] H. L. Goldsmith and S. Spain. Margination of leukocytes in blood flow through small tubes. *Microvascular research*, 27(2):204–222, 1984.

[86] H. L. Goldsmith and V. T. Turitto. Rheological aspects of thrombosis and haemostasis: basic principles and applications. ICTH-Report–Subcommittee on Rheology of the International Committee on Thrombosis and Haemostasis. *Thrombosis and haemostasis*, 55(3):415–35, June 1986.

[87] D. Goodsell. Tissue Factor. *RCSB Protein Data Bank*, March 2006.

[88] M. B. Gorbet and M. V. Sefton. Biomaterial-associated thrombosis: roles of coagulation factors, complement, platelets and leukocytes. *Biomaterials*, 25(26):5681–703, Nov. 2004.

[89] S. Goto, Y. Ikeda, E. Saldívar, and Z. M. Ruggeri. Distinct mechanisms of platelet aggregation as a consequence of different shearing flow conditions. *The Journal of clinical investigation*, 101(2):479–86, jan 1998.

[90] S. Goto, D. R. Salomon, Y. Ikeda, and Z. M. Ruggeri. Characterization of the unique mechanism mediating the shear-dependent binding of soluble von Willebrand factor to platelets. *The Journal of biological chemistry*, 270(40):23352–61, oct 1995.

[91] K. Gregory and D. Basmadjian. An analysis of the contact phase of blood coagulation: effects of shear rate and surface are intertwined. *Annals of biomedical engineering*, 22(2):184–93, 1994.

[92] W. Gropp, E. Lusk, and A. Skjellum. *Using MPI: portable parallel programming with the message-passing interface*, volume 1. MIT press, 1999.

[93] Z. Guo, K. M. Bussard, K. Chatterjee, R. Miller, E. a. Vogler, and C. a. Siedlecki. Mathematical modeling of material-induced blood plasma coagulation. *Biomaterials*, 27(5):796–806, 2006.

[94] R. D. Guy, A. L. Fogelson, and J. P. Keener. Fibrin gel formation in a shear flow. *Mathematical Medicine and Biology*, 24(1):111–130, oct 2006.

[95] M. Heise, S. Schmidt, U. Krüger, R. Rückert, S. Rösler, P. Neuhaus, and U. Settmacher. Flow pattern and shear stress distribution of distal end-to-side anastomoses. A comparison of the instantaneous velocity fields obtained by particle image velocimetry. *Journal of Biomechanics*, 37(7):1043–1051, jul 2004.

[96] Helena Laboratories, 1530 Lindbergh Dr. P.O. Box 752, Beaumont, Texas 77704 USA. *AggRAM^{TM}System Operator's Manual*, Nov 2013.

[97] R. Hellmuth, M. S. Bruzzi, and N. J. Quinlan. Analysis of Shear-Induced Platelet Aggregation and Breakup. *Annals of biomedical engineering*, jul 2015.

[98] H. C. Hemker and F. I. Ataullakhanov. Good Mathematical Practice: Simulation of the Hemostatic-Thrombotic Mechanism, a Powerful Tool but One That Must Be Used with Circumspection. *Pathophysiology of Haemostasis and Thrombosis*, 34(2-3):55–57, 2005.

[99] M. T. Hinds, Y. J. Park, S. A. Jones, D. P. Giddens, and B. R. Alevriadou. Local hemodynamics affect monocytic cell adhesion to a three-dimensional flow model coated with E-selectin. *Journal of biomechanics*, 34(1):95–103, Jan. 2001.

[100] M. F. Hockin, K. C. Jones, S. J. Everse, and K. G. Mann. A model for the stoichiometric regulation of blood coagulation. *The Journal of biological chemistry*, 277(21):18322–33, may 2002.

[101] M. J. Hounslow, R. L. Ryall, and V. R. Marshall. A discretized population balance for nucleation, growth, and aggregation. *AIChE Journal*, 34(11):1821–1832, Nov. 1988.

[102] P. Y. Huang and J. D. Hellums. Aggregation and disaggregation kinetics of human blood platelets: Part I. Development and validation of a population balance method. *Biophysical journal*, 65(1):334–43, July 1993.

[103] P. Y. Huang and J. D. Hellums. Aggregation and disaggregation kinetics of human blood platelets: Part II. Shear-induced platelet aggregation. *Biophysical journal*, 65(1):344–53, July 1993.

[104] P. Y. Huang and J. D. Hellums. Aggregation and disaggregation kinetics of human blood platelets: Part III. The disaggregation under shear stress of platelet aggregates. *Biophysical journal*, 65(1):354–61, July 1993.

[105] S. J. Hund and J. F. Antaki. An extended convection diffusion model for red blood cell-enhanced transport of thrombocytes and leukocytes. *Physics in medicine and biology*, 54(20):6415–35, Oct. 2009.

[106] J. Hurley. Sizing particles with a Coulter counter. *Biophysical Journal*, 10(1):74, 1970.

[107] Y. Ikeda, M. Handa, K. Kawano, T. Kamata, M. Murata, Y. Araki, H. Anbo, Y. Kawai, K. Watanabe, and I. Itagaki. The role of von Willebrand factor and fibrinogen in platelet aggregation under varying shear stress. *The Journal of clinical investigation*, 87(4):1234–40, apr 1991.

[108] J. Jesty, E. Beltrami, and G. Willems. Mathematical analysis of a proteolytic positive-feedback loop: dependence of lag time and enzyme yields on the initial conditions and kinetic parameters. *Biochemistry*, 32(24):6266–74, June 1993.

[109] J. Jesty, J. Rodriguez, and E. Beltrami. Demonstration of a threshold response in a proteolytic feedback system: control of the autoactivation of factor XII. *Pathophysiology of haemostasis and thrombosis*, 34(2-3):71–9, Jan. 2005.

[110] R. J. Johnson, K. E. Burhop, and D. E. Van Epps. Infusion of ovine c5a into sheep mimics the inflammatory response of hemodialysis. *Journal of Laboratory and Clinical Medicine*, 127(5):456–469, 1996.

[111] K. C. Jones and K. G. Mann. A model for the tissue factor pathway to thrombin. II. A mathematical simulation. *The Journal of biological chemistry*, 269(37):23367–73, sep 1994.

[112] S. A. Jones. A relationship between reynolds stresses and viscous dissipation: Implications to red cell damage. *Annals of Biomedical Engineering*, 23(1):21–28, jan 1995.

[113] A. Jordan, T. David, S. Homer-Vanniasinkam, A. Graham, and P. Walker. The effects of margination and red cell augmented platelet diffusivity on platelet adhesion in complex flow. *Biorheology*, 41(5):641–53, Jan. 2004.

[114] S. W. Jordan and E. L. Chaikof. Simulated surface-induced thrombin generation in a flow field. *Biophysical journal*, 101(2):276–86, jul 2011.

[115] J. Jung and A. Hassanein. Three-phase CFD analytical modeling of blood flow. *Medical engineering & physics*, 30(1):91–103, Jan. 2008.

[116] J. Jung, A. Hassanein, and R. W. Lyczkowski. Hemodynamic computation using multiphase flow dynamics in a right coronary artery. *Annals of biomedical engineering*, 34(3):393–407, Mar. 2006.

[117] L. C. Junqueira, J. Carneiro, and R. O'Kelley. *Basic Histology*. Appleton & Lange, 9 edition, 1998.

[118] H. Kamada, Y. Imai, M. Nakamura, T. Ishikawa, and T. Yamaguchi. Computational analysis on the mechanical interaction between a thrombus and red blood cells: Possible causes of membrane damage of red blood cells at microvessels. *Medical Engineering & Physics*, 34(10):1411–1420, 2012.

[119] S. V. Kao and S. G. Mason. Dispersion of particles by shear. *Nature*, 253(5493):619–621, Feb. 1975.

[120] T. Karino and H. L. Goldsmith. Adhesion of human platelets to collagen on the walls distal to a tubular expansion. *Microvascular research*, 17(3 Pt 1):238–62, May 1979.

[121] T. Karino and H. L. Goldsmith. Aggregation of human platelets in an annular vortex distal to a tubular expansion. *Microvascular research*, 17(3 Pt 1):217–37, May 1979.

[122] M. Kazatchkine and M. Carreno. Activation of the complement system at the interface between blood and artificial surfaces. *Biomaterials*, 9(1):30–35, 1988.

[123] K. H. Keller. Effect of fluid shear on mass transport in flowing blood. *Federation proceedings*, 30(5):1591–9, 1971.

[124] M. Khanin, V. Leytin, and A. Popov. A mathematical model of the kinetics of platelets and plasma hemostasis system interaction. *Thrombosis Research*, 64(6):659–666, Dec. 1991.

[125] M. Khanin and V. Semenov. A mathematical model of the kinetics of blood coagulation. *Journal of Theoretical Biology*, 136(2):127–134, Jan. 1989.

[126] S. Klaus, S. Körfer, K. Mottaghy, H. Reul, and B. Glasmacher. In vitro blood damage by high shear flow: human versus porcine blood. *The International journal of artificial organs*, 25(4):306–12, apr 2002.

[127] M. Kostoglou. Extended cell average technique for the solution of coagulation equation. *Journal of colloid and interface science*, 306(1):72–81, feb 2007.

[128] M. Kostoglou and a.J. Karabelas. On the self-similarity of the aggregation-fragmentation equilibrium particle size distribution. *Journal of Aerosol Science*, 30(2):157–162, feb 1999.

[129] T. Kramer and M. Clark. Incorporation of Aggregate Breakup in the Simulation of Orthokinetic Coagulation. *Journal of colloid and interface science*, 216(1):116–126, Aug. 1999.

[130] T. Kramer and M. Clark. Modeling Orthokinetic Coagulation in Spatially Varying Laminar Flow. *Journal of colloid and interface science*, 227(2):251–261, July 2000.

[131] T. A. Kramer and M. M. Clark. Influence of Strain-Rate on Coagulation Kinetics. *Journal of Environmental Engineering*, 123(5):444–452, May 1997.

[132] W. B. Krantz. *Scaling analysis in modeling transport and reaction processes: a systematic approach to model building and the art of approximation*. John Wiley & Sons, Inc., Hoboken, USA, 2007.

[133] M. H. Kroll, J. D. Hellums, L. V. McIntire, A. I. Schafer, and J. L. Moake. Platelets and shear stress. *Blood*, 88(5):1525–41, Sept. 1996.

[134] A. L. Kuharsky and A. L. Fogelson. Surface-mediated control of blood coagulation: the role of binding site densities and platelet deposition. *Biophysical journal*, 80(3):1050–74, mar 2001.

[135] S. Kulkarni, S. M. Dopheide, C. L. Yap, C. Ravanat, M. Freund, P. Mangin, K. A. Heel, A. Street, I. S. Harper, F. Lanza, and S. P. Jackson. A revised model of platelet aggregation. *Journal of Clinical Investigation*, 105(6):783–791, mar 2000.

[136] S. Kumar and D. Ramkrishna. On the solution of population balance equations by discretizationI. A fixed pivot technique. *Chemical Engineering Science*, 51(8):1311–1332, apr 1996.

[137] T. C. Lamson, G. Rosenberg, D. B. Geselowitz, S. Deutsch, D. R. Stinebring, J. A. Frangos, and J. M. Tarbell. Relative blood damage in the three phases of a prosthetic heart valve flow cycle. *ASAIO journal (American Society for Artificial Internal Organs)*, 39(3):M626–33, 1992.

[138] R. Landolfi, R. De Cristofaro, E. De Candia, B. Rocca, and B. Bizzi. Effect of fibrinogen concentration on the velocity of platelet aggregation. *Blood*, 78(2):377–381, 1991.

[139] P. Latimer. Experimental tests of a theoretical method for predicting light scattering by aggregates. *Applied optics*, 24(19):3231, Oct. 1985.

[140] M. Lattuada, P. Sandkühler, H. Wu, J. Sefcik, and M. Morbidelli. Aggregation kinetics of polymer colloids in reaction limited regime: experiments and simulations. *Advances in colloid and interface science*, 103(1):33–56, Mar. 2003.

[141] J. H. Lawson, M. Kalafatis, S. Stram, and K. G. Mann. A model for the tissue factor pathway to thrombin. I. An empirical study. *The Journal of biological chemistry*, 269(37):23357–66, sep 1994.

[142] K. Leiderman and A. L. Fogelson. Grow with the flow: a spatial-temporal model of platelet deposition and blood coagulation under flow. *Mathematical medicine and biology : a journal of the IMA*, 28(1):47–84, Mar. 2011.

[143] S. N. Levine. Enzyme amplifier kinetics. *Science (New York, N.Y.)*, 152(3722):651–3, Apr. 1966.

[144] M. Y. Lin, H. M. Lindsay, D. A. Weitz, R. C. Ball, R. Klein, and P. Meakin. Universality in colloid aggregation. *Nature*, 339(6223):360–362, June 1989.

[145] Linkam Scientific Instruments. *CSS450 - Optical Rheology Systems*. Albury Mill, Mill Lane, Chilworth, Guildford, Surrey GU4 8RU, England.

[146] M. Long, H. L. Goldsmith, D. F. Tees, and C. Zhu. Probabilistic modeling of shear-induced formation and breakage of doublets cross-linked by receptor-ligand bonds. *Biophysical journal*, 76(2):1112–28, feb 1999.

[147] T. G. Loof, M. Mörgelin, L. Johansson, S. Oehmcke, A. I. Olin, G. Dickneite, A. Norrby-Teglund, U. Theopold, and H. Herwald. Coagulation, an ancestral serine protease cascade, exerts a novel function in early immune defense. *Blood*, 118(9):2589–2598, 2011.

[148] R. G. Macfarlane. An Enzyme Cascade in the Blood Clotting Mechanism, and its Function as a Biochemical Amplifier. *Nature*, 202(4931):498–499, May 1964.

[149] C. Macilwain. Systems Biology: Evolving Into the Mainstream. *Cell*, 144(6):839–41, 2011.

[150] G. A. Marguerie, E. F. Plow, T. S. Edgington, J. B. Chem, and F. Plow. Human platelets possess an inducible and saturable receptor specific for fibrinogen . Human Platelets for Fibrinogen * Possess an Inducible and Saturable. *The Journal of biological chemistry*, 254(12):5357–5363, 1979.

[151] J. N. Marhefka, R. Zhao, Z. J. Wu, S. S. Velankar, J. F. Antaki, and M. V. Kameneva. Drag reducing polymers improve tissue perfusion via modification of the RBC traffic in microvessels. *Biorheology*, 46(4):281–92, Jan. 2009.

[152] M. M. Markiewski, B. Nilsson, K. N. Ekdahl, T. E. Mollnes, and J. D. Lambris. Complement and coagulation: strangers or partners in crime? *Trends in immunology*, 28(4):184–92, apr 2007.

[153] F. Martorana and A. Moro. On the kinetics of enzyme amplifier systems with negative feedback. *Mathematical Biosciences*, 21(1-2):77–84, Oct. 1974.

[154] M. Massoudi, J. Kim, and J. F. Antaki. Modeling and numerical simulation of blood flow using the Theory of Interacting Continua. *International journal of non-linear mechanics*, 47(5):506–520, June 2012.

[155] J. L. Moake, N. a. Turner, N. a. Stathopoulos, L. Nolasco, and J. D. Hellums. Shear-induced platelet aggregation can be mediated by vWF released from platelets, as well as by exogenous large or unusually large vWF multimers, requires adenosine diphosphate, and is resistant to aspirin. *Blood*, 71(5):1366–74, may 1988.

[156] J. L. Moake, N. A. Turner, N. A. Stathopoulos, L. H. Nolasco, and J. D. Hellums. Involvement of large plasma von Willebrand factor (vWF) multimers and unusually large vWF forms derived from endothelial cells in shear stress-induced platelet aggregation. *The Journal of clinical investigation*, 78(6):1456–61, Dec. 1986.

[157] G. Moiseyev and P. Z. Bar-Yoseph. Computational modeling of thrombosis as a tool in the design and optimization of vascular implants. *Journal of Biomechanics*, 46(2):248–252, Jan. 2013.

[158] A. Moro and A. Bharucha-reid. On the kinetics of enzyme amplifier systems. *Mathematical Biosciences*, 5(3-4):391–402, Nov. 1969.

[159] K. Murphy, P. Travers, M. Walport, and C. Janeway. *Janeway's immunobiology*. Janeway's Immunobiology. Garland Science, 7 edition, 2008.

[160] J. F. Mustard, R. L. Kinlough-Rathbone, M. A. Packham, D. W. Perry, E. J. Harfenist, and K. R. Pai. Comparison of fibrinogen association with normal and thrombasthenic platelets on exposure to ADP or chymotrypsin. *Blood*, 54(5):987–93, nov 1979.

[161] W. S. Nesbitt, E. Westein, F. J. Tovar-Lopez, E. Tolouei, A. Mitchell, J. Fu, J. Carberry, A. Fouras, and S. P. Jackson. A shear gradient-dependent platelet aggregation mechanism drives thrombus formation. *Nature medicine*, 15(6):665–73, June 2009.

[162] M. E. Nesheim, R. P. Tracy, and K. G. Mann. "Clotspeed", a mathematical simulation of the functional properties of prothrombinase. *The Journal of biological chemistry*, 259(3):1447–53, feb 1984.

[163] A. R. Nichols and H. B. Bosmann. Platelet aggregation: newly quantified using non-empirical parameters. *Thrombosis and haemostasis*, 42(2):679–93, aug 1979.

[164] B. Nilsson, K. N. Ekdahl, T. E. Mollnes, and J. D. Lambris. The role of complement in biomaterial-induced inflammation. *Molecular immunology*, 44(1):82–94, 2007.

[165] B. Nilsson, O. Korsgren, J. D. Lambris, and K. N. Ekdahl. Can cells and biomaterials in therapeutic medicine be shielded from innate immune recognition? *Trends in immunology*, 31(1):32–38, 2010.

[166] U. Nobis, A. R. Pries, G. R. Cokelet, and P. Gaehtgens. Radial distribution of white cells during blood flow in small tubes. *Microvascular research*, 29(3):295–304, May 1985.

[167] T. E. Oliphant. Python for Scientific Computing. *Computing in Science & Engineering*, 9(3):10–20, 2007.

[168] J. Pandya and L. Spielman. Floc breakage in agitated suspensions: Theory and data processing strategy. *Journal of Colloid and Interface Science*, 90(2):517–531, Dec. 1982.

[169] J. Pandya and L. Spielman. Floc breakage in agitated suspensions: Effect of agitation rate. *Chemical Engineering Science*, 38(12):1983–1992, Jan. 1983.

[170] S. Patankar and D. Spalding. A calculation procedure for heat, mass and momentum transfer in three-dimensional parabolic flows. *International Journal of Heat and Mass Transfer*, 15(10):1787–1806, oct 1972.

[171] J. M. Paulus. Platelet size in man. *Blood*, 46(3):321–36, Sept. 1975.

[172] F. Pedocchi and I. Piedra-Cueva. Camp and Steins Velocity Gradient Formalization. *Journal of Environmental Engineering*, 131(10):1369–1376, Oct. 2005.

[173] P. Pibarot and J. G. Dumesnil. Prosthetic heart valves: selection of the optimal prosthesis and long-term management. *Circulation*, 119(7):1034–48, feb 2009.

[174] A. S. Popel. Theory of oxygen transport to tissue. *Critical reviews in biomedical engineering*, 17(3):257–321, Jan. 1989.

[175] N. J. Quinlan and P. N. Dooley. Models of flow-induced loading on blood cells in laminar and turbulent flow, with application to cardiovascular device flow. *Annals of biomedical engineering*, 35(8):1347–56, aug 2007.

[176] B. D. Ratner. The catastrophe revisited: blood compatibility in the 21st Century. *Biomaterials*, 28(34):5144–7, Dec. 2007.

[177] B. D. Ratner. The biocompatibility manifesto: biocompatibility for the twenty-first century. *Journal of cardiovascular translational research*, 4(5):523–7, oct 2011.

[178] B. D. Ratner, A. S. Hoffman, F. J. Schoen, and J. E. Lemons. *Biomaterials Science*. Elsevier Academic Press, San Diego (USA), 2 edition, 2004.

[179] F. Reif. *Statistical physics*. McGraw-Hill, New York, USA, 1967.

[180] Z. M. Ruggeri. Platelet adhesion under flow. *Microcirculation (New York, N.Y. : 1994)*, 16(1):58–83, jan 2009.

[181] P. G. Saffman and J. S. Turner. On the collision of drops in turbulent clouds. *Journal of Fluid Mechanics*, 1(01):16–30, Mar. 1956.

[182] B. Savage, J. J. Sixma, and Z. M. Ruggeri. Functional self-association of von Willebrand factor during platelet adhesion under flow. *Proceedings of the National Academy of Sciences*, 99(1):425–430, jan 2002.

[183] H. Schima and G. Wieselthaler. Mechanically induced blood trauma: are the relevant questions already solved, or is it still an important field to be investigated? *Artificial organs*, 19(7):563–4, jul 1995.

[184] H. Schmid-Schoenbein, R. Wells, and R. Schildkraut. Microscopy and viscometry of blood flowing under uniform shear rate (rheoscopy). *Journal of applied physiology*, 26(5):674–8, May 1969.

[185] H. Schmid-Schönbein, E. Volger, and H. J. Klose. Microrheology and light transmission of blood. *Pflügers Archiv European Journal of Physiology*, 333(2):140–155, 1972.

[186] H. Schmid-Schönbein and R. Wells. Rheological properties of human erythrocytes and their influence upon the "anomalous" viscosity of blood. *Ergebnisse der Physiologie Reviews of Physiology*, 63:146–219, 1971.

[187] D. W. Schmidtke and S. L. Diamond. Direct observation of membrane tethers formed during neutrophil attachment to platelets or P-selectin under physiological flow. *The Journal of cell biology*, 149(3):719–30, may 2000.

[188] S. W. Schneider, S. Nuschele, A. Wixforth, C. Gorzelanny, A. Alexander-Katz, R. R. Netz, and M. F. Schneider. Shear-induced unfolding triggers adhesion of von Willebrand factor fibers. *Proceedings of the National Academy of Sciences of the United States of America*, 104(19):7899–903, May 2007.

[189] W. Schroeder, K. Martin, and B. Lorensen. *The Visualization Toolkit*. Kitware, 4 edition, 2006.

[190] K. Schulz-Heik, J. Ramachandran, D. Bluestein, and J. Jesty. The extent of platelet activation under shear depends on platelet count: differential expression of anionic phospholipid and Factor Va. *Pathophysiology of Haemostasis and Thrombosis*, 34(6):255–262, 2005.

[191] G. Segré and A. Silberberg. Behaviour of macroscopic rigid spheres in Poiseuille flow Part 1. Determination of local concentration by statistical analysis of particle passages through crossed light beams. *Journal of Fluid Mechanics*, 14(1):115–135, Mar. 1962.

[192] G. Segré and A. Silberberg. Behaviour of macroscopic rigid spheres in Poiseuille flow Part 2. Experimental results and interpretation. *Journal of Fluid Mechanics*, 14(1):136–157, 1962.

[193] H. Shankaran, P. Alexandridis, and S. Neelamegham. Aspects of hydrodynamic shear regulating shear-induced platelet activation and self-association of von Willebrand factor in suspension. *Blood*, 101(7):2637–45, apr 2003.

[194] J. Sheriff, D. Bluestein, G. Girdhar, and J. Jesty. High-shear stress sensitizes platelets to subsequent low-shear conditions. *Annals of biomedical engineering*, 38(4):1442–50, may 2010.

[195] J. Sheriff, J. S. Soares, M. Xenos, J. Jesty, and D. Bluestein. Evaluation of shear-induced platelet activation models under constant and dynamic shear stress loading conditions relevant to devices. *Annals of biomedical engineering*, 41(6):1279–96, jun 2013.

[196] A. M. Shibeko, E. S. Lobanova, M. A. Panteleev, and F. I. Ataullakhanov. Blood flow controls coagulation onset via the positive feedback of factor VII activation by factor Xa. *BMC systems biology*, 4:5, Jan. 2010.

[197] J. M. Siller-Matula, M. Schwameis, A. Blann, C. Mannhalter, and B. Jilma. Thrombin as a multi-functional enzyme. Focus on in vitro and in vivo effects. *Thrombosis and haemostasis*, 106(6):1020–33, Dec. 2011.

[198] I. Singh, E. Themistou, L. Porcar, and S. Neelamegham. Fluid shear induces conformation change in human blood protein von Willebrand factor in solution. *Biophysical journal*, 96(6):2313–20, mar 2009.

[199] T. Skorczewski, L. C. Erickson, and A. L. Fogelson. Platelet motion near a vessel wall or thrombus surface in two-dimensional whole blood simulations. *Biophysical journal*, 104(8):1764–72, Apr. 2013.

[200] S. Slomkowski, J. V. Alemán, R. G. Gilbert, M. Hess, K. Horie, R. G. Jones, P. Kubisa, I. Meisel, W. Mormann, S. Penczek, and R. F. T. Stepto. Terminology of polymers and polymerization processes in dispersed systems (IUPAC

Recommendations 2011). *Pure and Applied Chemistry*, 83(12):2229–2259, Sept. 2011.

[201] M. Soos, J. Sefcik, and M. Morbidelli. Investigation of aggregation, breakage and restructuring kinetics of colloidal dispersions in turbulent flows by population balance modeling and static light scattering. *Chemical Engineering Science*, 61(8):2349–2363, Apr. 2006.

[202] C. M. Sorensen. The Mobility of Fractal Aggregates: A Review. *Aerosol Science and Technology*, 45(7):765–779, July 2011.

[203] E. N. Sorensen, G. W. Burgreen, W. R. Wagner, and J. F. Antaki. Computational simulation of platelet deposition and activation: I. Model development and properties. *Annals of biomedical engineering*, 27(4):436–48, 1999.

[204] E. N. Sorensen, G. W. Burgreen, W. R. Wagner, and J. F. Antaki. Computational simulation of platelet deposition and activation: II. Results for Poiseuille flow over collagen. *Annals of biomedical engineering*, 27(4):449–58, 1999.

[205] P. T. Spicer and S. E. Pratsinis. Coagulation and fragmentation: Universal steady-state particle-size distribution. *AIChE Journal*, 42(6):1612–1620, June 1996.

[206] P. T. Spicer, S. E. Pratsinis, J. Raper, R. Amal, G. Bushell, and G. Meesters. Effect of shear schedule on particle size, density, and structure during flocculation in stirred tanks. *Powder Technology*, 97(1):26–34, June 1998.

[207] P. T. Spicer, S. E. Pratsinis, M. D. Trennepohl, and G. H. M. Meesters. Coagulation and Fragmentation: The Variation of Shear Rate and the Time Lag for Attainment of Steady State. *Industrial & Engineering Chemistry Research*, 35(9):3074–3080, jan 1996.

[208] T. A. Springer. von Willebrand factor, Jedi knight of the bloodstream. *Blood*, 124(9):1412–1425, aug 2014.

[209] L. W. Stevenson, L. W. Miller, P. Desvigne-Nickens, D. D. Ascheim, M. K. Parides, D. G. Renlund, R. M. Oren, S. K. Krueger, M. R. Costanzo, L. S. Wann, R. G. Levitan, D. Mancini, and REMATCH Investigators. Left ventricular assist device as destination for patients undergoing intravenous inotropic therapy: a subset analysis from REMATCH (Randomized Evaluation of Mechanical Assistance in Treatment of Chronic Heart Failure). *Circulation*, 110(8):975–81, aug 2004.

[210] S. Tang, Y. Ma, and C. Shiu. Modelling the mechanical strength of fractal aggregates. *Colloids and Surfaces A: Physicochemical and Engineering Aspects*, 180(1-2):7–16, May 2001.

[211] G. J. Tangelder, D. W. Slaaf, H. C. Teirlinck, R. Alewijnse, and R. S. Reneman. Localization within a thin optical section of fluorescent blood platelets flowing in a microvessel. *Microvascular Research*, 23(2):214–230, May 1982.

[212] H. te Velthuis, P. G. Jansen, C. E. Hack, L. Eijsman, and C. R. Wildevuur. Specific complement inhibition with heparin-coated extracorporeal circuits. *The Annals of thoracic surgery*, 61(4):1153–1157, 1996.

[213] P. Tengvall, A. Askendal, and I. Lundström. Ellipsometric in vitro studies on the activation of complement by human immunoglobulins m and g after adsorption to methylated silicon. *Colloids and Surfaces B: Biointerfaces*, 20(1):51–62, 2001.

[214] K. Tesch. Generalised Herschel Model Applied to Blood Flow Modelling. *TASK Quarterly*, 16(3-4):253–262, 2012.

[215] K. Tesch. On Invariants of Fluid Mechanics Tensors. *TASK Quarterly*, 17(3-4):223–230, 2014.

[216] a. a. Tokarev, a. a. Butylin, and F. I. Ataullakhanov. Platelet adhesion from shear blood flow is controlled by near-wall rebounding collisions with erythrocytes. *Biophysical journal*, 100(4):799–808, feb 2011.

[217] F. J. Tovar-Lopez, G. Rosengarten, E. Westein, K. Khoshmanesh, S. P. Jackson, A. Mitchell, and W. S. Nesbitt. A microfluidics device to monitor platelet aggregation dynamics in response to strain rate micro-gradients in flowing blood. *Lab on a chip*, 10(3):291–302, feb 2010.

[218] V. T. Turitto, A. M. Benis, and E. F. Leonard. Platelet Diffusion in Flowing Blood. *Industrial & Engineering Chemistry Fundamentals*, 11(2):216–223, May 1972.

[219] R. L. K. Virchow. Thrombose und Embolie. Gefässentzündung und septische Infektion. In *Gesammelte Abhandlungen zur Wissenschaftlichen Medizin*, chapter 4, pages 219–729. Meindinger Sohn & Comp., Frankfurt (Germany), 1856.

[220] M. R. von Smoluchowski. Zur kinetischen Theorie der Brownschen Molekularbewegung und der Suspensionen. *Annalen der Physik*, 326(14):756–780, 1906.

[221] M. R. von Smoluchowski. Über Brownsche Molekularbewegung unter Einwirkung äußerer Kräfte und deren Zusammenhang mit der verallgemeinerten Diffusionsgleichung. *Annalen der Physik*, 353(24):1103–1112, 1916a.

[222] M. R. von Smoluchowski. Drei Vorträge über Diffusion, Brownsche Molekularbewegung und Koagulation von Kolloidteilchen. *Physikalische Zeitschrift*, 17:585–599, 1916b.

[223] M. R. von Smoluchowski. Versuch einer mathematischen Theorie der Koagulationskinetik kolloider Lösungen. *Zeitschrift fuer physikalische Chemie*, 92(1912):129–168, 1917.

[224] N.-H. L. Wang and K. Keller. Augmented transport of extracellular solutes in concentrated erythrocyte suspensions in couette flow. *Journal of Colloid and Interface Science*, 103(1):210–225, Jan. 1985.

[225] S. P. Watson and K. S. Authi. *Platelets: A Practical Approach*. Practical approach series. IRL Press at Oxford University Press, Oxford, UK, 1996.

[226] H. G. Weller and G. Tabor. A tensorial approach to computational continuum mechanics using object-oriented techniques. *Computers in Physics*, 12(6):620–631, 1998.

[227] E. Westein, A. D. van der Meer, M. J. E. Kuijpers, J.-P. Frimat, A. van den Berg, and J. W. M. Heemskerk. Atherosclerotic geometries exacerbate pathological thrombus formation poststenosis in a von Willebrand factor-dependent manner. *Proceedings of the National Academy of Sciences of the United States of America*, 110(4):1357–62, jan 2013.

[228] J. G. White. Morphology and ultrastructure of platelets. In P. Gresele, P. C. Page, V. Fuster, and J. Vermylen, editors, *Platelets in Thrombotic and Non-Thrombotic Disorders Pathophysiology, Pharmacology and Therapeutics*, chapter 3, pages 41–69. Cambridge University Press, Cambridge (UK), 2002.

[229] G. M. Willems, T. Lindhout, W. T. Hermens, and H. C. Hemker. Simulation model for thrombin generation in plasma. *Haemostasis*, 21(4):197–207, Jan. 1991.

[230] D. F. Williams. Definitions in biomaterials. In *Proceedings of a Consensus Conference of the European Society for Biomaterials*, Chester, United Kingdom, March 1987. Elsevier Science Limited.

[231] D. F. Williams. On the mechanisms of biocompatibility. *Biomaterials*, 29(20):2941–2953, 2008.

[232] D. M. Wootton and D. N. Ku. Fluid mechanics of vascular systems, diseases, and thrombosis. *Annual Review of Biomedical Engineering*, 1:299–329, 1999.

[233] J. Wu, J. F. Antaki, T. A. Snyder, W. R. Wagner, H. S. Borovetz, and B. E. Paden. Design optimization of blood shearing instrument by computational fluid dynamics. *Artificial organs*, 29(6):482–9, June 2005.

[234] W.-T. Wu, N. Aubry, and M. Massoudi. On the coefficients of the interaction forces in a two-phase flow of a fluid infused with particles. *International Journal of Non-Linear Mechanics*, 59:76–82, Jan. 2014.

[235] W.-T. Wu, F. Yang, J. F. Antaki, N. Aubry, and M. Massoudi. Study of blood flow in several benchmark micro-channels using a two-fluid approach. *International journal of engineering science*, 95:49–59, Oct. 2015.

[236] Z. Xia and M. M. Frojmovic. Aggregation efficiency of activated normal or fixed platelets in a simple shear field: effect of shear and fibrinogen occupancy. *Biophysical journal*, 66(6):2190–201, jun 1994.

[237] Z. Xu, N. Chen, S. Shadden, and J. Marsden. Study of blood flow impact on growth of thrombi using a multiscale model. *Soft Matter*, 5:769–779, 2009.

[238] K. Yeleswarapu, M. Kameneva, K. Rajagopal, and J. Antaki. The flow of blood in tubes: theory and experiment. *Mechanics Research Communications*, 25(3):257–262, May 1998.

[239] V. I. Zarnitsina, F. I. Ataullakhanov, a. I. Lobanov, and O. L. Morozova. Dynamics of spatially nonuniform patterning in the model of blood coagulation. *Chaos (Woodbury, N.Y.)*, 11(1):57–70, mar 2001.

[240] V. I. Zarnitsina, A. V. Pokhilko, and F. I. Ataullakhanov. A mathematical model for the spatio-temporal dynamics of intrinsic pathway of blood coagulation. I. The model description. *Thrombosis research*, 84(4):225–36, nov 1996.

[241] V. I. Zarnitsina, A. V. Pokhilko, and F. I. Ataullakhanov. A mathematical model for the spatio-temporal dynamics of intrinsic pathway of blood coagulation. II. Results. *Thrombosis research*, 84(5):333–44, dec 1996.

[242] J.-n. Zhang, A. L. Bergeron, Q. Yu, C. Sun, L. V. McIntire, J. A. López, and J.-f. Dong. Platelet aggregation and activation under complex patterns of shear stress. *Thrombosis and haemostasis*, 88(5):817–21, nov 2002.

[243] R. Zhao, M. V. Kameneva, and J. F. Antaki. Investigation of platelet margination phenomena at elevated shear stress. *Biorheology*, 44(3):161–77, Jan. 2007.

[244] P. Zilla, J. Brink, P. Human, and D. Bezuidenhout. Prosthetic heart valves: catering for the few. *Biomaterials*, 29(4):385–406, Feb. 2008.

[245] A. L. Zydney and C. K. Colton. Augmented solute transport in the shear flow of a concentrated suspension. *PCH, PhysicoChemical Hydrodynamics*, 10(1):77–96, 1988.